
This item was submitted to [Loughborough's Research Repository](#) by the author.
Items in Figshare are protected by copyright, with all rights reserved, unless otherwise indicated.

A self-exciting system for percussive–rotary drilling

PLEASE CITE THE PUBLISHED VERSION

PUBLISHER

© A.D.L. Batako

PUBLISHER STATEMENT

This work is made available according to the conditions of the Creative Commons Attribution-NonCommercial-NoDerivatives 4.0 International (CC BY-NC-ND 4.0) licence. Full details of this licence are available at:
<https://creativecommons.org/licenses/by-nc-nd/4.0/>

LICENCE

CC BY-NC-ND 4.0

REPOSITORY RECORD

Batako, Andre D.L.. 2019. "A Self-exciting System for Percussive–rotary Drilling". figshare.
<https://hdl.handle.net/2134/34082>.



University Library

Author/Filing Title **BATAVO**

Class Mark **T**

Please note that fines are charged on ALL
overdue items.

--	--	--

0402948173



A SELF-EXCITING SYSTEM FOR PERCUSSIVE-ROTARY DRILLING

By

André Danonu Lignanmatéh Batako

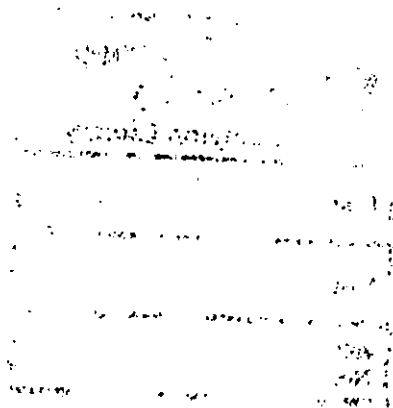
A DOCTORAL THESIS

Submitted in partial fulfilment of the requirement
For the Award of Doctor of Philosophy,
Loughborough University

© By A D L BATAKO, 2003.

ACKNOWLEDGEMENT

I would like to express my sincere gratitude to the British Gas Technology Research Centre and the Engineering Faculty of Loughborough University for the financial support of the project. My deep respect and thanks is expressed to Prof. Babitsky for his expertise, guidance, help and support throughout these years, and to my Director of Research, Prof. Halliwell the former Dean of Engineering for his help. I would like to thank Dr. T. Chung and Dr. S. Rothberg for their help and encouragement during this work. Equally, my gratitude is expressed to Mr. J. Guy, R. Potter and other technical staff of the Mechanical Engineering Department for their continuous technical assistance. I am thankful to Mr. D. Spendlove of the Civil Engineering Department for his assistance in the early experimental work. In addition, I would like to thank the Department of Electrical Engineering for providing appropriate technical equipment for experimental work.



ABSTRACT


A dynamic model for a new principle of self-excited percussive - rotary drilling is presented. The system uses the stick-slip phenomenon to generate an impact action superimposed on the drilling process. This is a strongly nonlinear mechanical system with two-degrees-of-freedom, in which friction-induced vibration is used for excitation of impacts. The model has to take account of the returning effect that the impacts have on the parameters of stick-slip motion. The model incorporates friction force as a function of sliding velocity, where the self-excitation of coupled vibration of the rotating bit and the striker tend to a steady-state periodic cycle. Dynamic coupling of vibro-impact action with the stick-slip process brings innovative adaptive features into the drilling process.

The dynamic behaviour of the system with and without impact is studied numerically. Special attention is given to the analysis of the relationship between the sticking and the impacting phase of the process to achieve an optimal drilling performance. This research gives the understanding of mechanics of the percussive - rotary drilling and the design of new drilling tools with advanced characteristics. Conventional rotary - percussive drilling requires two independent actuators and a special control for synchronisation of impact and sliding. In the approach presented here, a combined complex interaction of drill bit and striker is synchronised by a single rotating drive, allowing for the self-adjustment of vibro-impact activities.

The penetration of a drilling tool into a hard medium under periodic impact action is analysed. A phenomenological visco-elasto-plastic model of the media is used. The system response is studied numerically, first as a forced vibration and second as a result of the self-excited vibro-impact process. Some relief of the main drive was obtained and an increase in the rate of penetration was observed with increased impact intensity and hardening of the medium. Results of the preliminary drilling experiment with superimposed dynamic action have shown an improvement in the rate of penetration.

Content

Chapter 1	Introduction	1
1.	Importance of Drilling	1
2.	Research objectives	5
3.	Thesis outline	7
Chapter 2	Background to Drilling	2-1
1.	Historical Development of Drilling	2-1
2.	Percussive Drilling	2-3
2.1	The Cutting Tool	2-4
3.	Rotary Drilling	2-6
3.1	The Tool	2-8
3.2	Development of Down the Hole Motors	2-11
3.3	Rotary Drilling with Down the Hole Motors	2-12
4.	Combined Techniques	2-13
5.	Drilling Fluid	2-13
6.	Choice of Drilling Method	2-15
Chapter 3	Friction Modelling	3-1
1.	Introduction	3-1
2.	Mechanism of Contact Friction Induced Vibration	3-7
2.1	Phenomenological Description of the Friction using Impact Approach	3-7
2.2	The Origin of Lifting Phenomenon in Dry Friction	3-13
3.	Modelling of Dry Friction	3-16
3.1	Friction Characteristics – Category I	3-16
3.2	Friction Characteristics – Category II	3-18
3.3	Friction Characteristics – Category III	3-18
3.4	Friction Characteristics – Category IV	3-20
3.5	Friction Characteristics – Category V	3-21

 Loughborough University Pillington Library
Date <i>Aug 01</i>
Class
Acc No. <i>040294417</i>

2.1	Historical Evolution	5-2
2.2	Vibro-Impact Systems	5-6
2.3	Dynamic Model of Vibro-Impact System	5-9
3.	The Self-Excited System of Percussive-Rotary Drilling	5-12
3.1	Mechanical Model of The System	5-14
3.2	Characteristic of Friction Force	5-16
3.3	Equation of Motion	5-16
4.	Analysis of System Frequency Response without Impact	5-17
4.1	Numerical Simulation Of The System Motion without Impact	5-19
4.2	Identification of the System Synchronisation Frequency	5-20
5.	Discussion	5-47
6.	Vibro-impact Motion with Dry Friction	5-49
6.1	Numerical Solutions of the System in Vibro-Impact Motion	5-52
6.2	Effect of Frequency Ratio on the System in Vibro-Impact Motion	5-58
6.2.1	System Response for Values of $\gamma < 0.6$	5-58
6.2.2	System Response for $0.6 \leq \gamma \leq 0.8$	5-64
6.2.3	Remarks	5-74
6.2.4	System Response for $\gamma > 0.8$	5-74
6.3	Influence of Mass Ratio on the System in Vibro-Impact Motion	5-79
6.3.1	System Response for $\beta \in [0.1, 0.25]$	5-79
6.3.2	System Response for $\beta \in [0.25, 0.6]$	5-81
6.3.3	System Response for $\beta \in [0.7, 1[$	5-82
6.3.4	System Response for $\beta \geq 1.0$	5-82
6.3.5	Remarks	5-84
7.	Discussion	5-84

Chapter 6 Vibro-Impact Penetration of the Self-Excited Drill Bit **6-1**

1.	Introduction	6-1
2.	Early Vibro-Impact Penetration Concepts	6-1
3.	The Percussive-Rotary Drilling	6-3

3.1	Description of the Model of Impact Penetration	6-5
3.2	Equations of the System Motion	6-9
4.	Study of the Response of the System	6-10
4.1	Amplitude-Frequency Response with a Sweep-Sine Test	6-12
4.1.1	Remarks	6-15
4.2	Study of the System under Impact Loading.	6-15
4.2.1	Damped Motion of the System	6-18
4.2.2	Dynamic Effect of Impact Loading	6-20
4.2.3	Relationship Between Rock Stiffness and Rate of Penetration	6-22
4.2.4	Effect of Impact Frequency on the Penetration Rate	6-29
4.2.5	Influence of the Magnitude of Impact Force on Penetration	6-32
5.	Discussion	6-34
6.	Response of the self-Oscillatory System	6-36
7.	Discussion	6-45
Chapter 7	Conclusion	7-1
Chapter 8	Recommendation for Future Work	8-1
References		8-2

Appendices

Appendix 1	Published Papers and Views of Experts
Appendix 2	Actual View of the Drilling Rig
Appendix 3	Sample Programmes in MatLab Code
Appendix 4	Results of Rock Samples Test
Appendix 5	Further Simulation Results from Chapter 5
Appendix 6	Further Simulation Results from Chapter 6

List of Figures

Figure 2.1:	Main components of a percussive drill; (Beccue)	2-5
Figure 2.2:	Down The Hole Hammer, (Drillers Training)	2-5

Figure 2.3: a.- full-head bit with inserts; b.- button bit; (Chugh, 1985)	2-5
Figure 2.4: Rotary drilling system, (Chilingarian, et al)	2-7
Figure 2.5 Rotary drilling tools;	2-9
Figure 2.6: Rotary drilling tools, (Nougaro)	2-9
Figure 2.7: Main components of tricone bit, (smith tools)	2-10
Figure 2. 8: Setting of the rolling cones in a tricone bit, (Smith Tools).	2-10
Figure 2.9: Layout of the rolling cones, (Chugh)	2-10
Figure 3.1: Block riding on a belt	3-8
Figure 3.2: Sketch of compaction of asperity (after Tolstoi, 1967)	3-8
Figure 3.3: Micro-impact of asperities	3-8
Figure 3.4 Single asperity sliding over rough surface	3-10
Figure 3.5: Development of the vibration of the slider	3-10
Figure 3.6: Collision of a ball onto an inclined surface	3-10
Figure 3.7: Surface roughness in static and smooth slip phases.	3-17
Figure 3.8: Type of friction characteristics in category I	3-17
Figure 3.9: Type of friction characteristics in category II	3-17
Figure 3.10: Type of friction characteristics in category III	3-19
Figure 3.11: Type of friction characteristics in category IV	3-19
Figure 3.12: Sketch of block sliding over roughness represented as bristles	3-19
Figure 3.13: Type of friction characteristics in category v	3-23
Figure 3.14: Deformation of asperities for high velocity.	3-23
Figure 3.15: Interface model with pre-slip elastic deformation.	3-23
Figure 4.1: Flow diagram of the experiment.	4-3
Figure 4.2: Drill hub (left) and tricone bit (right)	4-3
Figure 4.3: Bit-hub-shaft assembly	4-6
Figure 4.4: Loading conveyor	4-6
Figure 4. 5: Schematics of the test rig	4-7
Figure 4.6: Left- phototransistor; right- principle of operation.	4-10
Figure 4.7: Set up of the opto-switch for rpm measurement	4-10
Figure 4.8: Digital display of the actual shaft speed	4-10
Figure 4.9: Current probe in the motor control unit	4-12

Figure 4.10: Screenshot of the Waveview software	4-17
Figure 4.11: Methods of testing rock strength, (Brown, 1981).	4-20
Figure 4.12: Core samples after UCS test.	4-20
Figure 4.13: Cutting action of a roller bit.	4-24
Figure 4.14: Borehole pattern	4-24
Figure 4.15: Typical signal of the weight on bit from experiment.	4-27
Figure 4.16: Actual signal of the penetration in sandstone.	4-27
Figure 4.17: Penetration rate in sandstone.	4-29
Figure 4. 18: Rate of penetration in limestone.	4-29
Figure 4.19: Rate of penetration in sandstone as a function of load	4-30
Figure 4.20: Penetration rate in limestone as a function of load	4-30
Figure 4.21: Actual signal of the weight on bit (3kN applied, 100rpm).	4-32
Figure 4.22: signal of the actuator displacement (WOB=3kN, 100rpm).	4-34
Figure 4.23: penetration into sandstone at different speed.	4-35
Figure 4.24: penetration into limestone at different speed.	4-36
Figure 4.25: drilling without flushing fluid.	4-38
Figure 4.26: Rate of penetration in sandstone.	4-38
Figure 4.27: Rate of penetration in limestone.	4-39
Figure 4.28: Test drilling rendering with a broken bit	4-39
Figure 4.29: Drilling in sandstone with vibration at 10hz.	4-42
Figure 4.30: Drilling in sandstone at 50rpm with and without vibration.	4-42
Figure 4.31: Drilling in sandstone with vibration at 10hz and 15hz.	4-43
Figure 4.32: Drilling in limestone with vibration at 15hz.	4-43
Figure 4.33: Rate of penetration in sandstone, drilling with and without vibration	4-45
Figure 4.34: Rate of penetration in limestone, drilling with and without vibration	4-45
Figure 4.35: Power at zero load on the bit.	4-47
Figure 4.36: Power with increasing weight on bit.	4-47
Figure 4.37: Power with increasing speed of rotation.	4-48
Figure 4.38: Compare vibro-power for sandstone.	4-48
Figure 4.39: Compare vibro-power limestone.	4-49

Figure 5.1: SDOF impact model after Tsaplin	5-5
Figure 5.2: Force vibrated ball, Kobrinskii (1969)	5-5
Figure 5.3: a- 2DOF system; b- dynamic equivalent, (Tsaplin)	5-5
Figure 5.4: Various arrangements of vibro-impact dampers, Babitsky (1978)	5-8
Figure 5.5: Force vibrated system with a double-sided impact, Massri (1972)	5-8
Figure 5.6: Hand-held hammer drill, Astashev et al (2000)	5-8
Figure 5.7: Linear single-sided impact oscillator	5-11
Figure 5.8: Phase portrait of system motion with impact, Babitsky (1978)	5-11
Figure 5.9: Vibro-impact regimes, Astashev et al (2000)	5-11
Figure 5.10: Typical structure of rotary drilling system	5-13
Figure 5.11: Planar model of then vibro-impact drilling system	5-13
Figure 5.12: Friction force characteristic	5-18
Figure 5.13: Equivalent model of the system without impact	5-18
Figure 5.14: Phase portrait of the bit motion	5-22
Figure 5.15: Bit frequency response	5-22
Figure 5.16: Phase portrait of the striker motion	5-23
Figure 5.17: Striker frequency response.	5-23
Figure 5.18: Friction force characteristics for various driving velocity	5-25
Figure 5.19: Bit velocity, ($v=0.5\text{m/s}$)	5-25
Figure 5.20: Bit velocity, ($v=1.5\text{m/s}$)	5-26
Figure 5.21: Bit velocity, ($v=2.5\text{m/s}$)	5-26
Figure 5.22: Settling time as a function of velocity	5-27
Figure 5.23: Velocity of the striker ($v=1.5\text{m/s}$)	5-27
Figure 5.24: Screen-shot of spectrum analyser (striker's initial displacement)	5-27
Figure 5.25: Frequency spectrum of bit velocity	5-29
Figure 5.26: Frequency spectrum of striker velocity.	5-29
Figure 5.27: Period of motion of the bit and striker	5-30
Figure 5.28: Bit absolute motion with time (zero initial condition)	5-30
Figure 5.29: Phase plot of bit in relative motion	5-32
Figure 5.30: Bit absolute motion with time ($x_1(0) = 0.010$, $v_1(0) = 3.5\text{m/s}$)	5-32
Figure 5.31: Stable limit cycle	5-32

Figure 5.32: Evolution of force of friction with stick-slip self-excitation	5-33
Figure 5.33 Force of friction and bit velocity in steady state periodic motion	5-33
Figure 5.34: Bit frequency response for $\beta=0.3$, $\gamma=0.8$ and $v=0.8\text{m/s}$	5-36
Figure 5.35: Phase plot of bit motion for $\beta=0.3$, $\gamma=0.8$ and $v=0.8\text{m/s}$	5-36
Figure 5.36: Striker frequency response for $\beta=0.3$, $\gamma=0.8$ and $v=0.8\text{m/s}$	5-37
Figure 5.37: System stabilisation time: $v=1.5\text{m/s}$ $\gamma=0.1, 0.5, 0.8$	5-37
Figure 5.38: Settling time as a function of frequency ratio	5-38
Figure 5.39: Decaying vibration for $v=1.5\text{m/s}$, $\gamma=0.9$	5-38
Figure 5.40: Decaying vibration for $v=1.5\text{m/s}$, $\gamma=1.2$	5-38
Figure 5.41: Bit velocity and frequency spectrum for $\gamma=1.2$, $v=0.5\text{m/s}$	5-40
Figure 5.42: Bit and striker motion for $\beta=0.3$ and $\gamma=1.0$	5-40
Figure 5.43: Bit and striker motion for $\beta=0.3$ and $\gamma=1.0$	5-40
Figure 5.44: Phase portrait of striker motion for $\beta=0.3$ and $\gamma=10$	5-42
Figure 5.45: Phase portrait of striker motion for $\beta=0.3$ and $\gamma=3$	5-42
Figure 5.46: Phase portrait of bit motion for $\beta=0.3$ and $\gamma=3$	5-43
Figure 5.47: Phase portrait of bit motion for $\beta=0.3$ and $\gamma=9$	5-43
Figure 5.48: Bit motion with time for $\beta=0.4$ and $\gamma=1.2$	5-45
Figure 5.49: Phase portrait of striker motion for $\beta=0.4$ and $\gamma=1.2$	5-46
Figure 5.50: Time history of the bit motion and frequency spectrum for $\beta=0.4$ and $\gamma=1.2$	5-46
Figure 5.51: Typical impact force obtained from equation (5.18)	5-51
Figure 5.52: Prescribed working cycle of the system in vibro-impact regime	5-51
Figure 5.53: Velocities of the bit and striker in vibro-impact regime for $\beta=0.4$ $\gamma=0.75$ and $v=1.5\text{m/s}$	5-53
Figure 5.54: Period of bit motion in impact regime	5-54
Figure 5.55: Time contained phase plot of the bit motion	5-54
Figure 5.56: Time history of bit velocity for $\beta=0.3$, $\gamma=0.6$ and $v=0.5\text{m/s}$	5-55
Figure 5.57: Phase portrait of striker motion	5-55
Figure 5.58: Displacement and velocities of bit and striker	5-57

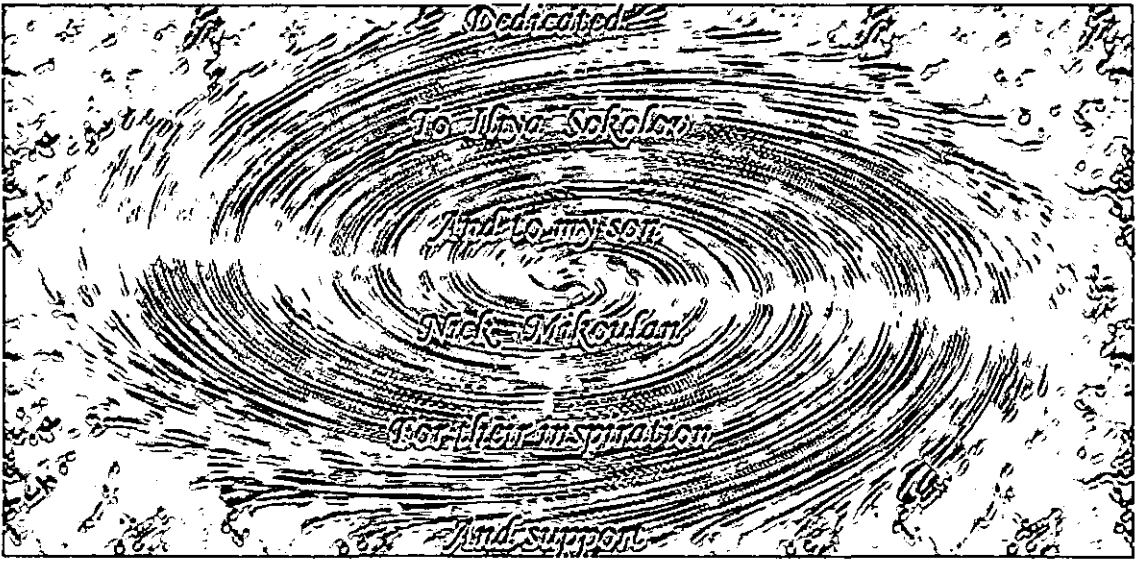
Figure 5.59: Bit absolute motion	5-57
Figure 5.60: Bit and striker displacement with velocity for $\beta=0.3$ and $\gamma=0.5$	5-59
Figure 5.61: Bit and striker displacement with velocity for $\beta=0.3$ and $\gamma=0.4$	5-59
Figure 5.62: phase portrait of bit motion for $\beta=0.3$ and $\gamma=0.4$	5-61
Figure 5.63: Phase portrait of striker motion for $\beta=0.3$ and $\gamma=0.4$	5-61
Figure 5.64: Force of impact for $\beta=0.3$ and $\gamma=0.4$	5-62
Figure 5.65: Bit and striker displacement with velocity for $\beta=0.3$ and $\gamma=0.3$	5-62
Figure 5.66: Phase portrait of striker motion for $\beta=0.3$ and $\gamma=0.3$	5-63
Figure 5.67: Displacement and velocity of bit and striker for $\beta=0.4$; $\gamma=0.6$	5-65
Figure 5.68: Phase portrait of striker and bit motion for $\beta=0.3$ and $\gamma=0.6$	5-66
Figure 5.69: Time history of striker motion with its frequency response	5-69
Figure 5.70: Displacement and velocity of bit and striker for $\beta=0.4$; $\gamma=0.8$	5-69
Figure 5.71: Phase portrait of bit and striker motion for $\beta=0.4$ and $\gamma=0.8$	5-70
Figure 5.72: Typical motion of the system	5-71
Figure 5.73: Typical bit acceleration; a.- $v=0.5\text{m/s}$; b.- $v=1.5\text{m/s}$	5-72
Figure 5.74: Typical impact and friction force.	5-72
Figure 5.75: Phase portrait of striker and bit motion for $\beta=0.3$ and $\gamma=0.9$ and velocity profile	5-75
Figure 5.76: Phase portrait of striker and bit motion for $\beta=0.4$ and $\gamma=0.9$ and frequency profile	5-76
Figure 5.77: Displacement and velocity profile for $\beta=0.4$ a.- $\gamma=1.0$; b.- $\gamma=1.1$; c.- $\gamma=1.2$	5-78
Figure 5.78: Phase plot of bit and striker motion for $\beta=0.1$	5-80
Figure 5.79: System displacement and velocity profiles for $\beta=0.1$	5-80
Figure 5.80: Phase portrait of striker motion for $\beta=0.25, 0.5$ and 0.6	5-83
Figure 5.81: Phase plane of striker and bit motion for $\beta=0.7$	5-84
Figure 5.82: System response with PSD (a) and velocity profile (b)	5-85
Figure 5.83: System response for $\beta=1.0$	5-86
Figure 5.84: Response of the system for $\beta=1.2$	5-87

Figure 6.1: Principles of cutting in drilling	6-4
Figure 6.2: Rock fracture and rheological models	6-6
Figure 6.3: Model of penetration in Simulink	6-11
Figure 6.4: Amplitude frequency response of the system	6-13
Figure 6.5: Velocity of vibration and displacement of the dry friction element	6-13
Figure 6.6: Amplitude of bit vibratory velocity with varying stiffness k_3	6-14
Figure 6.7: Displacement of the dry friction element with varying stiffness k_3	6-14
Figure 6.8: Typical motion of the system under impact loading	6-17
Figure 6.9: Underdamped motion of the system for $\zeta=0.5$	6-17
Figure 6.10: Critically damped motion of the system, $\zeta=1.0$	6-19
Figure 6.11: Overdamped motion of the system, $\zeta=1.5$	6-19
Figure 6.12: Average force P as a function of impact force and frequency	6-21
Figure 6.13: Drive relief P/D as function of frequency and threshold force D	6-21
Figure 6.14: Response of the system when the medium is very soft; $\zeta=0.5$	6-23
Figure 6.15: Response of the system with slip initiation of dry friction; $\zeta=0.5$	6-23
Figure 6.16: Displacement of dry friction element in very soft rocks	6-25
Figure 6.17: Speed of penetration for different values of stiffness k_3	6-25
Figure 6.18: Speed of penetration for different values of stiffness k_3	6-26
Figure 6.19: Penetration rate with increasing impact frequency	6-26
Figure 6.20: Penetration rate as a function of stiffness k_3 and the relief P/D	6-28
Figure 6.21: Penetration rate for different intensity of vibration	6-30
Figure 6.22: Penetration rate as a function of α_3 and the relief P/D	6-30
Figure 6.23: Penetration rate as a function of α_3 and the threshold force D	6-31
Figure 6.24: Penetration rate for different values of impulse magnitude	6-31
Figure 6.25: Penetration as a function of frequency and impulse magnitude	6-33
Figure 6.26: Penetration rate as a function of frequency and the relief P/D	6-33
Figure 6.27: Empirical estimation of penetration rate for $I=200\text{kN}$; $k_3=50\text{MN/m}$	6-35
Figure 6.28: Simulink model of the entire system with penetration	6-37
Figure 6.29: Screenshot of simulation process	6-37

Figure 6.30: Impact force as a function of the gap Δ	6-39
Figure 6.31: Displacement of bit-medium subsystem	6-39
Figure 6.32: Rate of penetration for various values of Δ	6-40
Figure 6.33: Rate of penetration for various values of k_3	6-40
Figure 6.34: Estimation of penetration rate as a function of P/D	6-42
Figure 6.35: Phase portrait of bit motion	6-42
Figure 6.36: Phase portrait of striker motion	6-44
Figure 6.37: Bit and striker velocities and frequency spectra	6-44

Symbols and Notations

α_3	Velocity
$\beta = m_2/m_1$	Mass ratio
δ	Dirac Delta function
Δ	Gap (clearance between striker and bit)
$\gamma = \omega_2/\omega_1$	Frequency ratio
φ, θ	Phase shift
λ	Average space between asperities
ψ_3	Relative displacement
ω	Angular frequency
ζ	Damping ratio
a	Angle
A, B	Arbitrary constants
c	Viscous damping
C	Constant
D, N, P	Force
F_r	Friction force
g	Gravity acceleration
h_c, H	Height
I	Impulse
\Im	Impact force
k	Stiffness
m	Mass
R	Coefficient of restitution
T	Period
v	Drive velocity
x	Displacement
\dot{x}	Velocity
\ddot{x}	Acceleration



Chapter 1

INTRODUCTION

INTRODUCTION

1. IMPORTANCE OF DRILLING

Drilling of man made or natural rocks in mining, tunnelling, petroleum exploration, road and construction engineering requires high power input. Efficiency, speed of penetration and energy consumption are major factors of drilling technologies. The resistance of the rock formation being drilled where penetration, separation and friction play the dominant role affects these factors. The overall effectiveness of the system is affected by the ability of the drill bit and drill string to keep to a target performance that is independent of the characteristics of the rock formations.

In 2001, over 5,600 drill rigs of different categories were counted worldwide (www.worldoil.com, 2002). These included land rigs, jack-up rigs, barges, drill ships, semi-submersibles and others. There exist two groups of drilling rigs, namely land rigs and offshore rigs. The land drilling rigs are mainly rated by their power and drilling depth, whereas the offshore rigs are rated by the depth of water in which they can operate. The offshore rigs come in the form of barges, jack-ups, drill ships, semi-submersibles and platform rigs. Barges operate in shallow calm water less than 20m deep. Jack-ups are mostly utilised in water less than 100m deep. Semi-submersible and the drill ships are used in depths of over 100m.

The bits and the equipment used in drilling for gas or petroleum are expensive. The cost of operating a drilling system depends on the rate of penetration and on bit life. Short bit life or frequent breakage of the drill string increases the cost of the operation. Once a drilling rig is set up it should operate for 24 hours a day 7 days a week. Offshore drilling costs about £104.16 per minute, which is £150,000 per day. Consequently, every effort is made to minimise the breakdown and servicing time, the activities on the drilling rig are reported every quarter of an hour. On average the drilling of a production well in the North Sea with an

offshore rig costs from £6 million to £20 million and the well can be active for 20 years at production rates between 2000 and 50,000 barrels of oil per day. The expenditure on a field development can reach £20 million; however a production of 40 million barrels of oil at \$22 per barrel will bring in \$880 million or £586 million (www.lealtd.com, 2002).

Current trends of drilling require a high rate of penetration, stable operation, long bit life and reduced consumption of energy. It is known that in rock drilling, friction consumes a great amount of the energy imparted to the drilling string, and this induces complex vibration, which harms the entire system in terms of productivity and life span. Dry friction induces negative side effects such as wear, squeal, noise and self-sustained vibration. It is also known that the stick-slip motion inducing torsional vibration in drilling leads to failure of drill pipes, intensive bit wear and an increase overall cost. Drill string vibration is complex in nature, and couples axial, bending and torsional vibration.

Investigations of vibration in drilling are generally carried out by studying each aspect independently of others, namely Finnie and Bailey (1960), Pasley and Bogy (1963), Dareing and Livesayn (1968), Mitchell and Allen (1985) and Kaski (1993). Elsayed *et al* (1997) suggested a model of coupled torsional and axial vibration caused by a fluctuation in the phase angle between surface undulation and cutters. In his work, Brett (1992) suggested that the bit torque dependence on bit velocity induces identical vibration. Jansen (1991, 1992 and 1995) has studied different dynamical behaviour of drill strings such as stick-slip motion, whirling and impact on the borehole. Bit stick-slip motion has been studied by Kyllingstad and Halsey (1988). Jansen (1995) suggested an active damping system for self-excited torsional vibrations and an interesting observation he made is that at impact against borehole vibration disappears. However, he did not point out the reason for such behaviour. Measurement of drill string velocity at the surface and at the bit has shown that drilling systems exhibit properties of torsional oscillation. This means that the surface table rotates at a constant velocity whilst the bit in the hole has a vibrational motion that consists of constant speed and

superimposed torsional vibration, (Jansen, 1992). Due to heavy thrust, the bit intermittently ceases to turn and throughout the standstill time, the drill-pipe is over-torqued (up to 10,000Nm, Jansen, 1995) until the bit breaks through freely. At this last instant, the rotational speed of the bit becomes much higher than the velocity at the surface table. This kind of motion has been identified as self-excited vibration, Dawson and Spanos, 1987, Brett, 1991 and Dufeyete, 1991. The frequency of this type of vibration is about 0.05-0.5Hz, which is below the first natural frequency of drill string torsional vibration (Jansen, 1992).

In drilling technologies, there is a variety of equipment available to suit a given drilling requirement. The hammer drill and rotary drill are widely in use. In rotary drilling, cutting of rock is achieved by a rotating drill bit under thrust. Material is removed in the form of dust or chips as a result of the scraping and shearing action of the cutting edges. To obtain big chips and a high rate of penetration, more thrust is required. Hence, this method of drilling suffers from twisting, breakage of the pipes and a high level of friction. Percussion drilling is preferable in very hard sedimentary rocks because of low bit wear and fast penetration but this method cannot produce the same rate of penetration at greater depth as rotary drilling.

To eliminate the aforementioned negative aspects, improvements are constantly brought in through new concepts of drilling and new designs. These new approaches have to consider the efficient use of energy as an important factor, bringing an increase in bit life, rate of penetration and a reduced overall cost. Simple rotary and percussive hammer drilling as conventional methods have had limited success. However, the combination of simultaneous rotation and percussive action, (the concept of vibro-impact drilling) introduced in the last decades has proven to be highly effective.

The US Patent Office holds a number of patents on the subject of rotary-percussive drilling or vibratory rotary drilling. In most patents, the suggested devices for rotary-percussive drilling require two independent actuators for

rotation and impact respectively, (Fish, 1956 and Lacabanne, 1955, US pat. No 5730230, 4430926, 41665074). Some use complex mechanisms, which need special synchronisation of their co-action. Others techniques employ different fluids such as drilling mud, oil or inert gas in specially designed cavities to generate the vibratory process, US pat. No. 3105560, 4502552 and 3016098.

These techniques often do not provide means of control of the frequency of impact, except those, that use a cam to drive the percussion unit, US pat. No 5730230 and 3132702. The hardness of rock formation randomly varies in the course of drilling and it is important to adjust the parameters of the drilling system accordingly, for example the impact frequency and the energy of blow. Although these apparatuses give acceptable results, they do not incorporate mechanisms simple enough for such adjustment. The US pat. No 5730230 given to Sisler discloses an apparatus, which provides a control of the frequency of impact in the form of interchangeable cams of predefined shapes. The problem of friction and friction-induced vibration is not addressed in these techniques.

Current drilling techniques have good performance and offer satisfactory results, yet these techniques still face the problem of friction and self-adjustment to the fluctuation of the hardness of the rock formation during the drilling process. If any adjustment is provided, it requires a complete stop of the drilling system and human intervention.

The aim of this investigation is to develop a new concept of percussive-rotary drilling, which combines the advantages of both rotary and hammer drilling. This is sought by maintaining and fine-tuning the existing vibration in the process of drilling. Because torsional vibration results from the bit's stick-slip motion, a proper correlation of friction properties with the driving velocity gives an opportunity to harness the detrimental effect of stick-slip. This investigation uses the friction-induced stick-slip motion to produce a hammering effect upon the bit. The intensity of impacts is regulated by the physical properties of the formation currently being drilled. A single source of energy is used to drive the bit in

rotation causing the percussion unit to be excited by the stick-slip process. This allows the eradication of the dynamic overloading of the main drive and offers an effective protection of the drill string from hazardous vibration.

This present work proposes a “*self-oscillatory system*” for generating a coupled rotary-impact-drilling mode. This provides an adaptive feature to the drilling system whereby the intensity of vibro-impact process is regulated by resistance of the medium. The system synchronises dynamically its stick-slip and impacting actions to ensure best use of driving energy. Torsional vibration therefore, is localised at bit suspension level. Because torsional vibration results from bit stick-slip motion, which is induced by dry friction, the organised correlation of friction properties and driving velocity gives the opportunity to convert a detrimental effect into a useful process.

2. RESEARCH OBJECTIVES

The main objective of this research work is to develop a mathematical model of a vibro-impact mechanism, which exploits the work of friction in rock drilling systems as a driving force. A further aim of this investigation to develop a mathematical tool to study numerically all the parameters of such a mechanism revealing its dynamic behaviour and to open a new area for designing drilling systems.

These objectives are approached through a number of tasks.

- i) A review of the existing techniques in the field of rock drilling is carried out. In coal mining, tunnelling, water well drilling and minerals, gas and oil exploration, different equipment and methods are in use. It is vital to comprehend the basics of operation of these techniques and the principle of interaction between the tool and the medium.

- ii) Friction is dominantly involved in the drilling process; thus, it is thoroughly investigated to develop a new hypothesis of the causes of friction-induced vibration.
- iii) Vibro-impact systems are studied in order to understand their dynamic behaviour and why they are important in this investigation.
- iv) A pilot study was carried out on an experimental rig with a 72mm tricone bit. This helped to evaluate the effect of the applied vibration, which was performed by a vibration generator. A uniaxial test was made for estimating the compressive strength of the rocks used in this research.
- v) The aforementioned stages helped to develop a novel mechanism, which exhibit a vibro-impact process applicable to drilling. This mechanism was studied at this stage and the dynamic behaviour of the model was investigated.

It is hoped that the outcome of this research will be a novel approach to vibro-impact drilling, which harnesses the detrimental effect of friction-induced vibration.

- A new concept for the design of such a mechanism will be brought forward with a clear understanding of its dynamical behaviour.
- The results from the numerical analysis should provide basic material for the development of new design concepts.
- The developed model will display self-synchronising and self-adjustment properties. The activities of the vibro-impact process will be automatically adjusted by the properties of the rock formation being drilled.
- This mechanism will provide us with an advancement of knowledge and show up ways of energy saving and drill string protection compared to existing prototypes.
- The developed numerical tool will allow the defining of actual parameters of the system useful for design purpose. This tool should be able to predict the dynamic behaviour of such a system.

3. THESIS OUTLINE

Due to the nature of this topic which involves systems with strong nonlinearities such as vibro-impact, dry friction, drill string dynamics and rock mechanics, some parts of the literature review are presented in the respective chapters on those topics. This is to ease the consistency and coherence of the material presented in this work. This thesis is concerned with four aspects of engineering, namely, rock drilling and drilling systems, dry friction and the phenomenon of lifting, vibro-impact assisted drilling of hard rock, and rock fracture.

Chapter 2 gives a review on drilling methods and systems. The historical development of techniques in this field is presented and some problems are exposed. Vibro-impact systems are also explored in this section.

Chapter 3 is devoted to the problem of friction and a description of the interfacial mechanism is made from a viewpoint of the vibro-impact process, which occurs at a micro level. A new hypothesis for the lifting of the slider is suggested.

A pilot study is carried out in chapter 4. The experimental work, which helped to develop the model of the new concept of drilling, is described.

Chapter 5 deploys the modelling and the development of the mathematical tool for extensive study of a proposed model for the self-oscillatory mechanism for percussive-rotary drilling.

The description of the model of percussive- (rotary) fracture of brittle hard rock is outlined in chapter 6.

Chapter 7 brings a closing discussion and summarises the effect of variation of the system parameter on the performance of the system.

The final chapter gives some recommendations and guideline for further work, which is supported by a grant from EPSRC.

Chapter 2
BACKGROUND TO DRILLING

BACKGROUND TO DRILLING

1. HISTORICAL DEVELOPMENT OF DRILLING

Human activities have always involved drilling in different aspects. The history of drilling dates from the ancient Egyptians who used corundum dust and pebbles to bore holes in porphyry. The ancient Chinese drilled deep holes for water in loess by the repetitive lifting, dropping and rotating of coupled bamboo rods, (McGregor, 1967).

In modern times, hand-hammer drills for shotholes were in use in tunnels, railway cuttings and mines until superseded by power drilling. These techniques could produce an overall rate of drilling of about 0.3m an hour when drilling a hole of 32 mm diameter to a depth of 0.6m, provided that the rock was not too hard, (McGregor, 1967). An alternative method, the hand churn drill, was suitable for drilling holes to 15m or so, with relatively larger diameters than the hammer drills. It is of interest to list some of the landmarks in the history of modern rock drilling, (McGregor, 1967):

- 1810-1820 Trivithick in Britain built a steam-driven rotary rock-drilling machine.
- 1830-1840 Steam churn drill developed by Isaac Singer (USA), of sewing-machine fame.
- 1850-1860 Drills with a power stroke were invented.
- 1860-1870 Compressed air used as an operating medium for rockdrills in an Alpine tunnel; a commercial piston drill was patented by Burleigh in America; a diamond-drill was produced by Bullock (USA) and diamond-tipped bits by Leschot (France); a toothed roller cutter bit was used in America.

- 1870-1880 A diamond-drill hole reached over 670m; Ingersol (USA) improved the rock-drill and invented the tripod; Rand (USA) developed mining drills; Hall (USA) produced the Sullivan diamond drill.
- 1880-1890 A diamond-drill hole reached 1750m; Holman (GB) produced a rock-drill.
- 1890-1900 Commercial pneumatic rock-drills were being produced by Cleveland, Chicago Pneumatic, Gardner-Denver, Hardy-Pick, Holman Bros., Ingersoll-Rand and others; rotary coal drills were in use; Davis (USA) developed a steam rotary oil-well rig; Leyner invented the hammer drill, the hollow drill steel and the shank, which still bears his name.
- 1900-1910 Hughes (USA) perfected the tricone bit.
- 1920-1940 Tungsten-carbide first used on drill bits (Germany)
- 1940-1966 Tungsten-carbide bits perfected; invention and general acceptance of down-the-hole drills; introduction of turbine drills.

Lummus, (1969) and Allen, (1981), have identified four periods in the establishment of drilling technology: 1888- 1920 conception stage, 1920- 1948 development period, 1948- 1968 scientific evolution, 1968 automation.

Above mentioned methods of drilling can be divided into the following groups; churn drilling, hammer drilling and rotary drilling.

The drop drill derived from the hand churn drills, had its drill bit lifted by a cam or crank and then dropped freely in similar fashion to a mill stamp. To accelerate the down blow, springs were used and later, a steam operated machine was introduced. The well (or diesel churn) drill was superseded by the pneumatic piston drill and other drilling machines, but all were obsolete by the early 1920's.

The air hammer drill introduced with similarity to the hand hammer method was the forerunner of the modern percussive rock-drill and pneumatic tools. The independent rotation drills and down-the-hole techniques appeared along with hand augering, and

these led to the diamond drill, the power auger, the coal drill, rotary table rigs, oil well rigs and top-drive rotary rigs.

Drilling in general can be divided into three operating groups. Exploration drilling is concerned with the lithological and structural configuration of deposits in the search of qualitative and quantitative data. The second group of drilling seeks for geotechnical data of formation for study purposes and makes use of core samples to determine the mechanical and behavioural performance of rocks. The third group covers special purposes namely, foundations in constructions, hydrological drilling, routes for roads and offshore drilling. In all these drilling groups, the fundamental drilling process can be divided into two types depending on how the energy is transmitted to the medium; namely, hammer (percussive) drilling and rotary drilling. Compressed air, water, foam and special mud are used to cool the tool, to clean the hole and to transport the cuttings up to the earth surface.

2. PERCUSSIVE DRILLING

This method of drilling is used for hard and very hard formations and it relies entirely on crack propagation and brittleness in the formation. The rock is cut off the formation by repetitive impact of the drill bit. Figure 2.1 presents a typical configuration of a percussive drilling system. Commonly, percussive drills consist of a piston that imparts blows to the drill rod. The piston strikes the drill rod through an adapter and the generated compressive pulse forces the bit to penetrate and fragment the rock. The energy is transmitted to the formation by means of impact waves travelling along the drill rod; thus at great depth percussion drilling suffers from loss of energy. A built-in rotation device is set to re-index the bit each time so that the intact rock is exposed to forthcoming blow. The motion of the piston in a cylinder is synchronised with the rotation, which occurs in the intervals between impacts. The

rotation occurs when the bit is about to rebound; therefore, it does not participate in the process of material removal.

Related to the percussive drill, are the rock-drill, the motor drill, the down-the-whole hammer drill (DTH) and the cable-tool drilling system.

The DTH drill has a cylindrical pneumatic hammer, which enters the hole immediately behind the bit, thus the loss of energy is reduced to minimum. Indexing is provided by the continuous rotation of the drill pipe from the earth surface. The DTH drill has excellent rate of penetration in sedimentary and igneous rocks with low feed pressure: there is no rock, which is known to be too hard for DTH, (Chugh, 1985).

2.1 The Cutting Tool

The main tools in this method of drilling are core-crusher bits, full head bits with insert (Figure 2.3 a) and button bits (Figure 2.3 b). The body of bits is made of special alloy steel and heat-treated to provide high fatigue strength. The name “button bit” comes from the semi-spherical shape of the cutting edge and as these bits have many points of contact with the formation, they provide good fragmentation. Button drills are able to drill about four times longer than full head bits, however in highly abrasive formation, full head bits with inserts have a better performance. The DTH hammer can drill up to 50cm/min in weathered limestone, 25cm/min in hard limestone. In weathered granite it drills at up to 25cm/min falling to about 10cm/min in hard fresh granite, (Chugh, 1985). Conventional percussive drills deliver holes up to 4.0inch/101 mm in diameter whereas the DTH drills give a larger diameter, about 8.5 inch/216mm. Figure 2.2 depicts the configuration of the down the hole hammer bit.

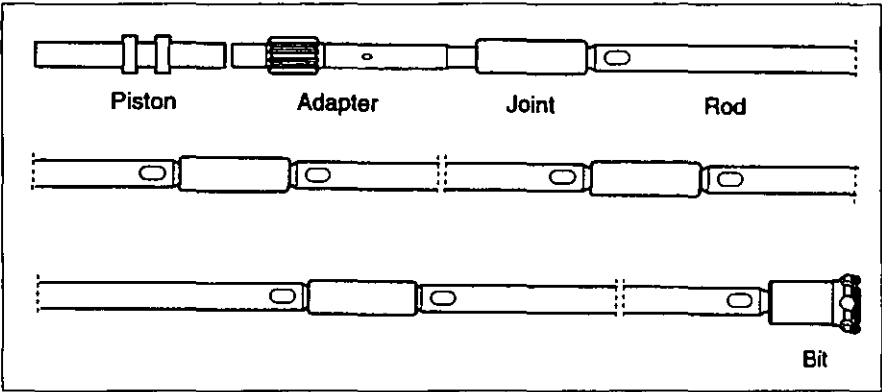


Figure 2.1: Main components of a percussive drill; (Beccue)

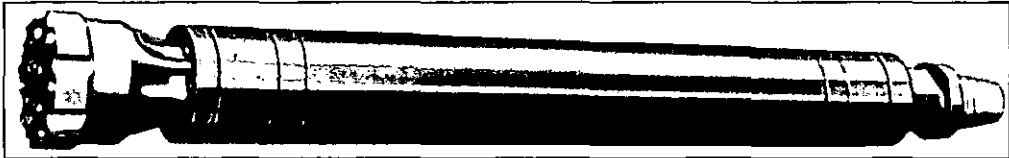


Figure 2.2: Down the hole hammer, (Drillers training)

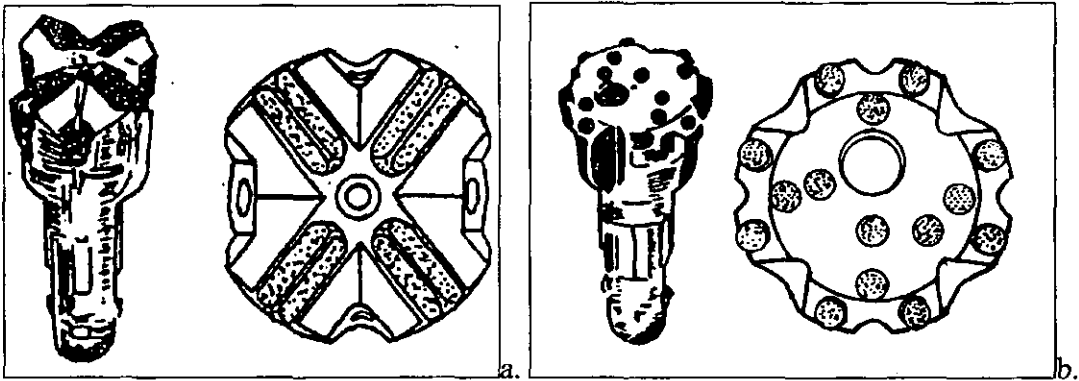


Figure 2.3: a.- full-head bit with inserts; b.- button bit; (Chugh, 1985)

Percussive drilling produces high rates of penetration in hard and very hard rock. However it has some limitation in soft and cohesive formations. In such cohesive rocks rotary drilling is preferable.

3. ROTARY DRILLING

Among all drilling methods and conditions, rotary drilling is economical and versatile giving the best performance in almost all rock formations. The material is removed from the rock formation in three different ways. In attritive cutting, the rock is ground away by abrasive action. For rotative-cutting, the rock is cut or planed away. In rotative-sharing, the rock is fragmented by wedge action and shear.

In rotary drilling, the energy of deformation is transmitted down to the bottom hole through a jointed steel pipe (drill string). The drilling systems are made up of a motor, rotary table, drill pipes, drill collar and bit. Through a gearbox, the motor drives the rotary table that rotates the drill string and the bit. The rotary table is typically a heavy flywheel that is use to smooth irregularities in angular velocity. Figure 2.4 depicts the main components of a rotary drilling rig where the arrows show the flow of the drilling fluid. The drill string is supported at the earth's surface such that the upper part of the string is in tension and the lower part in compression. The point separating the tension and compression section is known as the "neutral point", which is predetermined for a given drilling configuration. The cutting power in rotary drilling depends on the compressive stress exerted upon the rock by an extremely heavy weight on the bit. The load on the bit is secured by partially releasing the weight of the string on the bit. The thrust in some rock reaches 4200 kg per inch of bit diameter, (Driscoll, 1986). This sometimes leads to a twist and a breakage in the drilling string. The drilling capability of this method depends on concentration of a high pull down pressure on a small area.

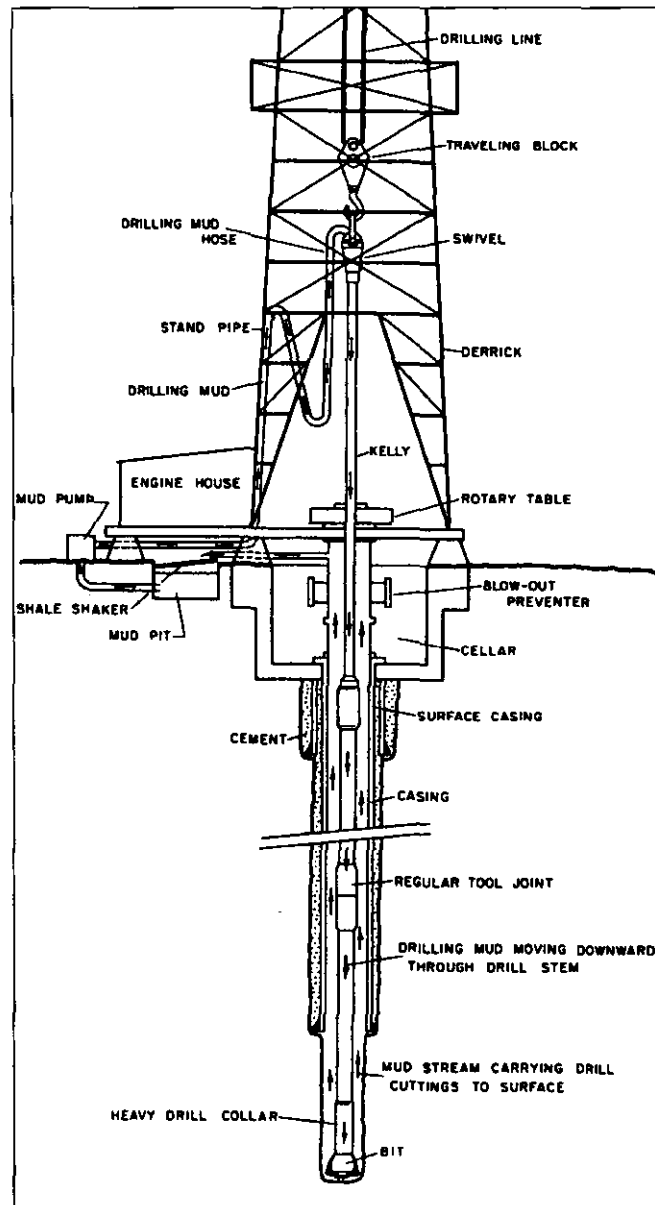


Figure 2.4: Rotary drilling system, (Chilingarian, et al)

In the case of drilling with a tricone bit, the total area of teeth is approximately $3/16^{\text{th}}$ of a (square inch) of bit diameter and, for a bit of 16 inch in diameter, the pull down pressure is concentrated only on 3inch square. In general, the weight on the bit varies from 1350kg/inch of bit diameter for soft and medium rocks to as much as 3000kg/inch for hard formations, (Chugh, 1985). The rotary drill provides a wide range of holes, up to 914mm in diameter, (Chugh, 1985) and can drill to great depth in sedimentary and hard rocks with a considerable variety of tools.

3.1 The Tool

Rotary drilling uses a variety of tools such as an auger, a tricone bit with milled teeth or tungsten carbide inserts, a full head bit with insert, a drag bit, a diamond bit, a core drill or retractable bits. The choice of the tool depends on the hardness of the rock and on the purpose of the drilling. Some tools are shown in Figure 2.5 and 2.6.

Among these tools, tricone bits have a special design, which makes them suitable for soft, medium or hard formations. The cutter has a form of rolling cone and the bit is made of three cones, bearing pins, bearing rollers, bearing balls and the bit body. The basic elements of a tricone bit are shown in Figure 2.7. The teeth are arranged in circumferential rows inter-fitting in between rows of adjacent cones. On the cone, the axes of the teeth are not parallel and this is seen in Figure 2.7. The cutting action is defined by the position of both apexes of the cone 1 and the offset of the cone centre lines so that they do not intersect at the bit rotation centre (see Figure 2. 8). The cone offset induces a scraping action, which increases the rate of penetration. Three types of design are encountered:- the true rolling design (Figure 2. 8a), the soft formation design and the hard formation design. The true rolling design has the cone apexes crossed in the bit rotation centre and the cones roll without slippage or scraping.

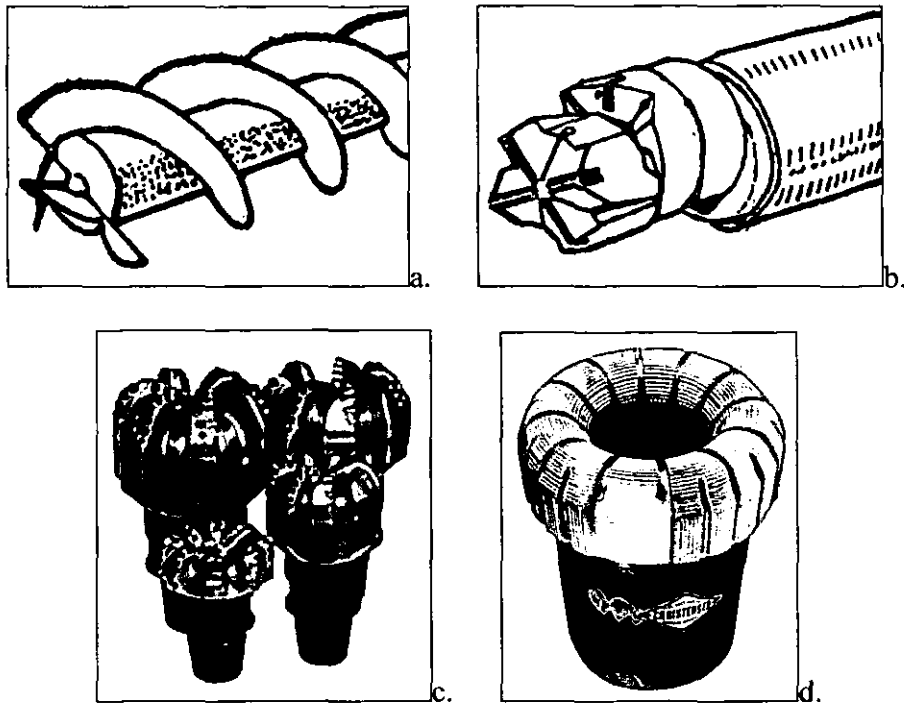


Figure 2.5 Rotary drilling tools;

a.- auger drill; b.- odex, (Chugh); c.- PDC bit;

d.- diamond core bit (Huge-Christensen)

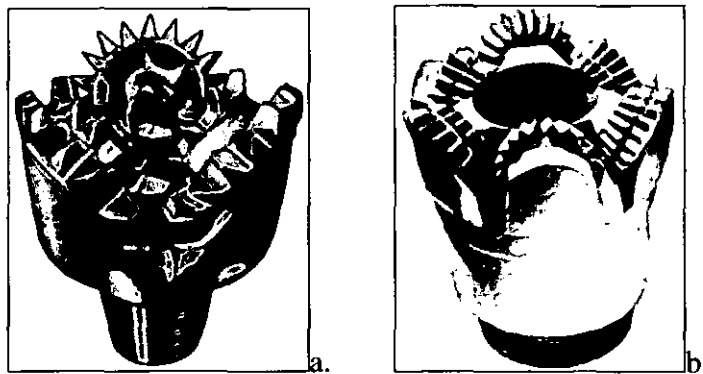


Figure 2.6: Rotary drilling tools, (Nougaro)

a.- tricone bit; b.- roller core bit

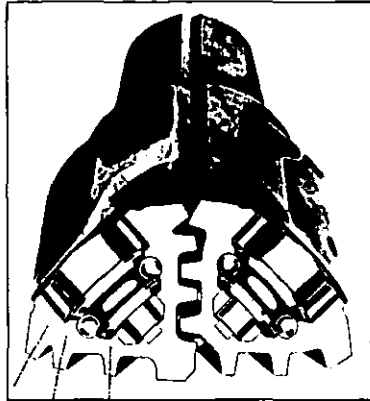


Figure 2.7: Main components of tricone bit, (Smith tools)

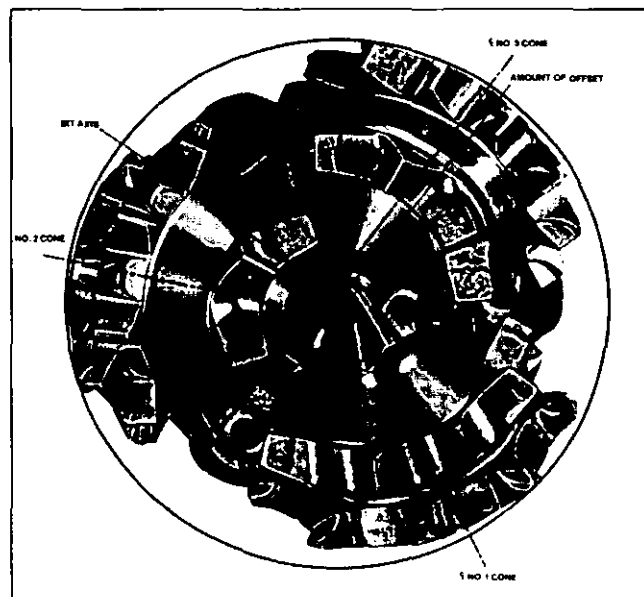


Figure 2. 8: setting of the rolling cones in a tricone bit, (Smith tools).

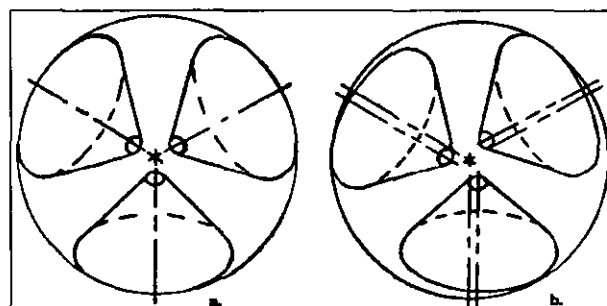


Figure 2.9: Layout of the rolling cones, (Chugh)
a. - true rolling cones; b.- offset cones

In the soft formation design, the cones have two basic cone angles and rotate with a scratching and chiselling action appropriate for soft rocks. For the hard formation design, the cones have a small offset from true rolling, which produces a crushing action on the medium. The roller bearings and the bushing friction bearing at the nose of the cone endorse the main part of the radial load. The ball bearings hold back the cone and stand both radial and thrust loads.

The cutting elements of a tricone bit are steel teeth or tungsten carbide inserts. Steel teeth are milled or forged and carbide inserts are of four major forms:- extended chisel for soft formations, chisel for medium and slightly abrasive rocks, blunt chisel for hard abrasive rocks demanding high weight on the bit, and long dome and ovoid for very hard abrasive formations with maximum weight on the bit.

Tricone bits are made of a special alloy steel, which provides high resistance to dynamic load and wear. The steel teeth cones are forged from nickel-molybdenum alloy steel AISI 4815, which contains 3.5 per cent nickel and 0.25 per cent of molybdenum, (Chugh, 1985). The cones are then carburised from a depth of 1.8mm up to 3.3 mm, then cooled and heat-treated. This process provides the cone with a tough outer sink, which is good for chipping and breaking resistance. The high carbon carburised case under the sink bears maximum strength and wear-resistance. The refined core has a best mixture of strength and toughness, hence has maximum impact resistance. Tungsten carbide teeth cones are made of similar steel specially designed for this purpose but containing more carbon.

3.2 Development of Down the Hole Motors

The early down-the-hole motors were patented in 1873. These motors are cylindrical and enter the drilled hole right behind the drill bit. In Western Europe, the first turbo drills appeared in 1938-1940 and were built by Voith, a

German firm. On the other hand, they did not have great success until 1956. However, in Soviet Union, turbo drills have been widely in use since 1934. Soviet turbines were adapted to use conventional rock drill bits (approx. 93-95 per cent of the bits used). The use of turbines in drilling reached 65 per cent in 1953 and up to 86.5 per cent in 1959 Cough, (1985). Another modification of the turbo drill is the bit-motor drive introduced in 1966 in USA. The turbo drill and the bit-motor drive with positive displacement, designed to operate at a standstill drill pipe are powered with hydraulic motors. Both motors differ in the way the hydraulic power is transformed into mechanical cutting energy.

The operating principle of a turbo drill is based on centrifugal fluid mechanics, whereby a fluid flowing directly on to rotary angular blades drives the tool. In the bit-motor, the drive has a progressive cavity design where a pressurised hydraulic fluid pushes a sealed cavity. The sealing being able to move, rotates under such force, and hence produces the necessary energy conversion. This type of drive performs better in directional drilling than in turbo drills.

With respect to performance, the torque of the turbo drill is a function of the rotational speed, whilst the motor-drill has a torque as a function differential pressure. It follows that the output power of a turbo drill depends on speed, whereas positive displacement motor bit delivers a power, which is a function of pressure.

3.3 Rotary Drilling with Down the Hole Motors

In rotary drilling, regardless of the depth, a rotary table spins a long drill string (made of pipes), collards and the bit. A heavy thrust is exerted on the bit to cause its penetration into the rock. It has been estimated that when drilling at a

depth greater than 2400m, less than 10 per cent of supplied power is transmitted to the bit, (Chugh, 1985). The introduction of down-the-hole motors puts the power right at the bit. Consequently, the requirement of power is minimised as well as the wear and torsional stresses in the drill pipe. Down-the-hole motors are used instead of conventional rotary drilling at depths greater than 2100 metres. This method does not suffer from speed and torque limitations as in conventional rotary drilling due to the dynamic torsional strength of the pipes.

4. COMBINED TECHNIQUES

Percussive drilling is fast and preferable in hard rocks; however this method drills relatively small holes in diameter. The rotary drilling can be used for almost all rocks but it requires an extremely heavy thrust, which harms the drill pipes and the tool. To use advantages of both percussive and rotary drilling, a combination of these methods has been used along with new techniques. In the early 1920s, a percussive-rotary method of drilling was invented and in 1927 a hydraulic vibratory drilling tool was patented, US pat. No. 1646959 to Fisher. In the 1940s, the down the hole motors and turbine drills were introduced to increase the efficiency of rotary drilling.

Other techniques had been explored in the 1950s and 1960s such as, spark drills, pellet drills, electro-hydraulic crushers, explosive drills, erosion drills, ultrasonic drills and heat drills.

5. DRILLING FLUID

In both types of drilling, the cuttings are transported up to the earth surface by means of a drilling fluid. Until 1863, the importance of drilling fluid was neglected (Chilingarian, 1983). The drilling fluid may be water-based, oil-based or gaseous.

The term “drilling fluid” relates to all flowing substances that are used to flush the cuttings out of the hole namely oil, water, mud, gas or air. The drilling mud is made up of a suspension of solid particles in water or oil or of a mixture of specially formulated liquids, often with the addition of chemical substances.

The viscosity and the specific weight of the drilling fluid are important properties in the drilling process. The lifting capacity of the drilling fluid augments with the increase of its specific weight. A high percentage of cuttings are lifted by a drilling mud with low viscosity, (Chiligarian et al., 1983)

The primary function of the drilling fluid is the flushing of the cuttings and the cleaning of the bottom of the hole. However, the drilling fluid is also used to cool and lubricate the bit and the drill string.

In Figure 2.4, the arrows indicate the circulation of the drilling fluid. Injected into the drill pipe, the drilling fluid carries the cuttings from the bottom of the hole and flows upward between the hole wall and the pipe. At the earth surface, the cuttings are removed by a shale shaker (vibrating screen), which is placed above the mud pit. The cleaned fluid from the mud pit is then pumped back into the drill pipe.

When using compressed air as a drilling fluid, the dust collector (cyclone separator) or filtering systems must be secured to protect the workers and the environment. Wetting systems are also used to reduce the dust produced by the compressed air flushing. This is accomplished by injecting a given quantity of water or a solution of water and drilling foam into the air flowing towards the bit. Any generated dust is wetted at the bottom and the damped particles with the cuttings are carried up out of the hole.

There is a wide range of commercially available drilling fluid and the choice of a fluid depends on several properties, which are functions of the drilling parameters.

Often for small holes, percussive drilling is the preferred option because only compressed air is required to drive the hammer and to flush the cuttings.

6. CHOICE OF DRILLING METHOD

The choice of drilling method is defined by the hardness and abrasiveness of the formation and the size of the hole. Percussive drilling produces relatively small holes. Thus, if the diameter of the hole to be drilled is greater than 250mm, a tricone bit will be used whatever the hardness of the rock. To drill holes with diameters between 100 and 165mm in hard rock, the percussive method is preferable and the DTH will be the most economical method because no drilling mud is required.

Chapter3
FRICTION MODELLING

FRICTION MODELLING

1. INTRODUCTION

Friction is the antagonistic force, which always exists between contact surfaces of two bodies in relative motion. It resists forthcoming motion (static friction) and dynamically stands against established motion in the system (dynamic friction). The classical Coulomb friction law assumes the coefficient of friction to be constant and equal or less than the coefficient of static friction. In engineering mechanisms with relative motion, dry friction induces negative side effects such as wear, squeal (high frequency noise), chatter (low frequency noise) and self-sustained vibration. Some examples of self-sustained vibration are the squeak of doors or shoes, the squealing of railway wheels or car brakes and the stick-slip motion in mechanical systems. In vibration control, dry friction finds useful application for its damping properties. Vibration generated by friction is often termed mechanical relaxation oscillation.

The force of friction between two surfaces in relative motion has been investigated since the works of Amontons (1699) and Coulomb (1785). The study of friction-induced vibration in the early years was carried out mainly at the experimental level with some analytical approximations. Stribeck (1902) noticed that at low velocities, the friction force decreases (Stribeck effect). Lord Rayleigh used the model in Figure 3.1 to study the self-sustained oscillation of violin strings. The model is made of a mass-spring system riding on an endless belt that moves with constant velocity v and considers the friction force as a decreasing function of relative speed. This model is still often used to investigate self-excited vibration in mechanical systems. In an attempt to measure the coefficient of kinetic friction, Wells (1929) recorded the stick-slip motion. Thomas (1930) used analytical and graphical

methods to solve the equation of vibratory motion of a system with solid friction. Den Hartog (1931) studied the stick-slip motion of a single-degree-of-freedom mass-spring system with periodic excitation and derived the exact analytical solution of for the full cycle of periodic motion.

On the subject of the origin of relaxation oscillation, many theories have been suggested by investigators such as Kaidanovskii and Khaikin (1933) amongst others. Kaidanovskii and Khaikin assumed that relaxation oscillation is produced by elastic friction during the inverse relationship between frictional force and relative velocity. Based on Rayleigh's conception, their theory did not find the source of the large magnitude of the first discontinuity (first slip). Other investigators suggested that the decrease in friction with velocity is an attribute of the electrostatic effect between rubbing surfaces and also assumed that the force of friction decreases with increasing velocity. However, the discontinuity in the motion was considered to be caused by the relationship between the magnitudes of the friction, velocity, inertia and the rigidity of the system.

A linearized expression of the friction-velocity curve was developed by Blok (1940) leading to the derivation of analytical solutions. He assumed that static friction is constant (though the static friction force does increase with the duration of contact.) Dudley and Swift (1949) used a graphical method to solve the equation of stick-slip motion. In their work, Sinclair and Manville (1955) concluded that frictional vibration is a consequence of the rise of the coefficient of friction during a decrease in relative velocity. Derjagin, *et al.* (1957) developed a theory of critical relative velocity at which slip-stick occurs. Kudinov, (1960) developed the mathematical theory of self-sustained frictional vibrations with feedback between normal displacement and sliding velocity provided that the system is subject to hydrodynamic or semi-hydrodynamic lubrication. In such a case, an increase of the thickness of lubricant layer induces a reduction of hydrodynamic resistance and when the sliding velocity vanishes, the slider sinks. Brockley *et al* (1967) in their

investigation obtained the critical speed which reduces the occurrence of vibration. In this expression, friction is a function of time and velocity, and the critical speed depends on system stiffness, normal load and damping.

Tolstoi (1967) highlighted the importance of the dynamic characteristics of frictional motion and stated that there must be a similarity between sliding contact friction and the reduction of hydrodynamic resistance. Many factors favour sliding friction force to be a decreasing function of slider normal rise. This is because with the rising of the slider (a) the depth of indentation diminishes leading to a reduction of the true contact area, (b) the non-contact area between the two surfaces increases, (c) the resistance of plastic and shear deformation is reduced.

Experimentally, Tolstoi revealed that the normal displacement of the slider is related to contact stiffness as follows: $k = -dN/dH$, where k is contact stiffness, N is the normal load and H is the normal displacement. From his data, he argued that sliding contact friction force decreases with the elevation of the slider. However, this relationship is highly sensitive to the normal motion of the slider which make this function very unstable.

Tolstoi stated that when there is no normal displacement of the slider, the force of contact friction is independent of relative velocity, and self-excited vibration ceases. He postulated three conditions under which self-excited frictional vibration could settle.

$$\frac{\partial f}{\partial H} < 0; \quad \frac{dH}{dv} > 0 \quad (2.1)$$

$$\frac{df}{dv} \equiv \frac{\partial f}{\partial H} \cdot \frac{dH}{dv} + \frac{\partial f}{\partial v} < 0 \quad (2.2)$$

$$\tau \frac{\partial A_r}{\partial H} \cdot \frac{dH}{dv} + A_r \frac{\partial \tau}{\partial v} < 0 \quad (2.3)$$

where, f is the friction force, H slider normal elevation, τ is the average shear stress in the softer material, v sliding velocity, A_r total actual contact area. The first part of equation 2.1 shows that friction force is a decreasing function but its second half reveals the instability of this function. However, equation 2.1 is not a sufficient condition for vibration to appear. The sufficient condition is that the total derivative df/dv must be negative (Block, 1940). The first member in equations 2.2 and 2.3 is always less than or equal to zero. The second term standing for the resistance to shear is positive for constant temperature, H and A_r are positive constants, and hence the condition for the total derivative to be negative is fulfilled. Consequently from equations 2.2 and 2.3 above it appears that if H is kept constant, then df/dv is positive, therefore tangential sliding motion will be smooth (Tolstoi, 1967).

Furthermore, Tolstoi had noticed a velocity that can maintain elevation H constant. This is the velocity at which the asperities squeeze each other down to half their initial height, see Figure 3.2. He derived this dependency in terms of shear stress τ , angle of shear γ , creep viscosity η , asperity spacing λ and asperity height h .

Moving at a velocity v , the slider (top element, Figure 3.2), needs time $t_1 = \lambda/v$ to move from asperity to asperity, but the time necessary for asperities to be compressed down to half their initial height can be derived from shear stress as follows

$$\tau = \frac{\eta h}{\lambda t_2} = \frac{\eta \gamma}{t_2} \quad (2.4)$$

here $\gamma = h/\lambda$ (angle of shear), $\tau = \mu \sigma_y$, σ_y the normal yield stress, μ is the coefficient of friction and η is the creep viscosity, hence he obtained

$$t_2 = \frac{\eta h}{\mu \sigma_y \lambda} \quad (2.5)$$

To keep the elevation H constant, the time t_1 must be greater than t_2 , ($t_1 \geq t_2$), thus

he expressed
$$v \leq \frac{\mu\sigma_y\lambda^2}{2\eta h} \quad (2.6)$$

and the critical velocity below which normal displacement vanishes is defined by

$$v_1 = \frac{\mu\sigma_y\lambda^2}{2\eta h} \quad (2.7)$$

Consequently if the slider velocity is less than v_1 ($v < v_1$), self-excited vibration cannot take place. However, whenever sliding velocity exceeds v_1 , vibration establishes a bumping-like motion.

Tolstoi concluded that the negative slope of friction-velocity curve is not a natural attribute of contact friction but this is the outcome of the normal degree of freedom. In addition, when the elevation H is kept constant the negative slop (the falling segment) on the friction-velocity characteristics no longer exist.

Tolstoi, Borisova and Grigorova (1971) in their investigation of kinetic friction concluded that the interface coefficient of friction does not explicitly influence sliding velocity. They stated that the divergence between apparent static and kinetic friction is an outcome of the micro-scale vibration conveying frictional sliding.

Mahalingam (1975), Rozhestvenkii (1979), Taukhan (1982), and Marui and Kato (1984) studied the vibration of systems in which Coulomb friction was incorporated. Sakamoto (1985, 1987) used Hertz's theory to define the relation between normal contact deflection and the coefficient of friction. A decrease in friction force was observed for acceleration in the normal direction greater than gravitational acceleration, Ibrahim (1994).

Thus many studies have been devoted to understanding the interfacial mechanism of the friction process. Most relevant to this study, there are two approaches in to the investigation of frictional properties of rubbing surfaces.

The first is a phenomenological approach, which uses a classical concept to describe friction force as a function of sliding velocity. The models involved in this context are considered as static friction models such as the classical Coulomb friction, Stribeck friction, viscous friction and their derivatives. These models do not account for the elastic deformation that occurs prior to the slip of rubbing surfaces. However, some models do allow for pre-slip deformation and are seen as dynamical models.

The second is a constitutive approach, which uses the finite-element method to treat friction force as a relationship between stress fields and displacement fields. Fractal models are also used to characterise the interfacial contact mechanism. The fractal model of Weierstrass-Mandelbort (WM), (Majundar et al., 1991) is employed in this approach to define a profile of the roughness of the surfaces in contact. Hertzian theory is then used to calculate pressure at the spots of contact. Statistical models of surface roughness are applied but require thorough measurement of surface parameters.

An experimental proof of the existence of a lifting force within the friction process was pointed out by Stribeck (reduction of friction) and Tolstoi (normal jump). The normal elevation (the lifting) of the slider was noted in the experiments of several other researchers. The following sections will explore the origin of the lifting phenomenon and a new hypothesis is suggested.

2. MECHANISM OF CONTACT FRICTION INDUCED VIBRATION

2.1 Phenomenological description of the friction using impact approach

When two bodies are exposed one upon another, after a certain finite time the harder body imprints itself into the softer one. The asperities of both bodies adhere and interlock with each other; this results in a maximum contact area. Several studies have shown that the interfacial process is of a complex nature and involves the destruction of a thin film between the surfaces, the elastic and plastic deformation of asperities, and the shear cutting and destruction of certain base material, Kragelskii (1965). Apart from the aforementioned complexity, micro-impacts occur within the process of relative displacement.

There exist several concepts when studying the process of friction; depending on the type of task to be performed, different models of interfacial mechanism are proposed. The nature and behaviour of friction is still the subject of ongoing research into some aspects that are puzzling researchers in order to develop a better model of friction. This is highlighted in the following section which investigates micro-vibration and micro-impact as a source of normal displacement.

If one of two bodies in static contact is given tangential motion, say the harder, it begins to compress opposite asperities of the softer body. The higher the velocity of relative motion, the shorter is the time allocated for elastic and plastic deformation of withstanding asperities. Therefore, the slider is compelled to slide from lower roughness to the highest (initiation of normal natural displacement), producing less and less deformation. This is because the given time is too little and the slider reaches the next asperity when the one underneath is not yet fully pressed down to the initial level. With the increase of relative velocity, micro-impacts occur as asperities of the slider collide with the opposite ones and micro-impulses are generated.

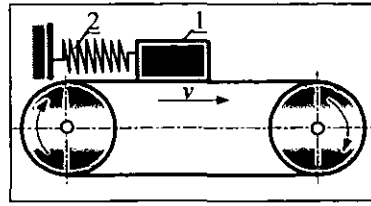


Figure 3.1: Block riding on a belt.
1- slider (block); 2-elastic element

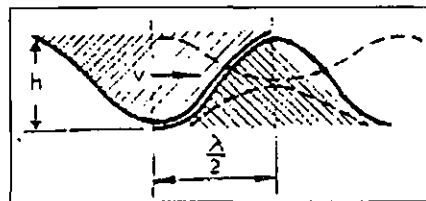


Figure 3.2: Sketch of compaction of asperity (after Tolstoi, 1967);

h -asperity height, λ - average spacing between asperity;

broken line – compressed asperities.

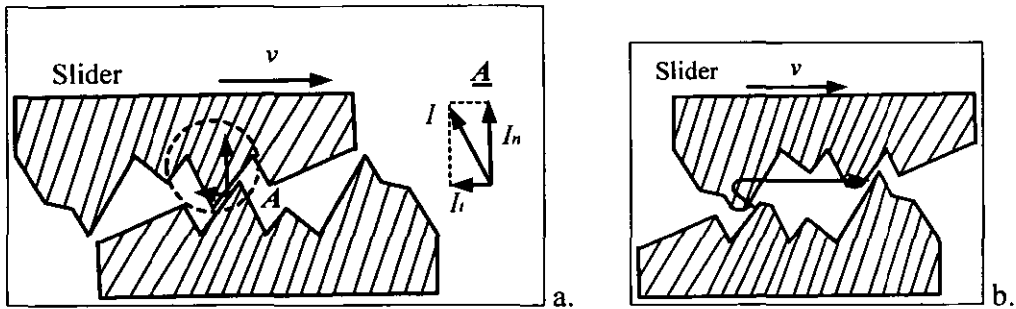


Figure 3.3: Micro-impact of asperities.

a.- Collision impulse; b.- path to next impact;

I resulting impulse, I_t tangential impulse component, I_n normal impulse component.

Because the impulse is a function of velocity, the total normal component of such micro-impulses over the surface propels the slider from lower to further and higher asperities, gradually incrementing the normal displacement (upwards motion). However, if a forthcoming asperity is lower than previous one and the nearest higher asperity can not be reached in the current time, the slider crashes down onto the nearest lower asperity. This generates a downward motion (see Figure 3.4). After such collisions, the slider bounces at a micro-scale level and loosens its bonds with the surface. This causes a reduction of the actual contact area, implying a decrease of friction force because the slider is partially lifted by the accumulated total normal impulse. The higher the velocity, the larger is the total normal (to surface) component of the impulse, ejecting the slider to further higher asperities, (see Figure 3.3). If there is no confining force applied to the slider in the normal direction, the slider at some stage will display a bumping motion. (This effect is often observed when pulling a relatively light table over a flat surface and it starts jumping).

Figure 3.3 shows a speculative illustration of the interaction between two contact surfaces in relative motion. Figure 3.3a shows that the tangential (parallel to velocity vector) component of the collision I_t may be small but the resultant impulse I could be large enough to generate a considerable normal impulse component I_n . Figure 3.3b illustrates the trajectory (path to next collision) of the slider motion, that causes plastic deformation of the highest asperities which were involved in the previous crashes. The lowest asperities have kept their initial shape, as they have not been in contact with asperities of the opposite body.

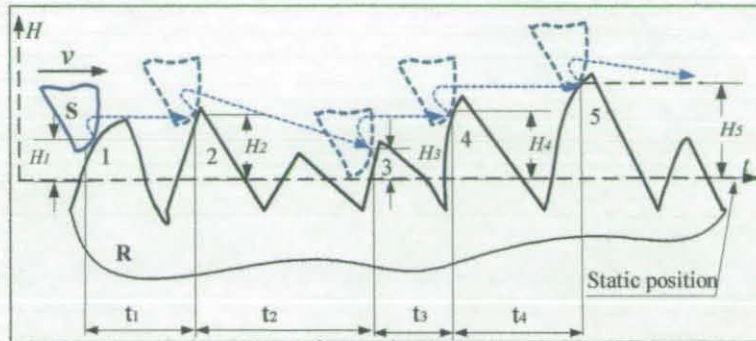


Figure 3.4 single asperity sliding over rough surface.

t_i time interval between successive impacts, H_i corresponding normal displacement.

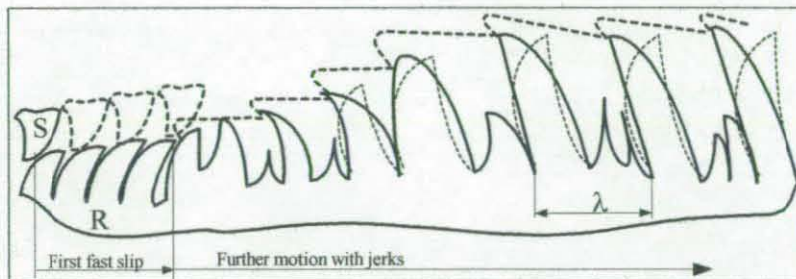


Figure 3.5: Development of the vibration of the slider.

S- sliding asperity; R-surface roughness.

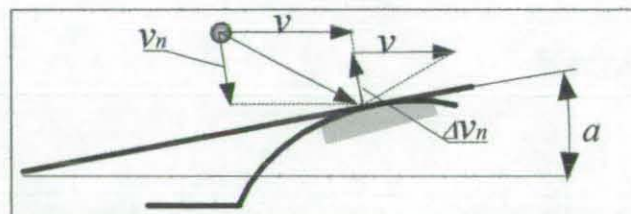


Figure 3.6: Collision of a ball onto an inclined surface.

v_n velocity normal to surface, Δv_n change in normal velocity.

Figure 3.4 shows an idealised motion of a single asperity S sliding over roughness R . The dot-arrows depict the trajectory of the asperity as it collides against the asperities of the surface. It is assumed that both the sliding asperity S and the surface R are rigid bodies. The sliding asperity S is given an initial velocity v ; due to the force of adhesion and the weight, the asperity S will stay at rest until the shifting force exceeds the force of contact. At the exceeding point, a sudden rupture of the bonds between the two bodies occurs, the sliding asperity slips with acceleration and collides with the roughness of the surface. After impact with the first asperity of the surface marked 1, the sliding asperity S will need time t_1 to reach the asperity marked 2. The collision 1 occurred at the asperity elevation H_1 from the static position of the slider. Due to the normal impulse component I_n of the impact, the asperity S is elevated to H_2 and hits the asperity marked 2 almost at the same height because of the short distance between the two peaks. After the second impact, the height is incremented but the time required to reach the next asperity is larger, thus the sliding asperity falls into a valley between high peaks (normal downward displacement). The next collision occurs at a low height H_3 , which is lower than the two previous elevations. The asperity bounces with an increment of its elevation and collides with the next peak marked 4. The height is again incremented and the asperity in its flight hits peak 5 at elevation H_5 . Further motion of the asperity will follow a pattern of upward and downward displacement depending on the space between the asperities and the driving velocity.

Figure 3.5 shows the development of the vibratory process of the sliding element S over the time. The dashed line indicates the path of the sliding asperity and the dotted line illustrates the deformation of the asperities. The first slip is fast and large in magnitude because the driving system has the required time to store enough elastic energy which is abruptly released. This suddenly dislocates the asperities from their static position (disengagement of the meshing) and the slider rides faster over a relatively long distance. At this phase, the energy accumulated is capable of delivering fast plastic deformation to a large number of asperities. Such “fast slip”

continues until the occurrence of an impact (collision with a rigid asperity), or until the accumulated energy is fully released. Depending on the system configuration, friction force may keep a value close to static friction, (Figure 3.8). The slider stops if the driving system is weak i.e. where the accumulated energy is released completely without the occurrence of an impact strong enough to generate an impulse able to lift the slider. During the slider's rest time, friction force increases up to the value of static friction due to compaction (increase of true contact area), adhesion and interlocking of asperities. If a strong impact occurs during fast sliding, the impulse energy and the remaining accumulated energy drive the system through a fast series of intermittent rupture of bonds and collisions. Thus fast vibration follows the first fast slip at the beginning of the motion. The frequency of this vibration stabilises gradually when the slider reaches the average height of asperities. The frequency of such a vibratory motion entirely depends on the configuration of the system in terms of contact stiffness, frictional elasticity, mass, micro and macro geometry of contacting surfaces and the driving velocity.

The description of sequences of events in Figure 3.4 and Figure 3.5 points out three major factors favouring the appearance of normal displacement of the slider. These are (i) the velocity of relative displacement, (ii) the nature of irregularity in surface roughness and (iii) the micro-impulses of the collisions. Elasticity in normal direction intensifies the vibratory process of the slider. The relationship between the relative velocity, the surface geometry and the slider mass is paramount in frictional vibration. For a given configuration of the system, relationship (2.8) shows the nature of normal displacement.

$$H_2 > H_1; H_3 < H_1 < H_2; H_4 > H_3; H_5 > H_4. \quad (2.8)$$

Assuming λ is the average spacing between higher asperities obtained from statistical analysis of the relief of the surface and v is the sliding velocity (Figure 3.5), then the period of the impact motion can be expressed as follows $T = \lambda/v$

2.2 The origin of lifting phenomenon in dry friction

The collision of the slider S (Figure 3.4) with asperities occurs at a random angle of contact. At such impacts, micro-impulses normal to the plan of impact are generated. These impulses contain components which are normal and tangential to the surface. To illustrate this, in Figure 3.6 the sliding asperity is represented by a ball. The ball moves at a velocity v and hits a peak of roughness at an angle α . Because it is confined to move in a given direction with a velocity v , the ball acquires a normal impulse due to this impact. A normal displacement will be noticeable if the acquired impulse exceeds the gravitational force; however, at each crash, the forces acting in the normal direction are decreased by the value of the normal component of the force generated by the impact. This decreases the normal reaction force hence diminishes the friction force. Depending on the total number of the micro-impulses, the slider may be lifted reducing the true contact area. These two processes lead to a reduction of the force of friction because the force of contact and the contact area are decreased. From Figure 3.6, the following relationships are derived:

$$\Delta I = m\Delta v_n \quad (2.9)$$

$$I_n = m\Delta v_n \cos \alpha \quad (2.10)$$

$$\Delta v_n = (1 + R)v_n \quad (2.11)$$

$$v_n = \sqrt{2g\Delta H}$$

Where ΔI is the impulse at the point of impact; Δv is the change in normal velocity; ΔH is the height gradient; I_n is the impulse normal to the surface; R is the coefficient of restitution and m the mass of the slider.

Taking into consideration, that both bodies allow elastic and plastic deformation, it can be deduced from Figure 3.4 that in mechanical systems, elasticity in normal direction favours the intensification of normal oscillations.

Over the surface, the micro-impulses are generated in immense number and the resulting normal-to-surface impulse is at times large enough to lift the sliding body to a relatively high height. The total normal impulse over the surface is expressed as

$$I_N = \sum_{n=1}^{\infty} I_n \quad (2.12)$$

This leads to a loss of contact between the two surfaces. If a complete loss of contact occurs, then the nature of the whole process changes because the character of the contact involves deformation of the layer beneath the roughness. When the total normal impulse exceeds the confining forces, the sliding element is detached from the surface and moves, increasing the gap. During the lifting process, those asperities which did not suffer from full plastic deformation will recover elastically and give an additional upward impulse to the slider. The lifting continues until the confining forces in normal direction equalise or overcome the impulse. The sliding element falls with gravitational acceleration onto the surface. In this case, if there is no normal confining force, the impact velocity is the resultant speed of both the free fall and tangential velocities. Such a collision causes plastic deformation of the roughness with further elastic deformation of the layer beneath the roughness. At this stage, contact stiffness plays a major role in establishing a bumping vibratory motion, the frequency of which depends on contact stiffness, the elasticity in normal direction and the slider mass.

Frictional vibration is a consequence of the following:

- The alternation of adhesion and sudden rupture of bonds followed by micro-impacts against opposite asperities;
- The lifting power of the total normal impulse, which reduces the true contact area;
- The contact stiffness, the elastic recovery of deformed asperities and the elasticity in normal direction as an amplification factor.

Considering the above discussions for a sliding mechanism to move smoothly with no vibration, the confining force normal to the sliding surface and the slider mass must be such that the relative velocity secures enough time for plastic deformation of the asperities. Thus, the system must comply with the conditions (2.1), (2.2) and (2.3). The first abrupt slip must disengage all meshing of the asperities so that further sliding produces a plastic deformation (bending) of asperities. In such a process, the higher asperities will be bent, squashed and forced to fill in the valleys of roughness. If during this process, a meshing occurs (due to a variation of relative velocity), the slider sinks, its elevation changes, and, depending on the location of the meshing, misalignment may take place. The displacement will continue in a non-uniform motion.

Figure 3.7 shows (a) interfacial asperities in a static position and (b) a smooth relative motion without normal vibration produced by a velocity which secures enough time to deform (bend or squash) the asperities down to an average level. The asperities overlap with each other and are compressed down to a height of h_c . The height h_c depends on the average thickness of asperities, the height h , the length of spacing λ , the creep viscosity of the materials and the time released for plastic deformation. In Figure 3.7, only plastic deformation takes place and micro-impacts will not occur due to a smooth transition from asperity to asperity.

In dry friction, the total impulse normal to the sliding surface produced by the micro impacts of asperities plays a role similar to the hydrodynamic lifting force in lubricated sliding. The factors described in the two sections above produce five main categories of friction characteristics and these are examined in the following section.

3. MODELLING OF DRY FRICTION

Following from the description given in the previous section, friction characteristics are explored in this section. Because of the complexity of the nature of friction, a hypothesis of the origin of each type of behaviour will be discussed.

3.1 Friction Characteristics – category I

In the first category, the type of motion incorporates a very slow changing (quasi-static) process in the interfacial materials inducing elastic-plastic deformation. From a static position, the friction force increases until a slip motion or plastic deformation begins. Once slip has occurred, depending on the material properties and the energy of the drive, the friction force may keep an invariant value or increase with the growth of the velocity. The growth in the frictional force is conditioned by the viscous properties of the materials and the formation of a bulk of material which runs at the front edge of the slider

Figure 3.8 shows the types of characteristics relating to this category which can be used to model system with slow interfacial process where a large time is dispensed for a progressive deformation of the asperities and the contact layer.

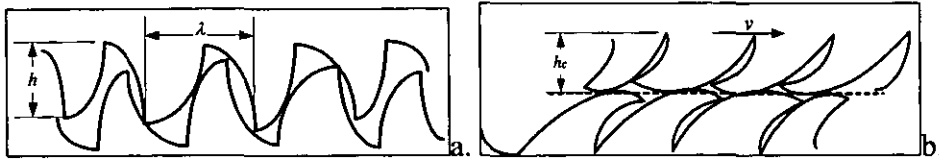


Figure 3.7: Surface roughness in static and smooth slip phases.
a.- interlocked asperities in static position b.- squashed asperities in relative slow sliding.
 h -asperity height, λ - average spacing between asperity, h_c -asperity height after compression.

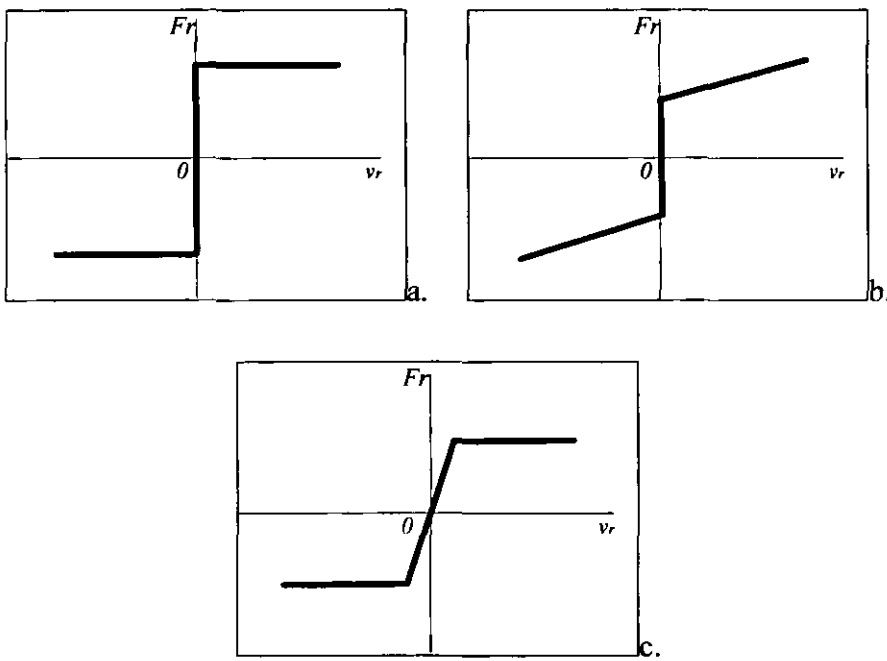


Figure 3.8: Type of friction characteristics in category I

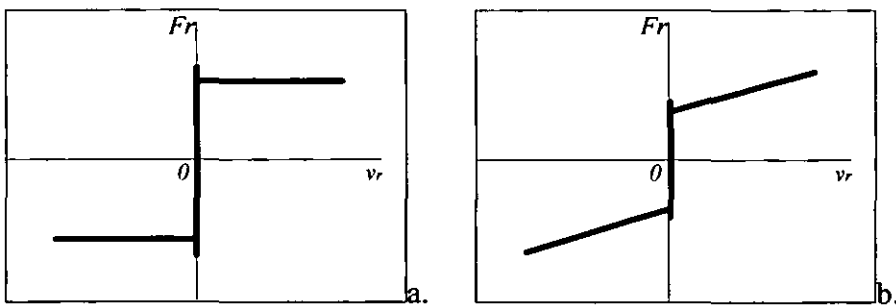


Figure 3.9: Type of friction characteristics in category II

The characteristics of the force of friction (F_r) shown in Figure 3.8 are stable functions of relative velocity (v_r), and only part (b) has a positive slope. Thus, these characteristics do not introduce instability into the motion of the system.

3.2 Friction Characteristics – category II

In this group, the interfacial process is identical to the first category but prompt change in friction occurs at the initiation of the relative motion. The steep reduction of the friction force (F_r) at the beginning of the motion is caused by a sudden dislocation of the sliding asperities from the static position which secures a large contact area at a higher level resulting in a small contact surface. This phenomenon was explored in section 2.2.1. Figure 3.9 illustrates the types of friction force characteristics of this category.

3.3 Friction Characteristics – category III

In this category, the interface exhibits two different processes. For low relative velocities, the interfacial resistance increases, gradually passes through a maximum value and begins to decrease slightly. Generally, the ascending part is treated as viscous properties of the materials in contact. However, apart from this, at low velocities, the meshing of asperities does not disengage. Thus, all asperities involved in the contact are deformed plastically and a bulk of material forms and runs right at the front edge of the slider. This considerably increases the resistance to motion. At the rear edge some asperities, which theoretically should not be in contact, remain under the slider because of plastic slip. This augments the density of asperities underneath the slider, hence the true contact area increases together with a volume of material that is undergoing a deformation.

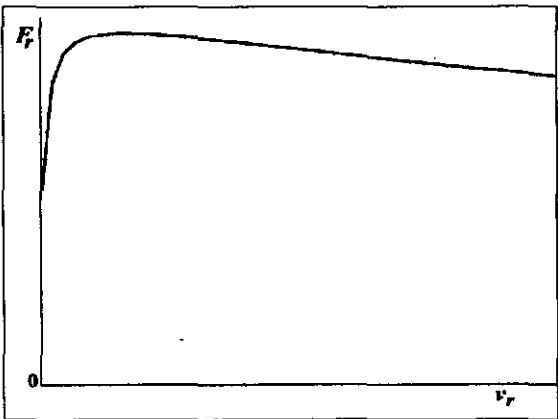


Figure 3.10: Type of friction characteristics in category III

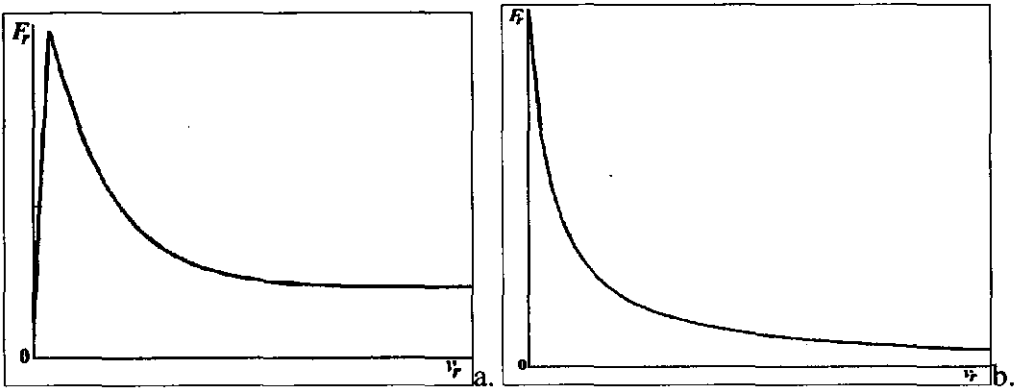


Figure 3.11: Type of friction characteristics in category IV

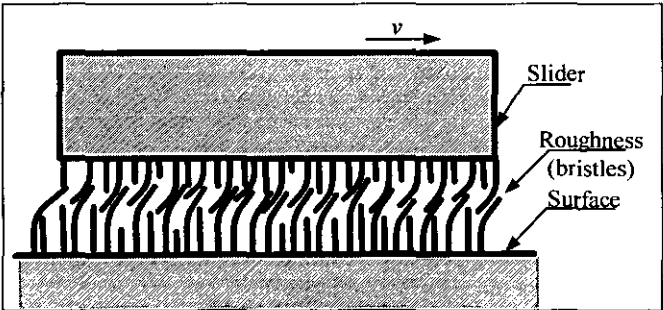


Figure 3.12: Sketch of block sliding over roughness represented as bristles.

When further growth of the bulk becomes impossible under the given conditions and subsequent micro cutting or fracture and removal of material does not occur, the resistance reaches its maximum. The slider slips over the bulge and this causes a normal displacement. As the velocity increases, with the help of such bulges, the slider gradually dislocates to higher asperities and enters a vibro-impact motion. Together with a heat effect, a reduction of the contact area occurs and the resistance to motion begins to decrease as at higher elevation the asperities act as bristles and deform with ease. The friction characteristic under such dual behaviour is depicted in Figure 3.10.

3.4 Friction Characteristics – category IV

The interfacial friction mechanism in this category incorporates the pattern described in the previous section. However, now the process has a fast changing character in which the normal component of the micro-impulses over the contacting area lifts the slider. As the velocity increases, the overall normal-to-surface impulse increases and the slider moves gradually to higher and higher asperities. The speed of change in the friction characteristics depends on the distribution of the height of asperities, the ratio between the minimum and the maximum height, and the mass of the slider. The rigidity of the asperities with average height and those with maximum height play an important role in the establishment of a given friction characteristic.

If the ratio of the height of successive asperities is such that the gradient is small and the overall normal impulse is capable of lifting the slider to the next height, the elevation will increase until the gradient becomes too large. At this point, the reduction of friction force ceases and may tend to a constant value. The decrease of friction force with the increase of the velocity (negative slop of the curve) is termed the “*Stribeck effect*” and the minimum force of friction is called “*Stribeck friction*”. Further development of friction properties will depend on the true area of contact,

formation and destruction of bonds, the rigidity of asperities in contact and the resistance to plastic deformation of the remaining higher asperities. Figure 3.11 shows some of the friction characteristics relating to this group.

If the gradient in height of consecutive asperities is such that with the increase of velocity, under the effect of micro impacts, the total normal impulse propels the slider gradually to the top of the highest asperities, friction force decreases steeply. The slider enters a floating state because it slides on the top of flexible bristles with a considerable reduction of contact area. Figure 3.12 illustrates the general case when the sliding element moves on the top of asperities which are treated as bristles. Depending on the sweep rate of the velocity, the friction force will tend asymptotically to zero (see Figure 3.11) and in certain cases, a loss of contact may occur.

If the ratio of height of succeeding asperities is large and the impulse due to impact is small, the shape of the friction force takes a different appearance which is explored in the following section.

3.5 Friction Characteristics – category V

In this group of friction characteristics, the interfacial process is similar to the mechanism described in the preceding section. In addition, the ratio of average height to the maximum height is large and the distribution of the asperities is such that the slider stays at the level of average height. This is because the energy of the normal impulse of the micro impact is not enough to lift the slider to a higher elevation.

With the increase in velocity, micro impacts occur and the resulting micro impulse raises the slider continuously to the average height. The friction force falls

gradually to a critical value due to the factors mentioned above. Beyond this critical point of minimum value, a further increase of the sliding velocity results in an opposite behaviour of friction characteristics. The friction force begins to display the viscous properties of the interfacial materials. Depending on the distribution of the remaining higher asperities, on their size and rigidity, and on the creep viscosity of the materials, the steepness of the resistance to motion will increase with the velocity of deformation. Figure 3.13 illustrates the characteristics of friction behaviour in this category. Figure 3.13b shows generalised friction force characteristics (Brokley and Ko, 1970), which take account of all aspects of friction mentioned above. The reason for this increase in force with the velocity was explored above, partially being caused by fast visco-elastic and visco-plastic deformation of the asperities at the sliding level. This is because the remaining higher asperities undergo a visco-plastic deformation on their summits whilst their bodies deform elastically and vibrate. Figure 3.14 demonstrates such a phenomenon. Sound and heat are emitted as energy in the system is dissipated. Due to the growth of the resistance to motion, the sliding velocity decreases to a certain value and then increases again. This decrease and increase in the sliding velocity brings a kind of self-balanced regulation, which controls the stability in the system's motion.

In force-velocity modelling of friction, the pre-slip elastic deformation is often dismissed to simplify the model, however it can be accounted for as shown in Figure 3.15. K_S and K_R are the stiffness in the slider system and the surface respectively, N is the normal load, C is the interfacial damping, f_r is the threshold friction force of the Coulomb element, k_{sr} and k_{Rr} are the stiffness of the asperities of the slider and the surface respectively. The springs K_s and K_R are shown as dot-lines because these elements may not be included in some models. Figure 3.15 is to some extent a mathematical interpretation of Figure 3.7.

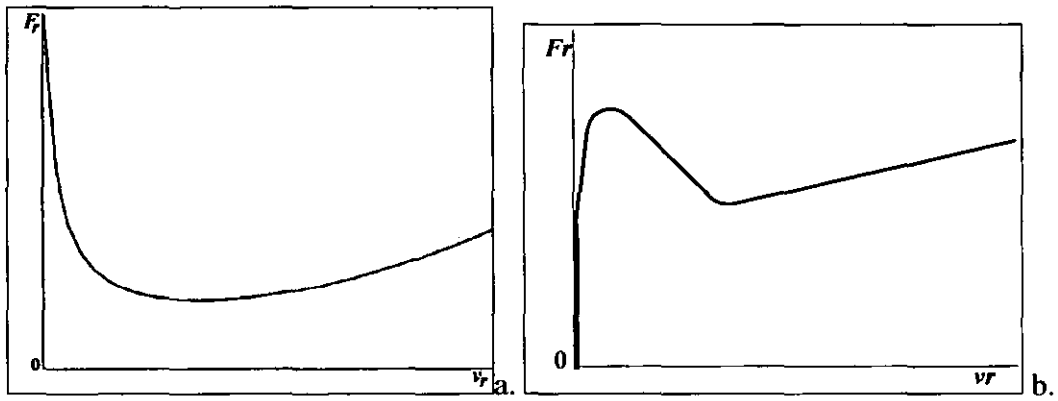


Figure 3.13: Type of friction characteristics in category V

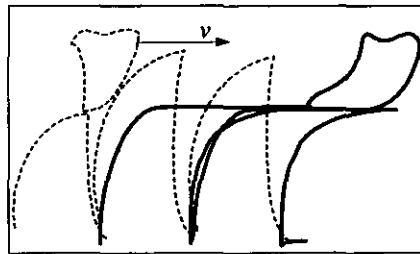


Figure 3.14: Deformation of asperities at high velocity.

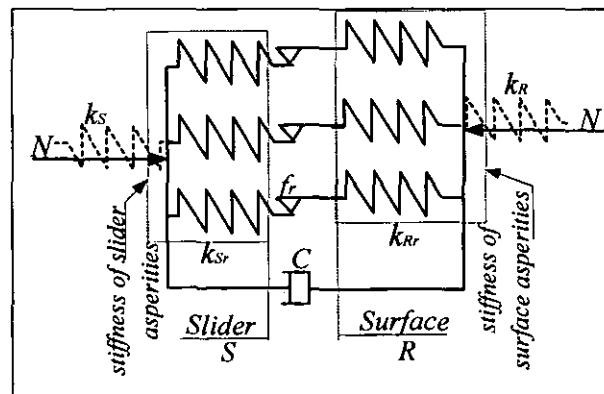


Figure 3.15: interface model with pre-slip elastic deformation.

3.6 Mathematical consideration

Mechanical systems incorporating relative motion with friction at contact interface often display friction-induced vibration in two forms, namely, stick-slip and quasi-harmonic oscillations. Self-sustained frictional vibration has detrimental effects on the performance of a system. So solutions are sought to alleviate or eradicate these oscillations. In solving such engineering problems with friction, mathematical modelling of frictional process faces difficulties because the process of friction is treated as two different states with a switch between them. The characteristics of friction force presented in Figures 2.8, 2.9, 2.10, 2.11 and 2.13 are non-smooth functions because they contain some discontinuities. These discontinuities engender complex nonlinearity in the dynamic behaviour of the system.

In frictional vibration caused by stick-slip motion, two distinct processes take place with a non-smooth transition between states. Thus, the mathematical interpretation of such a system (non-smooth system) requires three formulations:

- Mathematical expression of each continuous state.
- Statement of the scope of transition and the definition of the trigger (switch).
- Mathematical definition of the transmutation function.

For example, for the classical Coulomb friction coefficient depicted in Figure 3.8a, the friction force is described as follows:

$$\begin{cases} F_r = \mu N \text{ for } v_r > 0 \\ |F_r| \leq \mu N \text{ for } v_r = 0 \\ F_r = -\mu N \text{ for } v_r < 0 \end{cases} \quad (2.13)$$

Where, N is the normal load, v_r - the relative velocity, μ - the coefficient of friction.

There exist several methods for finding solutions to the above: such as piecewise algorithm, shooting method with smoothing techniques, mapping approach and numerical simulation. Commonly the shooting method is used when solving discontinuous differential equations. It aims at defining the new smooth system,

which may effectively replace the discontinuous system. However, the shooting method often results in stiff differential equations, which requires much time and large computational power. Other techniques such as the switching method (which is the method used in this investigation) employs the three formulations mentioned above. This method has been shown to require less mathematical manipulation and computational time (Leine et al. 1998).

The friction force illustrated in Figure 3.10 was obtained with a friction coefficient expressed as:

$$\mu(v_r) = 0.165[1 + e^{(c_1/v_r)}][1 + e^{c_2|v_r|}] \quad (2.14)$$

Where $c_1 = -0.02\text{m/s}$ and $c_2 = -0.25\text{s/m}$, (Popp, 1992). The friction force characteristics shown in Figure 3.11a is modelled with equation (2.15) where $a_1 = 0.14$, $a_2 = 1.14$, $b_1 = 2.0\text{m/s}$, $b_2 = 100\text{s/m}$ (Popp, 1992).

$$\mu(v_r) = [a_1(1 + a_2e^{(-b_1|v_r|)}\arctan(b_2|v_r|)] \quad (2.15)$$

Expression (2.16) produces the friction-velocity curve depicted in Figure 3.11b.

$$\mu(v_r) = \mu_0 / (1 + \delta|v_r|) \quad (2.16)$$

where, δ is a positive number expressing the rate at which friction decreases with increasing sliding velocity. The characteristics of the force of friction in Figure 3.13a. was modelled by equation (2.17) using $\mu_0 = 0.4$, $\mu_1 = 0.1$, $\lambda = 99.4\text{s/m}$, $\alpha = 0.7\text{s}^{-2}/\text{m}^2$, (Popp, 1992).

$$\mu(v_r) = \frac{\mu_0 - \mu_1}{1 + \lambda|v_r|} + \mu_1 + \alpha v_r^2 \quad (2.17)$$

4. DISCUSSION

In this chapter, a hypothesis on the phenomenon of the normal jump in sliding friction is developed from the viewpoint of the vibro-impact process, derived from the properties of the contacting surfaces. This description is in agreement with the experimental results of Tolstoi (1966) and other investigators. The development of the process of friction is described. Attention is paid to the first slip and the cause of its large magnitude. A source for the reduction of the friction with the increase of the velocity is explored and the origin of normal displacement of the slider was discussed. This phenomenon of friction reduction (*Stribeck friction*) is used in later chapters to develop a self-excited vibro-impact mechanism for percussive-rotary drilling. The introduced hypothesis intends to open up an area unexplored in the study of friction. This is an attempt to get an insight into the interfacial process and the cause of vibrational behaviour. However, the stated views on friction as a vibro-impact process cannot yet receive experimental support. This area needs to be investigated following up the abstract of a paper treating frictional vibration as a vibro-impact process as presented at a Russian symposium of vibro-impact systems by Gekker, (2001).

Chapter 4

EXPERIMENTAL PILOT STUDY

EXPERIMENTAL PILOT STUDY

1 INTRODUCTION

At the early stage of this investigation, a drilling test rig was developed to explore new opportunities in rock drilling with application to vibration and impact. The test rig intended to help in the practical understanding of the basics of rock drilling. The acquired knowledge and experience of using the test rig served as a forerunner of the study and the theory to be elaborated.

In rock drilling, there is a large variety of tools in use but the diamond bits and the tricone roller bits are the most widespread when operating in hard formations. However, these tools are very expensive in the frame of this university-based investigation. The principle of operation of the tricone bits involves a continuous collision of roller teeth with the medium. The engaging tooth impacts against the rock surface and sets a compressive load. This kind of impact loading is of interest because of the direct relation to the subject of this investigation. In order to be able to replace the tool in cases of bearing failure, a cost-effective roller cutter was chosen, namely a 72mm tricone bit. This is the smallest tricone bit commercially available and it can drill into hard and very hard limestone and sandstone. Because of its small diameter, it allows the use of relatively small rock samples.

Initially three types of rock (granite, limestone, and sandstone) were selected for this investigation. The rocks were cut into cubic blocks of about 300x300x300mm. In general, the quality and the hardness of rocks depend on their origin. Rocks from different locations of the UK display different mechanical properties. The geographical origin of the samples used in this work was unknown and this makes it

difficult to compare the physical properties of the samples with the data in handbooks.

2 DEVELOPMENT OF THE TEST RIG

The experimental rig was built up of a standard strength-of-material testing machine and specially designed drilling unit. In order to be able to monitor, record and analyse data from the experiment, the test rig was equipped with the necessary devices and sensors. Figure 4.1 shows the initial flow diagram of the experimental set up. The technical performance of each element is described in the corresponding section.

With respect to its functionality, the test rig may be regarded as being partitioned into four integrated systems: drilling unit, servo-hydraulic testing unit, sensors and data acquisition unit and visual monitoring devices.

2.1 The Drilling Unit

The drilling structure consists of a rigid frame DS on the top of which a DC motor DS1 is mounted. The frame made of U-shaped steel bars is bolted together to house the strength of material testing machine MTM (see Figure 4. 5). The frame is fastened to the floor. The strength-of-material testing machine has four columns, which are firmly attached to the top bars of the frame through clamps. This increased the rigidity of the entire rig and reduced vibration in the system.

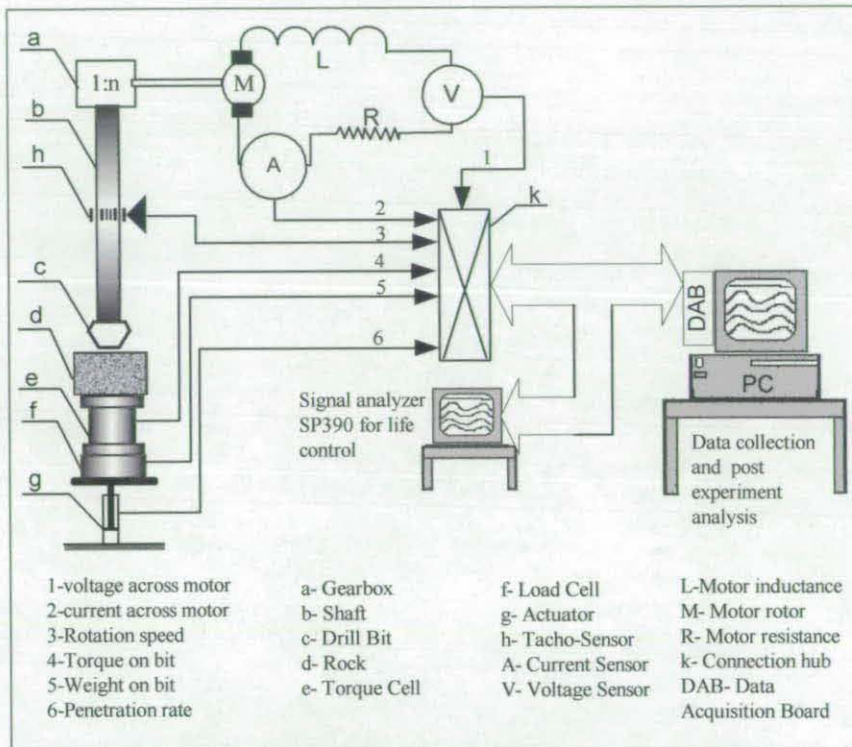


Figure 4.1: Flow Diagram of the Experiment.



Figure 4.2: Drill hub (left) and Tricone bit (right)

The DC drive is a separately excited single-phase motor and gives a maximum rotation speed of 3000 revolutions per minute with a current of 5 Amperes across the motor. Table 4.1 gives the technical data of the driving system. The drive is a thyristor controlled variable speed motor. The rig was installed in a workshop with other equipment; hence, the nearby operating electrical machines affected the performance of the motor because of the thyristor controller which was susceptible to variation in the supply voltage. There was no feedback control for keeping to a constant speed; therefore, the speed of rotation of the shaft often varied during the experiment. Consequently, from time to time the rotation of the bit fell from 50rpm to 30rpm or rose from 50rpm to 70rpm. A large switch was placed at front panel for emergency stop for the machine.

Table 4.1

Drive System Parameters		
Motor type	Shunt	
Current	DC 5Amp	
Voltage	180volts	
Maximum speed	3000 rpm	
Power	0.75 kW	
Type of controller	Thyristor	
Gearbox ratio	7:1	
Resistance	Field:	584 Ω
	Armature:	1.8 Ω
Inductance	Field:	62.9H
	Armature:	14.5mH

The DC motor drives a shaft with a bit at its lower end through a gearbox of ratio 7:1 and a bevel. A small screw with a conic end that sits in a slot secures the coupling system between the motor and the gearbox. The torque is transmitted through this screw which is set to slip out of the slot in case of extreme torque. The tricone bit is screwed in a drill bit sub which is mounted on the shaft. The connection between the shaft and the sub is secured by two screws similar to the previous one, sitting in small indentations made on the connection rod of the sub. Both screws could slip out of the

dents (seen in Figure 4.2) when unexpected high torque was exerted. Figure 4.2 shows the hub on the left and the tricone roller bit on the right.

A slip-ring in brass (shown in Figure 4.2) is mounted on the upper end of the hub. The ring runs free on the hub and has a tapped hole to which a hose was connected to supply water or air as flushing media.

As drilling requires a heavy load on the bit, the shaft was supported by roller bearings and ball bearings, one of which is located close to the lower end to take the axial load. Figure 4.3 shows the lower part of the shaft assembly with the bearing casing and the water hose. A tank is mounted on the upper part of the frame that supports the shaft. The tank, which can be seen in appendix 2, is used to host special drilling fluid if water or air is not used as the flushing medium.

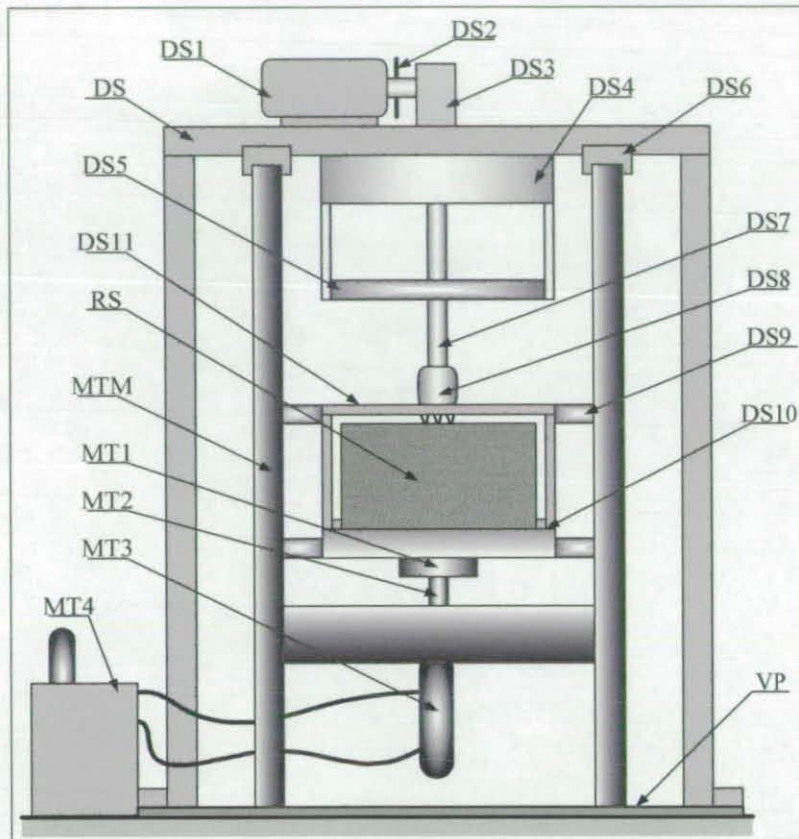
For a safe operation of the test rig, the hazardous area and the rotating parts of the rig are enclosed in cages. The cage protecting the cutting area has an opening door to facilitate the loading of rock samples. A roller conveyor was designed to assist the loading and unloading of the rock blocks because they were heavy (about 70kg each) and the lifting crane had no access to the cutting area. Figure 4.4 shows the conveyor fitted to the door of the protecting cage.



Figure 4.3: Bit-hub-shaft assembly



Figure 4.4: Loading conveyor



- | | |
|--------------------------------|--|
| MTM – Material testing machine | DS – Drilling Structure |
| MT1 – Load cell | DS1 – Electric motor |
| MT2 – Actuator shaft with LVDT | DS2 – Motor shaft and disc with flutes |
| MT3 – Actuator | DS3 – Bevel |
| MT4 – Hydraulic power station | DS4 – Drilling fluid tank |
| VP – Vibration isolation pad | DS5 – Supporting frame with bearing |
| RS – Rock sample | DS6 – Clamps |
| | DS7 – Shaft |
| | DS8 – Drill bit |
| | DS9 – V-block sliding guider (8 blocks) |
| | DS10 – Base plate of the Jig |
| | DS11 – supporting frame for the upper V-blocks |

Figure 4. 5: Schematics of the test rig

2.2 The Servo-Hydraulic Testing Machine

This is a standard strength of material testing machine provided by ESH testing Ltd. It is made of a hydraulic power station MT4, an actuator MT3, and a control panel unit (see Figure 4. 5). A load cell MT1 is mounted on the end of shaft MT2 of the actuator and serves as a feedback loop to the servo-controller. A jig is mounted on the top of the load cell to accommodate the rock specimen. This machine can provide up to 50kN of load and incorporates a function generator to produce vibration of three forms, namely saw tooth, square wave, and sine wave. The frequency of the generated vibratory motion can be varied discretely from 0.05Hz to the desirable level, (see appendix 4-2).

The servo-controller has two working regimes. It can operate either in “load mode” where the load on the actuator is the controllable parameter or in “stroke mode” where the displacement is controlled. In stroke control, a special programming unit is used in conjunction with a ramp generator producing trapezoidal command waveforms, with positive going or negative going ramp rates. Two ramps (Ramp1, Ramp2) and two holds (Hold1 and Hold2) can be set independently. When ‘Ramp1’, reaches its pre-set hold level, the programming unit initiates ‘Hold1’. When the pre-set hold time expires, ‘Ramp2’ is switched on. In load control, to exert a cyclic load on the actuator, the mean value of the required load and the amplitude of oscillation are set. The frequency of oscillation is secured with the help of the function generator.

Figure 4. 5 illustrates the schematics of the setting on the rig and the full view of the experimental test rig with the rock samples on the right and the computer for data acquisition as given in appendix 2.

2.3 The Sensors and Monitoring Devices

Six sensors were installed on the experimental rig to help monitor the performance of the machine and to acquire data for further analysis. The voltage and current across the motor, the speed of the rotation of the shaft, the weight (load) on the bit, and the rate of penetration were monitored. The transducers were located at the appropriate place on the rig.

2.3.1 MONITORING THE SPEED OF ROTATION

The speed of the drive can be varied linearly with a potentiometer. To monitor the speed of the motor, a rotating disc with 60 flutes is mounted directly onto the shaft. Because of the irregularity in the operation of the thyristor controller (which results in high fluctuation of the motor speed), the actual speed of rotation of the bit needs to be measured. To accomplish this task, a reflective opto-switch 2601 (RS307-913), shown in Figure 4.6 left was used.

The opto-switch consists of an infrared emitting diode and a phototransistor mounted in a rugged enclosure. The phototransistor reacts to the emitted radiation from the infrared diode if a reflective object is in the active field of the sensor. An infrared transmitting filter is built-in to eradicate problems from surrounding light. The principle of operation of the sensor is illustrated in the right hand side of Figure 4.6. Any object located near the sensor reflects the infrared light emitted by the diode. The reflected light triggers the phototransistor to generate an output signal (a pulse).

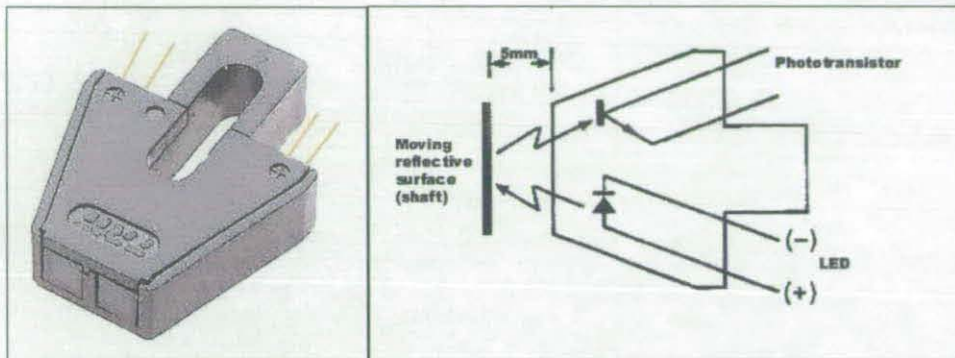


Figure 4.6: Left- phototransistor; right- principle of operation.

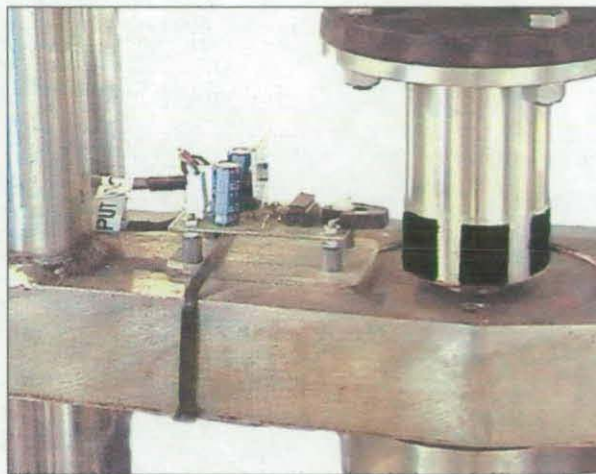


Figure 4.7: Set up of the Opto-switch for rpm measurement.



Figure 4.8: Digital display of the actual shaft speed

In this experiment, six equally spaced black patterns were stuck around the shaft and the sensor was positioned in front of the patterns at 5mm from the shaft as shown in Figure 4.7. The rotation of the shaft causes the sensor to generate six TTL pulses for each full revolution. The generated signal is conditioned and displayed digitally (Figure 4.8) in revolutions per minute. This allows visual monitoring of the actual speed of rotation of the bit during the drilling process. The signal is transmitted also to the data acquisition board.

The configuration of the opto-switch to measure the actual speed of rotation of the shaft-bit assembly gave an adequate result. However, higher resolution could be obtained by increasing the number of black patterns on the shaft. The disc with flutes mounted on the shaft of the motor was used in conjunction with another optical encoder during the setting up process to obtain the rotation speed of the motor and to calibrate the opto-switch. The electrical circuit of the configuration of this sensor is given in the appendix 4-1.

Table 4.2 shows the data obtained during the calibration process of the phototransistor. The speed of the motor was varied with the rotary potentiometer, one dial at a time, starting from its maximum speed down to a full stop of the motor, then speeding up again to the maximum speed. The calibration started from the top speed because the gearbox ratio and maximum speed of the motor were known. The obtained data confirmed that the configuration and the set up of the phototransistor would provide acceptable results.

Table 4.2

Potentiometer dial	Sensor output (pulses)	Digital display (RPM)
1	60	10
2	120	20
3	420	70
4	780	130
5	1260	210
6	1680	280
7	2040	340
8	2340	390
9	2520	420
10	2640	440

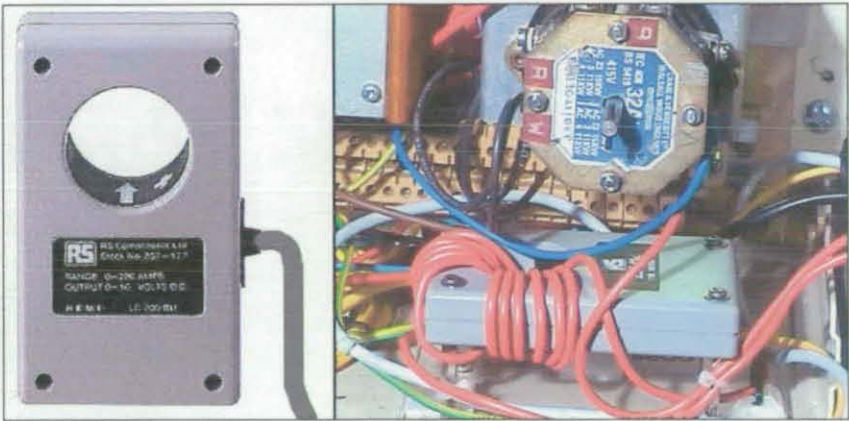


Figure 4.9: Current probe in the motor control unit

2.3.2 THE CURRENT AND VOLTAGE ACROSS THE MOTOR

The power consumed by the electrical motor was measured by recording the voltage and the current through the motor. The current was measured with the help of commercial transducers (HA 200-SU, RS257-414) with a solid core and the PR30 probe with a split core, manufactured by LEM Instruments. These are robust devices working on the Hall effect principle and can measure current up to 200A with a resolution of $\pm 1\text{mA}$. The live lead of the motor power supply is wound around the core of the sensor. To increase the sensitivity of the device, more loops could be wound. With the HA 200-SU, ten loops were used whereas with the PR30 probe only two loops was used. Figure 4.9 (left) shows the HA 200-SU solid core current sensor and its configuration in the motor control unit (right).

The magnitude of the voltage across the electrical motor was recorded with the help of a commercial differential probe similar to the one shown in Figure 4.9. This transducer operates on a 9V battery and utilises the Hall effect to measure voltage up to 1200V with a resolution $\pm 5\text{mv}$. The signal from both the current sensor and the voltage probe was logged straight to the computer through the data acquisition system.

Data given in Table 4.3 were obtained during the calibration process of the voltage and current sensors using digital multimeters. There was no load applied to the drill bit and to avoid interference, there was no other powerful electrical equipment operating in the workshop.

Table 4.3

Potentiometer dial	Voltage Sensor Volts	Current Sensor output	
		Volts	Amp
1	2.89	0.026	0.026
2	11.7	0.027	0.027
3	31	0.49	0.49
4	53.3	0.60	0.60
5	82.6	0.75	0.75
6	107.2	0.87	0.87
7	126.1	0.96	0.96
8	144.9	1.03	1.03
9	153.4	1.12	1.12
10	165.6	1.16	1.16

2.3.3. THE RATE OF PENETRATION AND THE WEIGHT ON THE BIT

The load or weight on the bit is gauged with the help of a load cell which is mounted on the upper end of the actuator. The load cell is the key device for controlling the entire test rig because the signal from the cell serves as feedback for the control loop of the hydraulic system.

The maximum load for the load cell was 50kN. The control panel allows for selection from three ranges of load, namely 10kN, 20kN and 50kN. The signal from the load cell is conditioned and fed to an analogue output and to a digital meter, which displays the current value of the load in voltage ($\pm 10\text{v}$) depending on the chosen scale. For example, if the scale selector was on 10kN and 1kN were applied, the digital meter would show 1v. In this experiment, the scale selector was set to 10kN.

One problem encountered when using the hydraulic system was a lack of feedback in cycling mode. This was because in the vibrating regime, the bit is in contact with the rock cyclically, thus creating a load; and out of contact, which means that there is no load at all on the cell. In cycling mode, the system operates mainly on the mean value of the load and the amplitude of oscillation. When the mean value becomes zero (no load), the system gets into a state of open loop. The company provider of this equipment confirmed this problem. When this happens, violent motion of the actuator can occur, causing failure of the bearing in the bit. In this investigation, the drill bits that failed due to this problem were repaired; however, they were destroyed during the next trials. A new drill bit was purchased and the work continued.

The rate of penetration is measured as the total displacement of the actuator which has a maximum stroke of 50mm (± 25 mm). The displacement of the piston generates a signal, which, processed by the signal conditioning system, is displayed by the digital meter. This signal was recorded through the analogue output integrated on the control panel. The signal-conditioning unit provides an analogue output signal of ± 10 v for the load and the displacement of the actuator.

2.4 The Visual Displays

Several visual displays were incorporated into the experimental rig to enable visual surveying of an ongoing experiment. These were digital meters, which displayed the actual load, actual displacement, and the rotational speed of the bit. A dual channel oscilloscope permits a view of the form and the amplitude of any two signals coming from the sensors. This allows a double-checking of the correctness of the settings of the experiment and the operation of the data acquisition system. Live analysis of the running experiment is conducted on the dual channel signal analyser SP390 manufactured by "Scientific Atlanta". The visual displays are of great assistance in

setting up and testing the performance of the rig, and capturing specific events of the running experiment.

2.5 The Data Acquisition System

The purpose of the test rig is to provide quantitative and qualitative data for post-experiment analysis. A fast sampling AD converter (PC30FS16), installed in a desktop computer was used to acquire data from the sensors. The PC30FS16 data acquisition board has a maximum sampling rate of 330ks/s with the ability to sample simultaneously up to 16 channels. This eliminates the skew time between channels and data are captured almost at the same instant on all lines. The board has a direct access to the computer memory (DMA) and can achieve a throughput of 330 kHz. This allows for streaming data directly to the hard disc almost at the same rate. The maximum input voltage of this board is $\pm 5\text{v}$.

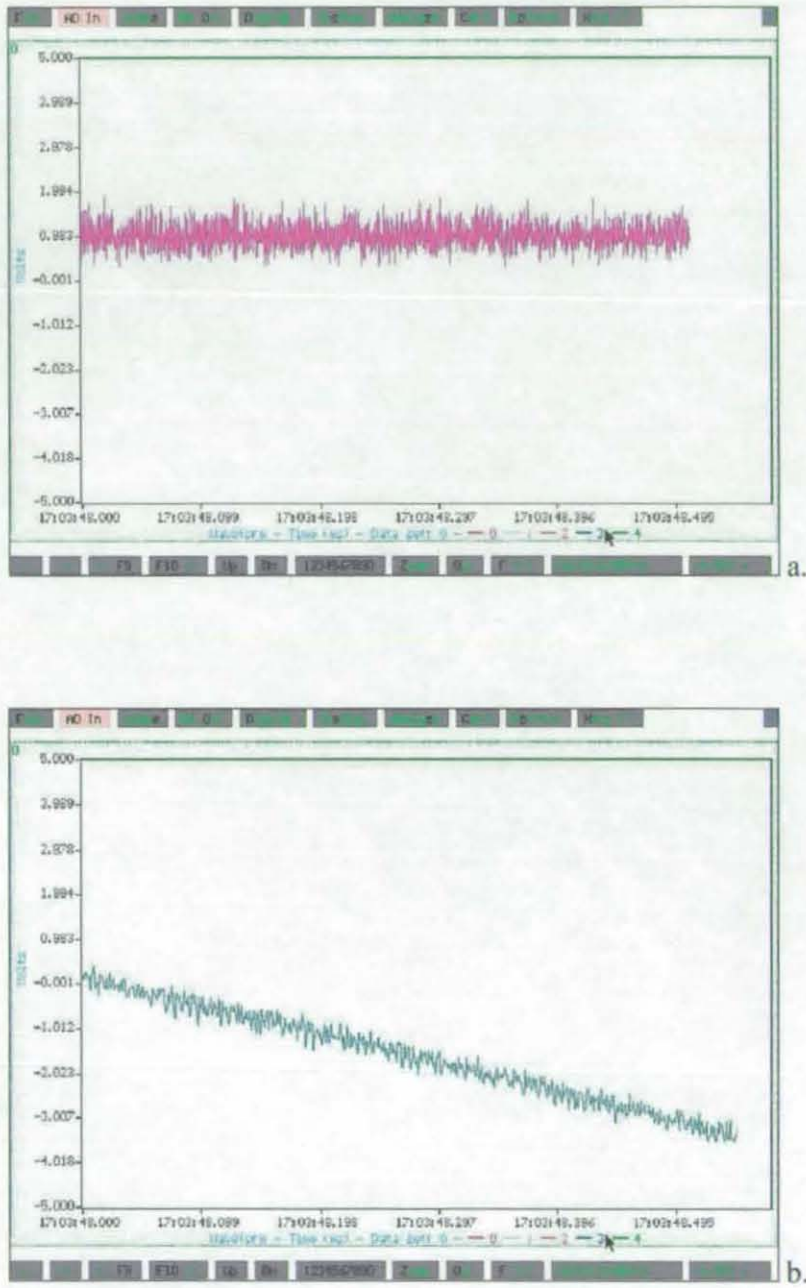


Figure 4.10: Screenshot of the WaveView software

2.5.1 THE SOFTWARE FOR DATA CAPTURING

The software (WaveView) used for data logging was provided by the manufacturer of the acquisition board (Eagle Company). This is a powerful software working under DOS and provides a wide range of services in data capturing and signal processing. The captured data can be saved in different formats suitable for transfer to other applications. The software allows the carrying out of FFT analysis of the acquired data. It is also possible to monitor continuously an incoming signal either in the form of a digital meter or in the form of a graph.

For a long lasting experiment, large data are generated and the software offers a continuous streaming of the data to the hard disc storage. Figure 4.10a and 4.10b show screenshots of the “WaveView” software for the weight on the bit and its penetration respectively.

2.5.2 SETTING UP THE EXPERIMENT

In this experiment, five parameters were monitored and recorded with the help of the data acquisition board (DAB in Figure 4.1). The board has a maximum input voltage of $\pm 5\text{V}$. The analogue output from the actuator displacement and the load cell is in the range of $\pm 10\text{V}$; therefore, these two signals were attenuated before feeding them into the data acquisition system. Table 4.4 gives the technical specification of the test rig.

Table 4.4

Unit	Device	Performance	Attenuation	Output
Drilling Unit	Motor	Shunt, single phase	-	-
	Current	DC, 5Amp	-	-
	Max. Speed	3000 rpm	-	-
	Gearbox ratio	7:1	-	-
Servo-Hydraulic	Load cell	Max.50kN ($\pm 10V$)	$\frac{1}{2}$	$\pm 5V$
	Displacement	50mm ($\pm 10V$)	$\frac{1}{2}$	$\pm 5V$
	Wave generator	0.05Hz – 5MHz	-	
Sensors	Torque cell	300Nm	-	$\pm 5V$
	Current	200A	$\frac{1}{2}$	5V
	Voltage	1200V	1/200	$\pm 5V$
	Optical encoder	TTL	-	6 pulses/rev.
DAB PC30FS16	Board type	Analogue to digital	-	
	Input voltage		-	$\pm 5V$
	Sampling rate	330kS/s	-	
	Channels	16 simultaneous	-	

3 THE EXPERIMENTAL WORK

Three types of rocks were initially involved in the experiment. There were 5 blocks of each type making a total of 15 blocks. Commonly, the mechanical properties of engineering materials can be found in textbooks. However, rocks are natural products, and a given specimen bears almost unique characteristics. The rocks used in this investigation originated from unknown places. Therefore, preliminary work was undertaken to identify the actual mechanical properties of the rock. One block of each type was taken for a compressive strength test. Series of test drilling were carried out varying the speed of rotation and the applied load. For each test a new flat face of the block was drilled.

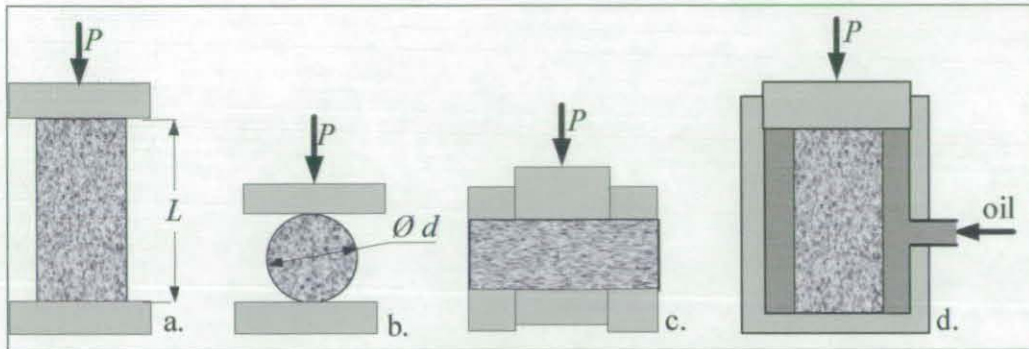


Figure 4.11: Methods of testing rock strength, (Brown, 1981).

a.- uniaxial (UCS); b.- Brazilian; c.- ring shear; d.- triaxial.



Figure 4.12: Core samples after UCS test.

3.1 Core Sample Test

There exist several methods for testing the strength of rock samples. These are the uniaxial compressive test, the triaxial compressive test, the Brazilian test, the point load test, the ring shear test and the Schmidt hammer test.

In a UCS (Unconfined Compressive Strength) or uniaxial test, a cylindrical core with a diameter equal to half of the core's length is loaded in compression in the direction of the longitudinal axis with an increasing load until the sample fails. The compressive strength of the rock is taken as the load (P_f) at which the core cracks down divided by the cross section of the specimen. $UCS = P_f / \pi(d/2)^2$, where d is the diameter of the specimen, (Brown, 1981). Typical testing methods are shown in Figure 4.11, (Brown, 1981). Figure 4.11a illustrates the setting for testing the compressive strength of the rock. The set up in Figure 4.11b (Brazilian test) provides the tensile strength of the sample. A test conducted according to the configuration in Figure 4.11c (shearing ring) produces the shear strength. To obtain the confined shear strength, the test must be carried out as shown in Figure 4.11d where the core sample is pressurised all round until it fails.

In this experiment, the cores were cut off the main rock blocks with a diamond core bit. The core samples and the test complied with the requirements of ASTM and the British Standard BS1610. The diameter (d) of the cores was 54mm and the height (L) 108mm; the ratio L/d was 2 and the standard requires that $2 \leq L/d \leq 4$. The uniaxial compressive strength (UCS) test was carried out in the civil engineering laboratory of rock mechanics on the "Denison" Block Testing System. A load was applied to each core at the rate of 0.17kN/second. The computer controlling the testing machine produced the plots of the load against the displacement. The obtained results are given in Table 4.5 and in appendix 4-2. Figure 4.12 shows the core samples after the

UCS test. The UCS values for limestone and the granite seem rather high because the rock blocks were of a very good quality, fresh and dry.

Table 4.5

Rock Sample	Length/ Diameter, mm	load at failure, kN	UCS, MPa	Density,k g/m ³	Slope, kN/mm	Young's modulus, GPa
Granite	108/54	204.5	280.5	2687	224.24	10.5
Limestone	108/54	140.3	192.4	2480	175.32	8.2
Sandstone	108/54	61.9	84.9	2382	100.68	4.7

The results of the computer controlled unconfined compressive strength test are given in appendix 4-3 in form of graphs of the load against displacement. The computer evaluated the trend of the graph to select an approximate linear section and computed the slope of the selected section. The calculated value is shown on the plot with ticks indicating the linear section. The Young's modulus of the rock samples was calculated using the value of the slope indicated on respective graphs. The obtained values are within the range of data found in handbook of rock mechanics (Vutukuri et al, 1974). However it should be noticed that the cores for the UCS test were taken from one block of each rock, therefore the result may not adequately portray the mechanical properties of the entire population of the samples involved in the experiment.

3.2 Test Drilling

The experiment was carried out in three stages. Firstly, at a given rotation speed, different loads were applied to the bit and the parameters of the system were recorded. Secondly, to investigate the rate of penetration under different conditions, both the load and the rotation speed of the bit were varied. Thirdly, the bit was subjected to oscillating loads and the rate of penetration was studied under these conditions.

3.2.1 GENERAL OBSERVATION

Vibration is widely used in engineering for intensification or amelioration of technological processes. The aim of this experimental test drilling was to seek an increase in the penetration rate by superimposing vibration to the drilling process.

In search of the effect of vibro-impact with a low frequency of oscillation, any aspect of conventional drilling involving impact is of interest. The observation on the evolution of cutting with the tricone bit has shown that an impact action exists within the process. The impact occurs when each successive tooth at the speed of rotation of the roller suddenly encounters the medium. This impact action and the increasing pressure of the tooth generate cracks which grow from the engaging tooth to the one indented into the material. The chiselling action depends on the geometry of the cutting element and the configuration of the bit.

The milled steel tooth has a flat top face which crushes a part of the formed chips into fine particles. In the absence of flushing, the cuttings (chips) are crushed into fine powder. As the tool goes deeper into the medium, this powder is compacted. The compacted powder begins to stick to the notches of the teeth and this leads to an increased friction, high torque and reduced penetration.

Figure 4.13 depicts the cutting mechanism of a tricone bit. In Figure 4.13a after Smith Tool (Smith International inc.) there is an illusion that the teeth A and B act at the same point of contact with the medium (I, II) and the tool somehow moves up and down. It gives the impression that at some stage, the drill bit loses the contact with the medium. However, observation from the experiment shows that two successive teeth encounter the rock at different places as illustrated in Figure 4.13b. With a true rolling cones bit as in this experiment, the contact of the teeth with the medium is similar to an epicyclic gear. Here, the medium is considered as the sun wheel and the cones as planet wheels.

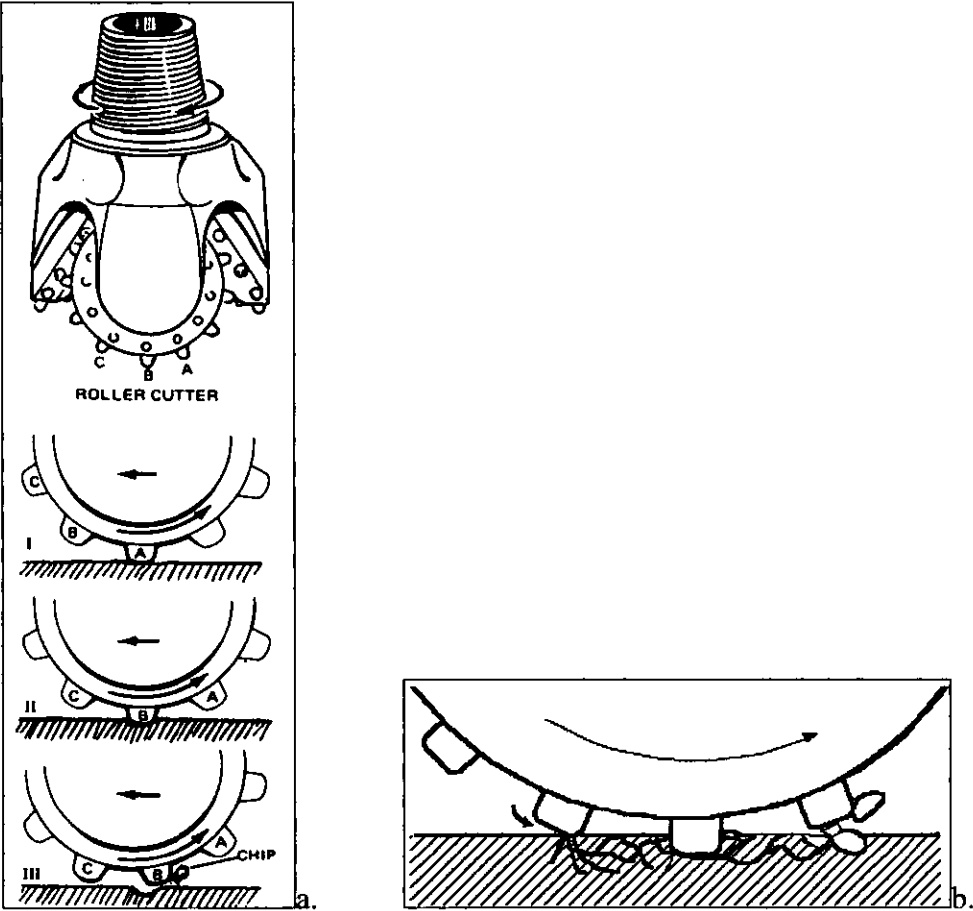


Figure 4.13: Cutting action of a roller bit.

a.- after Smith Tool; b.- observation from experiment.

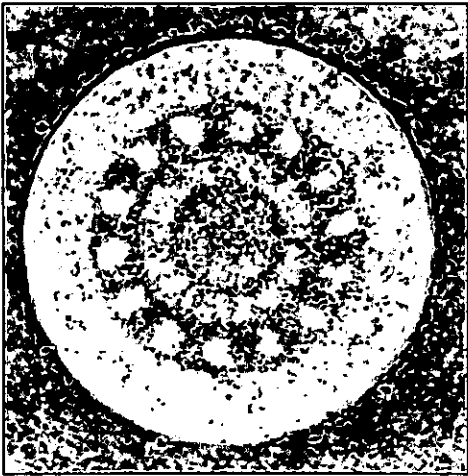


Figure 4.14: Borehole pattern

If the speed of bit rotation does not fluctuate over a wide range and if there is no slippage, a clear pattern of the teeth contact with the rock is seen at the borehole bottom. Figure 4.14 shows one of the patterns obtained in a sandstone block at a rotation speed of 40rpm. The teeth indentation (white) and the valleys (dark grey) between the teeth are remarkable in the middle ring but the outer ring cannot display this pattern because of the difference in the orientation of the teeth on the base of each cone. A similar pattern is observed in limestone.

3.2.2 THE TREND OF DRILLING FORCES

In rotary drilling with a tricone bit, the cutting forces are complex. Though a constant weight is applied on the bit, the resulting torque varies randomly. This is partially due to the unpredictable changes in the rock structure. These changes lead to an alternating hardness. Depending on the weight applied and the hardness of the rock layer being drilled, the bit will vibrate longitudinally. Both the structure of the tricone bit and the drilling fluid also emphasize the oscillation of the cutting forces. Figure 4.15 displays a typical shape of the weight on the bit recorded from the test rig. The signal of the weight on the bit obtained in the current experiment is similar to the torque and weight on the bit from a field drilling system reported in numerous papers on drilling. Though a given constant pressure is applied to the bit, the resulting actual weight and the torque on the bit varies randomly. This randomness is explained by the inconsistency in the hardness of the rock, the irregularity of the number of teeth in contact with the medium at a given time, the slippage of the cones, the fluctuation in pressure, the height of the teeth and the size of the inter-teeth notches. The build up of the pressure in the contact zone also oscillates with its maximum occurring at the instant when the tooth passes through the axis of the bit. After this point, the pressure reduces and gradually the tooth goes out of contact with the medium.

In this experiment, the hydraulic system was required to keep at a constant given load on the bit. During the drilling process, whenever the pressure becomes less or greater than the fixed value, the system automatically displaces the actuator in such a way to keep to the required pressure. The tricone bit is structured to produce maximum localised pressure exceeding the yield strength of the rock. This is done by concentrating the weight of the drill string on small area of the teeth in contact with the medium.

Because of friction and slippage, the rollers do not rotate continuously; excessive pressure occurs when fewer teeth (sometimes one tooth on each roller) support the entire drill string. In this case, all the weight applied to the bit rests on less than 18mm^2 (in this experiment). If the rock is very hard and the pressure on the bit is not enough to crush the medium, the drill string tends to bounce. This causes a normal oscillation of the drill string and for this test rig it leads to the lowering of the actuator.

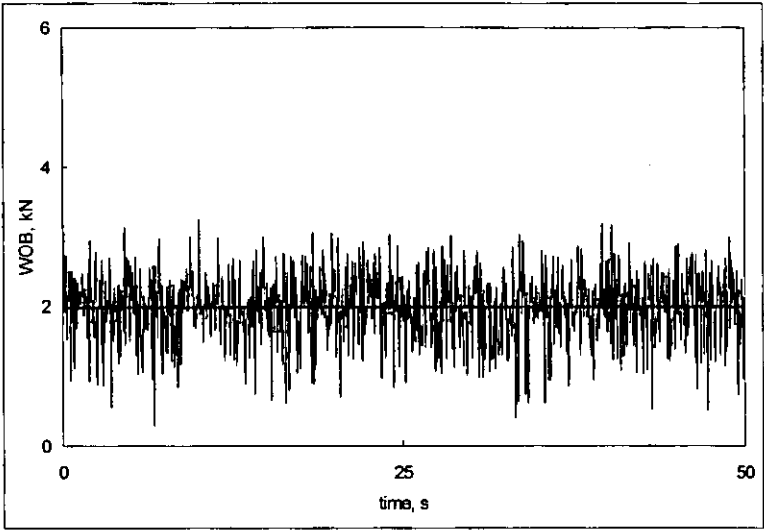


Figure 4.15: Typical signal of the weight on bit from experiment.

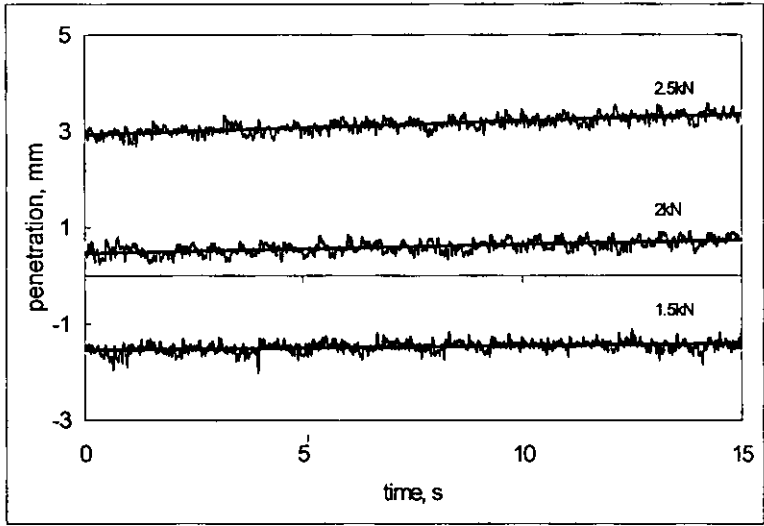


Figure 4.16: Actual signal of the penetration in sandstone.

3.2.3 TEST DRILLING WITH VARIABLE LOAD AT CONSTANT SPEED

Test drilling was undertaken at this stage to investigate the effect of an increasing load on the rate of penetration. As the cutting process involves the teeth impacting onto the medium, an increase in the load leads to an increase in the impact force. This causes deep cracks to be generated at the point of contact with the rock. The induced cracks weaken the rock matter and improve the cutting process

In this part of the experiment, the rotation speed of the bit was fixed at 50rpm. However, due to the type of motor controller described in its respective section and the resulting torque applied to the bit, the speed fluctuated between 40rpm and 50rpm. Therefore, an average speed of 45rpm is considered as the actual speed of rotation of the bit. Due to the limits in technical performance of the tricone bit used in this experiment, only small loads were applied. Trials with high values have caused failure in the bearing in the rollers. For each run of the experiment, different loads on the bit were applied: from 1kN to 3kN with an increment of 0.5kN. Generally, in rock drilling practice, the load applied to the bit is termed “weight on bit” (WOB) and this term will be used on the graphs. The data were sampled at a frequency of 50kS/s for a period of 15 seconds.

The actuator has a displacement of +25mm and -25mm with the zero position of the situated in the middle of its full extension. To obtain a full extraction of 50mm, the actuator was lowered to the extreme negative position. This explains the appearance of negative values in the penetration scale on some plots.

Figure 4.16 display the recorded signal of the penetration in the sandstone block when a load of 1kN, 1.5kN, 2kN and 2.5kN was applied to the bit. Using a linear regression curve fitting of each graph, the equation of the trend line, which represents the average rate of penetration, was obtained.

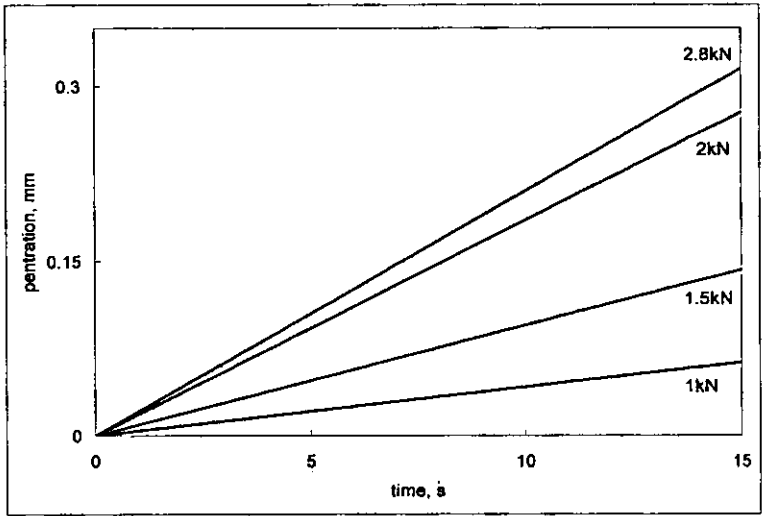


Figure 4.17: Penetration rate in sandstone.

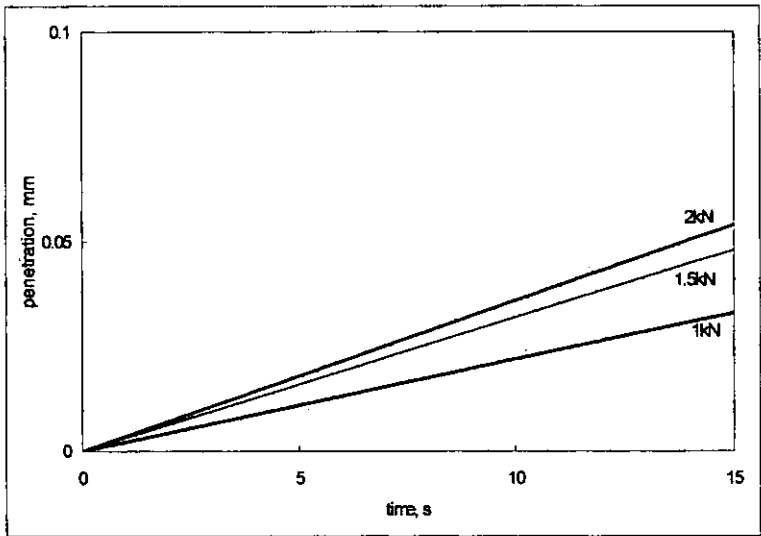


Figure 4.18: Rate of penetration in limestone.

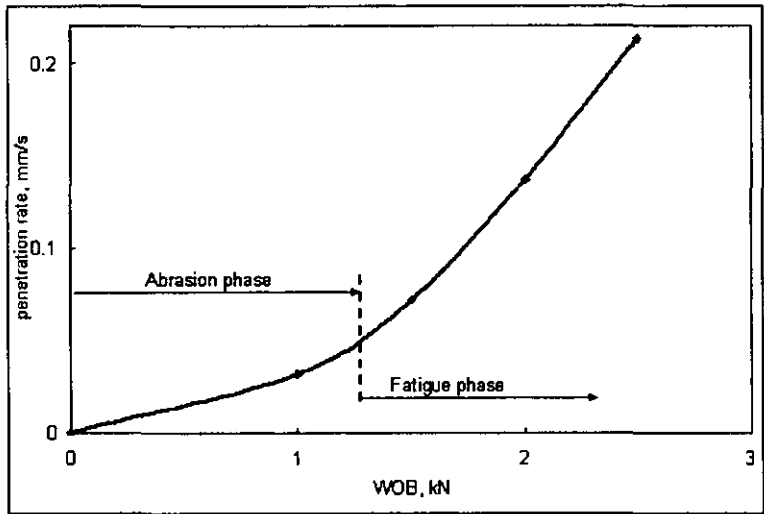


Figure 4.19: Rate of penetration in sandstone as a function of load

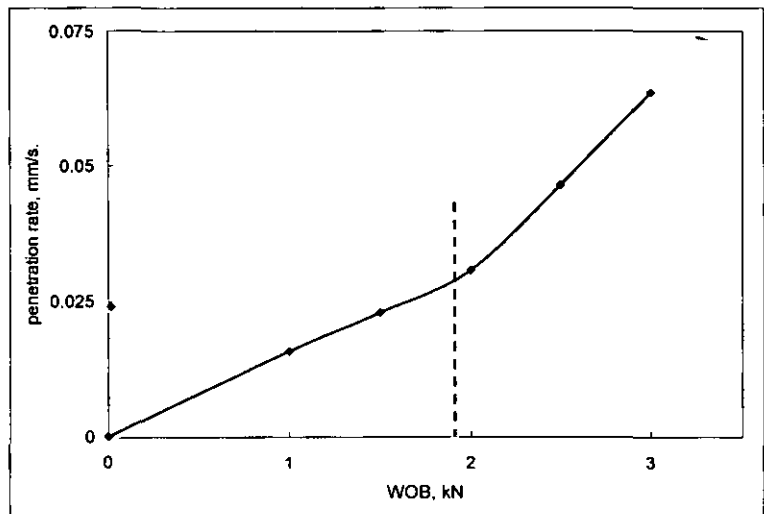


Figure 4.20: Penetration rate in limestone as a function of load

Penetration with the time into sandstone and limestone are illustrated in Figure 4.17 and 4.18 respectively, for different applied loads to the drill bit. These graphs were obtained from the equation of the trend line for each signal. It shows that for a given speed of rotation, penetration increases with the increase in the weight on bit.

An average penetration over the sampling time is taken from each test to express the speed of penetration into the rock as the load on bit increases. The obtained relationship is displayed in Figure 4.19 and 4.20 for sandstone and limestone respectively. These curves exhibit a pattern which is also observed in field drilling systems. On these plots, two sections are noticeable and are separated with a vertical dash line.

Within the section denoted “abrasion phase”, the cutting process is similar to grinding. This is because the weight on the bit is insufficient, thus, the rolling cutters contact the medium under a small load and the material is removed mainly by friction and a wearing action. In this phase the resulting cuttings are in the form of a fine dust.

With the increase of the weight on the bit, a small penetration occurs, cracks are initiated and tiny chips are formed. At this stage, the rock formation fails due to fatigue and this section is denoted the “fatigue phase”.

The rate of penetration will increase almost linearly with further increase in the weight on the bit until the rock begins to spall. This stage is known as the “spalling phase” (Chugh, 1985) where large chips are formed. In this phase, the load is at its optimum and any further increase of the load leads to a reduction in penetration. This is because after spalling, any further increase of the weight on the bit leads to a complete submersion of the teeth into the rock matter. Increased friction and wear occurs at the base of the cones and the body of the bit with greater potential for failure. This greatly affects the rate of penetration and the overall cost of the operation.

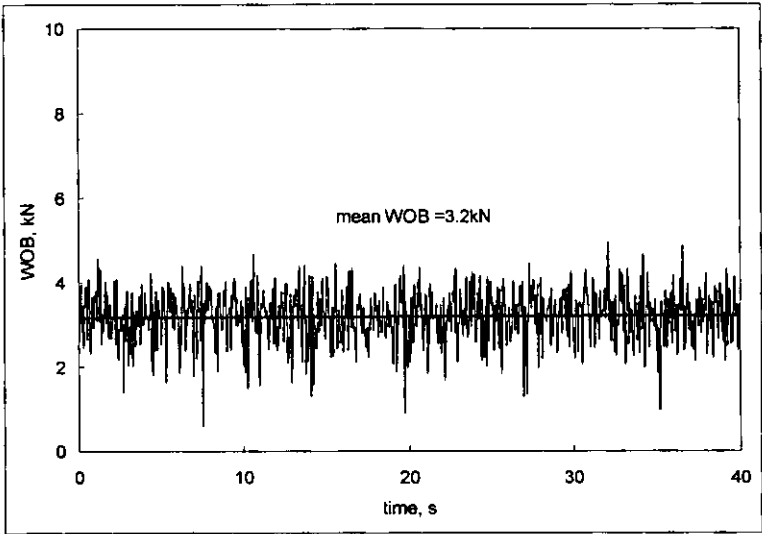


Figure 4.21: Actual signal of the weight on bit (3kN applied, 100rpm).

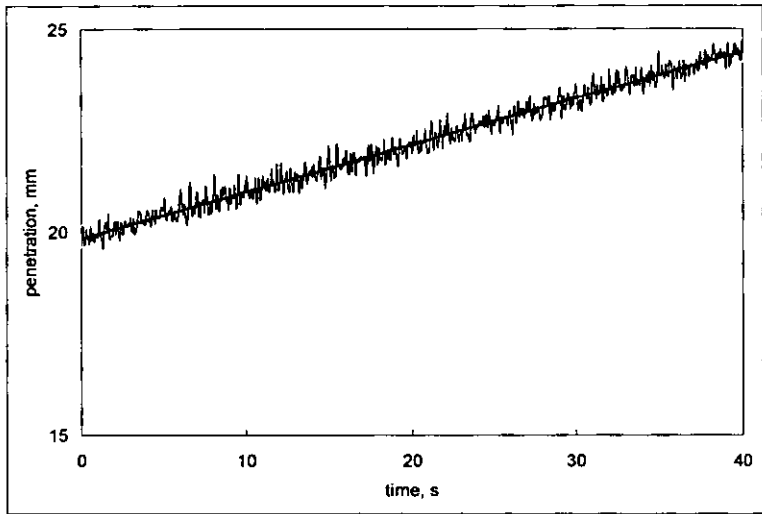


Figure 4.22: Signal of the actuator displacement (WOB=3kN, 100rpm).

Figure 4.19 and 4.20 show the drillability of the two types of rock. It is seen that sandstone is easy to drill in comparison with limestone. This matches with the results on the compressive strength test.

3.2.4 TEST DRILLING WITH VARIABLE LOAD AND VARIABLE SPEED

In this set of experiments, drilling is carried out varying both the load and the speed of rotation of the bit. This allows the investigation of varieties of drilling conditions i.e. the effect of the speed of rotation and the weight on bit on the rate of penetration. This test is designed to provide an estimation of the drilling rates for different operating regimes.

Figure 4.21 displays one of the signal of the weight on the bit recorded during the test from the load cell. 3kN was applied to the bit and the rotation speed was 100rpm. Though an average value of 3.2kN (central line) is observed, the signal depicts the random character of the forces experienced by the bit and the drill string. The drilling process lasted for a period of 40 seconds and produced a penetration of about 5mm in limestone. The corresponding signal of the penetration is shown in Figure 4.22.

A series of test drilling were carried out alternatively varying the weight and the speed of rotation of the bit. The weight on the bit covered a range from 0.5kN to 3kN and the speed of rotation from 30rpm to 140rpm. In exploitation field, the operation of a drilling system requires from the driller a specific aptitude in order to evaluate the hardness of the rock formation being currently drilled. This allows him to release the appropriate amount of weight on the bit. The performance, the bit life and the cost of drilling depend on an adequate balance of the speed and the weight on the bit.

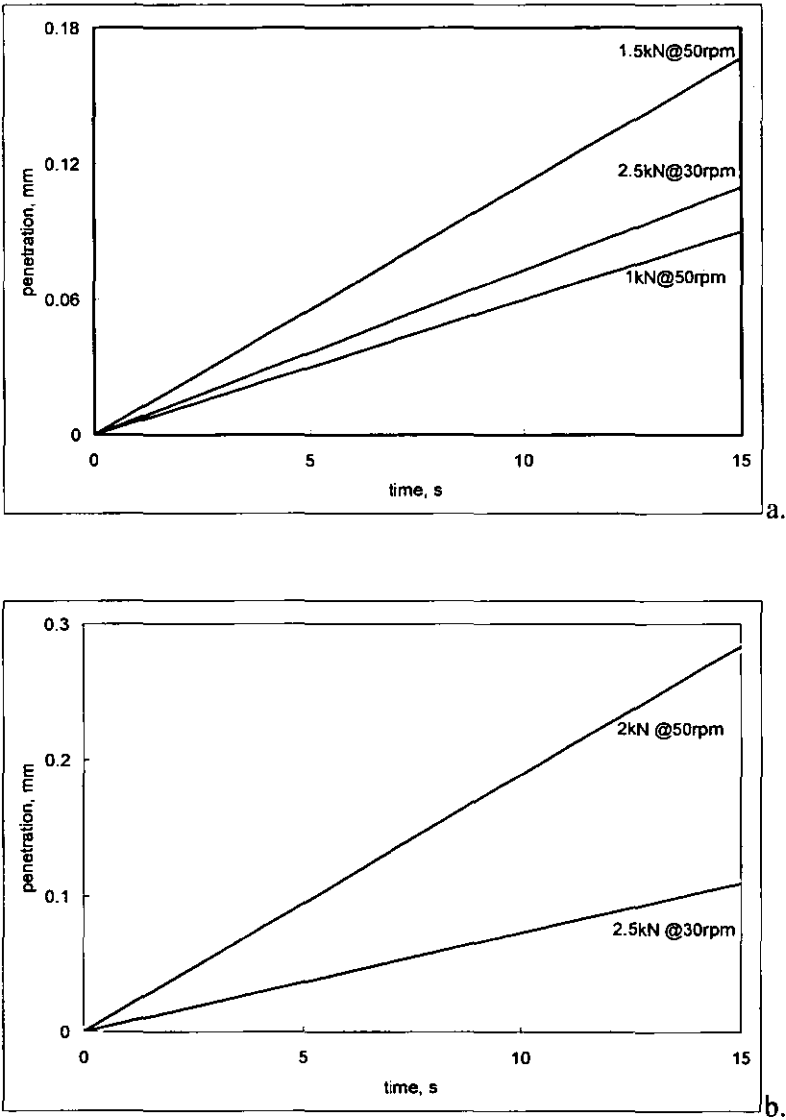


Figure 4.23: Penetration into sandstone at different speed.

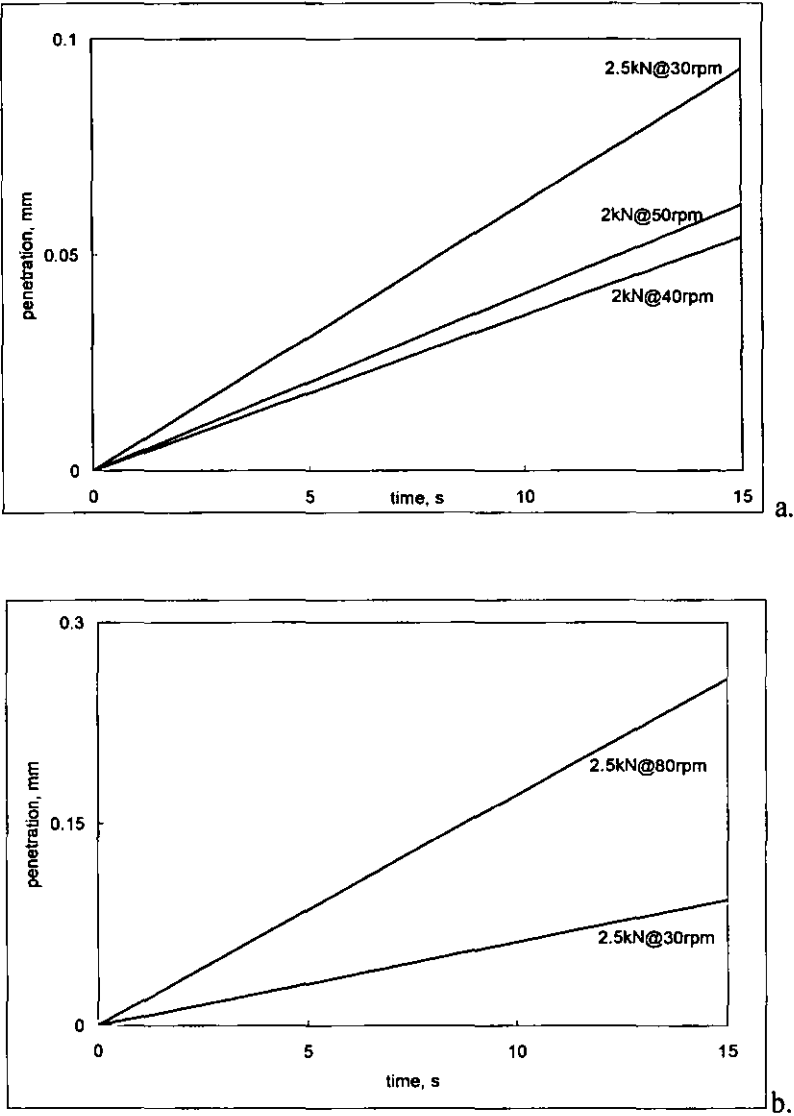


Figure 4.24: Penetration into limestone at different speed.

Cost effective drilling can be achieved by maintaining target drilling rates with a proper correlation of the weight on the bit with rotation speed. Figure 4.23a compares the rate of penetration in sandstone for a bit rotation speed of 50rpm when a weight of 1kN and 1.5kN was applied with a 2.5kN at 30rpm. Figure 4.23b puts side by side the penetration of 2kN at 50rpm and 2.5kN at 30rpm.

Figure 4.24a and 4.24b illustrate the penetration rate into limestone when 2kN and 2.5kN was applied to the bit; the rotation speed varied from 30rpm to 80 rpm. The results obtained for 1kN and 1.5kN are illustrated in appendix 4-4. It follows from these figures that a high speed of rotation produces high rates of penetration which are also proportional to the applied weight. However, high rotation speed with large weight on bit cause damage to the drilling system and shorten bit life. This is because in hard and abrasive formations, the wear of the bit is accentuated; therefore care must be taken in obtaining the relationship between the weight and the speed of rotation.

It should be noticed that there is no consistency in the rate of penetration between the different samples. The results differed from sample to sample because mechanical properties are specific for given rock sample. The penetration also varied from test to test depending on the direction of drilling. This could be explained by the fact that if the drilling were parallel to the formation layers, the rock matter would easily flake (similar to how a piece of mica flakes in the direction parallel to the layers). However if the drilling were perpendicular to the formation layers then the frontal resistance would be higher. All these aspects are not considered in this work; therefore some results of drilling in sandstone are close to those of limestone. It was observed that some samples of sandstone were hard to drill whilst some limestone blocks were drilled relatively fast. This case is illustrated in Figure 4.23 and 4.24 where the 2.5kN weight on bit at 30rpm produced almost the same depth of penetration (0.09mm and 0.11mm respectively) in limestone and sandstone for the same period of time. The results in Figure 4.23 show that sandstone blocks are soft to drill, whereas the curves

in Figure 4.24 demonstrate that limestone blocks require relatively high weight on the bit. This observation is in agreement with the results of the compressive strength (UCS) test, which showed that the limestone samples have a higher compressive strength compared to the sandstone.

The curve in Figure 4.25 was obtained when drilling without drilling fluid. It emphasises the importance of the flushing fluid in drilling. In petroleum or gas exploration, the drilling fluid is pumped down the hole through the drill pipe. The fluid is injected at high velocity and returns back to the surface flowing between the drill pipe and borehole wall carrying the cuttings. In the case of loss of circulation of the drilling fluid (low return velocity), large and heavy chips are not removed from the borehole. The remained chips are re-crushed down to small pieces, which are then transported by the fluid. The result of this process is a reduced rate of penetration (ROP). This effect is observed in this test (Figure 4.25): after 100 seconds of continuous drilling without flushing, the slope of the penetration changes. At the end of this test drilling (300 seconds) the cuttings were in the form of very fine powder, partially compacted in-between the teeth. The roller-cones appeared bulky-like with the teeth completely submerged in the compacted powder. The compacted powder formed a solid mass which strongly adhered to the body of the cones. This prevented any further indentation of the teeth in the rock matter and consequently it affected chip formation and reduced the rate of penetration.

To express the relationship between the rate of penetration (ROP) and the speed of rotation of the bit for a given weight, the average of penetrations at different rotation was taken. Figure 4.26 and 4.27 show the rate of penetration in sandstone and limestone respectively. It is observed that both in sandstone and in limestone, the rate of penetration increases linearly with the speed of rotation. The inconsistency of the hardness of the rock samples and the fluctuation of the weight on the bit due to performance of the hydraulic system have a considerable effect on the outcome of these tests. However, the obtained results follow the general trend of drilling practice.

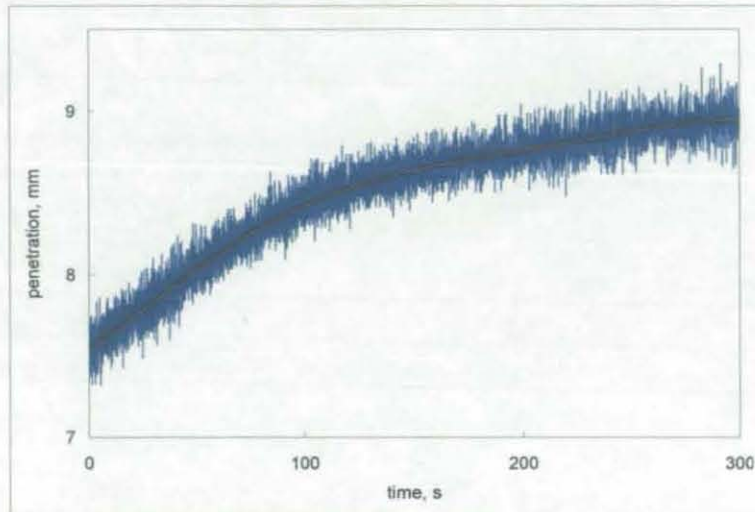


Figure 4.25: Drilling without flushing fluid.

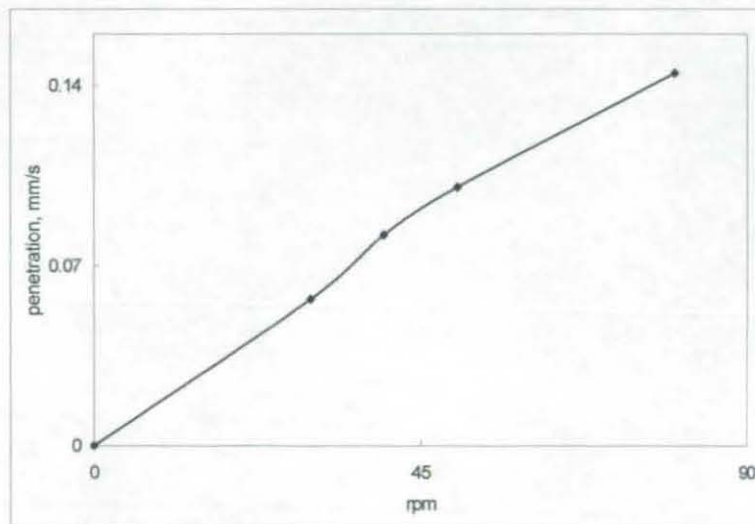


Figure 4.26: Rate of penetration in sandstone.

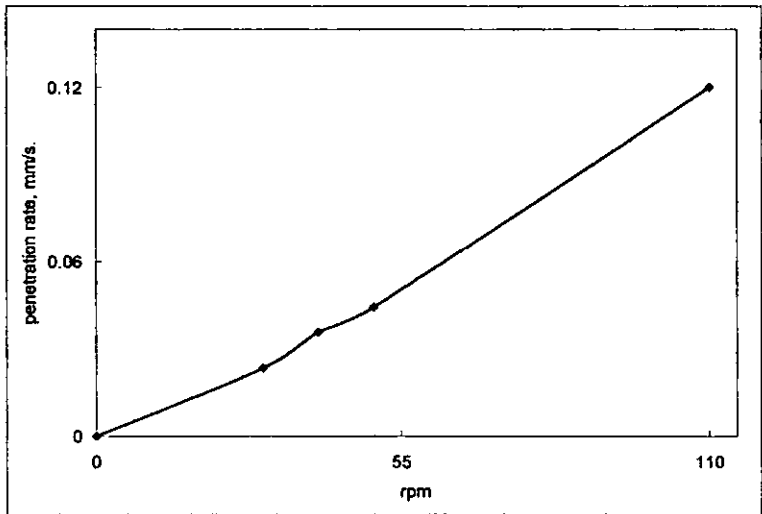


Figure 4.27: Rate of penetration in limestone.

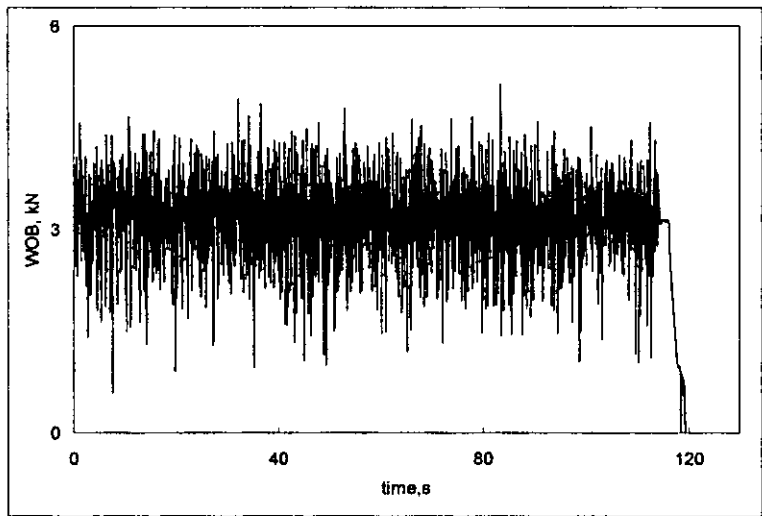


Figure 4.28: Test drilling ending with a broken bit

In general drilling practice, the rate of penetration increases with the rise in the speed of rotation up to a certain point where the penetration begins to decrease and the bit wear increases sharply. To obtain a maximum rate of penetration, first, a low speed of rotation is set; second, the weight on the bit is increasing until large chips are produced (spalling phase); third, the speed of rotation is increased to the target penetration rate.

3.2.5 *VIBRATIONAL DRILLING*

The third part of this experiment involves a set of drillings with application of vibration. The core of the entire experimentation was to explore a possible increase in the rate of penetration by superimposing low frequency vibration onto conventional rotary drilling. Therefore, this test was not designed to seek any optimal drilling parameters. The servo-hydraulic controller of the test rig incorporates a function generator which permits the oscillation of the displacement of the actuator. By this means a vibratory load is applied to the bit. A series of failure were encountered during this set of tests, resulting in two destroyed drill bits and a broken coupling mechanism between the gearbox and the bevel.

Figure 4.28 illustrates a signal of the weight on the bit when a failure occurred. Examination of the broken bit suggested that first the ball bearing in the roller cones failed and the bit became stuck in the borehole. This resulted in a high torque between the bevel and the gearbox leading to a breakdown of the coupling mechanism. The coupling was designed to protect both the motor and the drilling string, thus its failure was expected. The 72mm tricone bit is the smallest amongst rock drilling bits. Because of its milled steel teeth and relatively weak bearing, this type of bit is not used for drilling very hard rocks such as those involved in this test. This is the main reason of its frequent failure.

For this set of test drilling with vibration, a weight of 1kN, 1.5kN, 2kN, 2.5kN and 3kN was applied to the drill bit at different speeds of rotation. The load on the bit was oscillated sinusoidally at 10Hz and 15Hz. The amplitude of oscillation was set to 500N.

Figure 4.29 shows the penetration in sandstone at different weight on bit. The speed of rotation was set to 50rpm; however, due to a constant fluctuation an average of 45rpm is considered as the actual speed of the bit. The frequency of oscillation was 10Hz. Referring to previous results with the same parameters, a small enhancement can be seen, especially in the region of 2kN and above. With the increase of the vibration frequency and the speed of rotation, a noticeable improvement was observed.

Figure 4.30 compares the results of drilling in sandstone at 50rpm with 1.5kN applied to the bit. The frequency of the superimposed vibration was 15Hz. It is seen that for the same period of time, the process with added vibration has drilled 1.2 times deeper than the conventional drilling (with no vibration). In Figure 4.31, where the rates of drilling in sandstone with vibration at 10Hz and 15Hz are compared, the same trend is observed. The slopes here seem to be slightly greater than the ones in Figure 4.30; this is because of the drilling in two different samples, which obviously have different compressive strength. Moreover, each test was carried out on different sides of the block. This also accentuates the inconsistency in hardness which depends on the natural conditions when the rock was formed and the direction of drilling as stated previously. More results are presented in appendix 4-5.

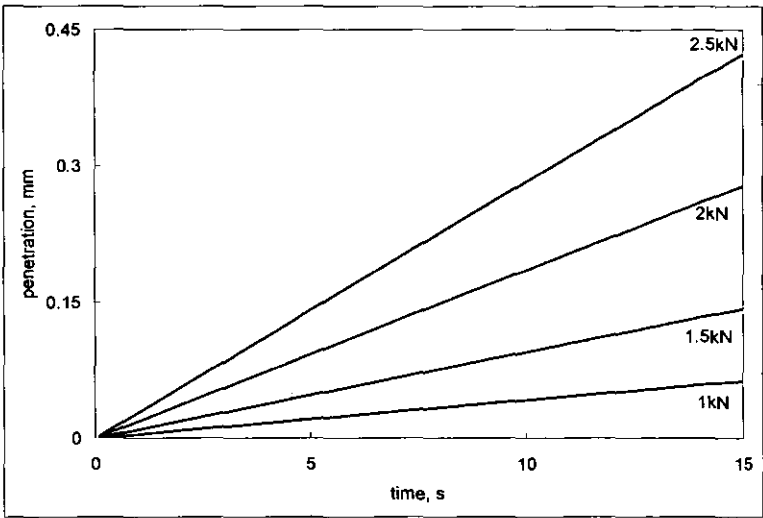


Figure 4.29: Drilling in sandstone with vibration at 10Hz.

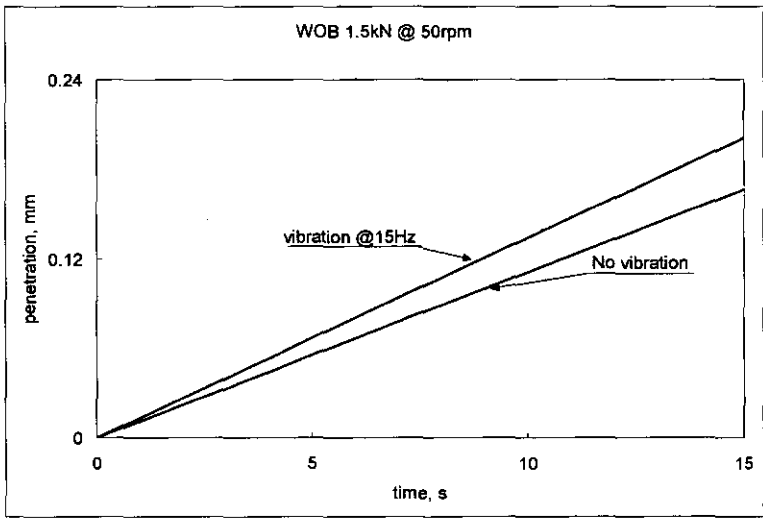


Figure 4.30: Drilling in sandstone at 50rpm with and without vibration.

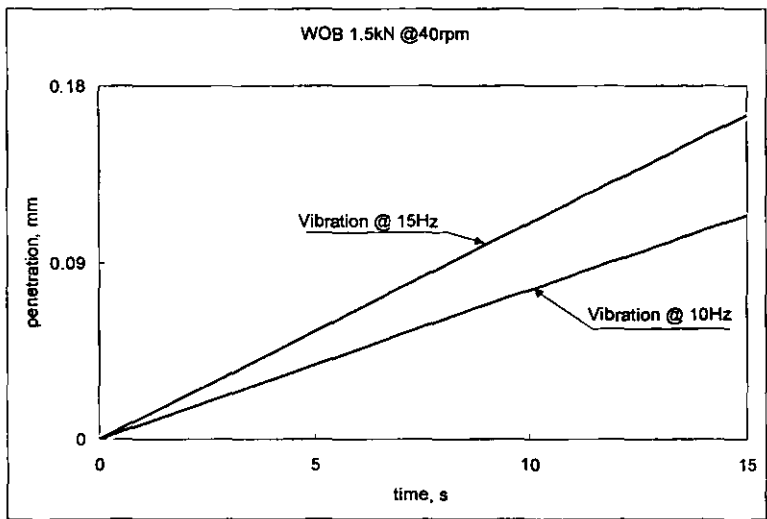


Figure 4.31: Drilling in sandstone with vibration at 10Hz and 15Hz.

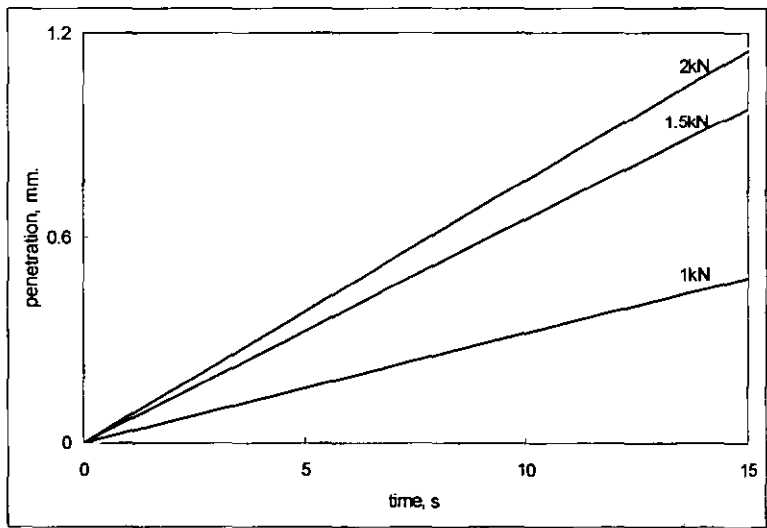


Figure 4.32: Drilling in limestone with vibration at 15Hz.

Contrary to sandstone, drilling in limestone with vibration proved to be more effective. Figure 4.32 represents the penetration rate obtained when drilling in limestone at 15Hz. These results are very high (almost double) if compared to other results of drilling in limestone. Such a large discrepancy between the two sets of results can be interpreted in different ways. As mentioned before, the constant change in rock hardness is one of the causes. On the other hand an error could have been induced in the system performance due to the superimposed vibration though the average weight applied to the bit being almost the same as set on the indicator. However, as will be shown in the theoretical modelling of penetration, the vibro-impact process is more effective in hard material. Therefore, this effect of a high rate of penetration in limestone is likely to be realistic rather than erroneous.

The average rate of penetration obtained when drilling in sandstone with superimposed vibration is presented in Figure 4.33. At 45rpm, the drilling with vibration has produced a rate of penetration which is slightly higher than the rate obtained with conventional rotary drilling at 45rpm (simple rotation). However in Figure 4.34 test drillings in limestone, which is harder, the added vibration at 15Hz gave a remarkable advantage over traditional drilling without vibration.

Though drilling with oscillation in sandstone showed a little improvement at 10Hz, an increased penetration is observed with an increase in vibration (Figure 4.31). This result and the outcome of drilling in limestone indicate that low frequency vibration can bring considerable improvement in rock drilling.

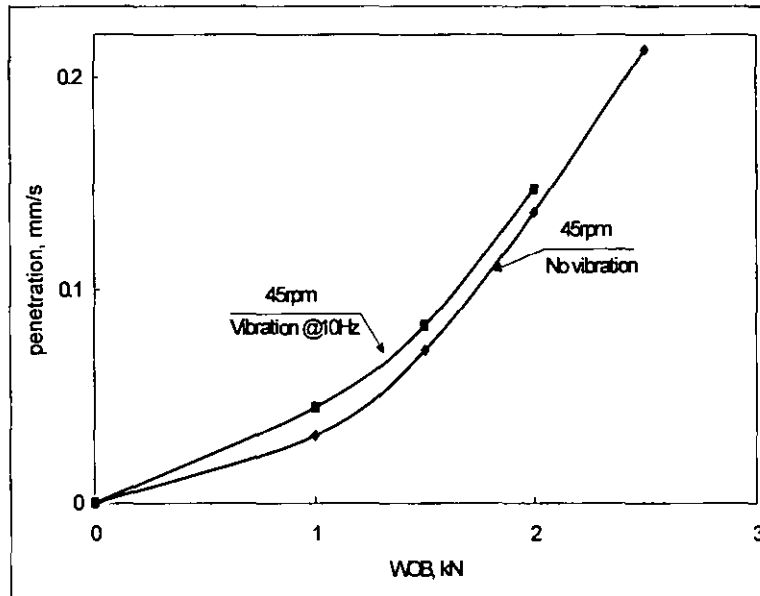


Figure 4.33: Rate of penetration in sandstone, drilling with and without vibration.

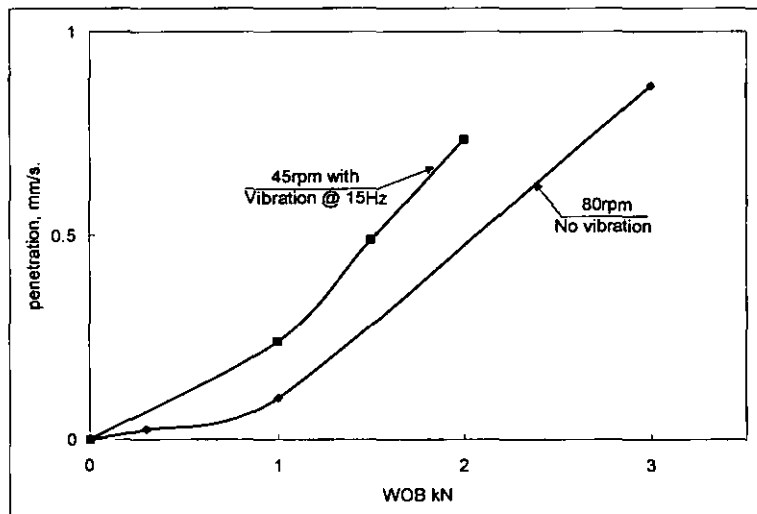


Figure 4.34: Rate of penetration in limestone, drilling with and without vibration.

3.2.6 POWER CONSUMPTION

During the calibration process and the test drilling, power was recorded using Hall effect transducers which were described in respective sections of this chapter. Analysis of the total power consumed over each test drill has revealed that the power decreases with the application of vibration.

Figure 4.35 shows the power consumed to rotate the drill shaft with no load applied to the system. The speed of rotation was increased from zero up 350rpm in a series of runs. For each run the speed was swept from zero to a given value and then a sample reading was taken. The picture indicates that there is a leakage of energy in the motor system. It shows that at zero rpm (1-10rpm) the motor consumed about 2W. This energy is partly spent in the form of losses in the bearings, the gearbox and the bevel and to spin up the rotor with the drill shaft. Also the thyristor controller has its threshold sensitivity and consumes a certain amount of energy. Ideally, the curve would originate from zero. It was noticed that between zero and 10rpm the rotor of the motor would rotate with deceleration and at times would stop for a while and then accelerate again. This may be caused by some irregularity in the control system or a malfunction of the motor or the thyristor controller.

The power recorded when drilling with different weight on bit at 45rpm is shown in Figure 4.36. The results show that sandstone required less power than limestone, which is harder. It is seen that in sandstone, the power increased linearly with an increase in the load. However, the trend of power consumption in limestone exposes some inconsistency due to the hardness of the rock samples mentioned earlier.

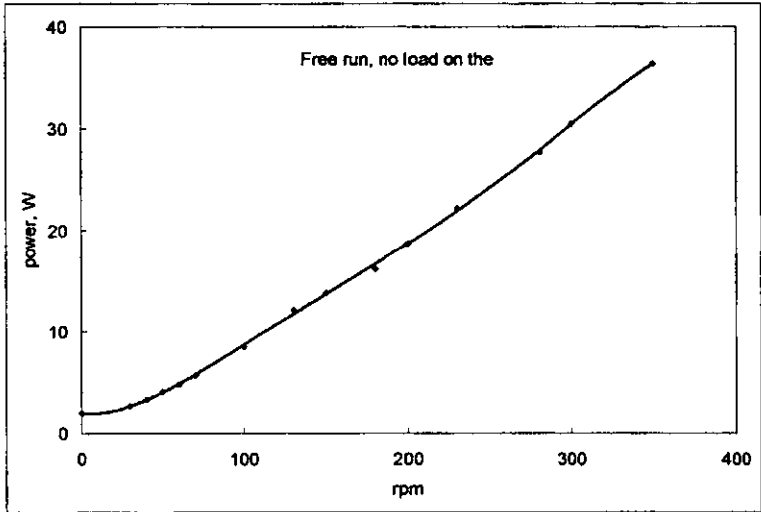


Figure 4.35: Power at zero load on the bit.

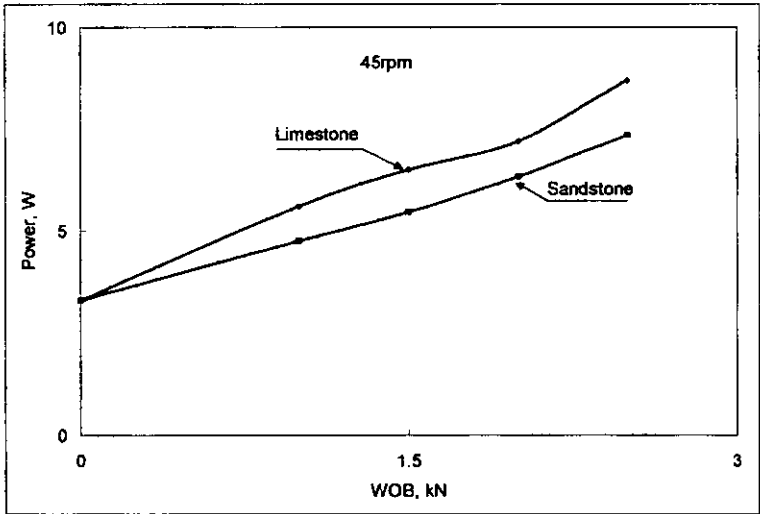


Figure 4.36: Power with increasing weight on bit.

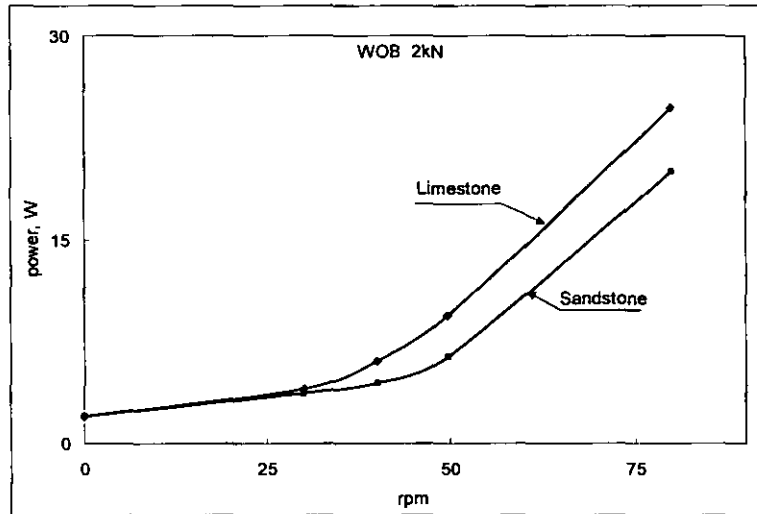


Figure 4.37: Power with increasing speed of rotation.

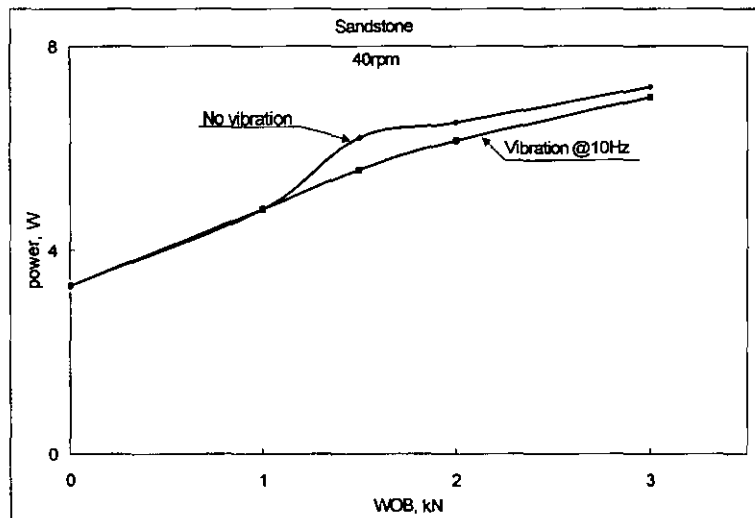


Figure 4.38: Compare vibro-power for Sandstone.

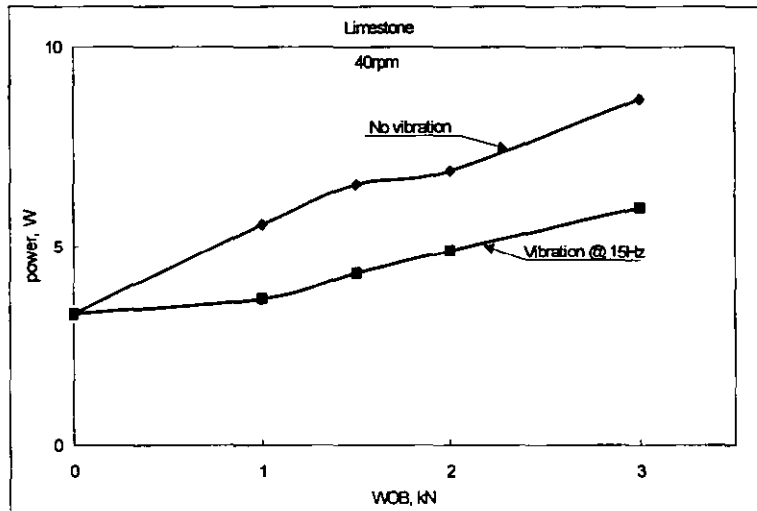


Figure 4.39: Compare vibro-power limestone.

In conventional rotary drilling without vibration, for a given weight on bit, the power consumption of drilling in sandstone and limestone is almost identical at low speeds of rotation, (see Figure 4.37). On the other hand, with an increase in speed, the power needed to drill in limestone becomes greater.

Test drilling with superimposed vibration produced considerable changes in the trend of power requirement. Figure 4.38 compares the results of drilling in sandstone with and without vibration. In this test drilling, the speed of rotation was set at 40rpm, the weight on bit varied from zero to 3kN and vibration at 10Hz was applied with 500N in amplitude. It was observed in the previous results that the power required to drill in sandstone increased linearly with the weight on the bit (Figure 4.36). In this set of data, the irregularity of the hardness of the sandstone samples is observed in the curve of the power of drilling with no vibration. A reduction in power consumption is observed with the introduction of vibration. For oscillation at 10hz, the reduction in power is not considerable.

Figure 4.39 demonstrates the results obtained from test drilling in limestone. The speed of rotation was 40rpm, the load was increased from zero to 3kN and vibration was applied at 15Hz. The irregularity in power on both curves, characterizing the discrepancy in the hardness of the samples, is also observed here. This test reveals a substantial decrease in power requirement. A reduction of about 40 percent is observed.

4. DISCUSSION

The results obtained show that the rate of penetration increases with the increase of rotation speed and the applied weight on the bit. However, with the conventional steel tooth bit, the increase of these two parameters beyond reasonable range causes failure of the bearing and rapid wear of the tool, consequently the bit life is reduced to

minimum. This was experienced in this investigation with broken bits at relatively high speeds (100-150) and 3.5kN applied to the bit.

Application of vibration to the drilling process has produced high rates of penetration. In limestone, the superimposed vibration has shown a considerable improvement. Drilling in sandstone with added vibration has provided acceptable results within the framework of this investigation.

Though the applied vibration was of low frequency (10 and 15Hz) with small amplitude, the obtained results have proved that periodic oscillation of the applied load on the bit and the resulting impact loading produces high penetration rates. Relatively high rates obtained in drilling with vibration in hard limestone give a practical support for the theoretical model of vibro-impact penetration.

The trend of power consumption shows that drilling in limestone requires more energy than in sandstone which is relatively soft. The power requirement obtained from this experiment indicates that conventional drilling with constantly applied weight on bit consumes more energy than vibration drilling.

Though the drill bit used in this experiment was not appropriate for drilling in very hard rock, the results are supportive and the following positive outcomes are deduced.

- Superimposed vibration increases the rate of penetration.
- The penetration rate increases with the frequency.
- Power consumption is reduced with the application of vibration.
- With a proper correlation of speed of rotation and WOB, a steel toothed bit can be used to drill in very hard rock.

Chapter 5
A SELF-EXCITING SYSTEM FOR
PERCUSSIVE-ROTARY DRILLING

A SELF-EXCITING SYSTEM FOR PERCUSSIVE-ROTARY DRILLING

1. INTRODUCTION

Vibration has always been regarded as having a destructive effect on human beings, construction and mechanical systems. However, in many technological processes such as sieving, ramming, transport, machining and drilling, vibration is widely used. Vibration is predominantly used in pile driving, road and construction equipment, tamping, hammer drills, in mills for fine ground materials, in machining of very hard materials, in conveying and transporting, also in moulding machines for reinforced concrete and many other hand-held machines. The impact action is used in a range of damping and vibration isolators. In many cases impact and vibration are viewed as separate events. Recently introduced vibro-impact theory has made it possible to design a new generation of machines and technological processes that use synergistic impact as a fundamental principle of operation.

Improvement is constantly sought when drilling in order to increase the rate of penetration, the time span between maintenance services, the life of the drilling system and to reduce the overall cost of the drilling process. Current drilling methods tend to increase the rate of penetration by balancing the speed of rotation and the weight on the bit. This often leads to failure of the drill string, which undergoes complex loading. The load is exerted in such a way that the upper part of the drill string is in extension and the lower part is in compression. To control the parameters of the drilling process (actual speed of rotation, weight on bit, and torque on bit), complex techniques are used in order to detect and monitor the whirl, stick-slip vibration, and the forces and stresses in the drill string. This increases the cost of operation and reduces efficiency, (Pavone, 1994).

2. DEVELOPMENT OF VIBRO-IMPACT SYSTEMS

2.1 Historical Evolution

Vibro-impact mechanisms have been studied and widely used in various fields of engineering, specifically in drilling and pile driving. After World War II, construction development in the former Soviet Union gave an enormous impetus to industrial promotion of vibro-impact systems. Major research was concerned in finding adequate parameters (maximum impact force) for the development of new machines and the intensification of technological processes with the help of different mechanisms of excitation of vibration and impacts.

The dynamic behaviour of the treated media was not accounted for in the early design of vibro-impact systems, consequently the machines were over-powered and the desired output parameters had to be sought via suitable adjustment in fieldwork. Basic models of machines were developed; some of them included the interaction with the medium during penetration as demonstrated by the work of the following investigators: Tsaplin (1953), Neimark (1953), Blekhman (1954), Brakan (1959), Savinov et al (1960), Tseitlin et al (1987) and Bessalova (1957). This led to a theory of vibro-impact mechanisms; Lukomskii (1959), investigated the operational modes of vibro-impact hammers. Batuev *et al*, (1977) thoroughly investigated impact processes. Babitsky (1978) developed the concept of resonant vibro-impact systems and accommodated vibro-impact systems within the general theory of non-linear systems. In Japan, Kumabe (1979), led research on machining with vibration and ultra-sonic machining, and some books were published on this subject.

The early single degree of freedom model of vibro-impact penetration of a tool into a medium is schematically shown in Figure 5.1. The system consists of the vibrating body 1 of a mass m suspended on springs 5 of a total stiffness k . The vibrating body has a striker 3 attached to its lower part. The two eccentric masses 2 counter-rotate in the direction as shown in Figure 5.1 and excite the oscillation

of the body 1. During the vibration, the striker 3 impacts on anvil 4, which is mounted on base 6. A gap 7 is secured between the striker and the anvil.

Tsaplin (1953) and Barkan (1963) carried out an analytical investigation of system motion. They considered only elastic deformation and assumed that the impact was instantaneous, thus they related velocities before and after impact through the coefficient of restitution. The equation of motion of the system was derived as follows, Tsaplin (1953)

$$\ddot{x} + \omega_n^2 x = F \sin(\omega t + \theta) - I[\delta(t) + (\delta(t-T) + \delta(t-2T) \dots)] \quad (5.1)$$

$$I = (1 + R) m \dot{x}_T \quad (5.2)$$

Where $\omega_n = \sqrt{k/m}$ is the natural frequency of the unit on the springs; F - the force developed by the rotating eccentric weight; t is the time; ω is the angular frequency of the rotation of the weights; $[\delta(t) + \delta(t-T) + \dots]$ is the series of impact forces at a time interval equal to the period T , θ is the phase shift between the force and the displacement x , R is the coefficient of restitution between the striker and the anvil (see Figure 5.1) and \dot{x}_T is the impact velocity of the vibrating unit at time $t=T$. The solution was sought by Laplace transform considering impact as successive impulses. A periodic motion was found when the ratio of the system's natural frequency and the frequency of excitation is an integer i.e. $\gamma = \omega/\omega_n = 1, 2, 3, \dots$

Bespalova (1957) carried a stability analysis and proved that a stable periodical motion exists for integer relationship between ω and ω_n . Later, Lukomskii examined the equation of impact velocity varying the frequency ratio and the coefficient of restitution and the results of his study were of the same order.

Later, it was shown (Babitsky, 1966, 1978) that the most effective vibro-impact regimes always exist outside the frequency relationship specified by Bespalova. Kobrinskii used a forced vibrating ball with gravity bouncing on a stairway to

model a pile driven by vibro-impact, see Figure 5.2. He introduced a damping term in the equation of motion of the system.

$$m\ddot{x} + c\dot{x} = F \cos(\omega t + \theta) + mg \quad (5.3)$$

Where $c\dot{x}$ is the coefficient of damping in the system, m - mass of the ball and F - is the force; ω is the angular frequency of the forced vibration and g is the gravitational acceleration. With this system, Kobrinskii identified several modes of impact regime.

To reflect the depth dependency, Tsaplin introduced a two-degree of freedom system, shown in Figure 5.3 with its dynamic equivalent. With reference to Figure 5.1, in this model all the numbers have the same meaning. As the pile 8 makes its way into the soil 6, the total resisting force increases. This is caused by the increase of the force of friction on the sides on the pile because of a greater surface of the pile's body entering in contact with the soil. The frontal resistance of the soil increases because of partial compaction of the soil ahead of the pile.

The progressive increase in total force is accounted for by gradually increasing the mass of the pile as it moves into the soil. This is shown in Figure 5.3b by the added mass ahead of the pile. The equations of motion are similar to equation (5.1).

$$\begin{aligned} m_1\ddot{x}_1 + k(x_1 - x_2) &= F \sin(\omega t + \theta) - S[\delta(t - T) + \delta(t - 2T) + \dots] \\ m_2\ddot{x}_2 + k(x_2 - x_1) &= S[\delta(t - T) + \delta(t - 2T) + \dots] \end{aligned} \quad (5.4)$$

Where m_1 and m_2 are respectively the mass of the vibrating unit and the pile. x_1 and x_2 are respectively the displacement of the vibrating unit and the pile. The other designations in equation (5.4) have the same meaning as in equation (5.1).

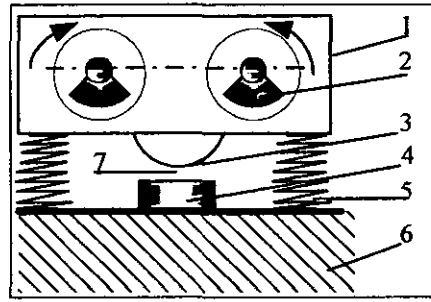


Figure 5.1: SDOF Impact Model after Tsaplin

1- vibrating unit; 2- eccentric mass; 3- striker;
4- anvil; 5- spring; 6- base (soil), 7- gap

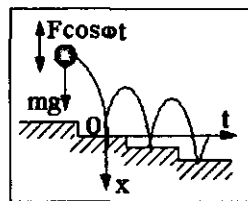


Figure 5.2: Force vibrated ball, Kobrinskii (1969)

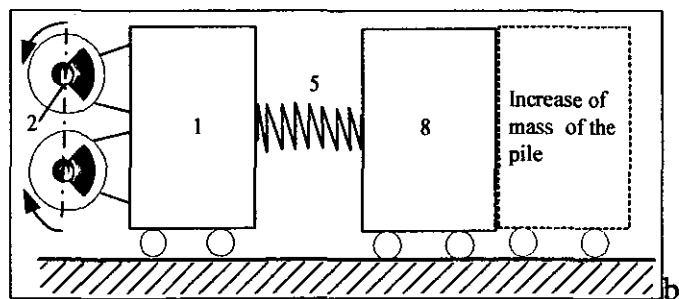
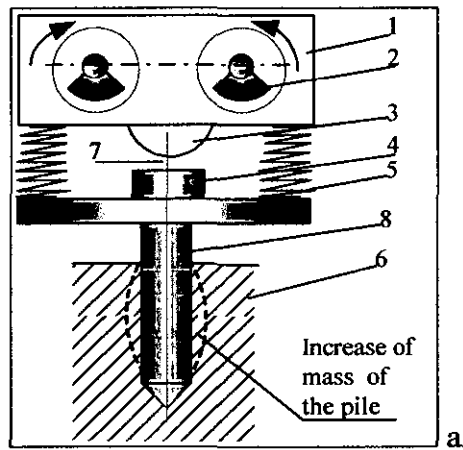


Figure 5.3: a- 2DOF system; b- Dynamic equivalent, (Tsaplin)

The concept of equivalent mass adopted by Tsaplin leads to inertial properties of the soil to be considered, whilst the resistance of the soil and damping in the system are omitted. Despite the lack of soil properties, Tsaplin argued that these models were adequate to provide the designer with all necessary parameters of the machine for design purposes.

2.2 Vibro-Impact Systems.

An impact is defined as a single collision of a moving body against another one which may be in motion or at rest, Harris, (1988). The following types of impact are possible: direct, oblique, central, eccentric, tangential and meeting. The collision develops through two major phases: loading and unloading. The loading stage goes from the instant of contact of bodies to maximum deformation; the unloading phase starts at maximum deformation and ends at the separation of the bodies. However, in constrained oblique impact with friction, Babitsky, (1978) noticed that the loading phase could be apportioned into two stages due to the change in sign of tangential velocity within this phase. Wang et al, (1992), have reported two phases (compression and restitution) with five modes in oblique impact: sliding, sticking in compression phase (C-sticking), sticking in restitution phase (R-sticking), reverse sliding in compression phase (C-reverse sliding), and reverse sliding in restitution phase (R-reverse sliding).

A vibro-impact system is defined as a mechanical system with systematic impact interactions of its elements, Babitsky (1978). Any two members of the system that are involved in a single impact are treated as an *impact pair*. There exist impact pairs with *single-sided* impact (see Figure 5.4a) and *double-sided* impact (see Figure 5.4b) depending on the number of surfaces involved in one-dimensional impact on each member. There are also certain vibration machines in which impact does not occur. Independently of their purpose, vibration and vibro-impact machines have an actuator or exciter and a vibration system. The actuator is supplied with energy to generate a periodically oscillating force which is applied

to the vibration system. The ratio of the energy supplied to the process to the energy dissipated by the actuator and the vibrating system defines the efficiency of the machine. Among vibration machines, resonant machines have a higher efficiency as they operate near the natural frequency of the system. Resonance is the selective response of the vibration system to periodic excitation at a frequency near the natural frequency, Astashev et al, (2000). This particular property of resonant machines affects the practical application of these machines because of the complexity of keeping resonance in conditions of unpredictable loads to observe the requirement of the operating system.

Many theoretical and experimental studies of vibro-impact systems are devoted to understanding impact vibration absorbers. Figure 5.4 illustrates various arrangements of vibro-impact dampers. These consist of a small mass attached to the main body with a clearance that allows for the collision between both elements. In Figure 5.4a, the impact vibration absorber, the “free absorber” has a loose mass set at clearance Δ to produce a double-sided impact. Figure 5.4b shows a single-sided vibro-impact absorber with an elastic element. A linear double-sided impact absorber with two restoring elastic elements is shown in Figure 5.4. A similar absorber with visco-elastic bumpers is illustrated in Figure 5.5.

Another typical field of application of vibro-impact systems is percussion machines. Figure 5.6 illustrates a hand-held electro-pneumatic hammer drill which operates as follows. The motor 1 drives the piston 4 through the crank mechanism 3 and the gear train 2. The piston, moving forward compresses air in the chamber 5; the hammer 6 is projected forth and impacts the intermediate anvil 7. The anvil conveys the impact impulse to the medium through the working tool 8. In the backward motion of the piston 4, the air in the chamber 5 tends to expand and sucks up the hammer 6. Thus, air comes alternately into compression and expansion and drives the hammer to impact periodically the anvil.

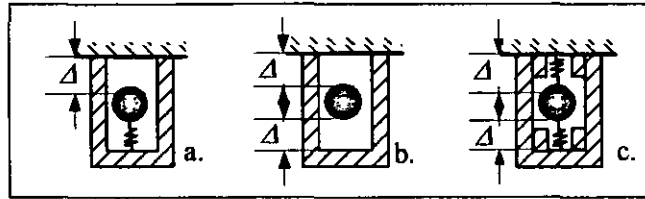


Figure 5.4: Various arrangements of vibro-impact dampers, Babitsky (1978)

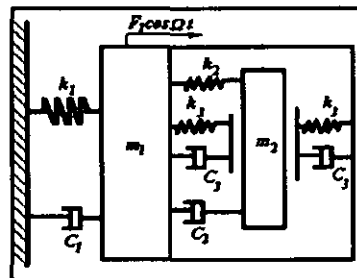


Figure 5.5: Force vibrated system with a double-sided impact, Massri (1972)

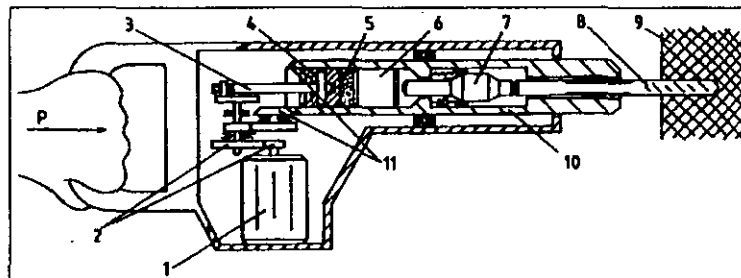


Figure 5.6: Hand-held hammer drill, Astashev et al (2000)

The barrel 10 supports the anvil with resilient elements. The bevel 11 rotates the barrel together with the percussion mechanism and the tool. The rotation of the tool takes out any chips produced by the percussive action. The operator applies the force P required to keep the tool in contact with the medium.

2.3 Dynamic Model of Vibro-Impact System

Dynamic behaviour of vibro-impact systems is often studied by investigating the motion and the amplitude-frequency response of an oscillator colliding with a rigid stop. The model of such an impact oscillator (see Figure 5.7a) is made of a mass M on a spring of stiffness k and the stop is placed with clearance at a distance Δ .

If there is no stop on the path of the mass M , the motion of the system under harmonic excitation is defined by a sine wave. Assuming that both the mass and the stop are made of perfectly elastic materials, their coefficient of restitution is theoretically equal to unity. Therefore, after impact the mass will bounce with a velocity equal by value to the velocity before impact.

In a vibro-impact system, the impact pair can be set with negative, positive or zero clearance. If in the system, the impact pair is set with interference (preload), the clearance Δ is considered as negative. The motion of a system with impact interaction is illustrated in Figure 5.7b where, for any different initial condition, the period T_I is greater than T_0 . However, the period of the free vibro-impact regime cannot exceed the period of the linear system without stop. Figure 5.8 displays the phase portrait of a vibro-impact system with different settings of the clearance Δ .

Vibro-impact systems are generally force vibrated and depending on the dynamics of the system; the impacting mass can produce a single impact per period (Figure 5.9a) or multiple impacts per period. However in multiple impacts, the amplitude

decays as the impacts are repeated. This case is depicted in Figure 5.9 for the motion of the hammer 6 of the hand-held drill illustrated in Figure 5.6.

Several studies have been devoted to the process occurring in-between two bodies during their impact in order to determine the coefficient of restitution, the impact force and the duration of impact. Considering a straight central impact of bodies with masses m_1 , m_2 and velocities \dot{x}_1 , \dot{x}_2 ; ($\dot{x}_1 > \dot{x}_2$), and using the law of conservation of momentum, the coefficient of restitution is expressed as follows

$$R = \frac{\dot{x}_{2+} - \dot{x}_{1+}}{\dot{x}_{1-} - \dot{x}_{2-}} \quad (5.5)$$

Where, \dot{x}_{1-} , \dot{x}_{2-} are the velocities of bodies before a collision; \dot{x}_{2+} , \dot{x}_{1+} are the velocities of bodies after a collision.

In a recent publication, Babitsky *et al*, (1998), investigating the evolution of collision, used a lumped body of mass m that collides with a visco-elastic (Kelvin-Voigt element) bumper mounted on a wall. The bumper is made of a spring and dashpot (with viscous damping c) mounted in parallel. An accelerometer attached to the mass records the acceleration during the collision in time based. The equation of system motion is solved for time τ , which is the duration of impact and is obtained as

$$\tau = -\frac{1}{\Omega_n \sqrt{1-2\xi^2}} \arctan \left(\frac{2\xi \sqrt{1-\xi^2}}{1-2\xi^2} \right) \quad (5.6)$$

Where, ξ is the damping loss factor; $\xi = \frac{c}{2m\Omega_n}$ and Ω_n is the natural frequency of

the system. It is observed that the impact duration depends only on system natural frequency and damping loss factor. During the evolution of the impact, the peak acceleration (i.e. max impact force) occurs at time τ_1 , which is expressed as follows:

$$\tau_1 = -\frac{1}{\Omega_n \sqrt{1-2\xi^2}} \arctan \left(-\frac{(4\xi-1)\sqrt{1-\xi^2}}{\xi(3-4\xi^2)} \right) \quad (5.7)$$

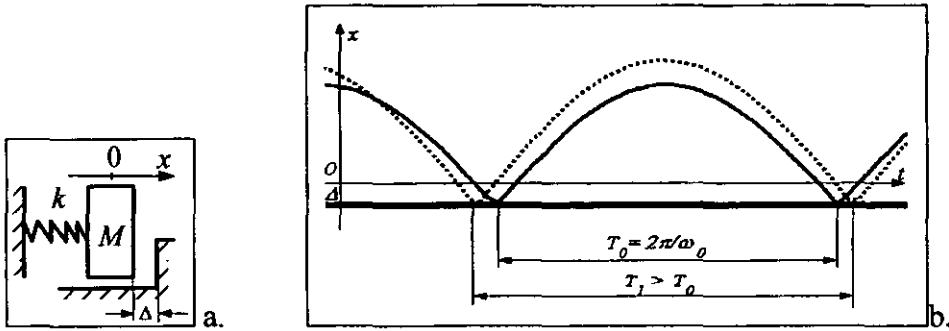


Figure 5.7: Linear single-sided impact oscillator
a- schematics of the oscillator; b- motion with time;

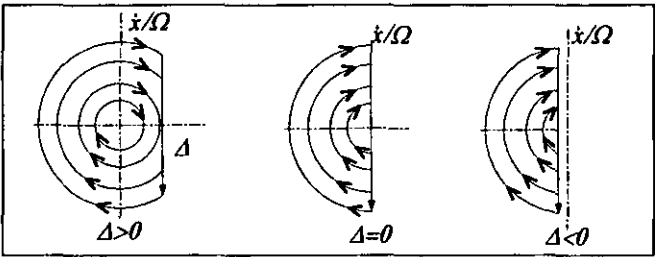


Figure 5.8: Phase portrait of system motion with impact, Babitsky (1978)

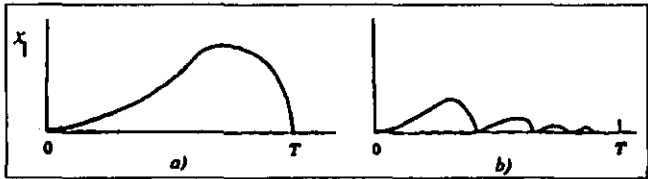


Figure 5.9: Vibro-impact regimes, Astashev et al (2000)
a- single impact; b- multiple impact per period.

Knowing the velocity at impact, the peak acceleration, the duration of impact and the velocity at the end of impact, it is possible to work out the dynamic properties of the system. The coefficient of restitution is also derived as a function of loss factor, hence, it is expressed as

$$R = \frac{\dot{x}(\tau)}{v} = \exp \left[-\frac{\xi}{\sqrt{1-2\xi^2}} \arctan \left(-\frac{2\xi\sqrt{1-\xi^2}}{1-2\xi^2} \right) \right] \sin \left[\arctan \left(-\frac{2\xi\sqrt{1-\xi^2}}{1-2\xi^2} \right) \right] \quad (5.8)$$

where $\dot{x}(\tau)$ is the velocity at the time of separation, v is the pre-impact velocity.

3. THE SELF-EXCITING SYSTEM OF PERCUSSIVE-ROTARY DRILLING

In drilling, there exists a wide variety of equipment and technique including percussive drilling, vibro-impact drilling and rotary percussive drilling. However, most of these techniques require at least two actuators and synchronizing mechanisms to perform vibro-impact or rotary-percussive drilling. A new model of percussive-rotary drilling is presented here and analysed. This model has a single actuator and utilises the stick-slip in the process of drilling to excite a percussive action through a coupling mechanism.

In general, a rotary drilling system consists of a drive, a gear train, a bevel, a rotary table, a drilling string, a collar and a bit. Figure 5.10 shows a sketch of a typical drilling system. The motor drives the rotary table through the gearbox and the bevel. The table rotates a long slim drill string made of jointed drill pipes with the collar at the lower end. The bit is mounted on the system through a drill hub.

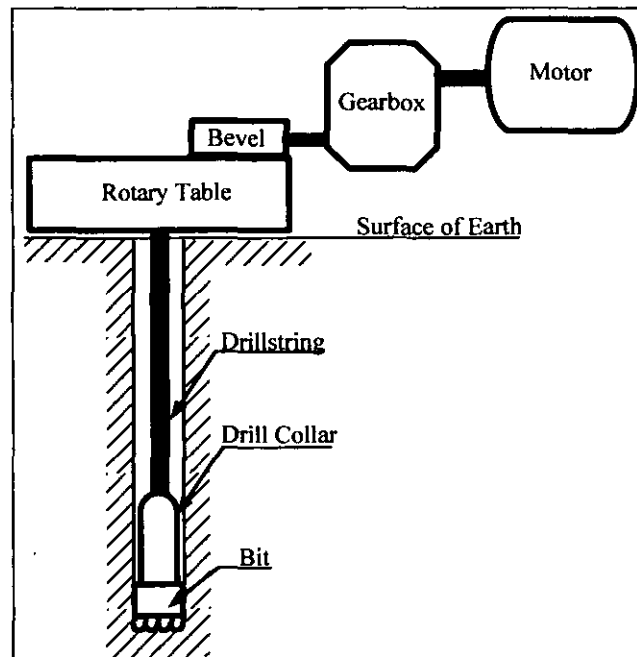


Figure 5.10: Typical structure of rotary drilling system.

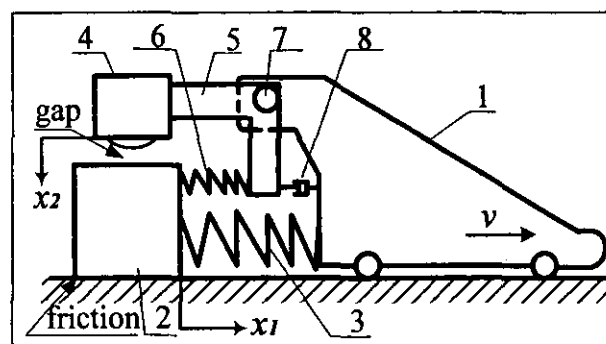


Figure 5.11: Planar model of the vibro-impact drilling system.

3.1 Mechanical Model of The System

Figure 5.11 shows a planar sketch of the model of the drilling system. The drive 1 moves with constant linear speed v . A bit 2 with mass m_1 is driven over a rough surface through spring 3 with stiffness k_1 . Lever 5 carries striker 4 at its upper end and rotates freely about the pin 7 mounted on the drive 1. The other end of the lever is linked from one side to the bit 2 through a secondary spring 6 with stiffness k_2 . From the other side, the lever is coupled to the drive by a dashpot with a viscous coefficient c_2 . There is dry friction between the bit and the surface. The drive 1 represents the entire drilling system shown in Figure 5.10 with a total mass greatly exceeding the mass of the drill bit. Therefore, it is considered that the drive 1 moves with a velocity v , which is not affected by the activity of the bit. The velocity v is the linear speed of bit rotation. The intention is to decouple the vibration of the bit from the drill string. This is performed with the help of a special mechanism which is represented by the springs 3 and 6, the dashpot and the lever 5. There are different ways of implementing this decoupling mechanism. Hydraulic actuators, cams, system of levers, specially designed springs or mechanically reciprocating devices could be used for this purpose.

The entire system operates as follows: when riding over the surface, due to dry friction, the bit moves stepwise sticking and sliding intermittently; thus spring 3 comes into compression and extension alternatively. Such motion evokes the deformation of spring 6, and consequently, the striker 4 oscillates around its equilibrium position. Both bodies will vibrate at different frequencies, exhibiting generally complex non-periodical motion. The aim of this structure is to use friction-induced vibration to generate an intensive periodic vibro-impact process with a proper synchronisation of the motion of the bit and the striker and to control the stick-slip.

At the beginning, the bit 2 will be at rest until the total pulling force in the springs becomes greater than the static friction force acting between the bit and the surface. This period of motionless state is known as the “*stick phase*”. Within this

phase, the drive moves constantly and spring 3 is extended. With the increasing distance between parts 1 and 2, the lever 5 rotates clockwise around the pin because its lower end is attached to the bit through spring 6 with stiffness k_2 . Consequently, during the sticking phase the striker moves upwards. The shoulders of lever 5 are of equal length with an angle of 90° between them, and this converts forces applied to the lower end in a horizontal direction into vertical forces, which are transferred to the striker. As soon as total pulling force exceeds the static friction force, bit 2 moves promptly following the drive. This period of motion is called the "*slip phase*". By its sudden motion, the bit pushes the lever anti-clockwise through spring 6. As a result, the striker is forced to hit the bit, which is in motion. During the slip phase, the force in spring 3 is released but the residual deformation of this element depends on how far the bit has moved towards the drive. The reduction of the forces in the springs by relaxation and the additional braking effect due to impact allows the static friction force to become greater than total pulling force. Consequently, the motion slows until the bit stops and sticking takes place again. The cycle repeats itself and such motion is known as "*stick-slip motion*".

The system is launched with a zero initial condition; thus, the amplitude of oscillation of the striker increases gradually until the striker begins to impact on the bit when the latter is moving. At impact, the friction force increases sharply and the total pulling force is reduced by relaxation of spring 3. These last two events confine the bit to decelerate and to come to rest. The parameters of the system strongly affect each other, therefore a proper correlation of masses and stiffness in the system is intrinsic for the process to converge to a stable solution. If the required relationship is satisfied, the motion of both subsystems synchronise and the entire system comes into steady state motion and locks into a limit cycle.

3.2 Characteristic of Friction Force

There exist several approaches for the mathematical representation of interface dry friction force in a given process. Some of these mathematical interpretations of dry friction were explained in chapter 3. The friction characteristics must be chosen carefully in order to reflect accurately the interface force between the rubbing surfaces. The characteristics of the interfacial frictional force $F_r(v)$ adopted in this investigation are given by the following relationship:

$$F_r(v) = \mu m_1 g \left(1 - \frac{|v|}{v_{cr}} + \frac{|v|^3}{3v_{cr}^3} \right) \text{sgn}(v) \quad (5.9)$$

Where, v is the sliding velocity, μ is the coefficient of dry friction, g is gravity acceleration. This expression is shown graphically in Figure 5.12 where, v_{cr} is the critical sliding velocity on the falling characteristics beyond which friction force begins to increase (Stribeck velocity, Stribeck, 1902), $F_{cr} = F_r(v_{cr})$ is the corresponding friction force. To obtain self-sustained vibration, the sliding velocity must be at some stage on the negative slope or $|v| < v_{cr}$.

3.3 Equation of Motion

The equations of motion of the entire system in Figure 5.11 are derived relative to drive 1. The bit co-ordinate relative to the drive is x_1 ; x_2 is the striker co-ordinate. Absolute displacement of the bit is defined by $x = x_1 + vt$. The equations of motion are:

$$\begin{aligned} m_1 \ddot{x}_1 &= -k_1 x_1 - k_2 (x_1 - x_2) - F_r(\dot{x}) + \Phi(x_2, \dot{x}_2) \\ m_2 \ddot{x}_2 &= -c_2 \dot{x}_2 - k_2 (x_2 - x_1) - \Im(x_2, \dot{x}_2) \end{aligned} \quad (5.10)$$

Here, $F_r(\dot{x})$ is the force of friction; $\Phi(x_2, \dot{x}_2)$ is the added friction impulse at the instant of impact of striker on the bit and $\Im(x_2, \dot{x}_2)$ is the impact force of striker 4 colliding with the bit. The friction force is then expressed in the following form:

$$F_r(\dot{x}) = \begin{cases} f_{st}(1 - \frac{|\dot{x}|}{v_{cr}} + \frac{|\dot{x}^3|}{3v_{cr}^3})\text{sgn}(\dot{x}) & \text{for } \dot{x} \neq 0 \\ \min[|k_1x_1 + k_2(x_1 - x_2)|, f_{st}]\text{sgn}(k_1x_1 + k_2(x_1 - x_2)) & \text{for } \dot{x} = 0 \end{cases} \quad (5.11)$$

Where $f_{st} = \mu m_1 g$ is the force of static friction. In this investigation, the coefficient of static friction μ is taken as equal to 0.4. The added friction force due to impact is

$$\Phi(x_2, \dot{x}_2) = \mu \Im(x_2, \dot{x}_2) \quad (5.12)$$

4. ANALYSIS OF SYSTEM FREQUENCY RESPONSE WITHOUT IMPACT

In order to understand the dynamic behaviour of the system, this analysis has been split into two parts: analysis of the system with and without impact. In the absence of impact, the system obtained is a two degrees-of-freedom system incorporating dry friction. The resulting equivalent subsystem is shown in Figure 5.13 where all referencing numbers have the same meaning as in Figure 5.11.

In Figure 5.13, there is no impact interaction between the striker 4 and the bit 2, therefore the impact force $\Im(x_2, \dot{x}_2) = 0$, and the added friction force due to impact $\Phi(x_2, \dot{x}_2) = 0$. The equations of motion of the system are reduced to the following:

$$\begin{aligned} m_1 \ddot{x}_1 &= -k_1 x_1 - k_2 (x_1 - x_2) - F_r(\dot{x}) \\ m_2 \ddot{x}_2 &= -c_2 \dot{x}_2 - k_2 (x_2 - x_1) \end{aligned} \quad (5.13)$$

Because dry friction has little effect on the system frequency response, the expression of friction force in equation (5.13) can be omitted to simplify the calculations.

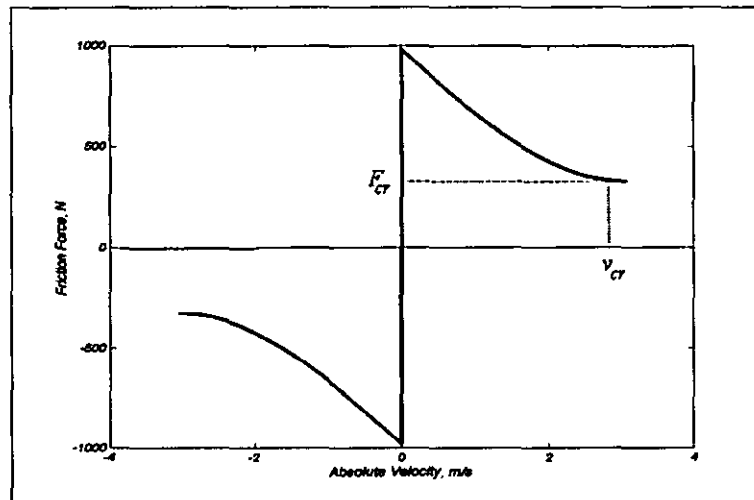


Figure 5.12: Friction Force Characteristic.

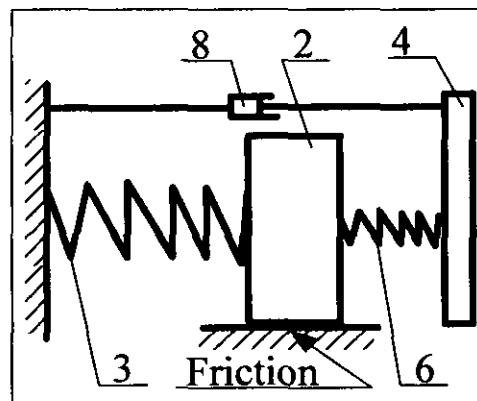


Figure 5.13: Equivalent model of the system without impact.

Assuming that the motion of the system is periodic and is composed of harmonics of different amplitudes and frequencies, the solution of equation (5.13) is represented in the following form.

$$x_1 = A \sin(\omega t + \varphi); \quad x_2 = B \sin(\omega t + \varphi) \quad (5.14)$$

Where, A , B and φ are arbitrary constants and ω is one of the natural frequencies of the system. Substituting equation (5.14) into (5.13) and rearranging, the natural frequencies of the system are obtained by equating the determinant to zero.

$$\begin{vmatrix} k_1 + k_2 - m_1 \omega^2 & -k_2 \\ -k_2 & k_2 - m_2 \omega^2 \end{vmatrix} = 0 \quad (5.15)$$

The frequency equation is obtained by expanding the determinant in equation (5.15). Solving equation for ω gives

$$\omega^2 = \frac{k_1 + k_2}{2m_1} + \frac{k_2}{2m_2} \pm \sqrt{\frac{1}{4} \left(\frac{k_1 + k_2}{m_1} + \frac{k_2}{m_2} \right)^2 - \frac{k_1 k_2}{m_1 m_2}} \quad (5.16)$$

Equally, the eigenvalue problem for vibration analysis can be used to obtain the natural frequencies of the system. Both approaches were use in a MatLab code to calculate the natural frequencies of the system and the obtained results were identical.

4.1 Numerical Simulation of System Motion without Impact

MatLab-Simulink package software was used for numerical simulation of equations of motion of the system. This package offers a range of facilities for dynamic simulation of mathematical models. In Simulink, the differential equations are represented in a set of diagrams similar to solving differential equation on an analogue computer. Solutions of the system are visually displayed dynamically in the form of a plot on an oscilloscope; the data may be stored on a hard disc in matrix form for further manipulation using MatLab or other software.

To solve the equations of motion of the system, a Simulink model was developed. The model has seven main sections which are marked from I to VII as shown in appendix 5-1. The first section computes solutions of the subsystem bit-spring 3;

the second section computes the solution of the subsystem striker-spring 6 (see Figure 5.11). These two sections are coupled through spring 6 which drives the striker. The third section is more complex because of decision making on the state of the friction force. In this section, the force of friction is calculated and a series of logical and relational operators are set to determine the actual state of bit 2. At each integration step, the current value of bit velocity is compared with zero. If the velocity is not equal to zero then the friction force is calculated as a function of absolute velocity given by the first part of equation (5.11). As soon as the velocity becomes zero, the current value of the spring force is estimated. This value is then compared to the static friction force to decide which of these two (in absolute values) should be taken as actual friction force. The friction force is set to be the smaller of these two values. Subsequently, the sign of spring deformation is determined and the direction of friction force is set opposite to spring deflection. The output of this section is either dynamic friction force (if the velocity differs from zero) or the minimum force between static force and the force of deflection in springs (if the velocity is zero). Upon making this decision, integration continues.

The fourth section searches for impact occurrence and computes the force of impact using equation (5.18). Section five is triggered by the signal of the impact from section four and calculates the instant increase of the friction force due to the impact. The sections marked VIa VIb are identical and process the signal in a frequency domain. The output of these two sections is the period and the average power spectrum of the system response. Additional sections were designed to record integration time and system variables and to display continuously the solutions of the system on the screen. The diagram of the Simulink model is shown in appendix 5-1

For greater accuracy, a Runge-Kutta fourth and fifth order solver is used in this simulation. In Simulink, this method has a variable step of integration that allows special events to be tracked. It automatically reduces the step size when needed

and this feature has been used to accurately capture the zero crossing of the bit velocity, and the interaction of the striker with the bit.

4.2 Identification of the System Synchronisation Frequency

The equation of motion of the system (5.13) was solved numerically using the Simulink model illustrated in appendix 5-1. The motion and the frequency response of the system were initially studied with an arbitrary variation of mass, stiffness and damping over a wide range. This allowed for a full investigation of the relationships between the parameters of the system, especially the preferable amount of damping. The mass varied from 5kg to 800kg, the stiffness from 25N/m to 5MN/M and the damping from zero to 500N.s/m. Three types of motion were observed, namely: aperiodic motion, periodic unstable with two frequencies and stable periodic motion with a single frequency component.

Figures 5.14 5.15, 5.16 and 5.17 give an example of phase portrait and frequency response of the bit and the striker respectively for an unstable periodic motion with two natural frequencies with the following configuration. $k_1 = 306250$ N/m $k_2 = 914260$ N/m; $m_1 = 150$ kg, $m_2 = 400$ kg; $c_2 = 250$ N.s/m.

To obtain synchronised motions of the bit and the striker, proportionality factors were introduced in terms of mass ratio $\beta = m_2/m_1$ and frequency $\gamma = \omega_2/\omega_1$. An empirical study was undertaken by varying β and γ and a careful selection of damping. This investigation allowed for proper correlation of the system parameters and an identification of a narrow band of values β and γ where the system exhibits stable periodic motion with synchronisation. Empirically, it was established that for an acceptable periodic motion, the mass ratio must less than 0.5. This factor is studied in the vibro-impact section where it has an important effect on the system motion.

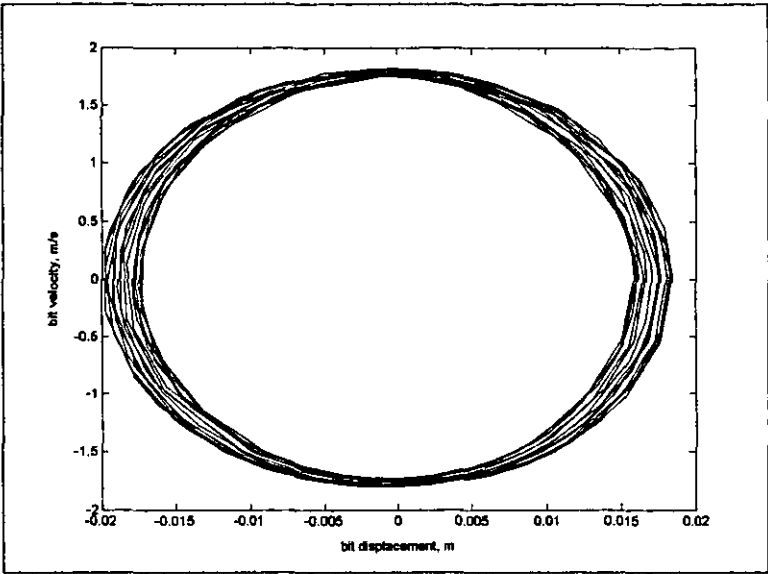


Figure 5.14: Phase portrait of the bit motion

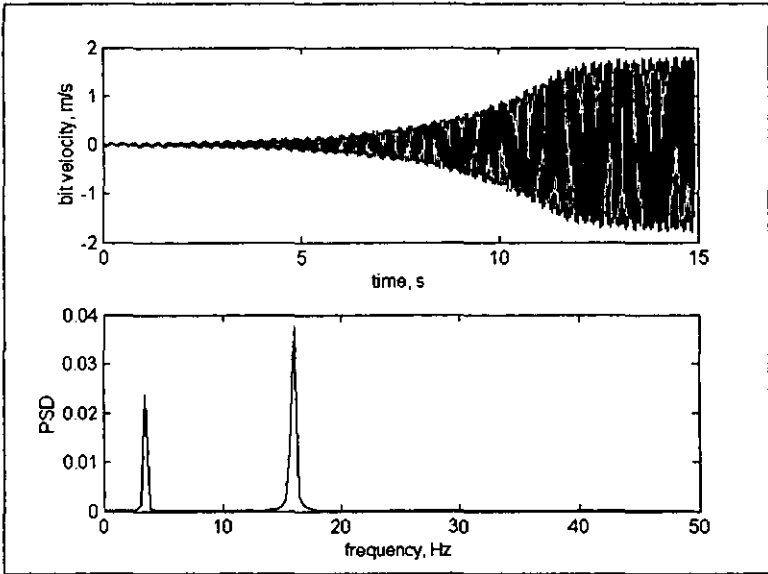


Figure 5.15: Bit frequency response

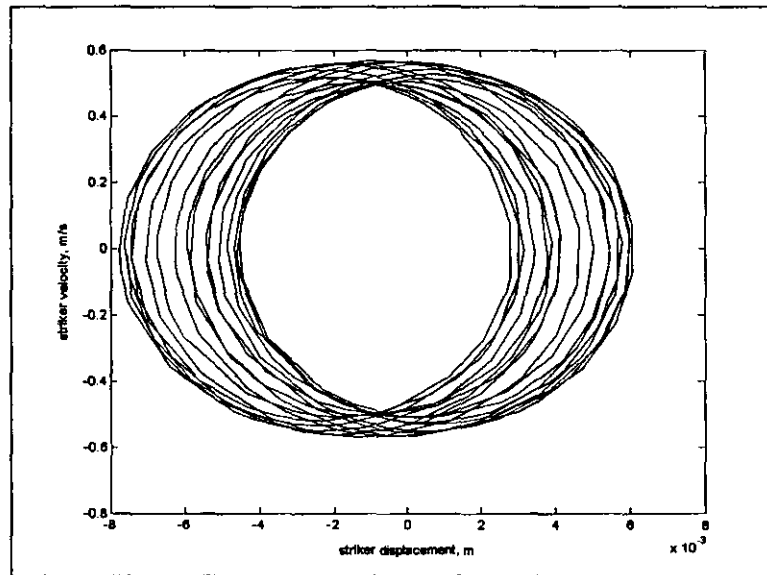


Figure 5.16: Phase portrait of the striker motion

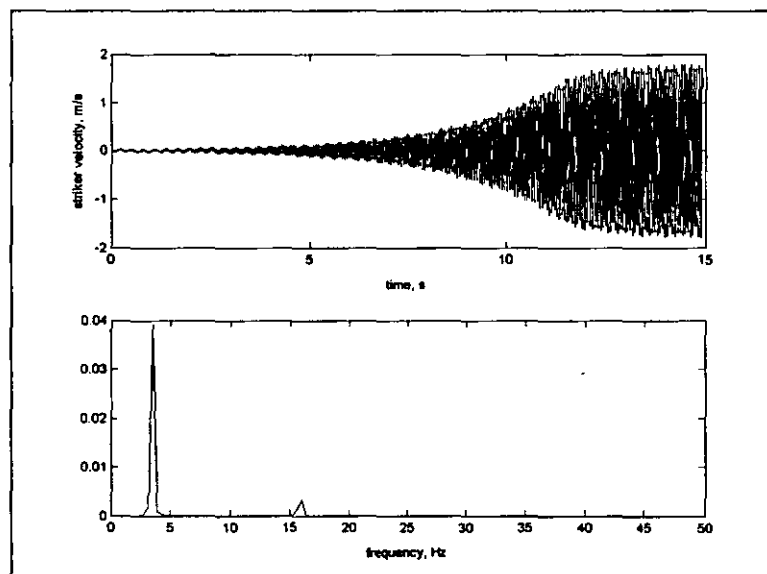


Figure 5.17: Striker frequency response.

A set of friction characteristics was obtained for different values of the driving velocity v . Figure 5.18 shows the force of friction in the system for different driving velocities and Table 5.1 gives the numerical values of these parameters.

Table 5.1

Parameter	Numerical values
Driving velocity, m/s	$v = 0.5, 1.0, 1.5, 2.0, 2.5$
Mass, kg	$m_1 = 250; m_2 = 100$
Stiffness, N/m	$k_1 = 156250; k_2 = 35156$
Viscous damping, N.s/m	$c_2 = 250$

Considering the subsystems bit-spring 3 and striker-spring 6 with natural frequencies $\omega_1 = \sqrt{k_1/m_1}$ and $\omega_2 = \sqrt{k_2/m_2}$ respectively and substituting the numerical values from Table 5.1, we obtain $\omega_1 = 25 \text{ rad/s}$ and $\omega_2 = 18.75 \text{ rad/s}$. The response frequencies of the system is obtain from equation (5.16): $\omega_{n1} = 29.34 \text{ rad/s}$ and $\omega_{n2} = 15.97 \text{ rad/s}$.

Figures 5.19 - 5.21 show the velocity of the bit for different values of the driving velocity. These graphs illustrate the process of self-excitation and stabilisation. It is seen that the amplitude of oscillation increases gradually and reaches a steady state value for a stable motion and there is no further growth of the amplitude. The time required from launch to the steady state motion (settling time) depends on the value of the driving velocity. Observation of the graph shows that as the driving velocity increases, the settling time becomes larger. Figure 5.22 shows the settling time as a function of the driving velocity.

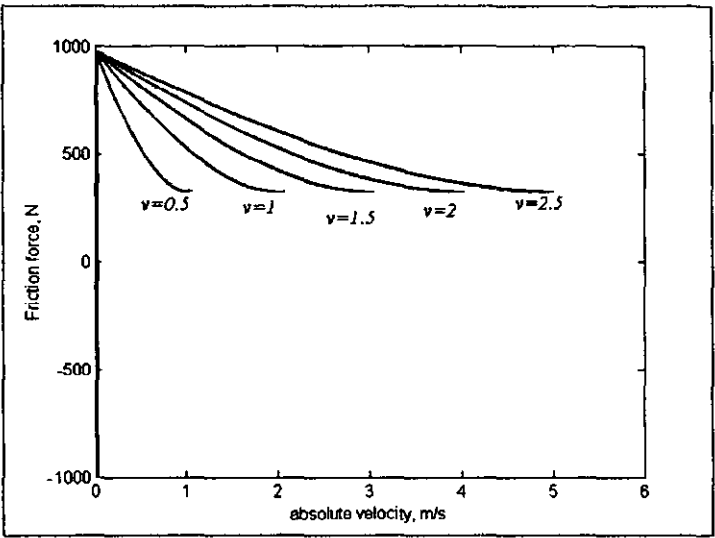


Figure 5.18: Friction force characteristics for various driving velocity

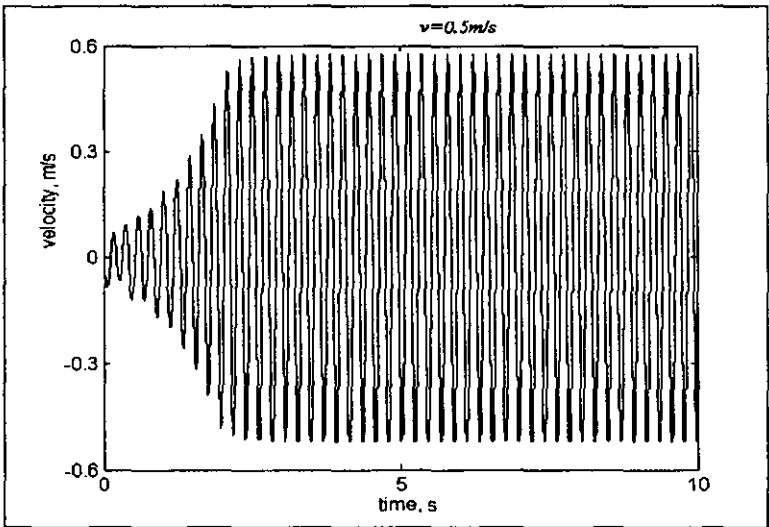


Figure 5.19: Bit velocity, ($v=0.5$ m/s)

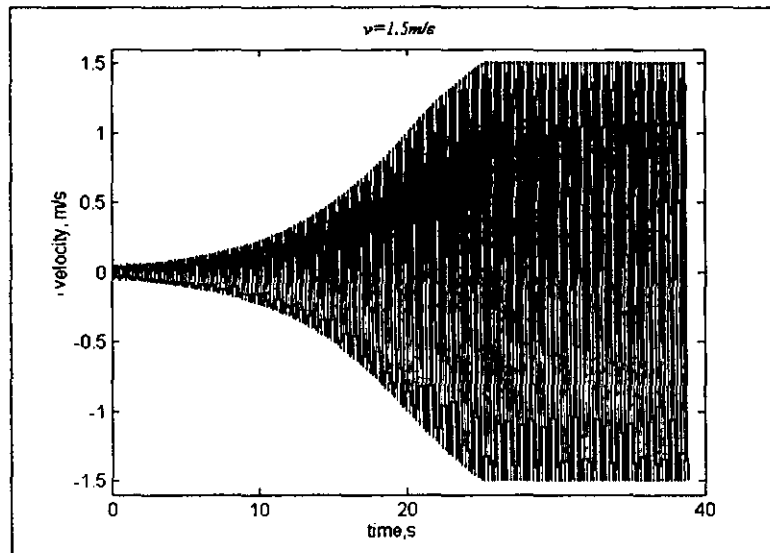


Figure 5.20: Bit velocity, ($v=1.5\text{m/s}$)

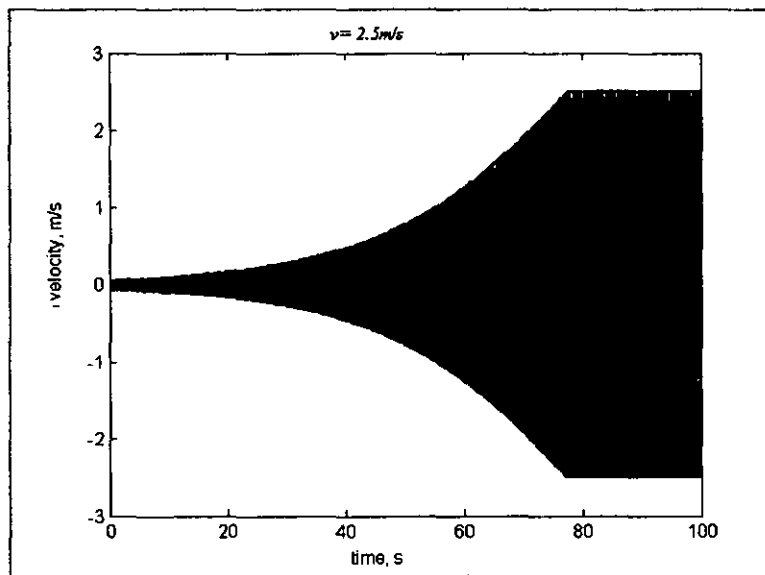


Figure 5.21: Bit velocity, ($v=2.5\text{m/s}$)

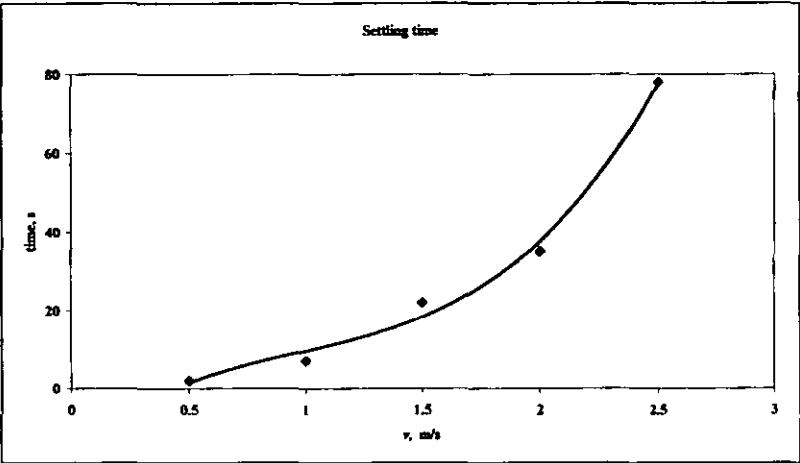


Figure 5.22: Settling time as a function of velocity

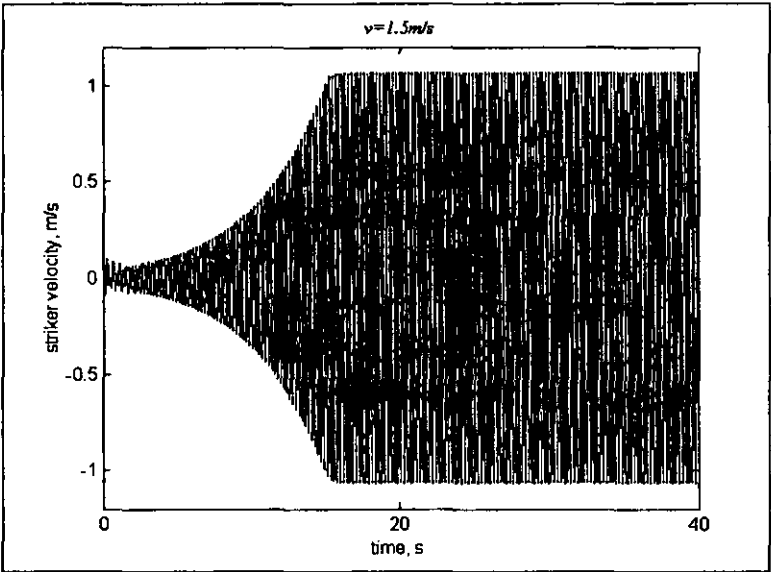


Figure 5.23: Velocity of the striker ($v=1.5\text{m/s}$).

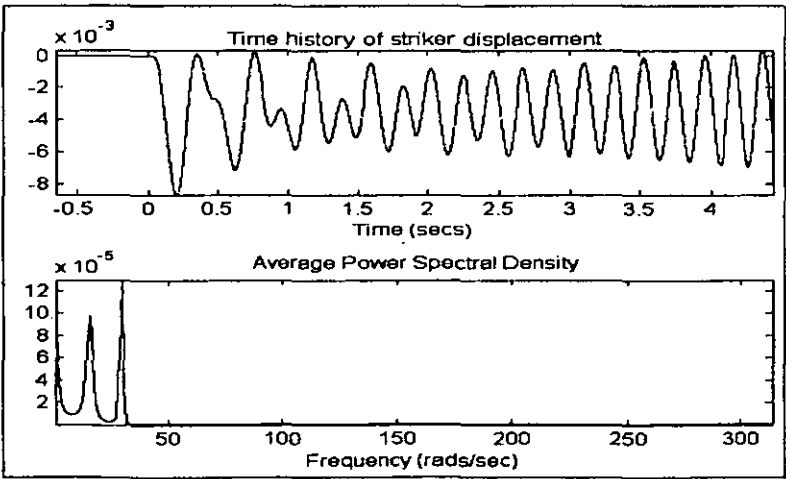


Figure 5.24: Screen-shot of spectrum analyser (striker's initial displacement)

Low driving velocities require a few seconds for the system to reach its steady state motion. This is an important feature because for a bit of a given mass (250kg, approx. 445mm in diameter) in a hard abrasive formation, the bit will be rotating at 30 to 60rpm (Driscoll, 1986), providing a linear velocity of 0.69 to 1.4m/s. A higher speed of rotation is used when drilling in soft rock formation. The application of vibration in soft rock drilling is less efficient therefore; soft formation is not a field of application for this investigation.

Figure 5.23 illustrates the velocity of the striker, displaying a similar pattern of self-excitation and stabilisation process which was observed with the bit. Figure 5.24 is a screen-shot of the frequency spectrum analyser incorporated in the Simulink model that shows the initiation of the striker's motion. The time history of striker displacement is shown at the top where it is seen how the striker begins its motion from rest.

The bottom graph shows that for the first 3~4 seconds there are two frequency components in the striker's motion. Gradually the lower component vanishes and both the bit and the striker synchronise their motion to a single frequency $\omega_{n1}=29.34rad/s$. It was observed that the lower frequency component seen for the striker hardly appears in the bit signal.

Figures 5.25 and 5.26 illustrate the velocities of the bit and the striker with the frequency response, which shows that the entire system vibrates at its highest natural frequency. $\omega_{n1}=29.34rad/s$ (4.6Hz on the graphs).

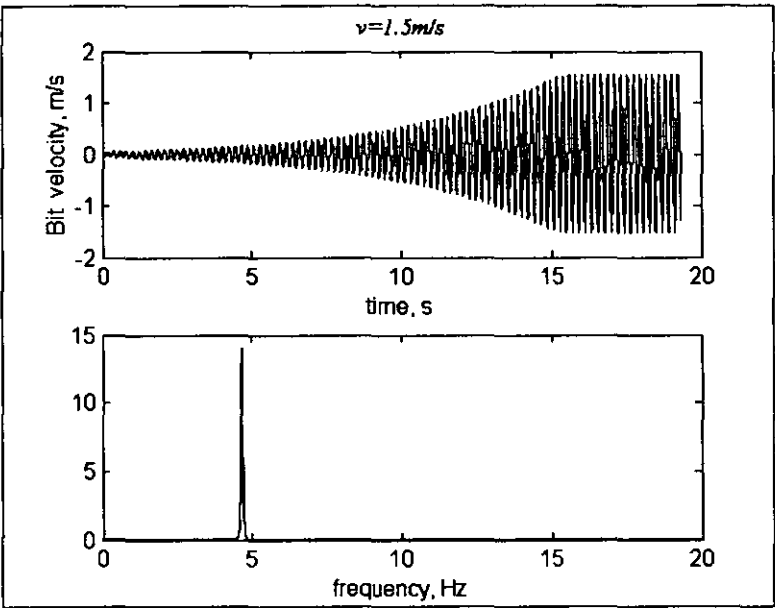


Figure 5.25: Frequency spectrum of bit velocity.

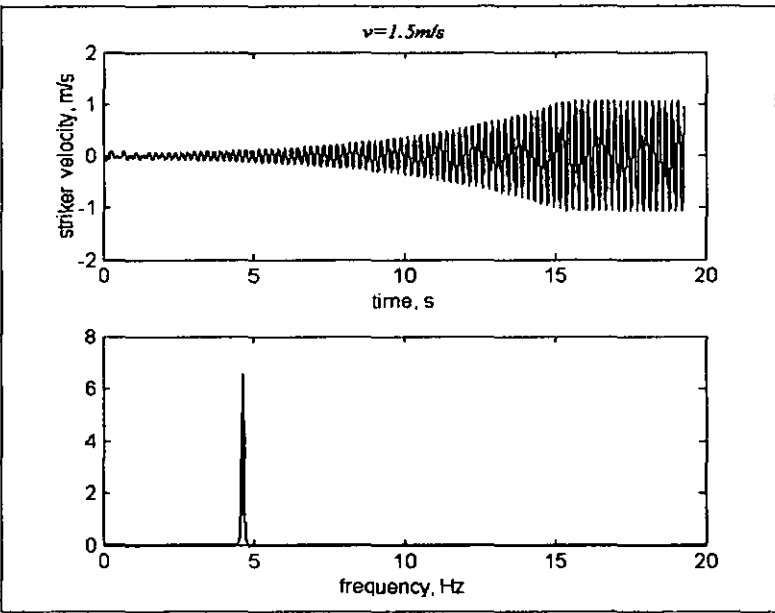


Figure 5.26: Frequency spectrum of striker velocity.

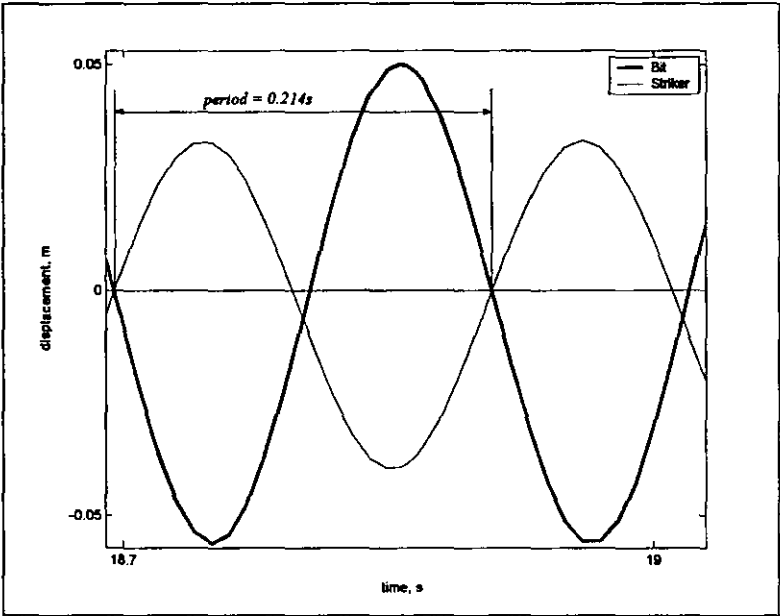


Figure 5.27: Period of motion of the bit and striker

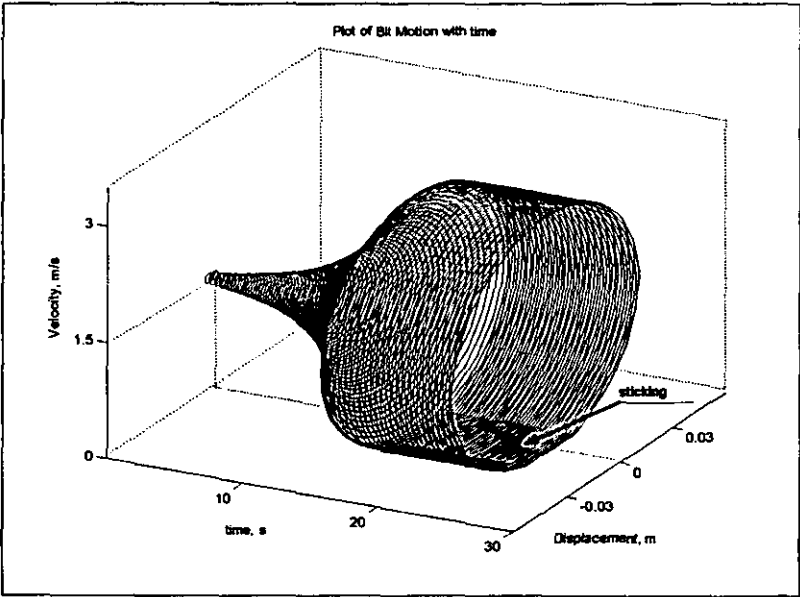


Figure 5.28: Bit absolute motion with time (zero initial condition)

As the motions of the striker and the bit are synchronised, both bodies exhibit identical periodic properties. Figure 5.27 shows the period (0.214s) of the synchronised motion of the bit and the striker.

Figure 5.28 shows the development of the process of self-excitation and its stabilisation. Figure 5.29 displays the phase portrait of bit motion with an arrow showing the direction of the evolution towards the limit cycle. It is seen that velocity goes from zero (zero initial condition - centre) and increases until it reaches the value of driving velocity. Once both velocities are equal, any further increase of bit velocity is impossible because friction force reaches its static value and holds the bit, causing it to enter a sticking phase. In both Figure 5.28 and 5.29 it is seen that the system is attracted towards the outer circle where the system locks into a stable limit cycle.

Equally, if launched with initial conditions, the system tends to the same limit cycle. Figure 5.30 shows the motion of the bit launched with an initial displacement $x_1 = 0.010m$ and an initial velocity $\dot{x}_1 = 3.5m/s$. It is seen that the motion of the system rapidly converges to the limit cycle. With reference to Figure 5.28 and Figure 5.30 the solutions of the system for a given configuration always converge to a single limit cycle.

The motion of the system is schematically represented by the picture in Figure 5.31 and can be treated as a stable limit cycle. This is because either with initial conditions (from outside the limit cycle) or without initial condition (from the centre) the motion of the system converges to the limit cycle as shown in the picture with the arrows.

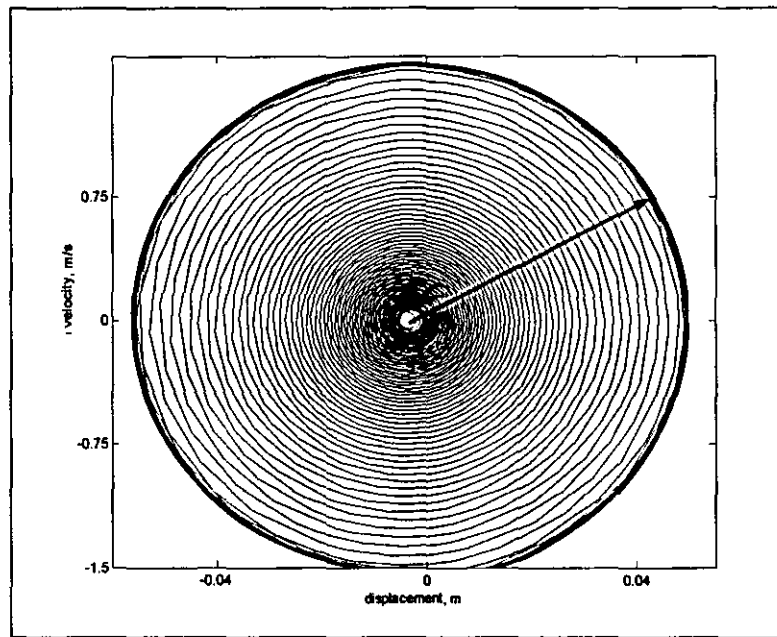


Figure 5.29: Phase plot of Bit motion

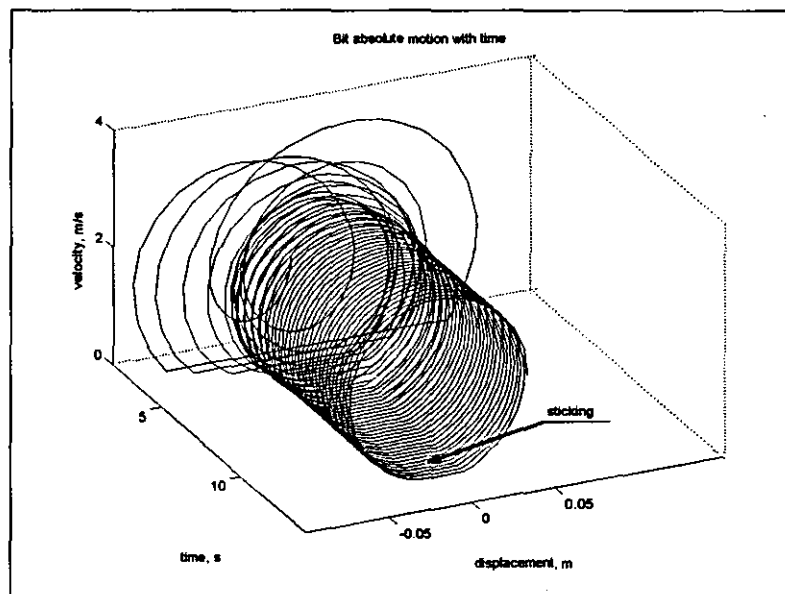


Figure 5.30: Bit absolute motion with time ($x_I(0) = 0.010$, $v_I(0) = 3.5\text{m/s}$)

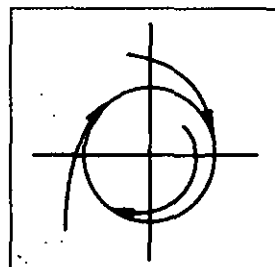


Figure 5.31: Stable limit cycle

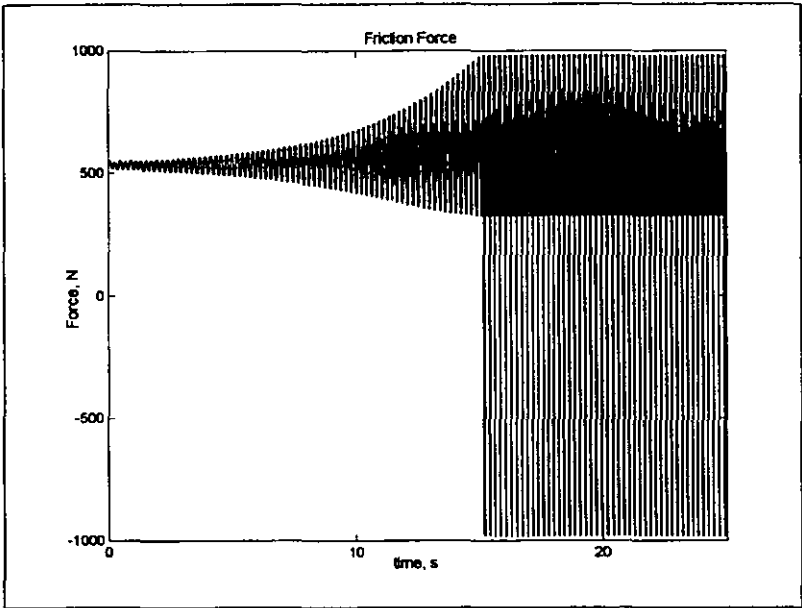


Figure 5.32: Evolution of force of friction with stick-slip self-excitation

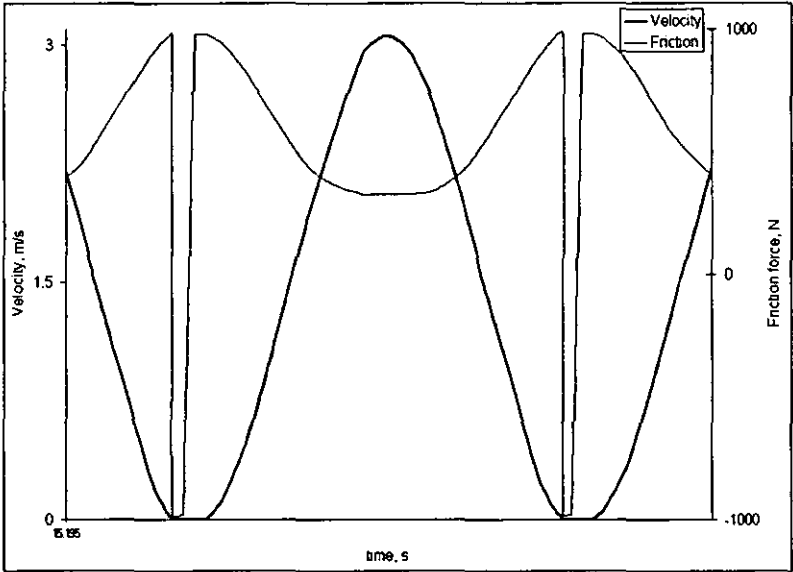


Figure 5.33 Force of friction and bit velocity in steady state periodic motion

The evolution of friction force is illustrated in Figure 5.32. In actual practice, the bit comes into contact with the surface with the speed of the drive. Therefore at the instant of contact (time $t=0$), friction force is estimated as kinetic friction by equation (5.11) and consequently is less than static friction. Observation from this picture shows that friction force increases until the value of static force is reached and the sign of the force changes to the opposite. Because in terms of absolute displacement the bit does not move backwards, the system operates only on the positive side of friction force characteristic.

In Figure 5.33, friction force is shown together with velocity when the system is in steady state motion. It is noticed that once the static force is reached, the sign of the friction force changes. At this instant, a sticking phase occurs (the bit is considered motionless) and friction force is evaluated as the minimum force between static friction and the force of springs deformation. The total pulling force of spring deformation will then grow until it exceeds static friction force causing the bit to be freed with acceleration. From this instant, friction decreases to its critical value F_{cr} , where the bit reaches its maximum velocity. The velocity is limited at this point by the effect of the cubic term in the expression of the friction force in equation (5.11). Consequently, friction force starts to increase causing a deceleration of the bit until full stop where the friction force attains its static value and the cycles repeats.

It was observed that within the identified range of β and γ values, for some configuration the system displayed two frequency components with stable periodic motion. Therefore, further simulations were undertaken in order to obtain synchronisation with a single frequency and to obtain an estimate of this frequency. This would allow the design of systems with a given frequency response and avoid multiple frequency responses.

At this stage the simulation was carried out varying the mass of the bit, the frequency ratio and the driving velocity. The values for bit mass m_I and the driving velocity were chosen to reflect real drilling conditions. A wide range of

values of the system parameters were covered and more results are presented in appendix 5-2.

Figures 5.34 and 5.36 illustrate the frequency response of the bit and the striker respectively with velocities shown on the top of the figures and the power spectral density at the bottom. It is seen that in steady state motion both the bit and the striker vibrate at 6.1 Hz for the system configuration given in Table 5.2. A single limit cycle is observed in Figure 5.35 which shows the phase portrait of the bit motion for that same configuration.

Table 5.2

Parameter	Numerical values
Driving velocity, m/s	$v = 0.8$
Mass, kg	$m_1 = 300;$
Stiffness, N/m	$k_1 = 326700$
Viscous damping, N.s/m	$c_2 = 250$
Ratio	$\beta = 0.3; \gamma = 0.8$

Figure 5.37 shows how the settling time varies with the frequency ratio. The simulation was carried out with fixed values of bit mass $m_1=250\text{kg}$, $\omega_f=25\text{rad/s}$, $c_2=250\text{N.s/m}$ and mass ratio $\beta=0.3$. The frequency ratio γ varied from 0.1 to 3. Observation of the results shows that an increment of the frequency ratio leads to an exponential growth in settling time. This relationship is shown in Figure 5.38, where for $\gamma=0.7$ the settling time increases steeply. For $\gamma=0.9$ it is impossible to sustain the vibration. Figure 5.39 reveals that self-excitation cannot be sustained for this particular system configuration and the oscillation, though periodic decays over the time.

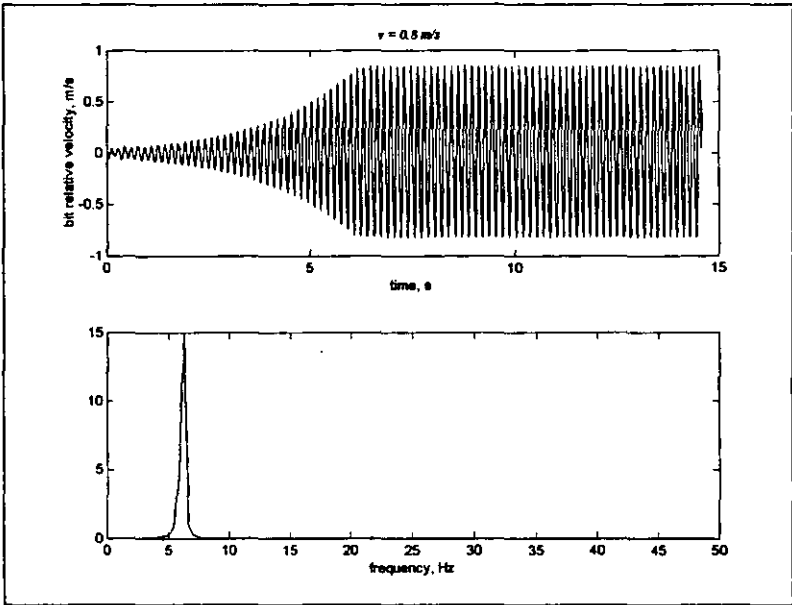


Figure 5.34: Bit frequency response for $\beta=0.3$, $\gamma=0.8$ and $v=0.8\text{m/s}$

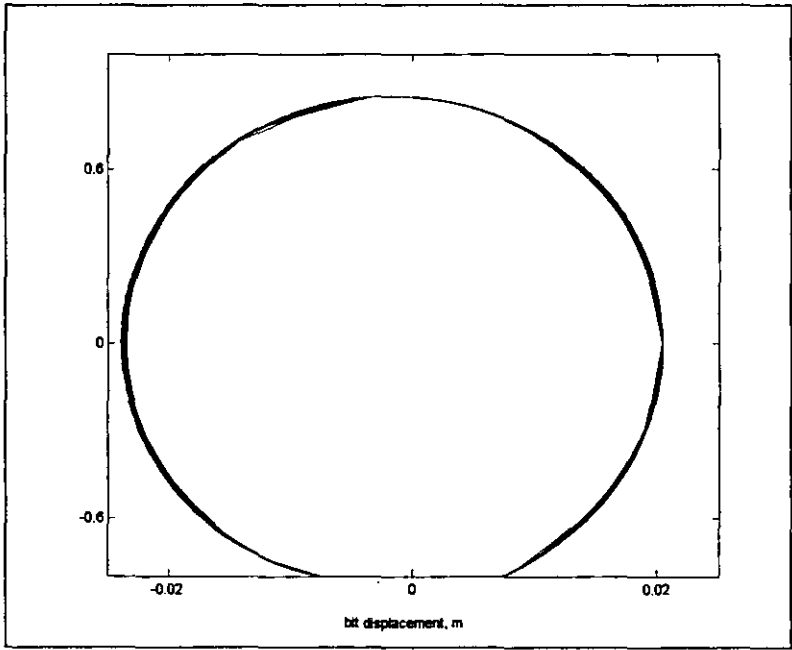


Figure 5.35: Phase plot of bit motion for $\beta=0.3$, $\gamma=0.8$ and $v=0.8\text{m/s}$

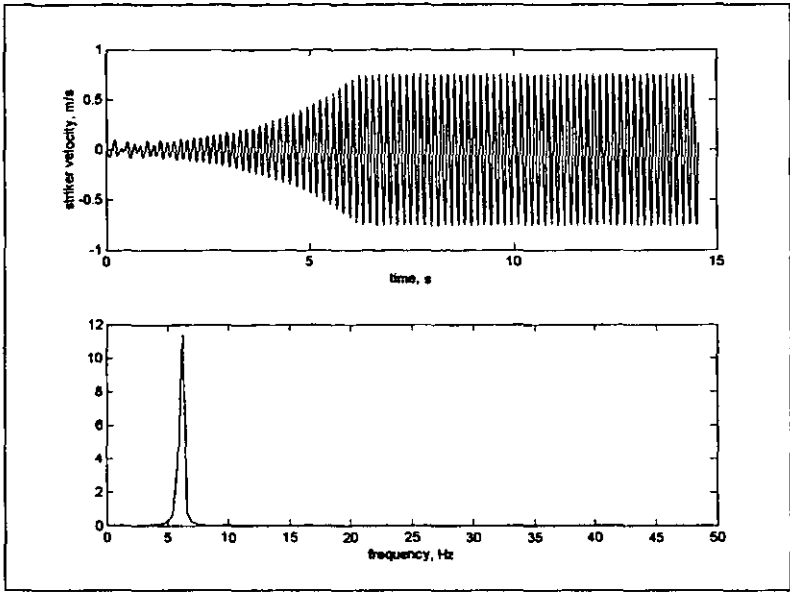


Figure 5.36: Striker frequency response for $\beta=0.3$, $\gamma=0.8$ and $v=0.8\text{m/s}$

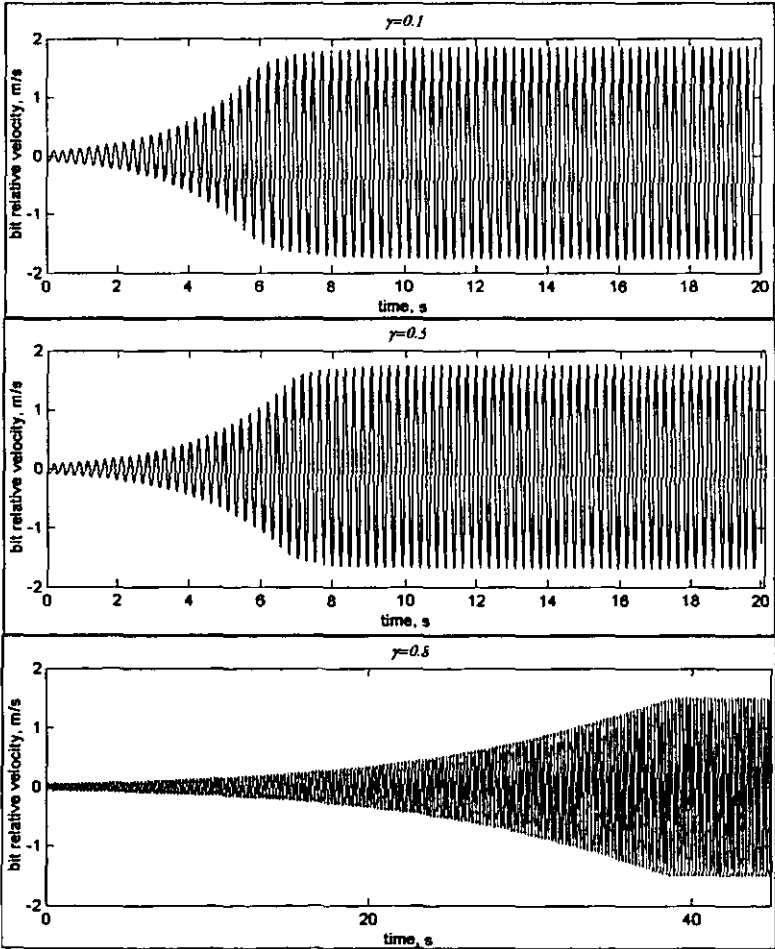


Figure 5.37: System stabilisation time: $v=1.5\text{m/s}$ $\gamma=0.1, 0.5, 0.8$

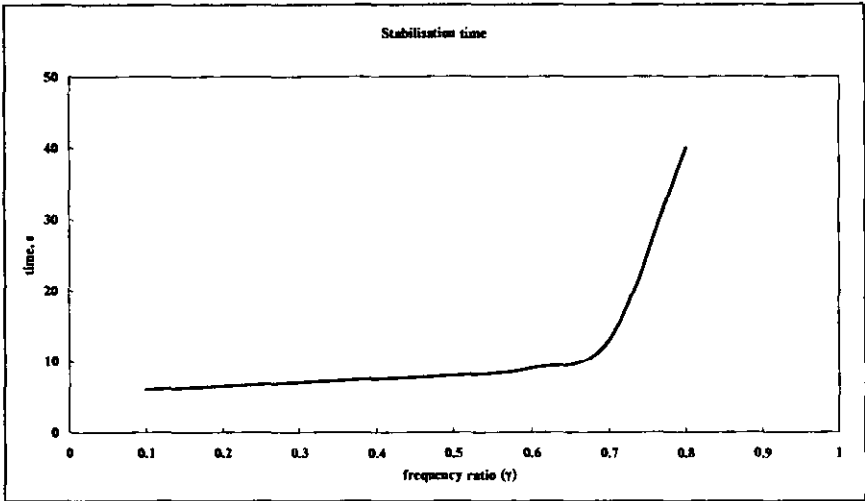


Figure 5.38: Settling time as a function of frequency ratio

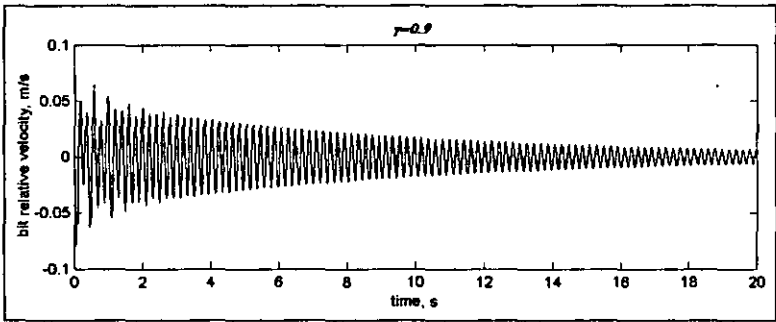


Figure 5.39: Decaying vibration for $v=1.5\text{m/s}$, $\gamma=0.9$

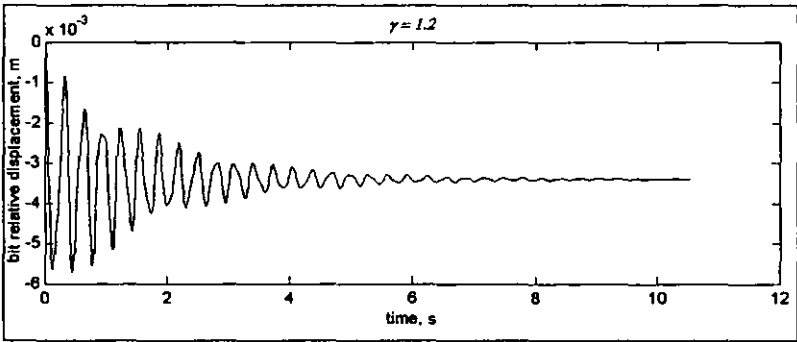


Figure 5.40: Decaying vibration for $v=1.5\text{m/s}$, $\gamma=1.2$

It was noticed that settling time depends not only on the driving velocity; the frequency ratio γ also has a substantial effect on the settling time and the ability of the system to sustain any oscillation. Observation showed that with an increase of γ , the settling time increases and at any frequency ratio higher than 0.8 the amplitude of oscillation decays. For values of γ over 0.8, the spring 6 becomes stiffer and restricts the bit to oscillate towards the drive. The drive 1 pulls the lever 5, and as spring 6 is stiff enough it helps to extend spring 3 at the initiation of the motion but the dashpot 8 does not permit ample oscillation of both the striker and the bit. This behaviour is shown in Figure 5.40 for $\gamma=1.2$ and $v=1.5\text{m/s}$, where the motion of the bit decays rapidly after a few oscillations. For higher driving velocities, any variation of the amount of damping in system does not lead to a stable steady state oscillatory motion.

However, it was found that to sustain the vibration for values of γ greater than 0.8, it is necessary that the friction force reaches its static value in a few cycles after the launch. This is achievable at low driving velocities and for a small amount of damping in the system. Figure 5.41 shows the velocity of the bit for the following configuration: $v=0.5\text{m/s}$, $c_2=75\text{N.s/m}$, $m_I=250\text{kg}$, $\omega_f=25\text{rad/s}$, mass ratio $\beta=0.3$ and frequency ratio $\gamma=1.2$.

It was observed that for values of γ less than or equal to 1, the striker and the bit synchronise their motions but they move in counter phase as the second mode is excited. This is shown in figures 5.27 and 5.42 for $\gamma=0.75$ and $\gamma=1.0$. For other values of γ ($\gamma > 1.1$) at the steady state synchronised motion, the striker and the bit move in phase as shown in Figure 5.43 for $\gamma=1.2$ because the system switches back to its first mode of excitation. It is seen from this picture that the amplitude of both displacements are different.

However, with the increase of the frequency ratio the amplitudes of both motions move towards each other until they equalise because spring 6 becomes stiffer. During this interval, the response of the system is unstable.

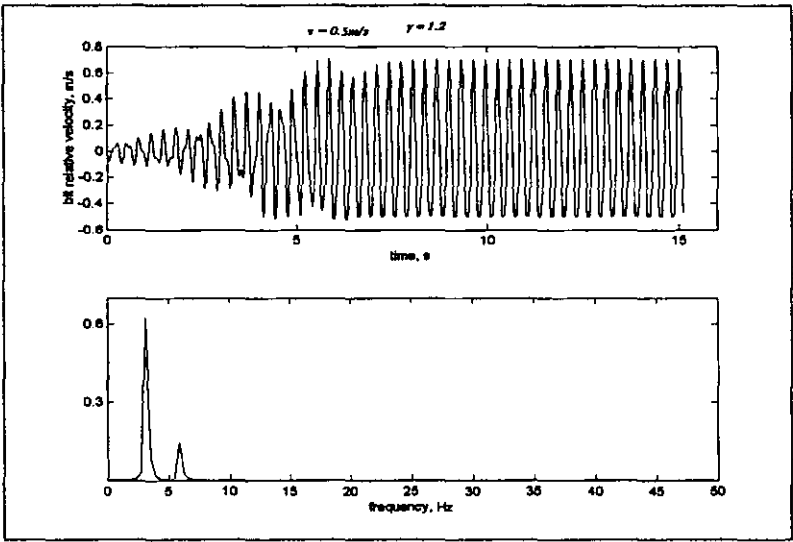


Figure 5.41: Bit velocity and frequency spectrum for $\gamma=1.2$, $v=0.5\text{m/s}$

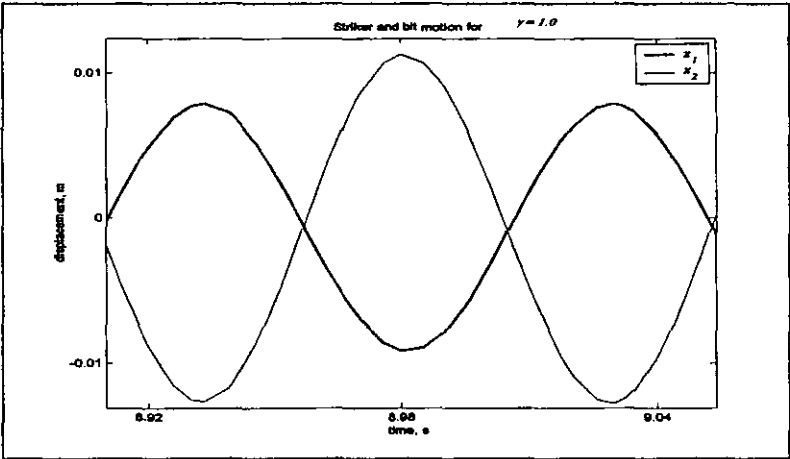


Figure 5. 42: Bit and striker motion for $\beta=0.3$ and $\gamma=1.0$

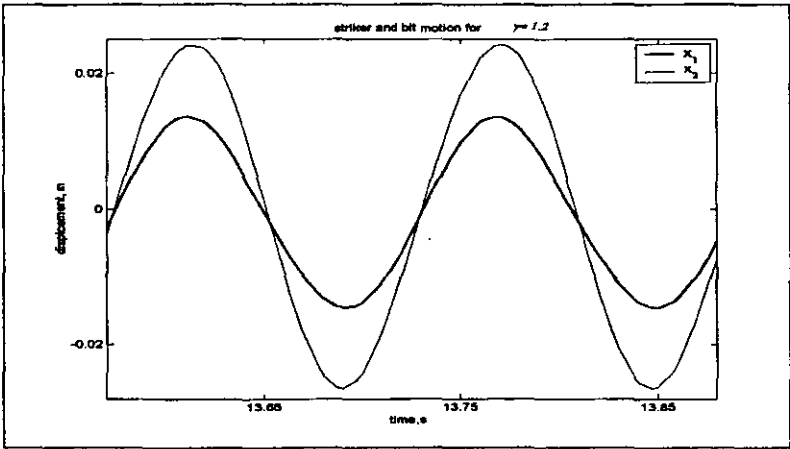


Figure 5. 43: Bit and striker motion for $\beta=0.3$ and $\gamma=1.2$

For $\gamma = 2, 3, \dots, n$, $n < 8$ real number, the phase portrait of the motion displays lobes the number of which is equal to the whole part of n . Observation of the results revealed that for even numbers, the lobes are spread symmetrically to the abscissa. This is illustrated in Figure 5.44 by the motion of the striker for $\beta=0.3$, $\gamma=10$, $v=0.5\text{m/s}$, $c_2=75\text{N.s/m}$, $m_I=250\text{kg}$, $\omega_f=25\text{rad/s}$. The small lobes close to the abscissa are not considered as they appear constantly in all results. For odd values of γ , the lobes are not spread evenly and Figure 5.45 shows the phase plane of the motion of the striker for $\beta=0.3$ and $\gamma=3.0$, where three lobes are observed. The corresponding motion of the bit is shown in Figure 5.46.

For frequency ratio γ in the interval between 8 and 9 inclusively, the amplitude of motions of the bit and the striker equalise and the lobes disappear. Any value of γ in this interval produces a positive result. This particular case is illustrated in Figure 5.47 with a stable limit cycle for $\beta=0.3$ and $\gamma=9$ where the lobes are less pronounced. However with the increase of the stiffness of spring 3 the segments vanish and a continuous and uniform circular limit cycle is obtained.

The dynamic response of the system varies according to the configuration. Both mass ratio β and frequency ratio γ have a strong effect on the convergence of the solutions. For $\beta=0.4$, the system vibrated at both natural frequencies. This parameter is investigated in the next section as an important factor in vibro-impact motion.

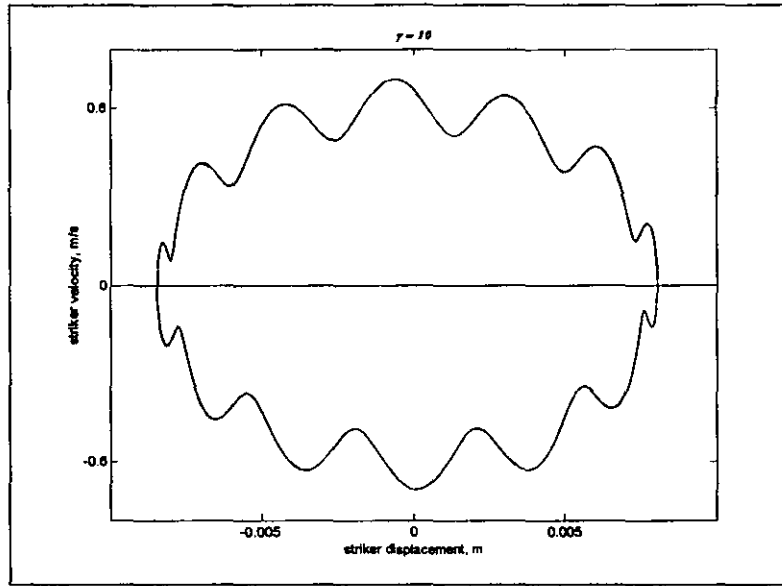


Figure 5.44: Phase portrait of striker motion for $\beta=0.3$ and $\gamma=10$

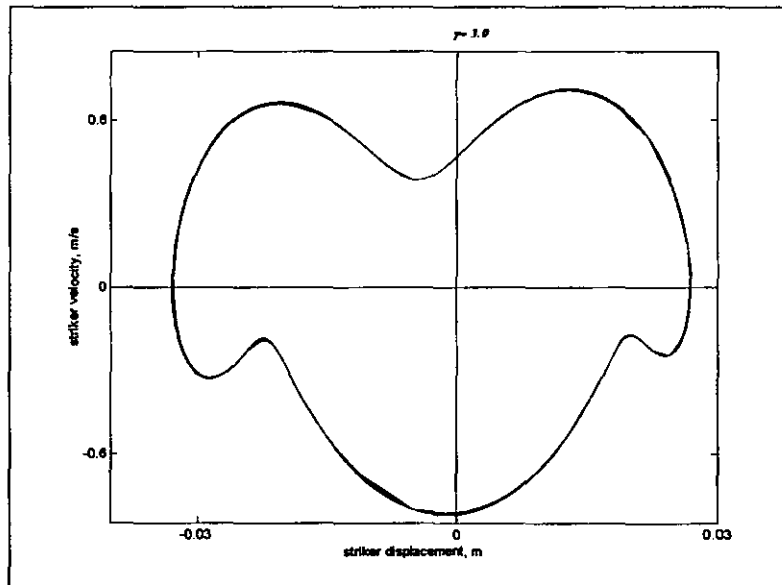


Figure 5.45: Phase portrait of striker motion for $\beta=0.3$ and $\gamma=3$

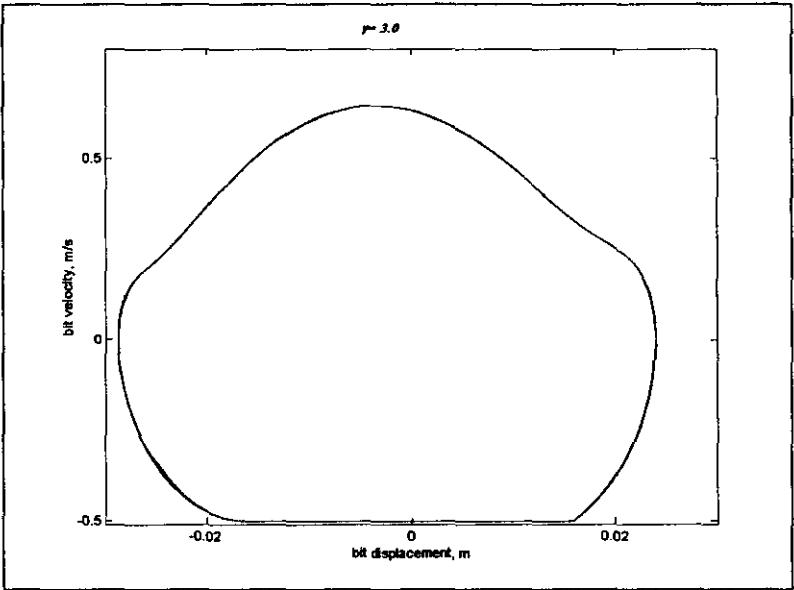


Figure 5.46: Phase portrait of bit motion for $\beta=0.3$ and $\gamma=3$

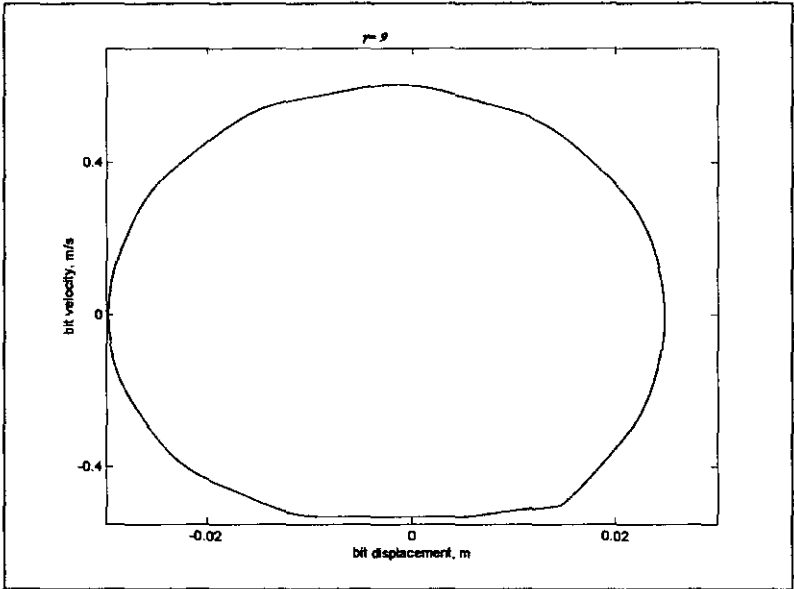


Figure 5.47: Phase portrait of bit motion for $\beta=0.3$ and $\gamma=9$

Figure 5.48 illustrates 3D plots of the motion of the bit, seen from the side of time and velocity plane (a.) and in the plane formed by displacement and velocity (b.). The configuration of the system was as follows: $m_I = 250$ kg; $k_I = 625000$ N/m; $c_2 = 75$ N.s/m; $\beta = 0.4$; $\gamma = 1.2$. It shows two stable processes of vibration happening simultaneously. The initiation of both processes is seen in Figure 5.48a. It was observed during that the simulation the system started to vibrate at its lower frequency component (6.14Hz for this configuration). Then as the second process (central dark part, see Figure 5.48a and Figure 5.50) grew in amplitude, between the 6th and 8th second of simulation the frequency meter showed intermittently 6.2Hz and 12.8Hz. Between the 8th and 9th second 12.3Hz predominated and from the 10th second the system displayed constantly 12.7Hz with 6.2Hz appearing from time to time. The 6.2Hz appeared rarely because the frequency meter in the Simulink model was design to capture the period of the signal fed to its input; therefore it showed the most predominant frequency component.

Figure 5.49 shows that the phase portrait of the striker displays the same behaviour as the bit. An illustration of the time history of the bit motion is given in Figure 5.50 with its frequency component.

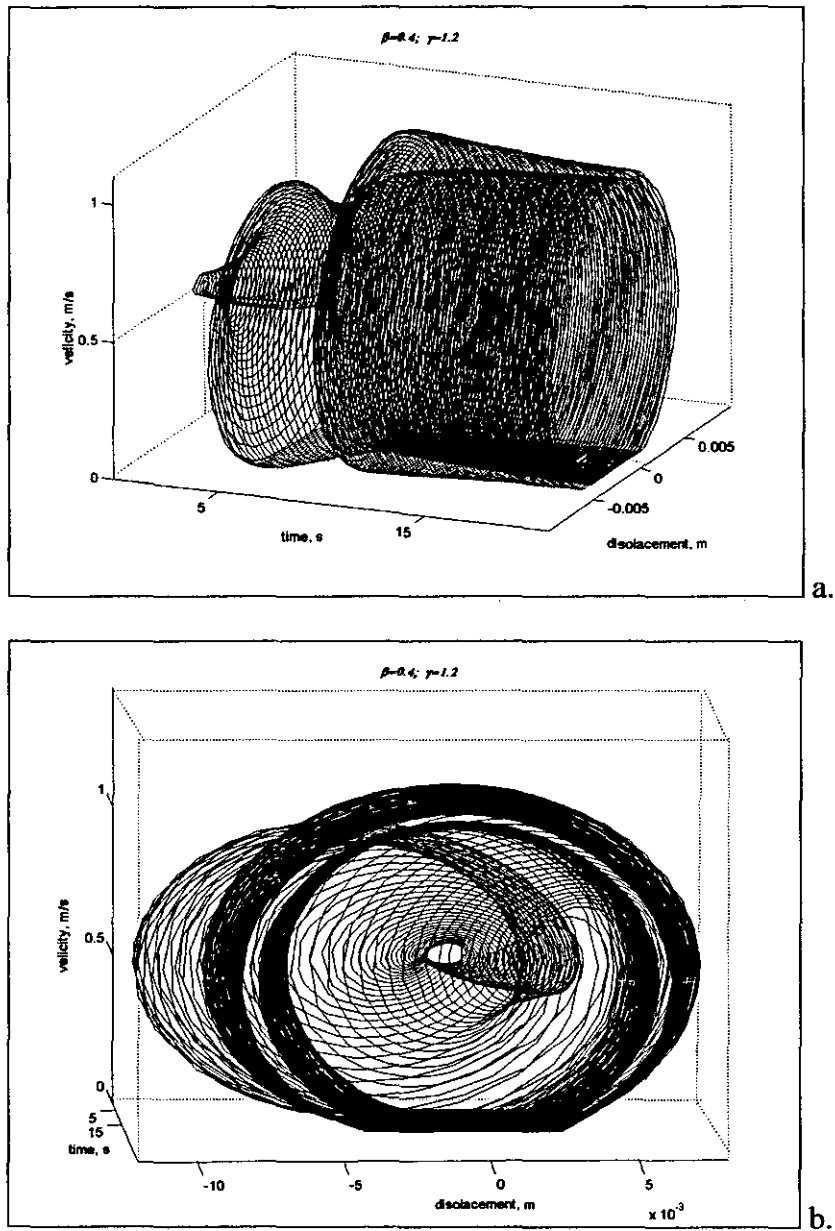


Figure 5.48: Bit motion with time for $\beta=0.4$ and $\gamma=1.2$

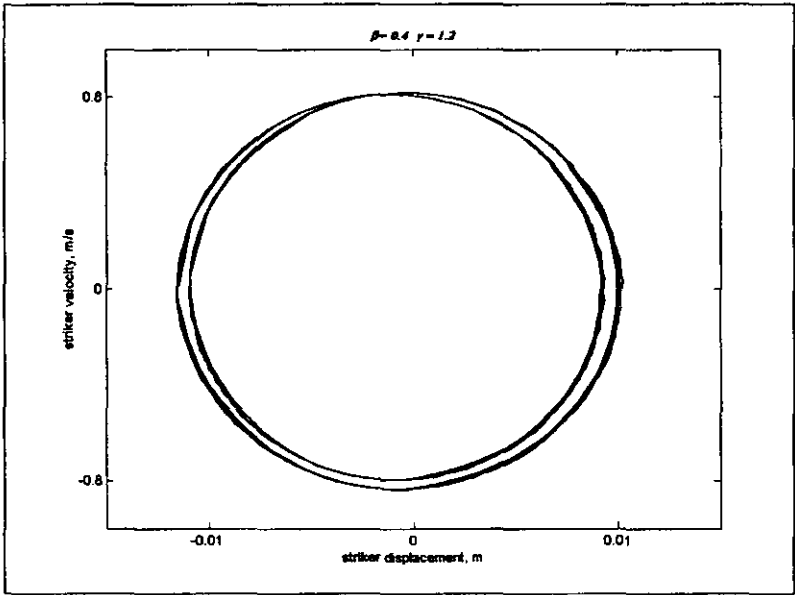


Figure 5.49: Phase portrait of striker motion for $\beta=0.4$ and $\gamma=1.2$

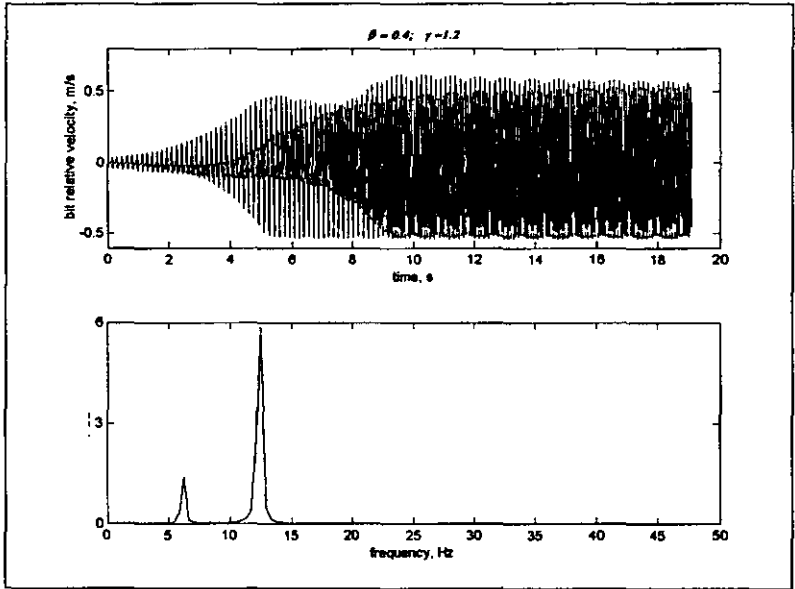


Figure 5.50: Time history of the bit motion and frequency spectrum for $\beta=0.4$ and $\gamma=1.2$

5. DISCUSSION

A large number of simulation results were analysed and an empirical expression of the frequency of synchronised motion was derived as follows:

$$\omega = \sqrt{\frac{k_1 + k_2}{m_1} + \frac{k_2}{4m_2}} \quad (5.17)$$

Table 5.3

ω_1 , rad/s	ω_2 , rad/s	v , m/s	β	γ	Synchronisation frequency		
					ω_{nl} , rad/s		
					eq. 5.16	eq. 5.17	Simulation
25	22.5	1.5	0.3	0.9	30.8	30.0	30.7 decay
25	20	1.5	0.3	0.8	29.1	29.0	29.0
25	17.5	1.5	0.3	0.7	27.8	28.0	27.6
25	15	1.5	0.3	0.6	26.8	27.3	26.7
25	12.5	1.5	0.3	0.5	26.1	26.6	26
25	7.5	1.5	0.3	0.3	25.3	25.6	25.2
25	2.5	1.5	0.3	0.1	25.0	25.0	24.8
33	26.4	0.8	0.3	0.8	38.5	38.4	38.3
50	37.5	1.5	0.4	0.75	58.7	58.4	58.6
66	49.5	0.8	0.4	0.75	79.6	78.5	79.6
81	60.7	1.0	0.4	0.75	95.1	94.7	95.0

Table 5.3 gives some comparative results of the simulation, theoretical and empirical estimation of the frequency of synchronisation. It is seen that the values obtained from equations 5.16 and 5.17 are in agreement with those from the simulation.

An analysis of the results of the simulation shows that for values of the frequency ratio $\gamma \leq 1$, the bit and the striker move in counter phase and vibrate at the highest natural frequency. Values 1.1 and 1.2 are in the transition zone, where, depending on the mass ratio, both bodies may move either in phase or counter phase and

vibrate at both natural frequencies. For values of $\gamma \geq 1.3$ both the striker and the bit move in phase and the frequency of oscillation is the lower natural frequency.

The results obtained for $\beta=0.4$ and $\gamma=1.2$ are valuable results because it reveals the limit of the performance of the structure in the frame of this application. It gives practical limiting values for both β and γ . The conditions for which the striker and the bit move in phase or counter phase have been defined and the limiting values where the system exhibits bifurcating properties have been identified.

Values of $\gamma > 1$ do not present any particular interest for the development of the current application; however from a mathematical point of view; results covering the range of value of $1 < \gamma \leq 15$ are given in the appendix 5-3. Observation showed that, for given m_I , k_I and β , the lower natural frequency increases with an increase in frequency ratio up to $\gamma=1.2$. Thereafter no increase of lower natural frequency was observed for values of $\gamma \geq 1.2$. However, higher natural frequency does increase but the system responds only at the lower frequency.

6. VIBRO-IMPACT MOTION WITH DRY FRICTION.

The structure in Figure 5.11 was developed to produce a vibro-impact process where striker 4 periodically collides with the bit. Results from the above section have shown that the solutions of the system converge into a limit cycle. The state of the limit cycle depends upon the relationship between masses and frequencies. Three intervals of frequency ratio have been identified where the system exhibits different dynamic responses. These findings will be used in this section to study the response of the system in vibro-impact motion.

To impart blows periodically onto the bit, the striker must be set at a given clearance to the bit. Because the system is self-excited, the amplitude of oscillation of the striker increases until it starts to impact on the bit. The time required from the initiation of oscillation to full impact depends on the value of the clearance between the bit and the striker.

The magnitude of the force of impact depends on the clearance, the stiffness and the damping properties of the colliding surfaces. The contact surfaces can be specially treated to secure the desired properties of the interface layer. A non-Hertzian model of contact was used assuming that in the contact zone, the impacting bodies have viscoelastic properties. This was modelled as a “Kelvin-Voigt” element to allow the strain and the deformation of the contact layer to develop through the loading and the unloading phases. Though the impact is of a very short duration, it is possible for such a model to calculate the force developed during both phases. The impact force was defined as follows, (Babitsky, 1998 and Soundranayagam, 2000).

$$\mathfrak{I}(x_2, \dot{x}_2) = \begin{cases} k_0(x_2 - \Delta) + c_0\dot{x}_2 & \text{for } x_2 \geq \Delta \text{ and } \mathfrak{I}(x_2, \dot{x}_2) > 0 \\ 0 & \text{for } x_2 \geq \Delta \text{ and } \mathfrak{I}(x_2, \dot{x}_2) < 0 \\ 0 & \text{for } x_2 < \Delta \end{cases} \quad (5.18)$$

Where k_0 is the contact stiffness of the bits shank, c_0 is contact damping and Δ is the initial gap between bit and striker. As mentioned earlier, the clearance (gap)

can be positive or negative (preload) and the force of impact increases with the increase of the gap and the contact stiffness. Figure 5.51 shows a typical impact force obtained from equation (5.18) for $k_0 = 9 \times 10^6 \text{ N/m}$, $c_0 = 0.1 \text{ N.s/m}$, Soundranayagam, (2000) which were obtained using two semi-spherical bodies made of soft steel and $\Delta = -0.005 \text{ m}$.

The impact on the bit steeply increases the friction force and the total pulling force is reduced by relaxation of spring 3. Subsequently, the force of friction becomes greater than the force of spring deformation. When the spring force exceeds the static friction force, the bit is propelled and accelerates. Lever 5 is pushed counter-clockwise and striker 4 imparts a blow on the bit. Consequently, the velocity diminishes quickly, and the bit comes to a standstill. To implement a cycle of motion as aforementioned, the impact must occur at a given time within the period of motion. This is achieved by an accurate correlation of mass and frequency ratio and by an adequate amount of damping between the striker and the drive. Figure 5.52 shows the expected working cycle of the entire structure in steady state vibro-impact motion.

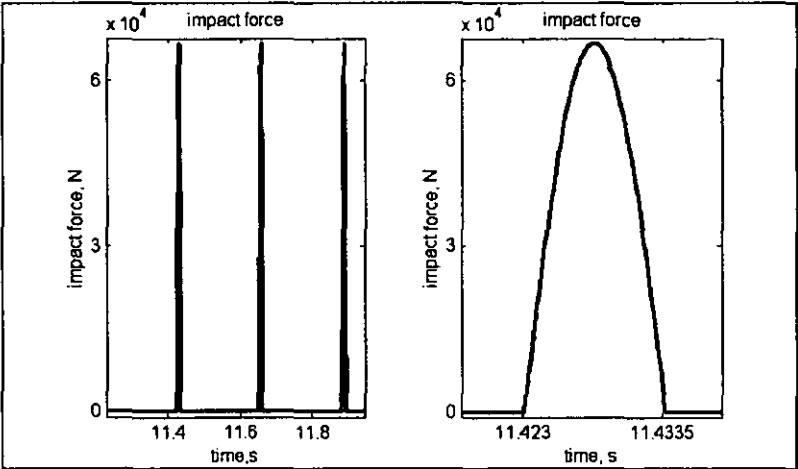


Figure 5.51: Typical impact force obtained from equation (5.18)

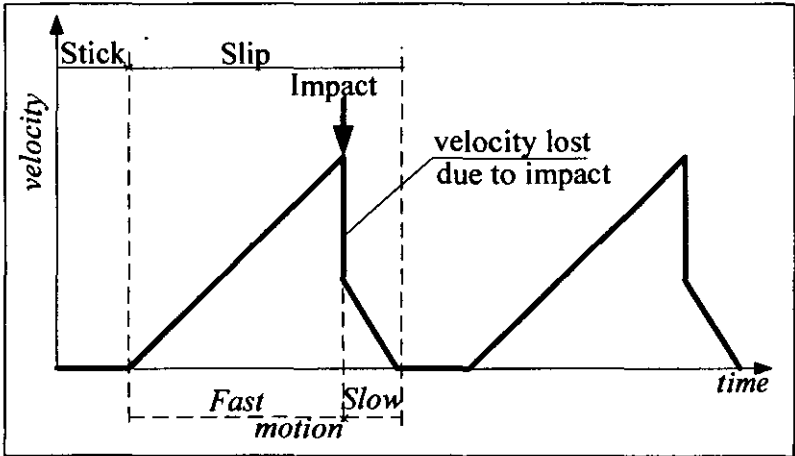


Figure 5.52: Prescribed working cycle of the system in vibro-impact regime

6.1 Numerical Solutions of the System in Vibro-Impact Motion

In the vibro-impact regime described above, the striker 4 periodically imparts blows on the bit. Equations (5.10), (5.11), (5.12) and (5.18) govern the motion of the entire system. The introduction of impact changes the nature of the response of the system. The settling time is considerably shortened due to the impact which increases the friction force. As described earlier, the increase in amplitude of oscillation stops when the friction force reaches its static value (occurrence of sticking). Figure 5.53 illustrates the time history of the velocity of the bit and striker respectively. For the same configuration of the system ($m_I=250\text{kg}$, $k_I=156250\text{ N/m}$, $c_I=250\text{Ns/m}$, $\beta=0.4$, $\gamma=0.75$ and $v=1.5\text{m/s}$), Figure 5.53 shows that the settling time in this vibro-impact regime is very short in comparison with the results in figures 5.25 and 5.26 for the system without impact.

In vibro-impact motion, the system resonant frequency is less than the one obtained without impact. The impact not only reduces the velocity but it retards the motion with the impact-induced additional friction force (which acts only during the time of collision). Consequently, a premature sticking occurs and steady state motion is reached earlier (after a few cycles). Figure 5.54 represents the period of motion in an impact regime where a steep reduction of velocity is seen. In vibro-impact motion the system natural frequency is 27.45 rad/s .

Figure 5.55 is a 3D-phase plot of the bit motion with impact. Here we see that the system is quickly attracted to the limit cycle.

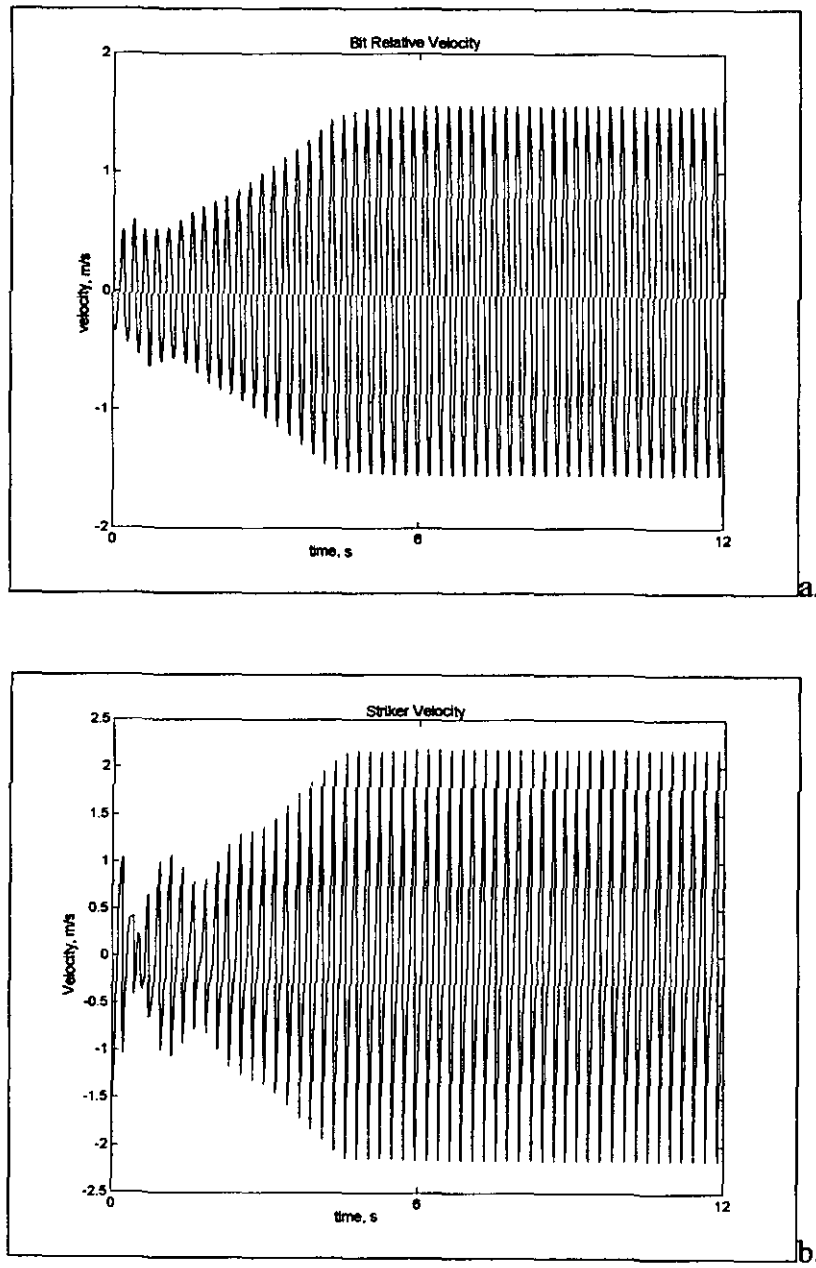


Figure 5.53: Velocities of the bit and striker in vibro-impact regime for $\beta=0.4$ $\gamma=0.75$ and $v=1.5\text{m/s}$

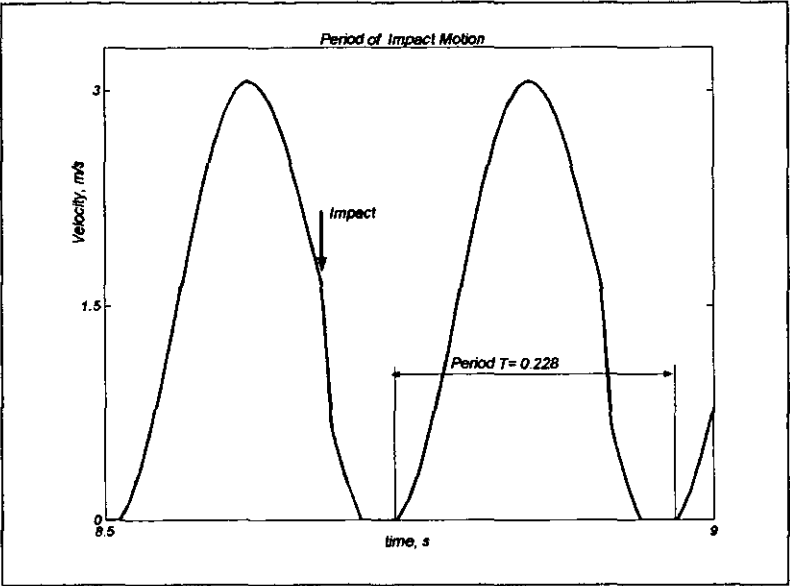


Figure 5.54: Period of bit motion in impact regime

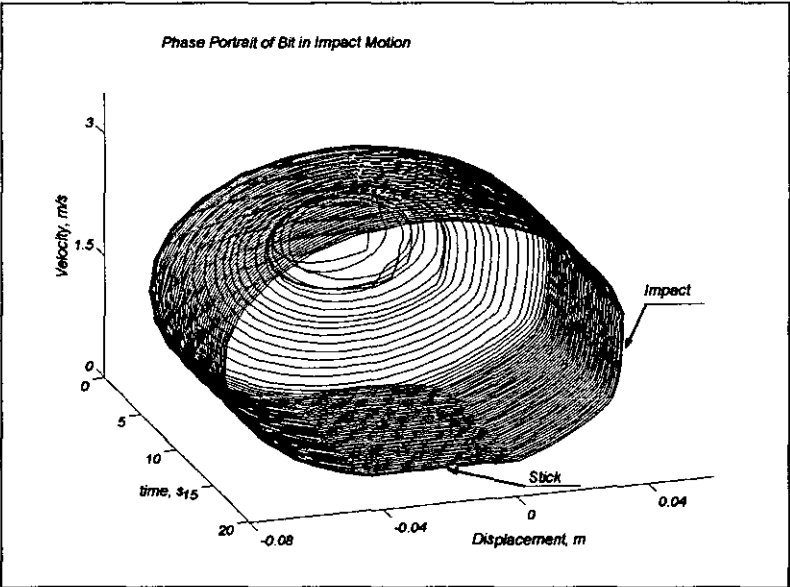


Figure 5.55: Time contained phase plot of the bit motion

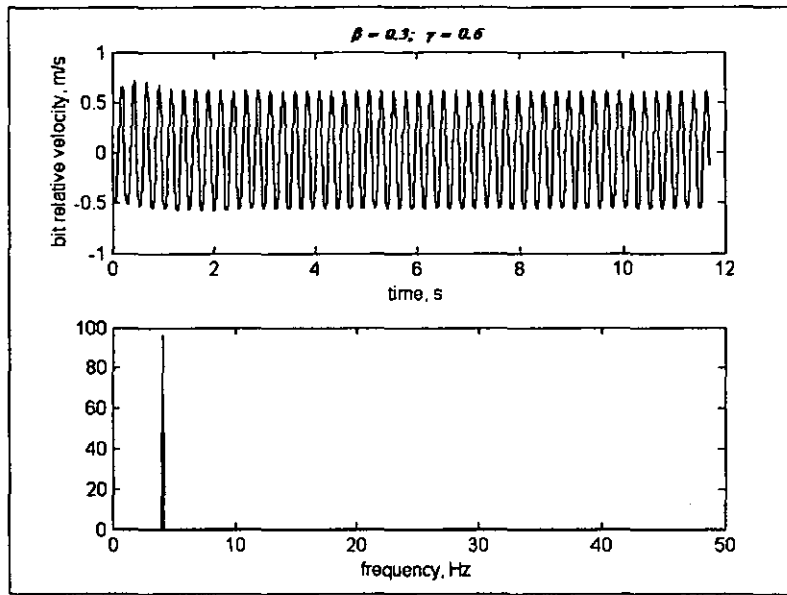


Figure 5.56: time history of bit velocity for $\beta=0.3$, $\gamma=0.6$ and $v=0.5\text{m/s}$

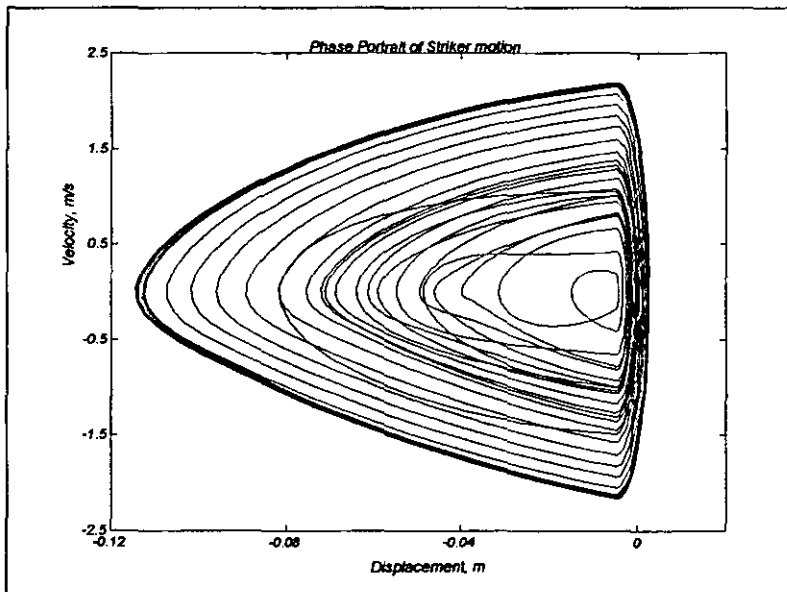


Figure 5.57: Phase portrait of striker motion

At low driving velocity, the system settles down very fast (after a few oscillations) and this is illustrated in Figure 5.56 for $m_I=250\text{kg}$, $k_I=156250\text{ N/m}$, $c_2=250\text{Ns/m}$, $\beta=0.3$, $\gamma=0.6$ and $v=0.5\text{m/s}$. This result is important because in all attritious and abrasive rock formations, the drill bit is rotated very slowly to avoid high damage.

The striker exhibits the same periodic behaviour as the bit because the response of the bit impels a similar reaction in the striker subsystem. Figure 5.53b, shows that the change in striker velocity is about 4m/s . With reference to Figure 5.57 which displays the phase portrait of the striker motion, it is observed that the striker is attracted towards a limit cycle where the steady state motion is reached.

Figure 5.58 displays the synchronised motion of both the bit and the striker and their respective velocities. Figure 5.59 shows the absolute displacement of the bit undergoing a stick-slip motion. This picture unfolds the rotational displacement of the bit and illustrates it in a linear form. The normal displacement (penetration) is not included here. This motion is investigated in the next chapter.

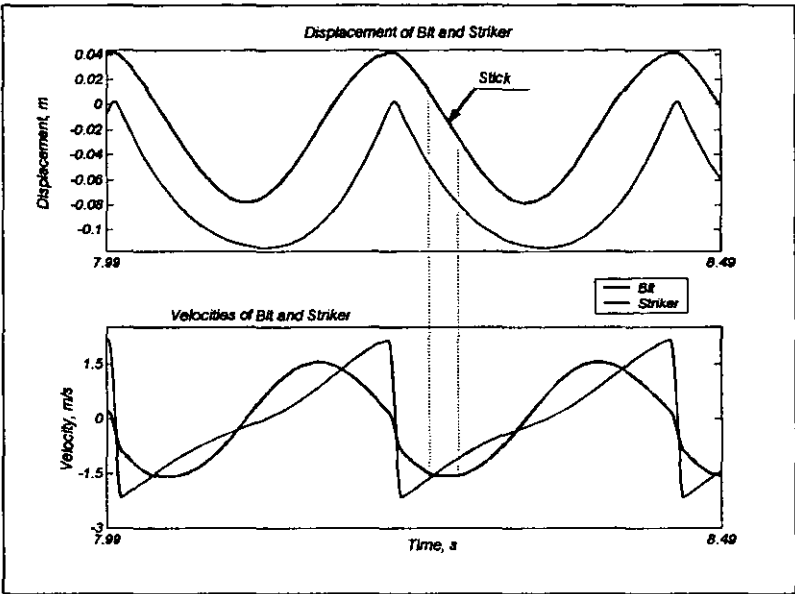


Figure 5.58: Displacement and velocities of bit and striker in steady state vibro-impact motion

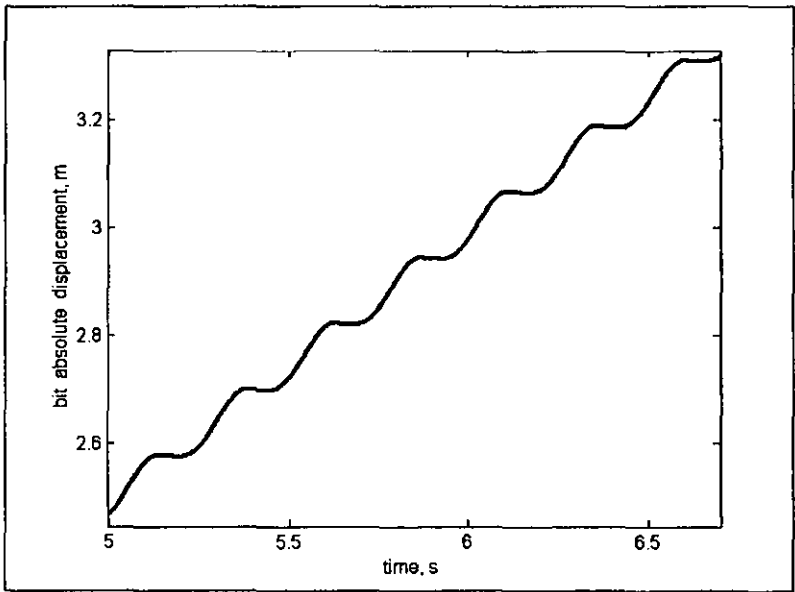


Figure 5.59: Bit absolute motion

6.2 Effect of Frequency Ratio on the System in Vibro-Impact Motion

The results in section 4 above have shown that for a frequency ratio $\gamma > 1.2$ it is still possible to obtain a periodic synchronised motion of the system at a low driving velocity and with a relatively small amount of damping. Superimposing impact to the moving bit changes the dynamic behaviour of the system and the motion in phase starts already at $\gamma = 0.6$. A little change is observed in the system resonant frequency. The system dynamic response can be sectioned into three intervals of values of γ namely $\gamma < 0.6$; $\gamma \in [0.6, 0.8]$ and $\gamma > 0.8$ where the system performs irregular multiple impacts, a single impact per cycle and intermittent single and double impacts respectively.

6.2.1 SYSTEM RESPONSE FOR VALUES OF $\gamma < 0.6$

It was observed that for values of $\gamma < 0.6$ the bit and the striker vibrate in counter phase. In counter phase motion, the impact occurs when the velocity of the bit is ascendant. This is illustrated in Figure 5.60 for the configuration of the system given in Table 5.4.

Table 5.4

<u>Parameter</u>	<u>Numerical values</u>
Driving velocity, m/s	$v = 1.5$
Mass, kg	$m_1 = 250$;
Stiffness, N/m	$k_1 = 156250$;
Viscous damping, N.s/m	$c_2 = 250$
Ratio	$\beta = 0.3$; $\gamma = 0.5$

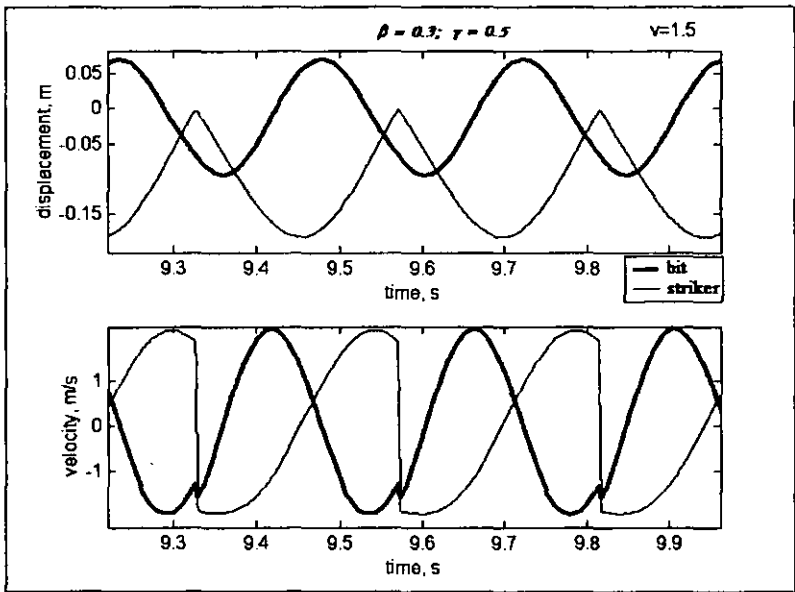


Figure 5.60: Bit and striker displacement with velocity for $\beta=0.3$ and $\gamma=0.5$

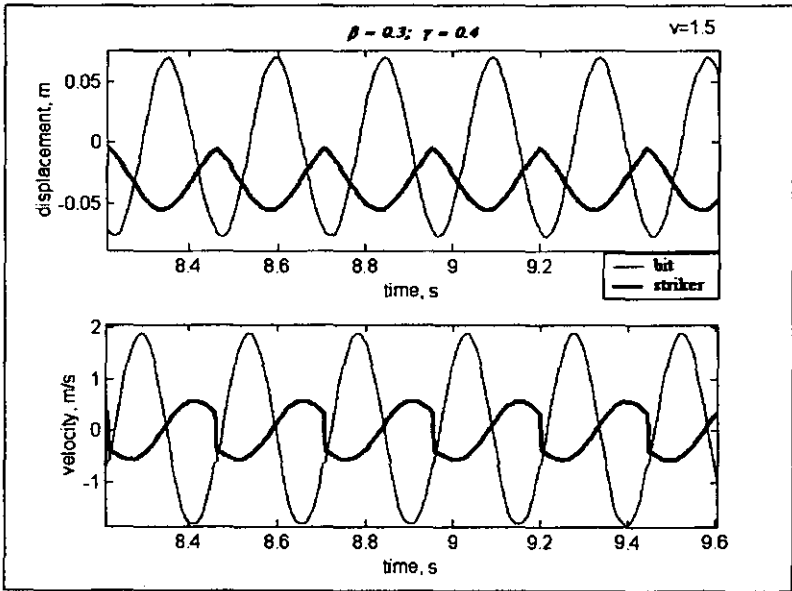


Figure 5.61: Bit and striker displacement with velocity for $\beta=0.3$ and $\gamma=0.4$

In Figure 5.61 for $\beta=0.3$; $\gamma=0.4$, it is seen that the impact induces a negligible effect on the motion of the bit. Figure 5.62 shows the phase portrait of bit motion with an indication of the location of impact. During this impact, the exerted compression results in the elastic deformation of the contact layers, consequently on the phase plot, the impact side can be seen as being slightly convex. In Figure 5.63, which is the phase plot of the motion of the strike, it is observed that the striker does not exert a strong compression on the bit. The resulting impact force is shown in Figure 5.64. The value of the impact force reduces considerably with the decreasing of γ .

As γ decreases, spring 6 becomes relatively soft and irregular oscillations are observed in the striker motion. This behaviour is illustrated in Figure 5.65, where the striker produces irregular multiple impact. The magnitude of velocity is important in obtaining a strong impact force. In Figure 5.66 showing the phase plane of striker motion for $\beta=0.3$ and $\gamma=0.3$, it is seen that the maximum change in the velocity of the striker is about 0.2m/s. Consequently, generated impact force is negligible and has almost no effect on the motion of the bit. More simulation results are given in appendix 5-4. In this range of values of γ , the bit and the striker are still moving in counter phase and the frequency response is identical to the one of the system without impact.

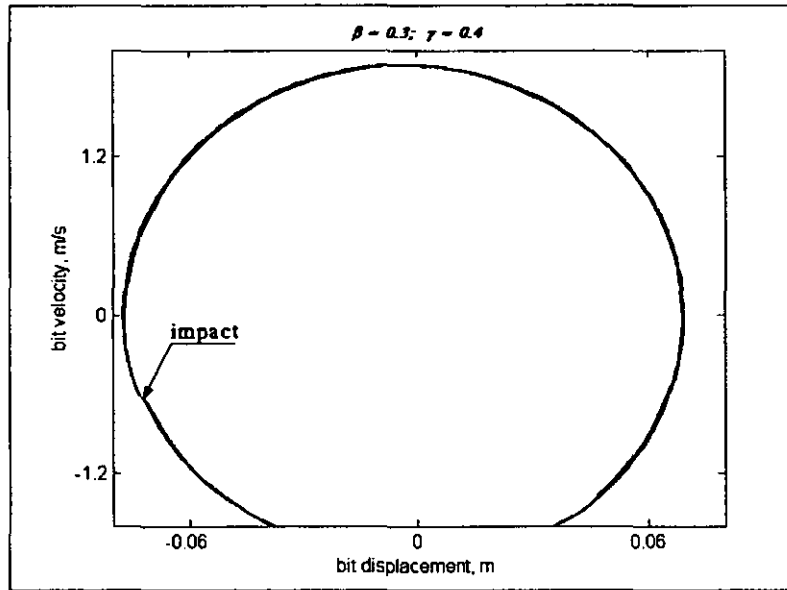


Figure 5.62: Phase portrait of bit motion for $\beta=0.3$ and $\gamma=0.4$

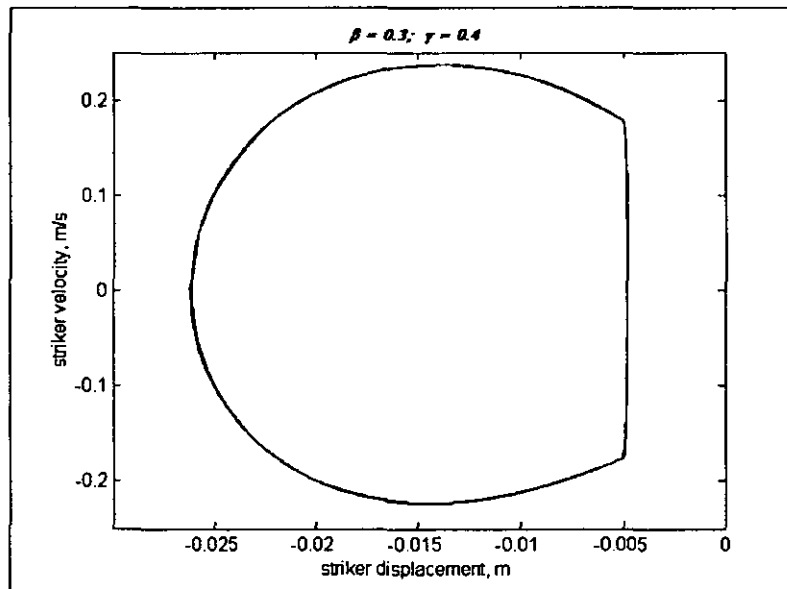


Figure 5.63: Phase portrait of striker motion for $\beta=0.3$ and $\gamma=0.4$

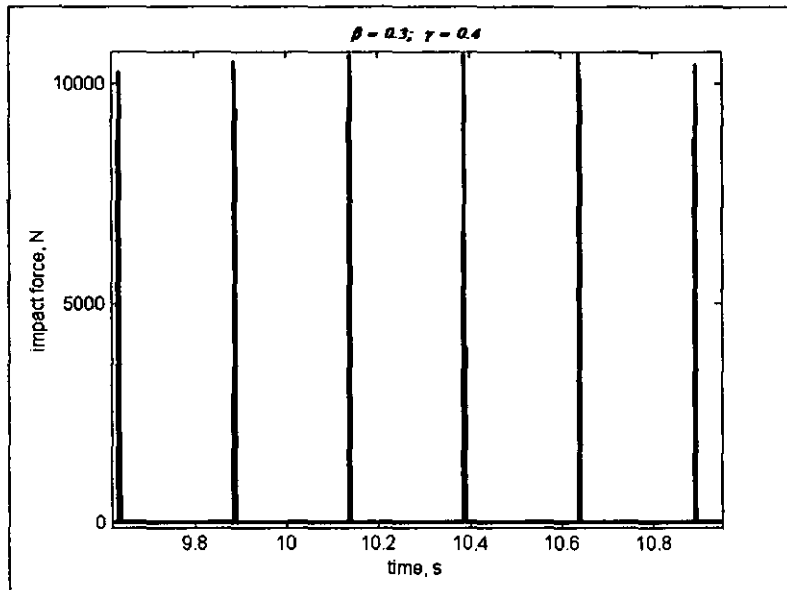


Figure 5.64: Force of impact for $\beta=0.3$ and $\gamma=0.4$

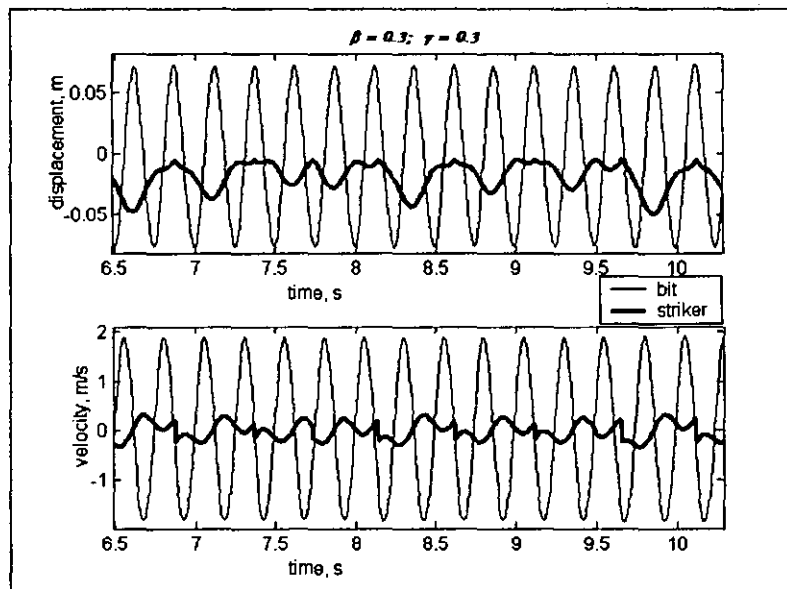


Figure 5.65: Bit and striker displacement with velocity for $\beta=0.3$ and $\gamma=0.3$

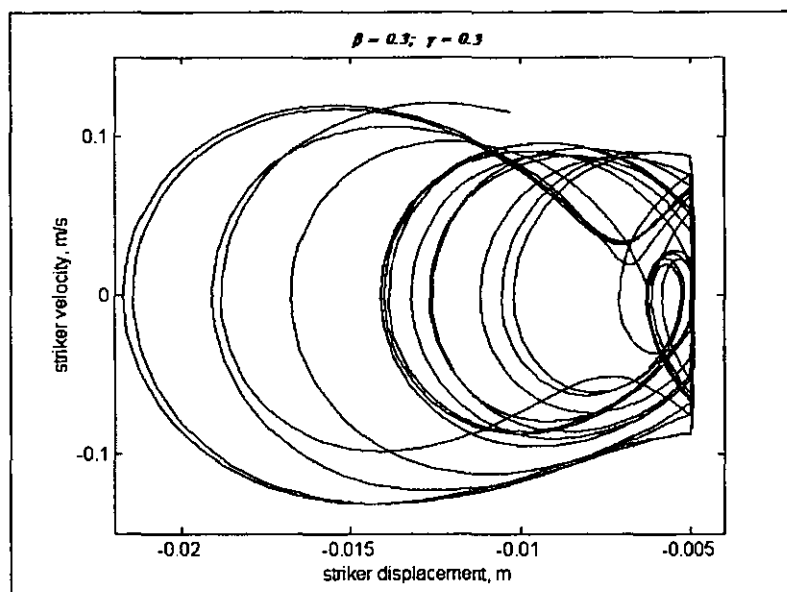


Figure 5.66: Phase portrait of striker motion for $\beta=0.3$ and $\gamma=0.3$

6.2.2 SYSTEM RESPONSE FOR $0.6 \leq \gamma \leq 0.8$

For a frequency ratio in the range of $0.6 \leq \gamma \leq 0.8$, the introduction of impact confines the bit and the striker to move in phase. This behaviour is opposite to the response of the system without impact. After the transient process, which lasts a few cycles, both the striker and the bit synchronise their motion and vibrate in phase. Within this interval of the frequency ratio, the dynamic response of the system was stable, given that all relationships between parameters were observed. It was found that the system was less sensitive to variation of configuration parameters used in this investigation. The system exhibited a stable periodic motion with a single strong impact period.

Figure 5.67 shows the displacement and the velocities of the bit and the striker for two different values of the driving speed. Table 5.5 gives the values of configuration of the system.

Table 5.5

Parameter	Numerical values
Driving velocity, m/s	$v = 0.5; 1.5$
Mass, kg	$m_I = 250$
Stiffness, N/m	$k_I = 156250$
Viscous damping, N.s/m	$c_2 = 250$
Ratio	$\beta = 0.3; \gamma = 0.6$

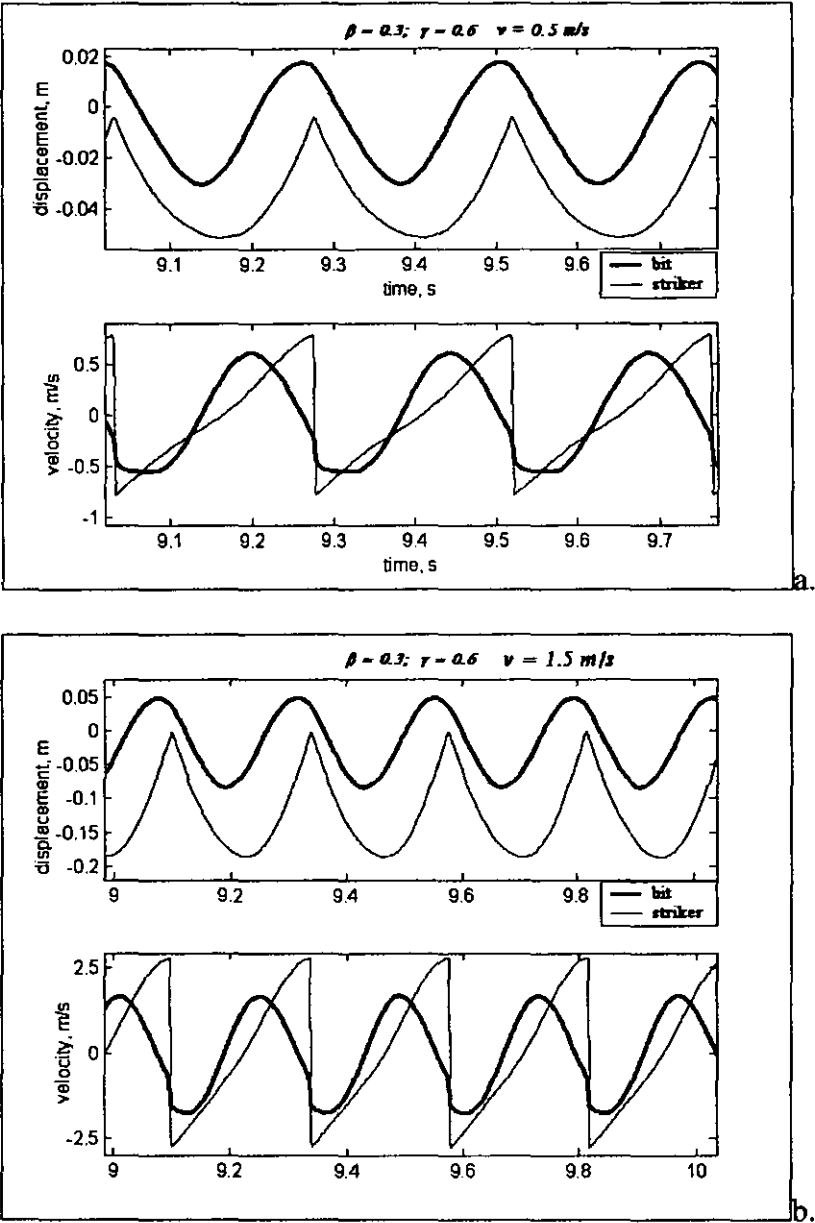


Figure 5.67: Displacement and velocity of bit and striker for $\beta=0.4$; $\gamma=0.6$

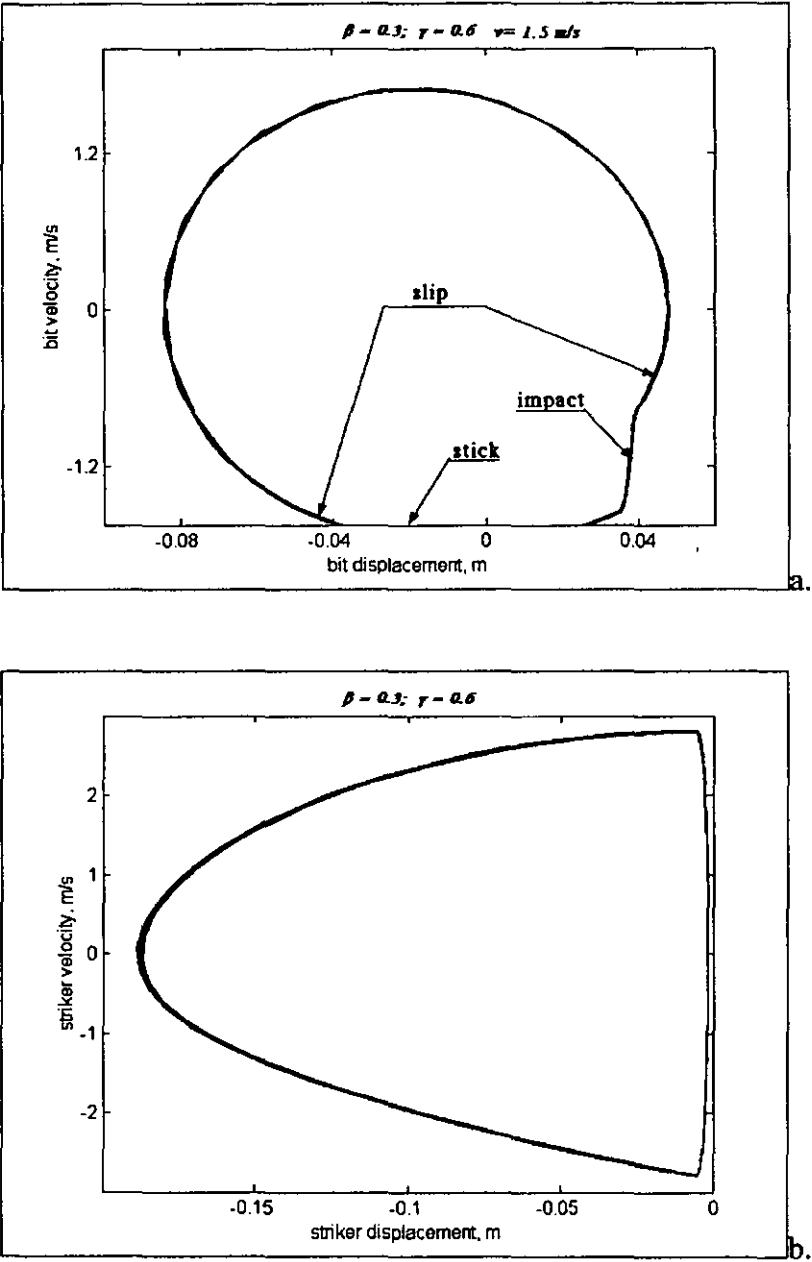


Figure 5.68: Phase portrait of striker and bit motion for $\beta= 0.3$ and $\gamma=0.6$

It is observed from Figure 5.67 (a) and (b) that for a given system configuration, it is possible to control the location of the impact within a cycle by varying the driving velocity. However, such a control is achievable only when the velocity of the bit is falling because on the ascendant part of the bit velocity, the impact introduces irregular (asynchronous) motion of the system. The striker velocity increases with any increase in driving velocity. This is seen in Figure 5.67b, where the change of the impact velocity reaches 6m/s. Figure 5.68 shows the phase portrait of the bit (a) and striker motion (b). In Figure 5.68a, the three phases of the bit motion, namely stick, slip and impact are noticeable and are shown with arrows. Figure 5.69 illustrates the time history of the motion of the striker with the frequency response. It was observed that the variation of frequency ratio mainly affects the striker motion. For this particular interval of frequency ratio, the bit kept to a steady stable periodic process.

With the increase of frequency ratio, the impact velocity decreases. This is illustrated in Figure 5.70, where the change in the velocity of the striker is 3.8m/s. This is because the striker at its maximum displacement stops accelerating (zero acceleration for 35ms in this case) or begins making additional oscillations. The configuration of the system is given in Table 5.6

Table 5.6

Parameter	Numerical values
Driving velocity, m/s	$v = 1.5$
Mass, kg	$m_1 = 250$
Stiffness, N/m	$k_1 = 625000$
Viscous damping, N.s/m	$c_2 = 250$
Ratio	$\beta = 0.4; \gamma = 0.8$

Figure 5.71 shows the phase plot of the motion of the bit and the striker respectively; mass ratio $\beta = 0.4$ and frequency ratio $\gamma = 0.8$. In the striker phase plane (Figure 5.71b), the velocity changes rapidly with an instantaneous transition from negative to positive values. Other results for $\gamma \in [0.6 \ 0.8]$ showed a smooth

transition. For further increase of frequency ratio, the striker will perform an additional loop close to zero velocity.

Figure 5.72 gives a typical synchronised motion of the system. The response of the bit is shown in Figure 5.72a where the displacement, the velocity and the acceleration are depicted over time. In this picture, all specific aspects of the bit motion are illustrated. It is seen that the main feature of frictional vibration (sticking) occurs when the bit reaches zero acceleration. The duration of the sticking phase (bit at zero acceleration) is shown with two dotted lines. Figure 5.72b shows the motion of the striker together with its velocity and acceleration. The striker performs a periodic motion with a single impact per cycle.

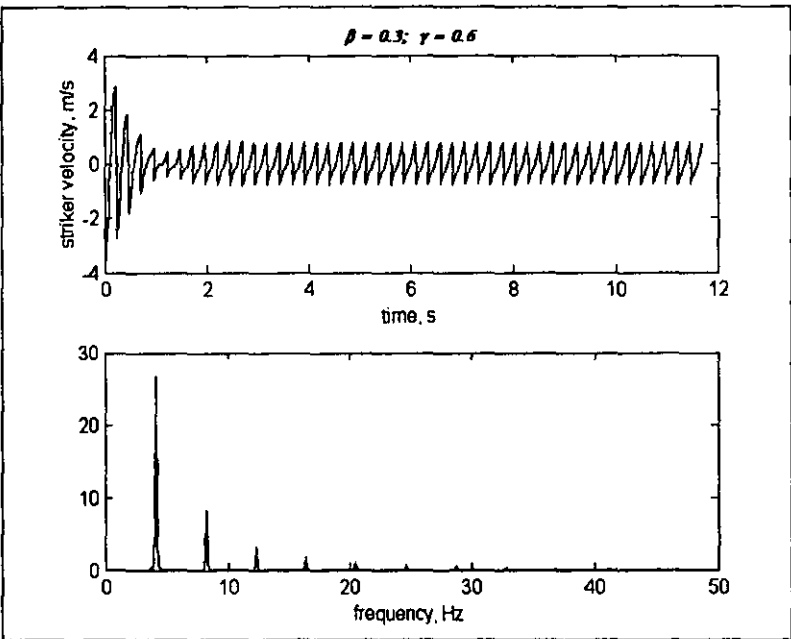


Figure 5.69: Time history of striker motion with its frequency response

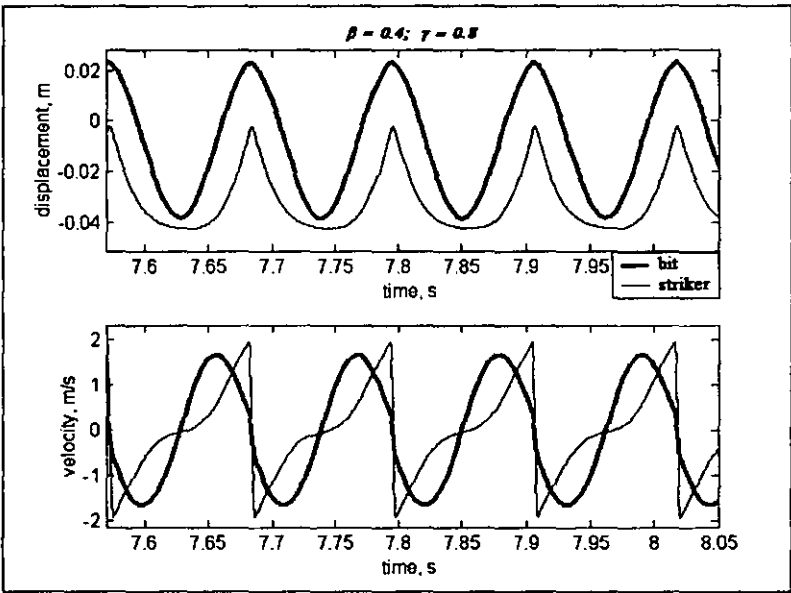


Figure 5.70: Displacement and velocity of bit and striker for $\beta=0.4; \gamma=0.8$

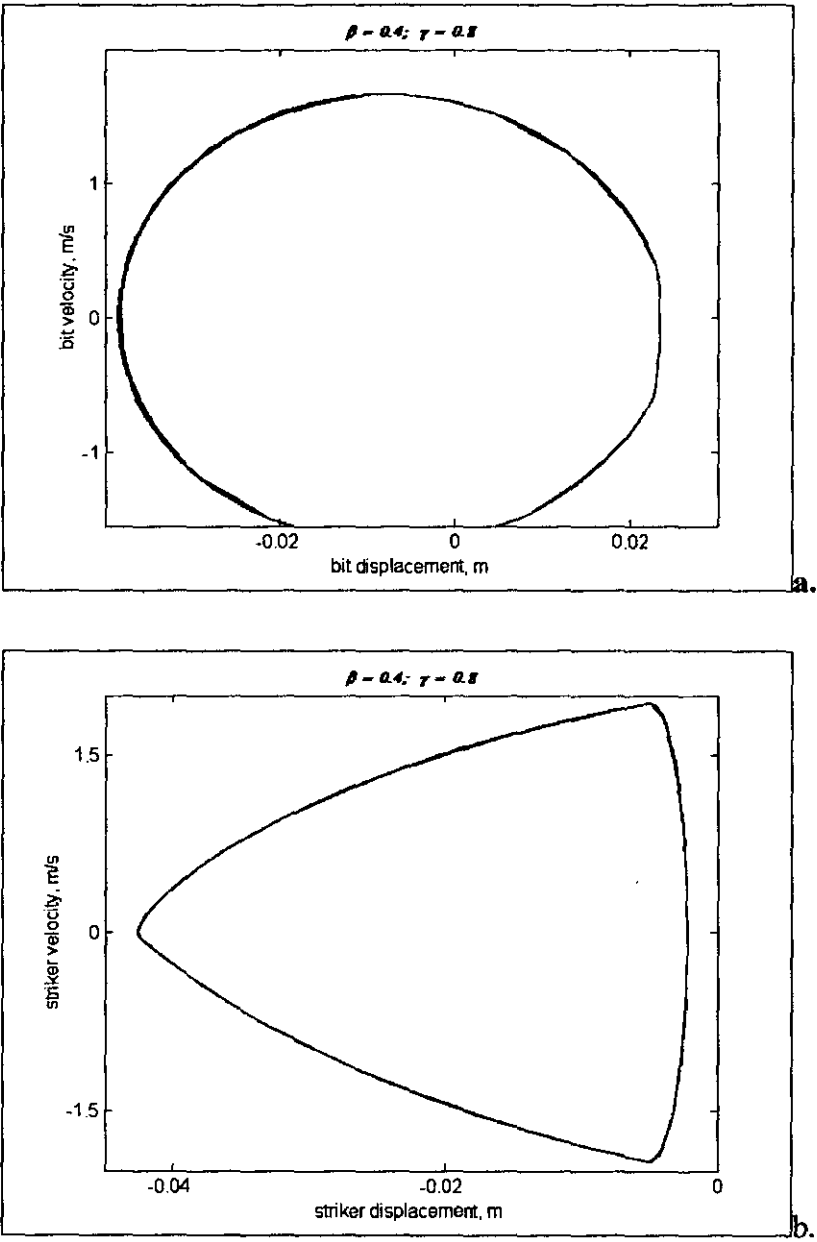


Figure 5.71: Phase portrait of bit and striker motion for $\beta= 0.4$ and $\gamma=0.8$

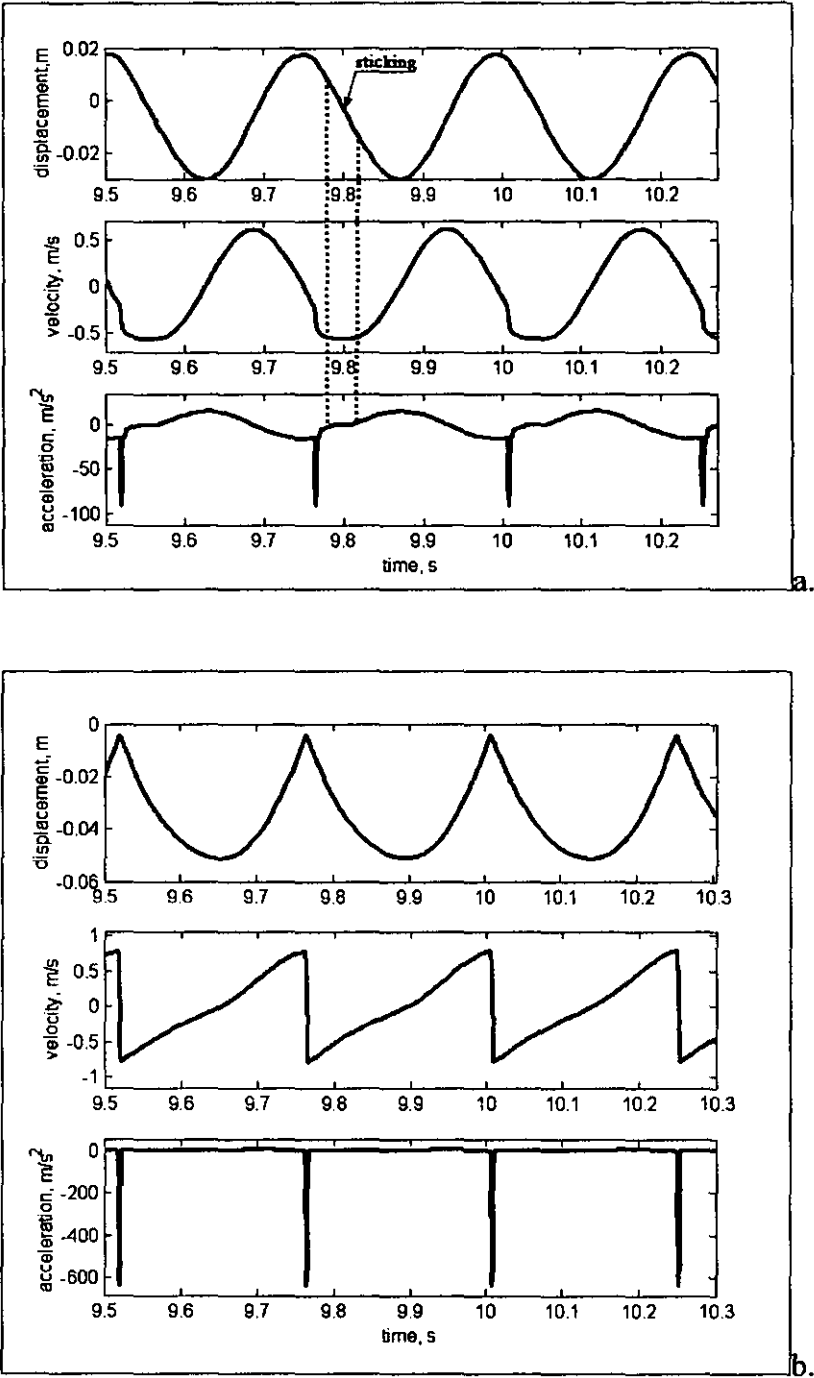


Figure 5.72: Typical motion of the system

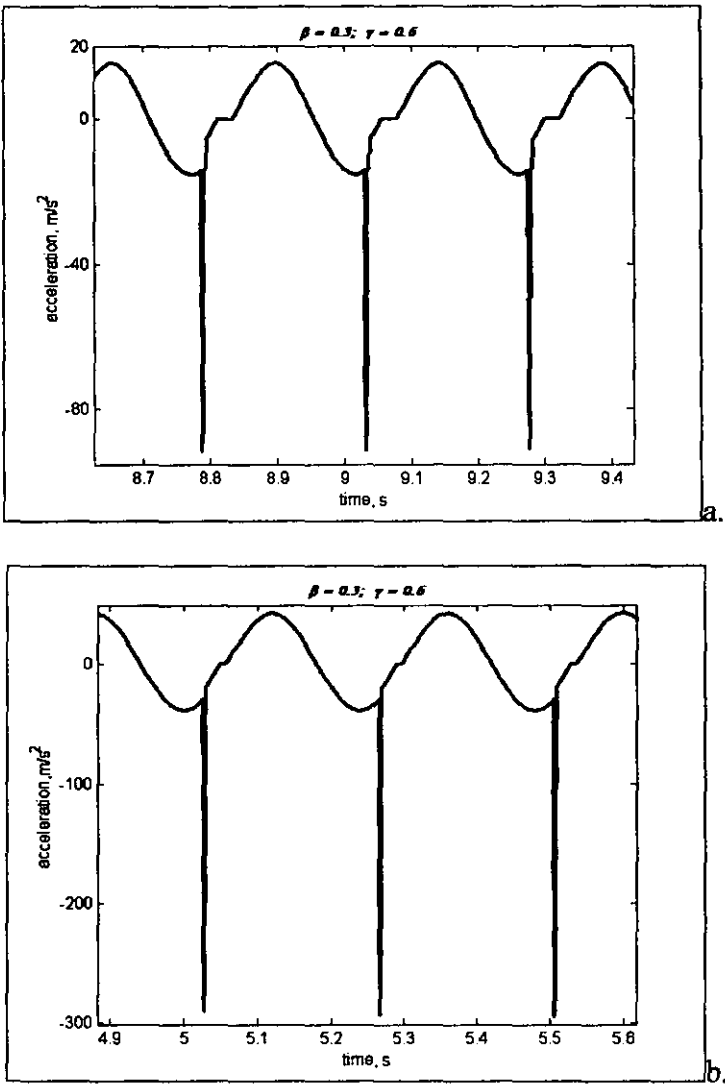


Figure 5.73: Typical bit acceleration; a.- $v=0.5\text{m/s}$; b.- $v=1.5\text{m/s}$

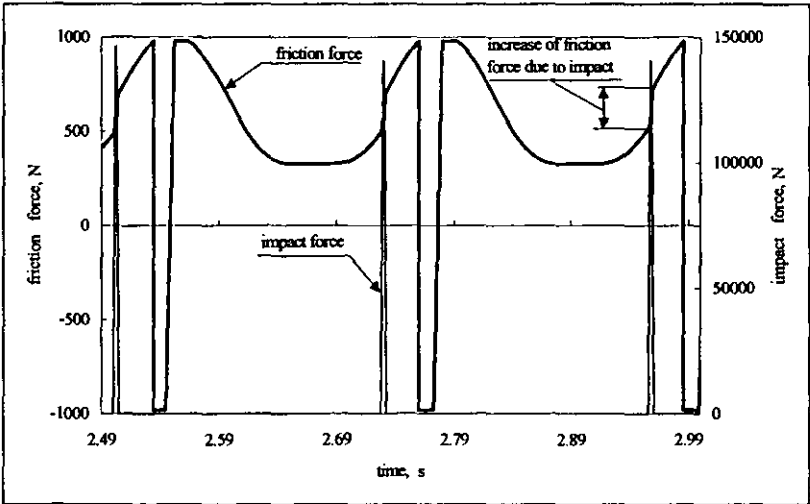


Figure 5.74: Typical impact and friction force.

Figure 5.73 shows a typical acceleration of the bit. It was observed that for a given configuration, the duration for which the bit stays at zero acceleration decreases with any increase in the driving velocity v . This is seen in Figure 5.73a where $v=0.5\text{m/s}$, and in Figure 5.73b where $v=1.5\text{m/s}$. This does not affect the bit response frequency as the damping effect of dry friction has little influence on the system frequency response. However, with the increase of driving velocity, the velocity of the bit increases, and consequently, the impact velocity increases. This is because at high driving velocities, the striker is promptly excited. As a result it obtains a large amplitude of velocity leading to a considerable rise in acceleration.

In Figure 5.74, a typical impact force is illustrated together with the friction force. This picture shows the stepwise increase of the friction force at the instant of impact. In this investigation the value of the dry friction coefficient was taken as $\mu=0.4$. This gives a static friction force of 981N for bit mass $m_I=250\text{kg}$ and $g=9.81\text{m/s}^2$ (gravitational acceleration).

The magnitude of the impact force depends on the driving velocity v , the velocity of the striker \dot{x}_2 , the contact stiffness k_0 and the gap between the striker and the bit. It was assumed that the contact surfaces of the bit and the striker are specially heat-treated to provide the desired stiffness. Table 5.7 shows the configuration of the system for which the results in Figure 5.74 were obtained.

Table 5.7

Parameter	Numerical values
Driving velocity, m/s	$v = 1.5$
Mass, kg	$m_I = 250$
Stiffness, N/m	$k_I = 156250$ $k_0 = 50\text{MN/m}$
Viscous damping, N.s/m	$c_2 = 250$ $C_0 = 0.1$
Gap, m	$\Delta = 0.005$
Ratio	$\beta = 0.4; \gamma = 0.75$

6.2.3 REMARKS

For a frequency ratio between 0.6 and 0.8, the response of the system and its performance is adequate for practical applications. The values 0.6 and 0.8 are seen to be boundary values because the response of the system is critical and for high driving velocities, the dynamic behaviour of the system is quite near to the response of neighbouring intervals.

6.2.4 SYSTEM RESPONSE FOR $\gamma > 0.8$

For values of $\gamma > 0.8$, the system becomes very sensitive, especially the striker; solutions, though periodic, do not always converge. All frequency ratios between 0.8 and 0.9 are seen as transitional values because the solutions of the system converge in a single limit cycle. However, the striker begins to deviate from its trajectory, performing additional undesired motion. For any frequency ratio greater than 0.9, the system becomes unstable.

Figure 5.75 shows the phase plane of the motion of the bit (a) and the striker (b). Both the striker and bit display a single limit cycle. However, after impact, the striker performs an undesired oscillation, see Figure 5.75b. The displacement and the velocity profiles are illustrated in Figure 5.75c. The velocity of the striker drops in the middle of the cycle, initiating a period doubling. This is seen in the frequency profile of the striker in Figure 5.76 that shows the phase portrait of the bit and the striker together with the frequency response of the striker. For this configuration, the calculated synchronisation frequency was 4.9Hz (no impact) and the value obtained from simulation was 4.6Hz. However, in the frequency spectrum of the striker, 4.6Hz and 9.3Hz were observed with 9.3Hz being dominant. This effect becomes strong when the striker is either too light or too heavy. This aspect is covered in the next section.

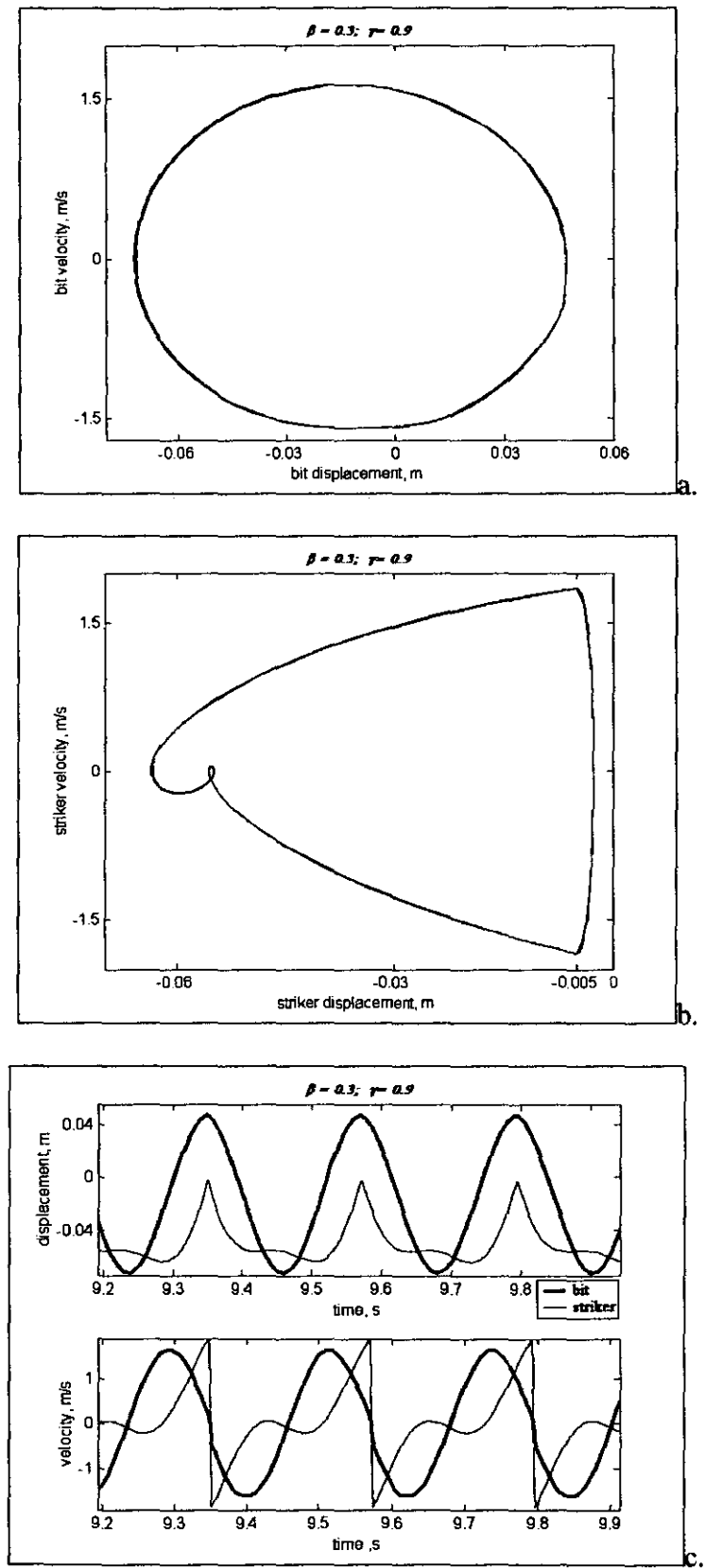


Figure 5.75: Phase portrait of striker and bit motion for $\beta=0.3$ and $\gamma=0.9$ and velocity profile

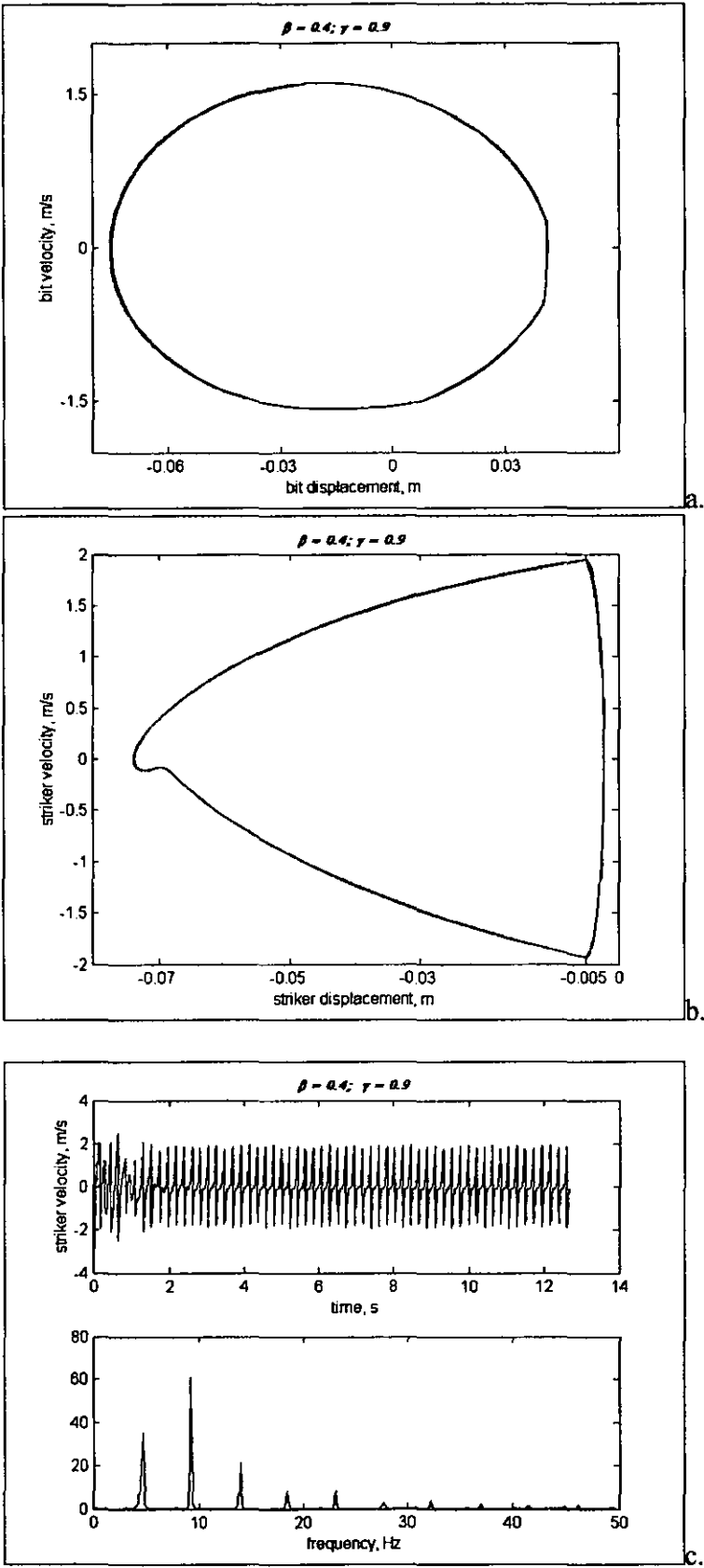


Figure 5.76: Phase portrait of striker and bit motion for $\beta=0.4$ and $\gamma=0.9$ and frequency profile

Table 5.8 gives the numerical values of the parameters of the system for the results shown in figures 5.75 and 5.76.

Table 5.8

Parameter	Numerical values
Driving velocity, m/s	$v = 1.5$
Mass, kg	$m_I = 250$
Stiffness, N/m	$k_I = 156250$ $k_0 = 50\text{MN/m}$
Viscous damping, N.s/m	$c_2 = 250$ $C_0 = 0.1$
Gap, m	$\Delta = 0.005$
Ratio	$\beta = 0.3, 0.4; \gamma = 0.9$

As the frequency ratio increases, the lowering of the striker increases until the striker begins to perform multiple impacts. This process is shown in Figure 5.77 for $\beta = 0.4$. Figure 5.77b shows a stable steady state motion of the striker performing alternately single and double impacts per cycle. In Figure 5.77c, the striker executes intermittently, single impact, double impacts; single impact, triple impacts and so on. Due to the irregularity in the motion of the system with an increase of frequency ratio, impact force decreases because of reduced impact velocities. For $\gamma > 1.0$, the impact force is between 10 and 70kN; more results are given in appendix 5-6. Inconsistency of impact force per cycle reduces the productivity of the system. In the case of alternate single with double impacts, the effectiveness of the structure is lowered by half; in the case of single, double and triple impacts the efficiency is reduced by two thirds because the force of double and triple impacts is not sufficient to produce the desired work.

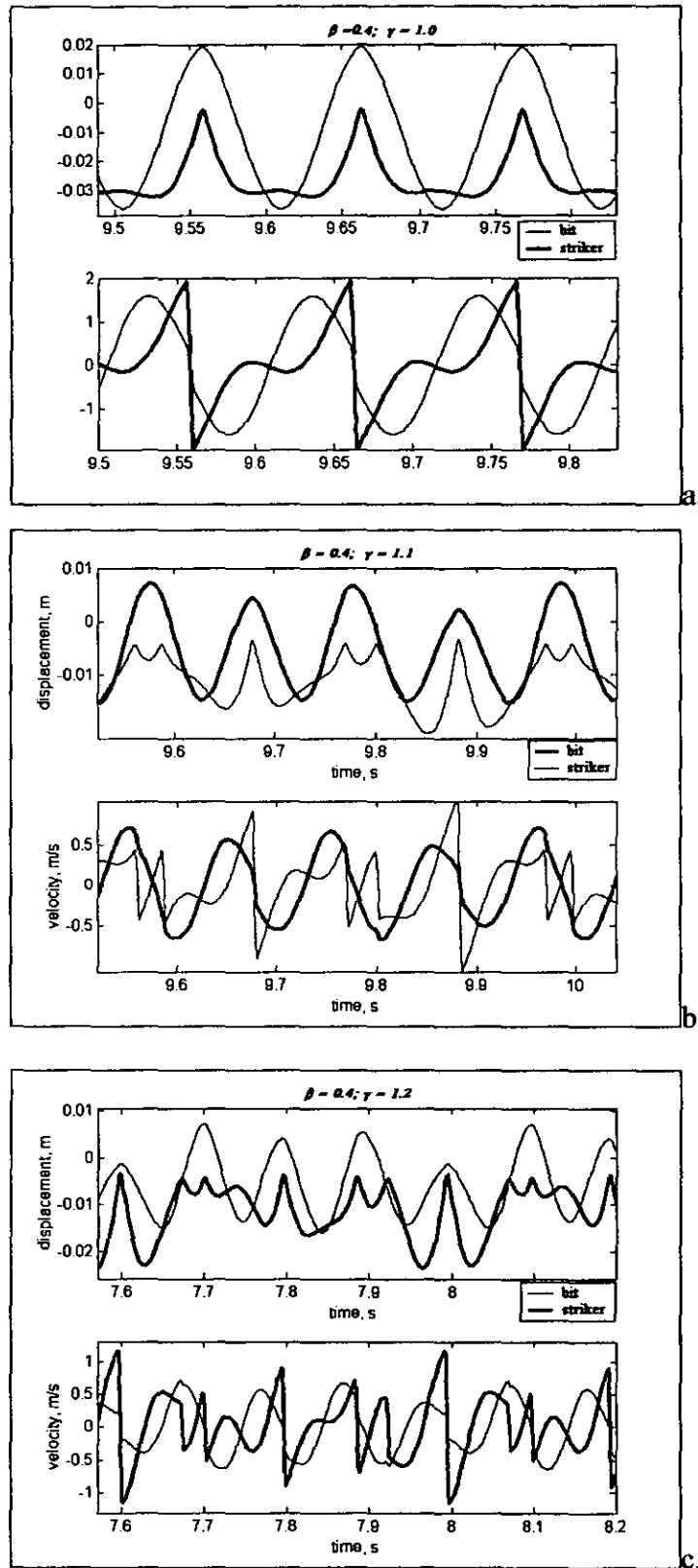


Figure 5.77: Displacement and velocity profile for $\beta=0.4$
a.- $\gamma=1.0$; b.- $\gamma=1.1$; c.- $\gamma=1.2$

6.3 Influence of Mass Ratio on the System in Vibro-Impact Motion

In impact motion, the mass ratio β is of great importance in obtaining a stable periodic vibro-impact process where the solutions converge in a single limit cycle. The mass ratio introduces divergence into solutions of the system if other parameters are not well correlated. The study in this section is divided into four areas depending on the response of the system to different values of β . Stable and unstable behaviour was observed, and this includes bifurcation. In the previous section, the region of steady state periodic motion with stable single impact per cycle was found to be between 0.6 and 0.8. Within these limits, a value of $\gamma = 0.75$ was chosen and adhered to whilst exploring in this section the effect of variation in the mass ratio on the response of the system.

Table 5. 9

Parameter	Numerical values
Driving velocity, m/s	$v = 1.5$ (unless specified)
Mass, kg	$m_1 = 250$
Stiffness, N/m	$k_1 = 156250$ $k_0 = 50\text{MN/m}$
Viscous damping, Ns/m	$c_2 = 250$ (unless specified) $C_0 = 0.1$
Gap, m	$\Delta = 0.005$
Ratio	$\gamma = 0.75$; $\beta = \text{variable}$

6.3.1 SYSTEM RESPONSE FOR $\beta \in [0.1, 0.25]$

For a mass ratio in the range of 0.1 to 0.25, the striker seems to be too light and in between impacts, it performs additional oscillations. Depending on the configuration of the system, the phase plane of the striker displays additional oscillation before the striker reaches its maximum displacement. Figure 5.78 shows the phase portrait of the motion of the bit (a) and the striker (b).

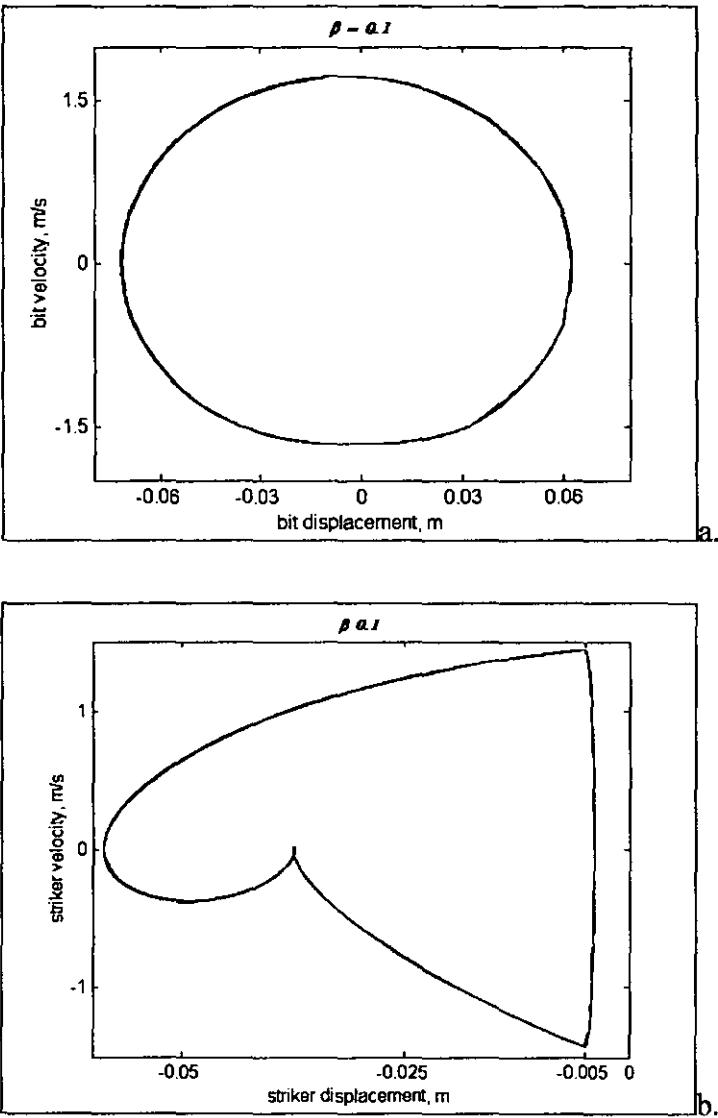


Figure 5.78: Phase plot of bit and striker motion for $\beta = 0.1$

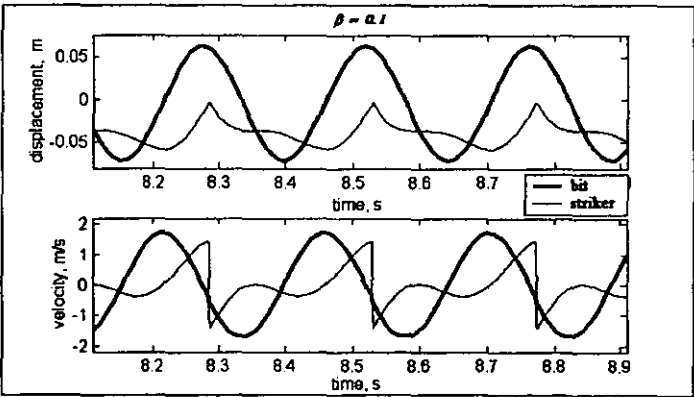


Figure 5.79: System displacement and velocity profiles for $\beta = 0.1$

Similar behaviour was observed previously when investigating the effect of frequency ratio. In Figure 5.78a, it is seen that the impact is very weak because the striker is light and it performs an unnecessary additional oscillation during the first half-cycle following impact. Consequently, the striker develops relatively small velocities. In Figure 5.79 the displacement and the velocity profiles are shown. Typical of this behaviour, the striker displays a downward motion in the middle of the cycle causing a reduction of the change in striker velocity.

6.3.2 SYSTEM RESPONSE FOR $\beta \in [0.25, 0.6]$

Studies of mass ratio between 0.25 and 0.6 confirmed the results obtained in previous sections with frequency ratio between 0.6 and 0.8. The system in a steady state motion showed a stable periodic motion with a single impact per period. In general for values of $\beta < 1$, any variation in the mass ratio does not affect system performance in terms of frequency response. However, the striker response is sensitive to changes in mass ratio. Therefore, only the phase plot of the striker is illustrated in this section. More simulation results are given in appendix 5-7. Figure 5.80 illustrates the phase plane of striker motion. Observation shows that with an increase in mass ratio, the amplitude of the striker oscillation increases. The stiffness of spring 3 controls the total swing of the striker. The amplitude of the swing decreases with the increase of stiffness k_1 but the impact force increases. The system is more efficient with a small swing of the striker because the response frequency increases with the increase of stiffness k_1 . Using this interval of values for β , the system gives an optimal performance provided that a value of frequency ratio is chosen between 0.6 and 0.8.

6.3.3 SYSTEM RESPONSE FOR $\beta \in [0.7, 1]$

For this range of values of β , the solutions of the system are periodic but the system is sensitive. This behaviour is illustrated in Figure 5.81, showing the phase portrait of the bit (a) and the striker (b). It is observed in Figure 5.82b, (where the velocity of the bit is shown) that there is no sticking phase because the system develops a small velocity which does not reach zero sliding velocity. The system becomes sensitive to the amount of damping. Reducing the amount of damping results in stable periodic motion with a single impact per cycle. The total amount of damping in the system should be less than or equal to 25 percent of the amount used for $\beta \leq 0.6$. Results obtained after such adjustment are given in appendix 5-7.

6.3.4 SYSTEM RESPONSE FOR $\beta \geq 1.0$

For $\beta = 1.0$, solutions are periodic with a single impact per cycle but the system is unstable. No stabilisation occurs and the amplitude of oscillation slowly but continuously increases. This is illustrated in Figure 5.83 where the displacement and velocities profiles (a) show that the amplitude creeps up over time. In Figure 5.83b, a slope is observed in the envelope of the signal, though both the striker and the bit vibrate at the synchronised frequency.

For $\beta = 1.2$ the system responded at various frequencies which were different from those obtained with equations 5.16 and 5.17. As shown in Figure 5.84, neither periodic nor synchronised motion was obtained. Varying driving speed and the amount of damping in the system did not bring system behaviour under successful control. This is because the striker is heavier than the bit and imparts very strong blows, which disrupt the motion of the bit. Although the bit is the exciter, its power is not enough to overcome the inertia of the driven striker.

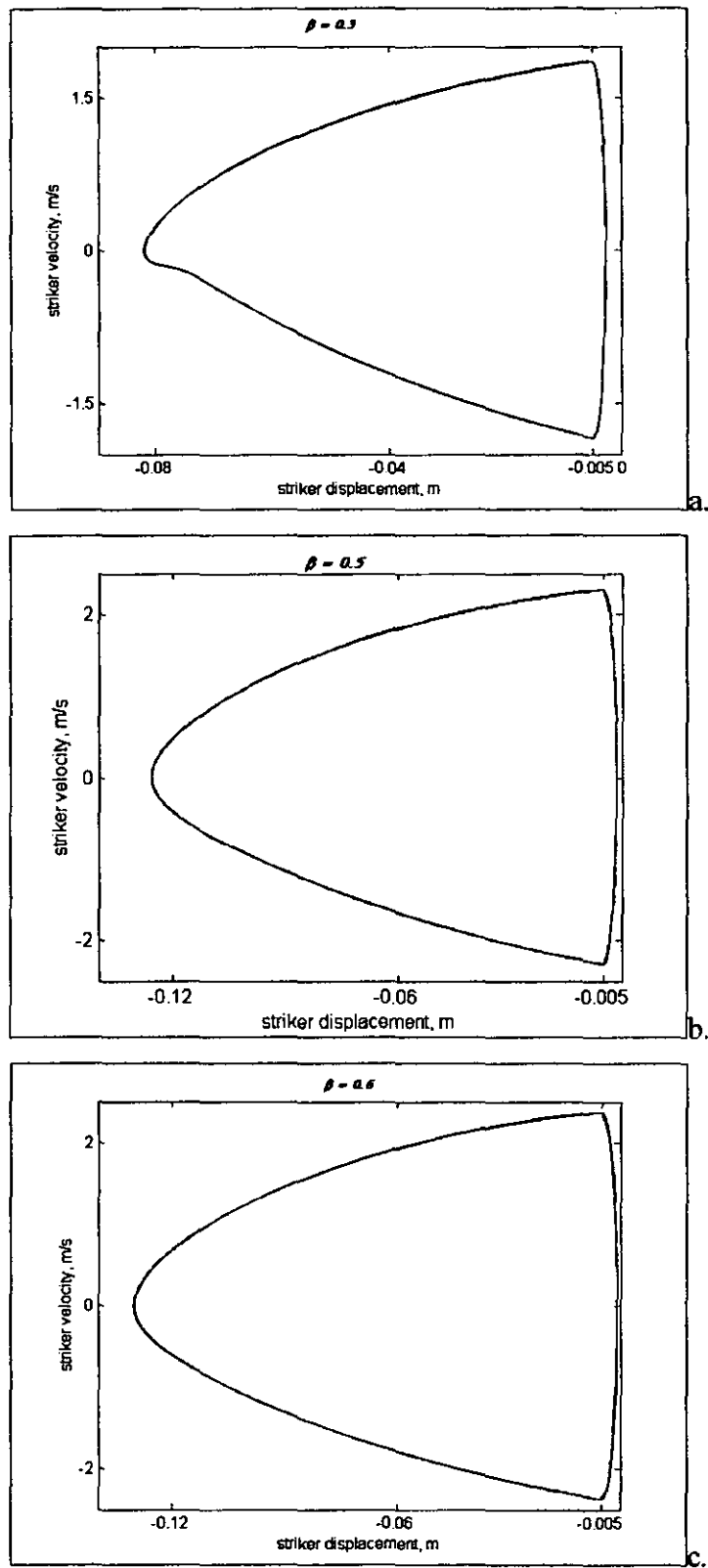


Figure 5.80: Phase portrait of striker motion for $\beta = 0.25, 0.5$ and 0.6

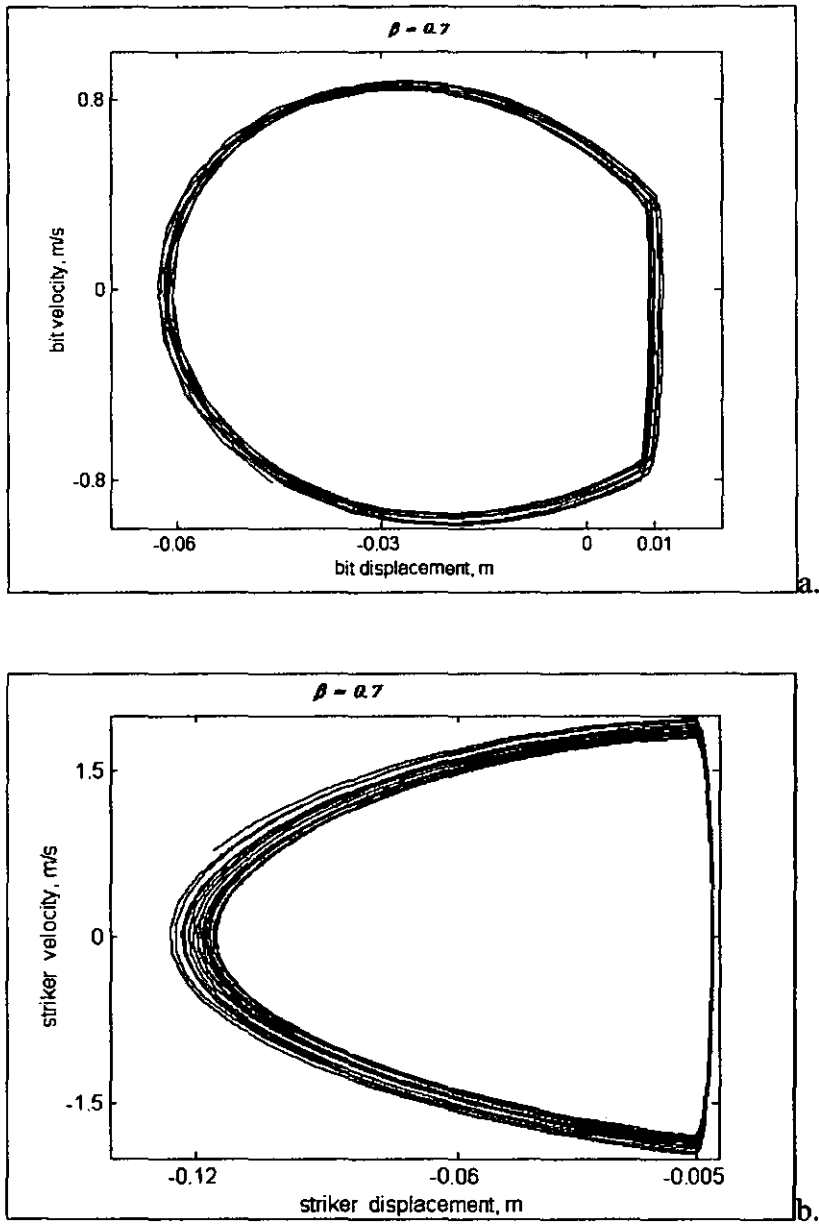


Figure 5.81: Phase plane of striker and bit motion for $\beta = 0.7$

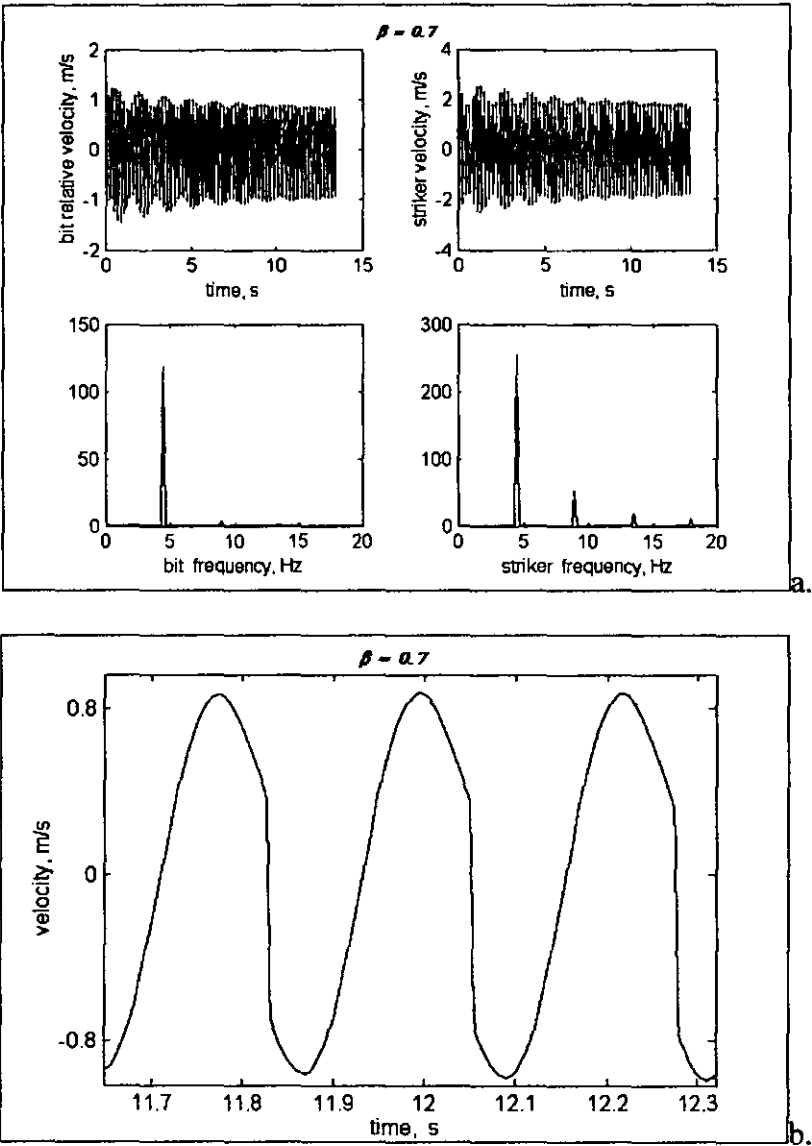


Figure 5.82: System frequency response (a) and velocity profile (b)

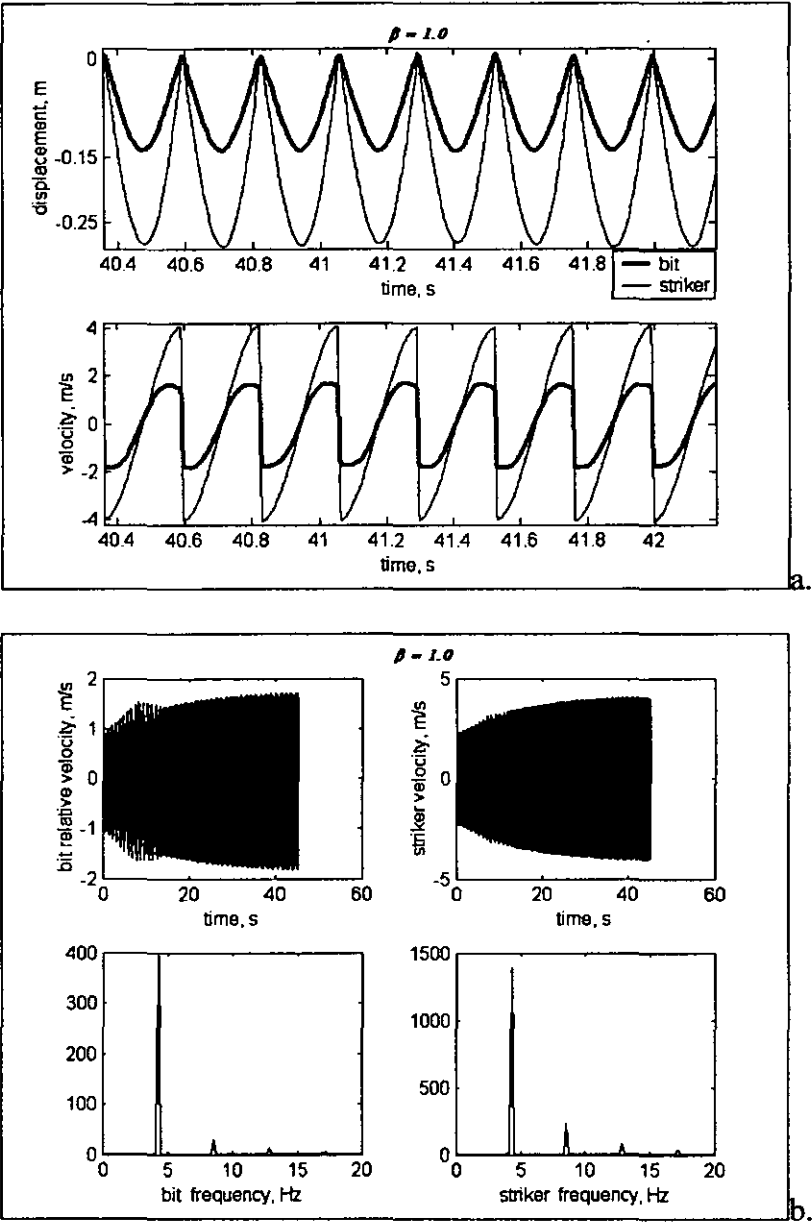


Figure 5.83: System response for $\beta=1.0$

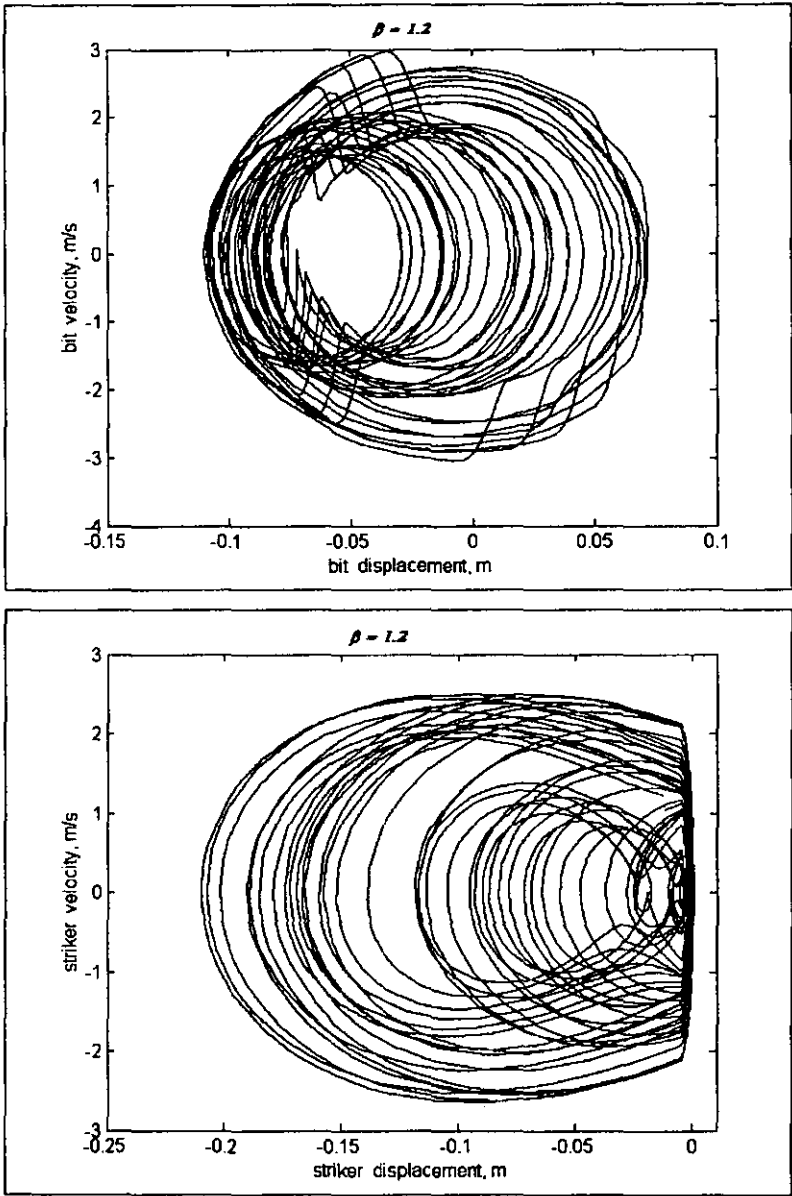


Figure 5.84: Response of the system for $\beta=1.2$

Also, for the given frequency ratio (0.65, 0.8), spring 6 seems too soft to drive the striker. With this observation, the frequency ratio was increased to 1 and a stable steady state periodic motion was obtained with single impact per period. The results for $\beta=1.2$ and $\gamma=1.0$ are shown in appendix 5.7.

6.3.5 REMARKS

Investigation of the influence of mass ratio on the response of the system has shown that for $\beta < 0.25$ solutions are not stable and the system may display bifurcation properties. The range of values from 0.25 to 0.6 is of interest in engineering practice of vibro-impact systems. A stable vibro-impact process was obtained within this range. It was shown that for $\beta > 0.6$, it is possible to configure the system so that it performs synchronised vibro-impact motion.

7. DISCUSSION

This study of the proposed rock drilling system has shown that the dynamic response varies depending on the system configuration. Mass and frequency ratio are the main parameters strongly affecting the dynamic behaviour of the system. Within the frame of values used in this investigation, driving velocity and damping had a moderate effect on the system response. If vibration frequency increases, to reduce settling time, low driving velocity and a small amount of damping are recommended. Bifurcation properties appeared for a mass ratio less than 0.25 and a frequency ratio greater than 0.9. The structure developed a stable vibro-impact process for $\beta \in [0.25, 0.6]$ and $\gamma \in [0.6, 0.8]$. These intervals of values for β and γ define the region of best performance of the system. Within these intervals are the values which appropriate for practical engineering applications.

The results obtained are of theoretical, practical and engineering significance. The theory of bifurcation in smooth dynamic systems is well established, whereas bifurcation of non-smooth systems is still attracting researchers. On the mathematical front, further discontinuous bifurcation analysis could be carried out (see recommendation for future work). However, within the framework of this project, the obtained intervals for achieving a stable vibro-impact regime brings into engineering practice a new concept of a mechanical device that changes the perception of friction in drilling technology. The system developed in this study effectively uses and exploits friction. This is unique because in most systems, especially in drilling efforts are made to reduce friction.

Chapter 6
VIBRO-IMPACT PENETRATION
OF THE SELF-EXCITING DRILL BIT

VIBRO-IMPACT PENETRATION OF A SELF-EXCITING DRILL BIT

1. INTRODUCTION

In chapter 5, the synchronisation parameters and the conditions of stable periodic motion with single impact per cycle were described. The force of impact of the striker on the bit is used in this chapter to estimate the rate of penetration. The physical properties of the rocks obtained experimentally in chapter 4 are used as basic values in the study of tool medium interaction. A visco-elasto-plastic model of the media is used and the system response is studied numerically, first as a forced vibration, and second as a result of a self-exciting vibro-impact process.

2. EARLY VIBRO-IMPACT PENETRATION CONCEPTS

Early models of vibro-impact penetration of a tool into a medium were introduced by Tsaplin, (1953). He assumed an instantaneous impact force; the velocities before and after impact were related through a restitution coefficient. Later, Tsaplin introduced a depth dependency factor by gradually increasing the mass of the driven element as it moves into the medium. Neimark, (1953) and Blekhman, (1954) who made the initial theoretical analysis of vibro-penetration process. The practical application of vibration and vibro-impact methods of penetration into different media became more widespread due to the works of Barkan, (1959) Savinov et al, (1960) and Tseitlin et al, (1987).

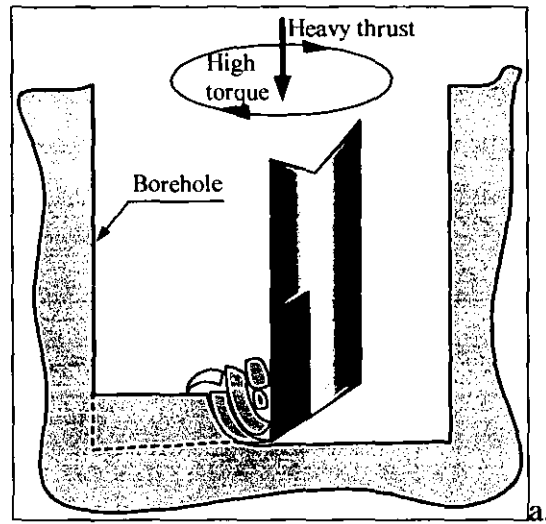
Two models of the indenter-footing resistance were mainly used to interpret the primary experimental data. In the purely plastic model, (Savinov et al, 1960 and Azbel et, 1981) the resistance was presented as a weightless plug held in the borehole by a permanent force. The advance of the plug is possible when the sum

of the applied forces exceeds the resistance force. Under these circumstances, the plug followed the movement of the indenter.

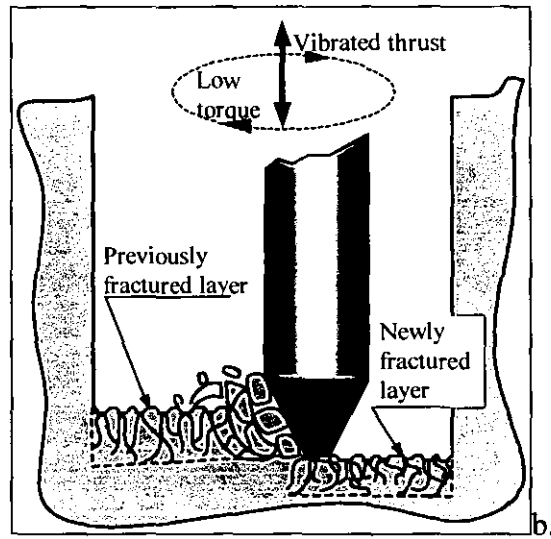
An elasto-plastic model, known as the Prandtl model, took into consideration the elasticity of the medium by adding an ideal spring between the indenter and plug (Savinov et al, 1960 and Azbel et, 1981). In this model, the movement of the plug is only possible when the elastic force of the spring exceeds the resistance of the medium. More complex rheological models of the medium were also used by Savinov, (1960) Azbel et al, (1981), Spektor, (1981 and 1983) and Neilson et al, (1995).

3. THE PERCUSSIVE-ROTARY DRILLING

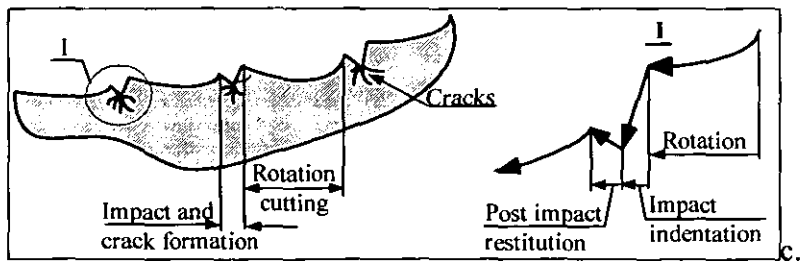
In percussive-rotary drilling, the tool moves into the medium by an impact-scratching action and inherently removes cuttings. This allows the use of a simplified model of the medium to estimate the rate of penetration due to impact. In contrast in conventional rotary drilling, the cuttings are moved by shear action and this is shown in Figure 6.1a for the case of a drag bit. An approximate principle of percussive-rotary drilling is illustrated in Figure 6.1b. It is seen that rotary drilling requires high torque to shear an intact rock formation, whereas in percussive-rotary drilling, the impact generates a multitude of cracks which aids the rotary cutting action. Consequently, percussive-rotary drilling requires less torque as it cuts the pre-fractured layer of rock. The depth at which the cracks propagate depends on the magnitude of impact force, on the compressive strength and on the characteristics of the rock. Figure 6.1c shows the cutting action of percussive-rotary drilling. The process of cutting is made up of a succession of rotation-impact-rotation-impacts (see Figure 6.1c left). Three phases are observed in this process. During rotation cutting (the rotation phase), a blow is imparted to the bit. In the contact zone, a zone of high pressure is formed. The instantaneous build up pressure exceeds the yield point of the rock and the zone of high pressure is pulverised; the tool tip dips into the rock and cracks are formed (the impact indentation phase). This phase is followed by a small restitution phase (see Figure 6.1c right). Restitution is characterised by the elastic properties of the medium which always exists to some extent. Within this phase, the tool moves elastically upwards and may bounce, leaving a crater on the surface. Rotation cutting follows this phase and the whole cycle is repeated.



Conventional rotary



Percussive-rotary



Phases of vibro-impact cutting

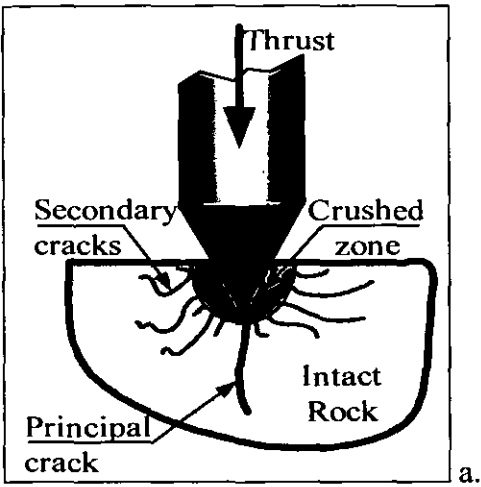
Figure 6.1: Principles of cutting in Drilling

In conventional rotary drilling, the rate of penetration depends mainly on the heavy weight on the bit which must exceed the frontal resistance of the rock. In percussive-rotary drilling, in addition to this dependency, each imparted blow generates cracks which weaken the surface layer and pushes the bit to penetrate further into the rock. With the application of vibration, less thrust is required as the impact force greatly exceeds the frontal resistance of the rock. This gives a definite practical advantage for percussive-rotary over conventional rotary drilling.

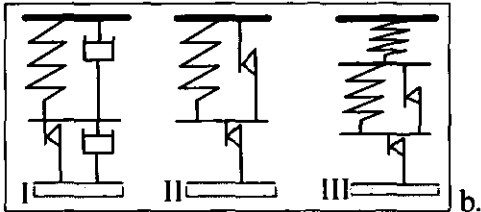
3.1 Description of the Model of Impact Penetration

There exist several views on how a rock fails under the action of a cutter. Figure 6.2a shows a rock fracture pattern caused by the indentation of a sharp tool into a rock formation. Straight beneath the tool where the pressure is extremely high, the rock is highly fractured into fine chips. The area of fine chip around the tool tip with is called the “crushed zone”. Cracks radiate from the crushed zone and principal (primary) cracks are formed in line with the direction of the acting cutting force. Secondary cracks are generated from the crushed zone laterally to the main crack and flow towards the surface. In the fracture mode shown in Figure 6.2a the thrust is increased until the rock fails; therefore the layer underneath the tool tip is crushed and forms a clearly delimited crushed zone.

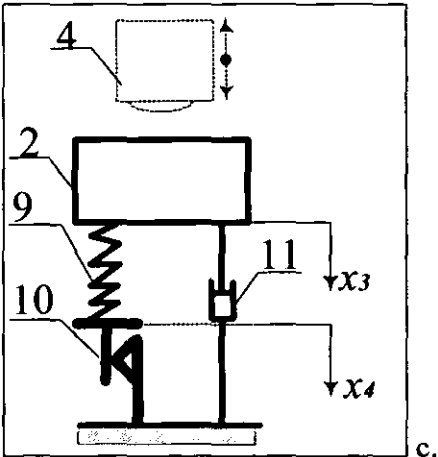
Studies of impact loading of a chisel and dropping masonry drill bits on granite and hard limestone has shown that chip formation is instantaneous and the crushed zone is difficult to observe. However, in sandstone, the crushed zone could be seen when chip formation was absent. Impact loading probably causes a mixed fracture of compressive and shear failure. The imparted blow sets an instantaneous impulse which generates extreme compressive stress exceeding rock yield point at the tip of the tool. This causes a compressive failure at the upper layer as the tool tip initiates its intrusion into the matter, creating chips by a shear action.



Rock fracture pattern due to wedge indentation



Typical rheological models of rocks



Model of vibro-impact penetration into rock medium

Figure 6.2: Rock fracture and rheological models

In general, rock fragmentation is treated as a discontinuous process of chip formation originating from the crushed zone by initiation and propagation of cracks. Depending on the shape of the tool, rock fragmentation may occur as tensile fracture or shear breakage. Tensile failure will mostly take place in hard rock when a tool with a large rake angle is used. A cutter with a small rake angle ($<10^\circ$, Göktan, 1990) can also produce a shear fracture in rocks.

In fracture mechanics, two basic chip formations are used, termed mode A and mode B by Déliac, (1988). In mode A, rock failure is predominantly shear and compressive fracture, thus chip formation can be modelled by the Coulomb criterion. Mode B produces tensile fracture, a specific outcome from using sharp tipped tools. Mode A is suitable for modelling the penetration in percussive rotary drilling.

Because rocks are produced in nature under different conditions, it is difficult to define a universal model which adequately reflects the mechanical behaviour of all rocks. Consequently, there exist a number of models mathematically describing the behaviour of rocks, (Savinov, 1960; Azbel et al, 1981 Rebrik, 1979; Spektor, 1981; Neilson et al, 1995; Palmov, 2000).

Figure 6.2b illustrates three basic rheological models used to describe mechanical properties of rocks in drilling. In model “I”, there is a mathematical and mechanical inconsistency caused by the top dashpot. A close look at this model suggests that at the instant when the dry friction element together with the lower dashpot slips downwards, the force in the upper dashpot is not determined. Thus, the upper dashpot works only during elastic oscillation but causes problems during actual penetration. Model “II” requires two yield points for the same medium. The identification of values for both frictional elements involves complex experimental work. The model illustrated in “III” describes the behaviour of soft rocks. Here, the identification of two elastic and two frictional elements necessitates more accurate experimental design which may be time consuming and costly. To avoid the aforementioned inconveniencies and to keep

all the main features of the medium's response, a simple classical model is used in this work.

Figure 6.2c illustrates schematically a model of vibro-impact penetration into a medium with visco-elasto-plastic features. This model is built upon considerations (after Rebrik, 1979 and Spektor, 1981) of the rheological behaviour of materials under vibration and impact loading. The frontal resistance of the medium is accounted for as elasto-plastic properties with viscous dissipation during the vibration of the bit. With reference to Figure 6.2c, the model consists of a spring 9, which is mounted in series with a dry friction element (plug) 10. A viscous element 11 is set parallel to the elasto-plastic element. The model provides a stepwise downward displacement of the bit provided the overall forces exceed the threshold of the force D .

The model works as follows: after a blow imparted by the striker 4 to the bit 2, the spring 9 and the dashpot 11 are deformed gradually due to the visco-elastic properties of the medium. If the overall force developed in the spring is less than the threshold force D , the medium produces visco-elastic resistance only. At this stage, the bit will oscillate about its current point of equilibrium defined by the position of the dry friction element. Whenever the force produced by the elastic element during the compression stage becomes equal or greater than the threshold force D , the footing resistance of the medium instantly changes its nature and becomes plastic. This transformation, however, does not change the instant position and velocity of the bit. This means that the downward movement of the bit and dry friction element continues further as a coupled rigid body motion under a permanent resistance force D and the force developed by viscous element until the bit's motion is held up. The downward displacement during this latter stage defines the rate of penetration of the drilling bit. The dry friction element slips only in the positive direction of x_4 .

After a full compression stage, ending with a plastic slip, the bit executes a backward motion (restitution stage) due to the accumulated elastic energy in the

medium corresponding to its yield point. The restitution process is carried out relative to the new position of equilibrium, shifted downward by the value of the plastic deformation. The nature of restitution is determined by the visco-elastic properties of the medium. Restitution is completed when the dynamic component of the contact force between the bit and the medium vanishes.

3.2 Equations of the System Motion

The equation of motion of the bit relative to its position of equilibrium $x_3 = 0$ associated with the current position x_4 of the dry friction element is defined as follows:

$$m_1 \ddot{x}_3 + c_3 \dot{x}_3 = -N + I \sum_{n=1}^{\infty} \delta(t - nT) \quad (6.1)$$

$$N = \begin{cases} k_3(x_3 - x_4) & \text{if } 0 < k_3(x_3 - x_4) < D \\ D & \text{if } k_3(x_3 - x_4) \geq D \\ 0 & \text{if } k_3(x_3 - x_4) < 0 \end{cases} \quad (6.2)$$

$$\dot{x}_4 = \begin{cases} \dot{x}_3 & \text{for } k_3(x_3 - x_4) \geq D \\ 0 & \text{for } k_3(x_3 - x_4) < D \end{cases} \quad (6.3)$$

In equations (6.1) and (6.2), m_1 and x_3 are the mass and the normal co-ordinate of the drill bit when the weight of the bit is equalised by the spring response. \dot{x}_3 and \ddot{x}_3 are the drill bit velocity and acceleration respectively. k_3 is a coefficient of medium elastic resistance to penetration; c_3 is the damping coefficient for the bit oscillation, x_4 is the co-ordinate of the dry friction element. \dot{x}_4 is its velocity and D the threshold force, at which the dry friction element slips downwards. I is the instantaneous impact impulse generated by the striker; $\delta(t)$ is the Dirac delta function. T is the period at which the impacts occur; t is the time and $n=1, 2, 3, \dots$. It is assumed here that when the overall force of the spring exceeds D , the dry friction element instantly achieves the same velocity as the bit.

The analysis of the system is undertaken in two steps. In the first stage, the system in Figure 6.2c is subjected to different prescribed force excitations and its dynamic response is studied. In the second stage, the behaviour of the entire model of the self-exciting system is investigated. The latter model results from the interaction of the model in Figure 5.11 with the model in Figure 6.2c.

4. STUDY OF THE RESPONSE OF THE SYSTEM

The physical parameters of the medium were obtained by a UCS (Uniaxial Compressive Strength) test of rock samples, i.e. the threshold force D , the Young modulus and subsequently the stiffness. The results are given in Table 4.5.

The equations of motion of the system are solved in a similar fashion to those in chapter 5. To obtain numerical solutions of the system, a mathematical tool was developed from the MatLab-Simulink package. Equation (6.1) was integrated continuously, whereas conditions (6.2) and (6.3) were checked at each integration step.

Figure 6.3 shows the integration model in Simulink. Five sections are observed in Figure 6.3. Section (I) computes the solutions of equation (6.1), section (II) checks the conditions (6.2) and (6.3). Within this section, the slip of dry friction element 11 is identified with the help of a variable integrating step. The integration step is reduced to a possible minimum close to and during impact, allowing an accurate detection of any dislocation of the dry friction element. This phase is important for the estimation of the downward displacement of the entire system. Once this position is determined, the equilibrium position of the system is moved to this point and integration continues. Section (III) computes the average of the impact force applied over time. In section (IV), the amplitude of the bit oscillation is calculated as half of the total swing.

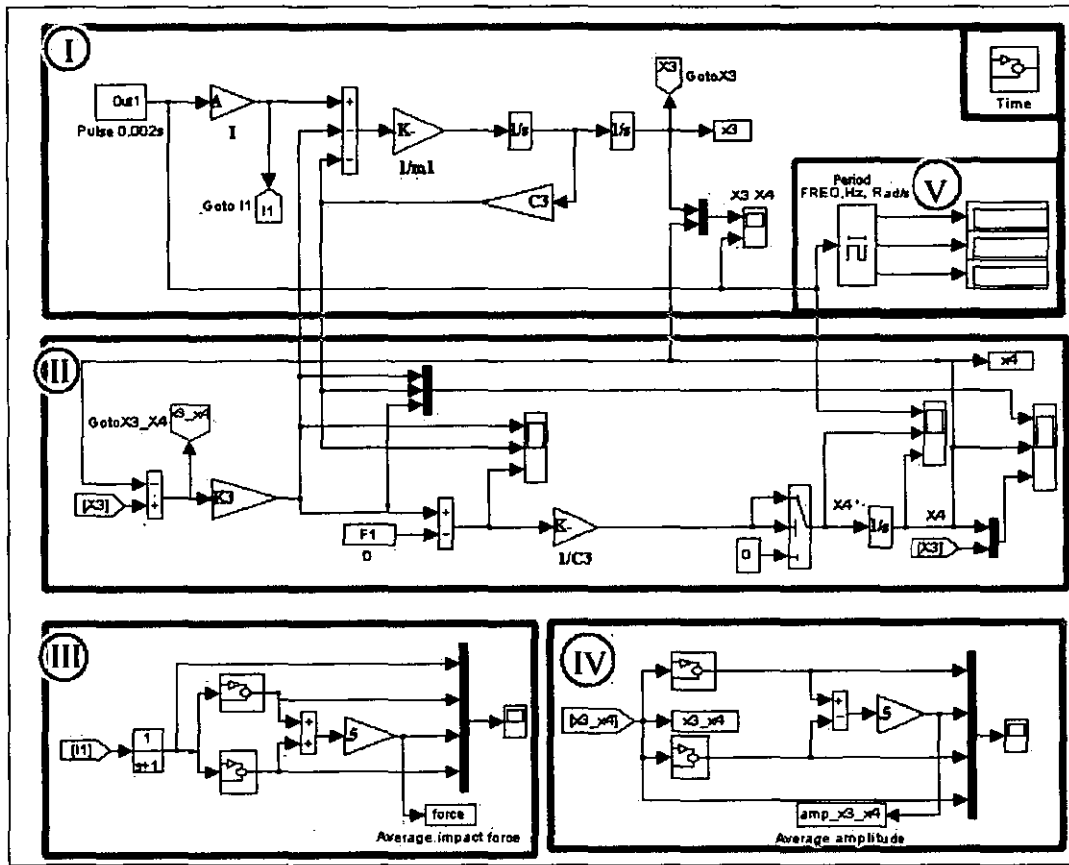


Figure 6.3: Model of penetration in Simulink

Section (V) evaluates the period of system motion (system frequency response). The input of this section can be connected to any part of the diagram to obtain the frequency response of the system.

The system was subjected firstly to a sweep sine test, secondly to periodic impact loading using pulses of variable frequency. Finally, it was subjected to the impact force generated from the main system shown in Figure 5.11.

4.1 Amplitude-Frequency Response with a Sweep-Sine Test

A sine wave excitation with increasing frequency was used to study the response of the system under a sweep test. In order to identify the resonant frequency, the sweep rate was set at 0.25Hz, 0.5Hz and 1Hz per second. The following short notations are introduced for this analysis: $\alpha_3 = \dot{x}_3$ and $\psi_3 = x_3 - x_4$; where α_3 is the velocity of the bit relative to the medium and ψ_3 is the displacement of the bit with reference to the current position of the dry friction element.

Figure 6.4 illustrates the amplitude-frequency response of the system shown in Figure 6.2c under a sweep-sine test. The thin line curve displays the amplitude of the displacement and the thick curve shows the amplitude of bit velocity as the frequency of excitation increases. The amplitude of the velocity of the bit and the corresponding amplitude of the displacement of the dry friction element are illustrated in Figure 6.5. It is observed that after resonance, any further increase of the frequency does not produce slippage of the dry friction element. This is because with an increase in driving frequency, the time between successive impulses becomes very short and the average constant force due to the impulses increases. This gradually compresses the bit against the medium and the amplitude of oscillation decays. Consequently, the force developed in spring k_3 is very small compared to the yield of the rock, thus slippage does not occur.

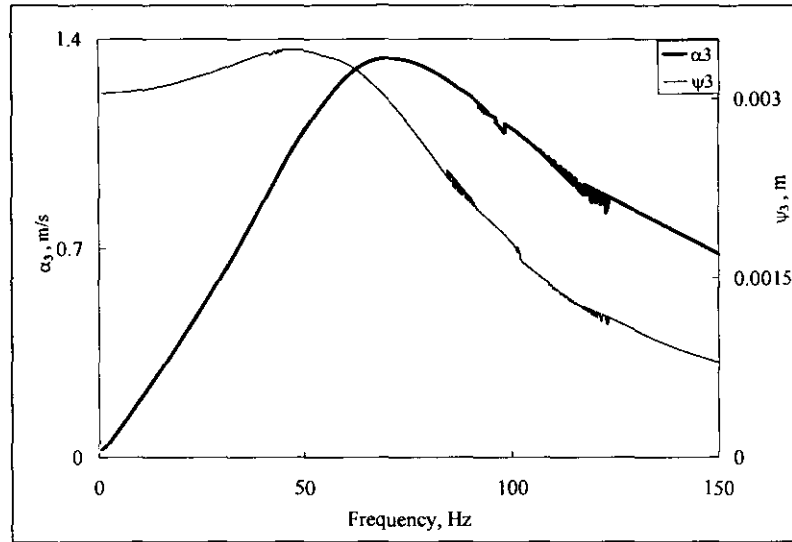


Figure 6.4: Amplitude frequency response of the system

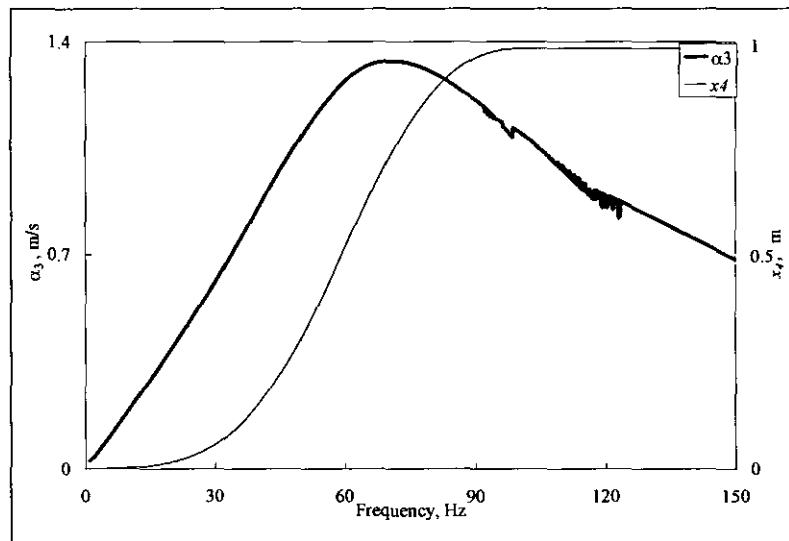


Figure 6.5: Velocity of vibration and displacement of the dry friction element

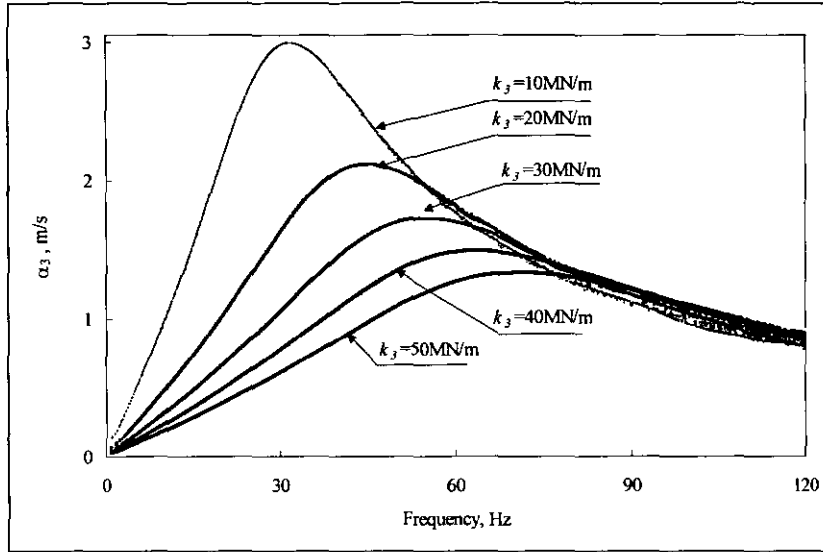


Figure 6.6: Amplitude of bit vibratory velocity with varying stiffness k_3

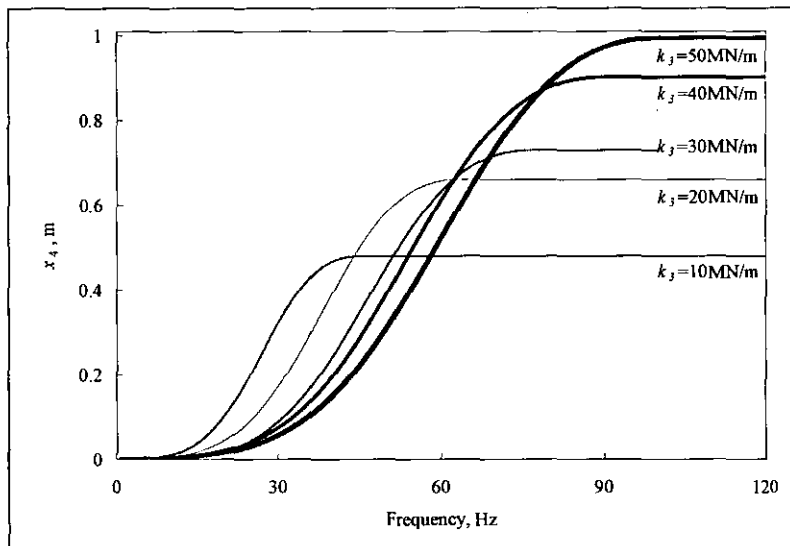


Figure 6.7: Displacement of the dry friction element with varying stiffness k_3

Figure 6.6 displays the amplitude of the bit vibration velocity depending on the frequency for different values of the stiffness k_3 . Figure 6.7 shows the respective response of the dry friction element. It is observed that the displacement of the dry friction element increases with the increase of stiffness k_3 .

In a soft medium, the energy imparted to the bit is consumed by the relatively high amplitude of the bit oscillations. The major part of the energy is dissipated in viscous friction and internal friction. Only a small part of the energy is transferred to the dry friction element and this produces a small displacement. In hard material, the impact produces small deflections with fewer losses in internal and viscous friction but the overall force developed in the spring is large. This force, transmitted to the dry friction element, generates large displacement.

4.1.1 REMARKS

The obtained amplitude-frequency characteristics give an indication of the frequency range within which the applied vibration has a positive effect on the rate of penetration. It is seen that a high speed of penetration is reached when the system is in or close to resonance. Therefore, for better results the system must be excited near the resonant frequency. However, in practice this will be difficult to accomplish because the properties of rocks are unknown during the development of drilling project.

4.2 Study of the System under Impact Loading.

To study the response of the system under successive impacts, a pulse generator was used to simulate impact force at a given frequency. The duration of the pulses used were 0.002 and 0.004 seconds.

The mechanical properties of the rock samples were obtained from the results of the UCS test. A stiffness of the rock cores was estimated to be 100MN/m, 175MN/m and 224MN/m for the sandstone, limestone and the granite samples respectively. The threshold force D was also obtained as 61.9kN, 140kN and 204kN for the respective types of rock. Consequently, the investigation was undertaken within a range covering these values and the following setting were used: $k_3 \in [100, 500]$ MN/m, $D \in [50, 300]$ kN with a damping ratio $\zeta \in [0.5, 1.5]$. These values of the damping ratio allow the observation of the underdamped, critically damped and overdamped motion of the system under impact excitation. Figure 6.8 shows the general motion of the system in a time domain where the dry friction element (x_d) displays a stepwise displacement.

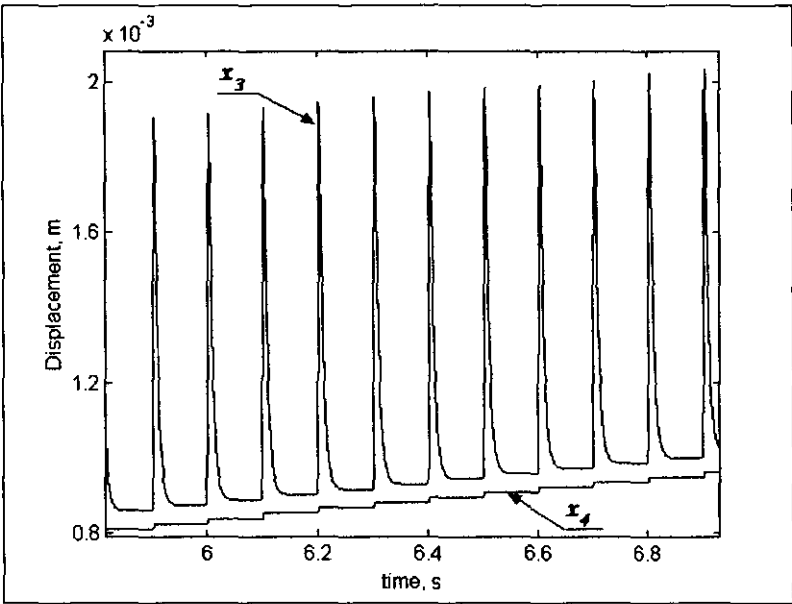


Figure 6.8: Typical motion of the system under impact loading

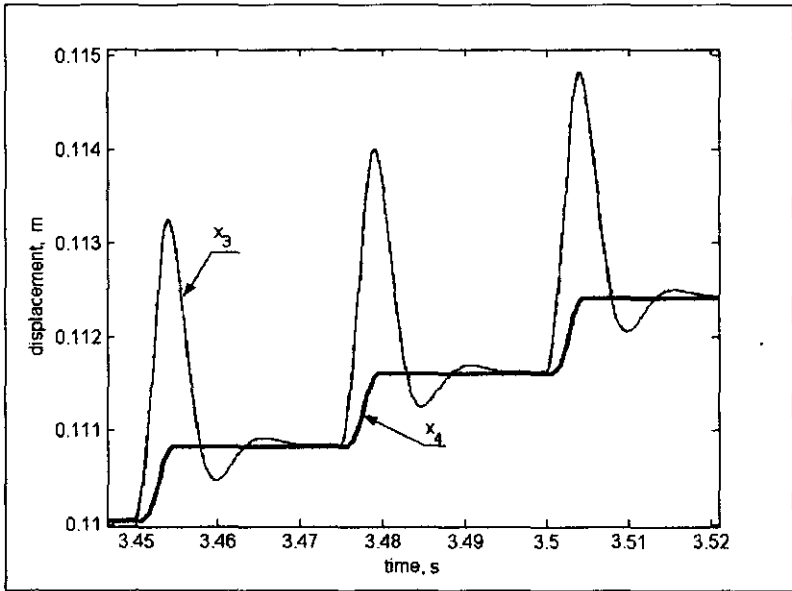


Figure 6.9: Underdamped motion of the system for $\zeta=0.5$

4.2.1

DAMPED MOTION OF THE SYSTEM

The study of the underdamped motion of the system was undertaken with variations in the stiffness k_3 , the damping ratio ζ , the threshold force D , the amplitude and the frequency of impact force. The response of the system was studied under various combinations of the aforementioned parameters. The aim of this investigation was to estimate the response of different media to impact loading and the rate of penetration without considering specifics of the tool geometry. Table 6.1 gives the numerical values of the parameters used for the simulation of the damped motion.

Table 6.1

Parameter	Numerical values
Impact frequency, Hz	40
Impact force, kN	300
Threshold force, kN	$D=150$
Mass, kg	$m_I=250$
Stiffness, MN/m	$k_3=100$
Damping ratio	$\zeta = 0.5; 1.0; 1.5$

Figure 6.9 shows the underdamped motion of the system. If the system is lightly damped, the bit tends to jump after the restitution phase as observed in this graph. This is not desirable because bouncing of the bit induces additional axial vibration into the structure.

Similar to the study of the underdamped motion, the response of the system with damping ratios equal to 1.0 and 1.5 was investigated. The response of the system with critical damping is illustrated in Figure 6.10 and the overdamped motion is shown in Figure 6.11 for $\zeta = 1.5$. The numerical values of the system parameters are given in Table 6.1. The results suggest that the system must be critically damped or overdamped in order to avoid a bouncing of the bit.

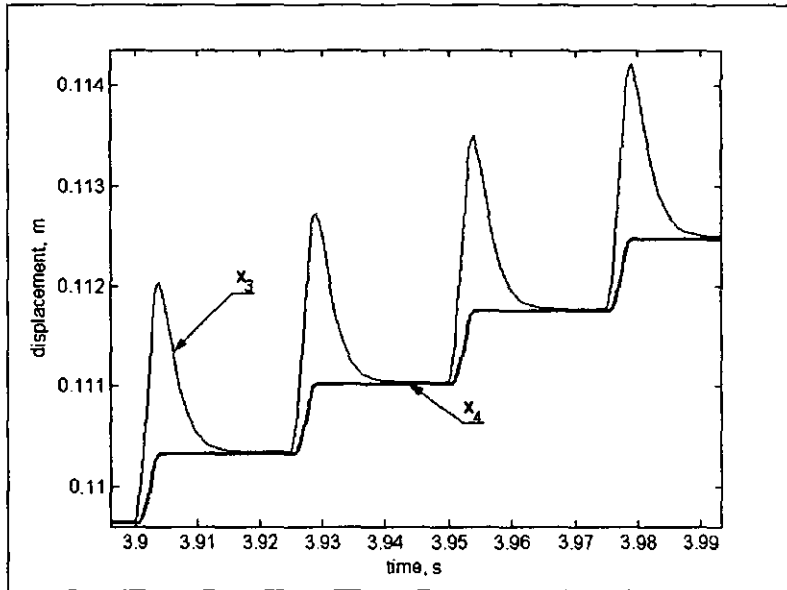


Figure 6.10: Critically damped motion of the system, $\zeta=1.0$

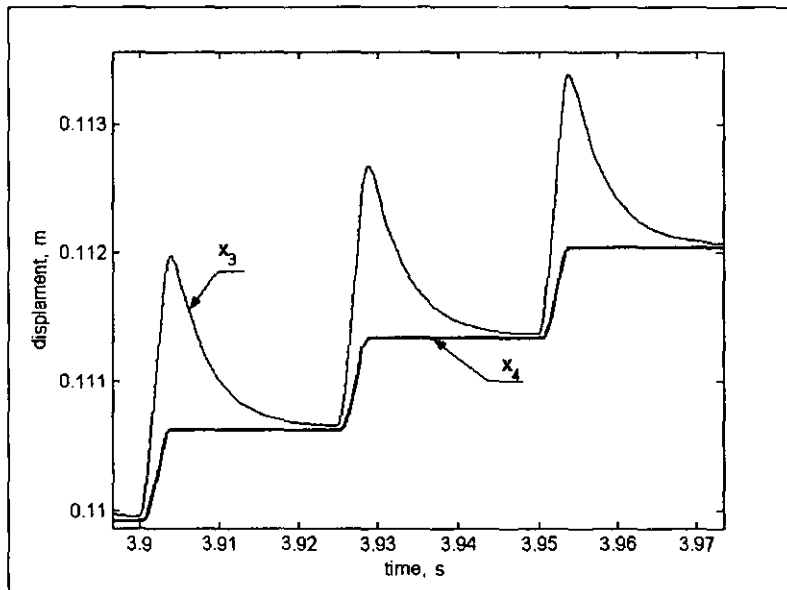


Figure 6.11: Overdamped motion of the system, $\zeta=1.5$

4.2.2 DYNAMIC EFFECT OF IMPACT LOADING

To displace the dry friction element 10 in Figure 6.2c, a static load equal or greater than the threshold force D must be applied. The application of a periodic impact force with very short duration results in an equivalent constant force P , an average of the impact force applied over time. The ratio of this constant component P by the threshold force D expresses the dynamic effect of the applied periodic impact force, Astashev, (2000). The smaller the ratio, the higher is the relief of the thrust; consequently, the required working load is equal to the value of P . The ratio P/D is referred to as the relief of the thrust required from the drive.

Figure 6.12 shows the average force P as a function of the magnitude of impact force and frequency. The average force P increases with the increase of frequency and the magnitude of the impulse. It is observed that for the range of values used in this investigation, the average force is very small compared to the required force for overcoming the threshold force D ; in this case 10kN to 50 kN, whereas the threshold force D is between 61.9kN and 204kN.

For a given threshold force D , the ratio P/D increases with the increase of frequency and also the impact force magnitude has the same trend as the average force P . However, for fixed values of frequency and magnitude of impact force, P/D decreases with the increase of threshold force D (as shown in Figure 6.13 for the force magnitude of 250kN).

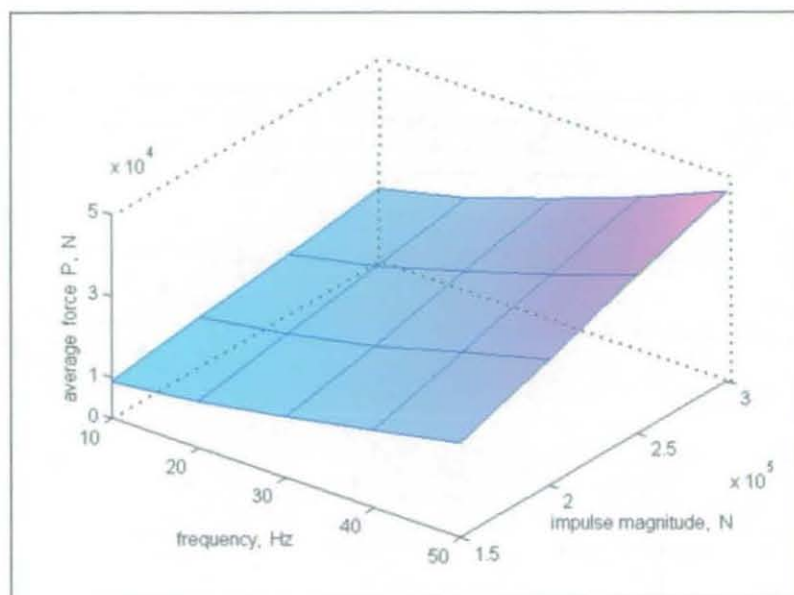


Figure 6.12: Average force P as a function of impact force and frequency

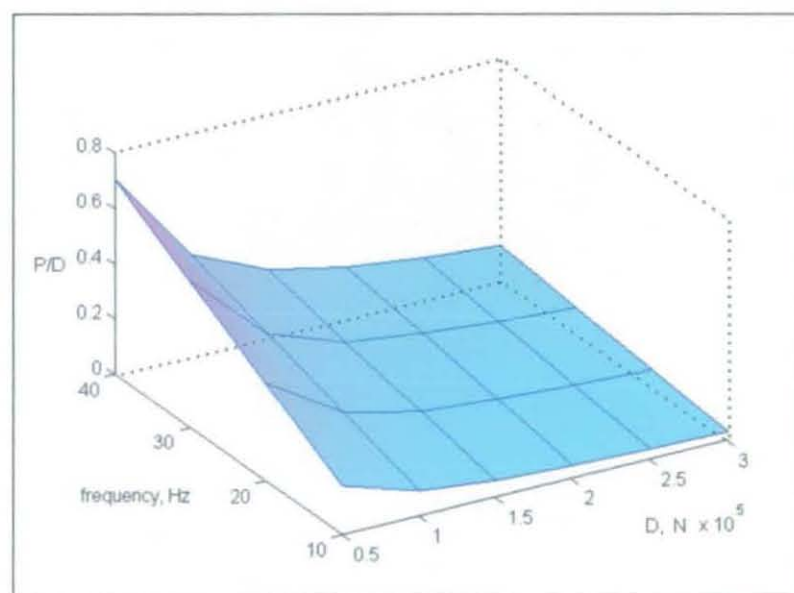


Figure 6.13: Drive relief P/D as function of frequency and threshold force D

4.2.3 RELATIONSHIP BETWEEN ROCK STIFFNESS AND RATE OF PENETRATION

Referring to the results obtained in the sweep sine test, two types of medium were noticed, namely soft and hard. It was observed that in softer materials only elastic displacement occurs. However, the shape of the tool, the frequency of impact and the natural frequency of the system bit-medium are important factors to consider. This is because soft material will display plastic deformation depending on the shape of the tool and the frequency of impact. A harder rock displays more plastic motion with a smaller initial elastic deformation. Considering damping properties of rocks, it is difficult to draw a line between a very soft, soft, medium and hard rock from the point of view of their response to impact loading. This is because both soft and hard rocks will display to some extent elastic and plastic deformations. However, in conventional rotary drilling, depending on the ability of the tool to cut a formation, rocks are classified as soft, medium, hard, very hard and hard-brittle.

In a soft medium, the energy imparted to the bit produces a large elastic deformation of the spring (see Figure 6.6) and a part is dissipated in viscous friction, internal friction and into heat. The resulting force transmitted to the dry friction element is negligible and does not lead to a displacement. This case is shown in Figure 6.14. The displacement (x_3) of the bit is large enough but it does not cause the displacement (x_4) of the dry friction element regardless of the impact force (150 - 250kN). The configuration of the system is given in Table 6.2.

Table 6.2

<u>Parameter</u>	<u>Numerical values</u>
Impact frequency, Hz	10
Impact force, kN	150
Threshold force, kN	$D=150$
Mass, kg	$m_1=250$
Stiffness, MN/m	$k_3=0.01; 0.1$
<u>Damping ratio</u>	<u>$\zeta = 0.5$</u>

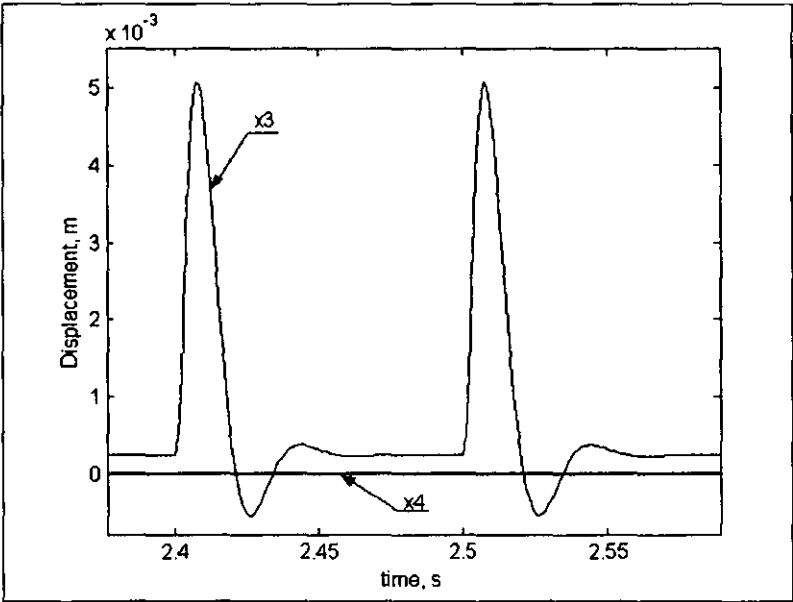


Figure 6.14: Response of the system when the medium is very soft; $\zeta=0.5$

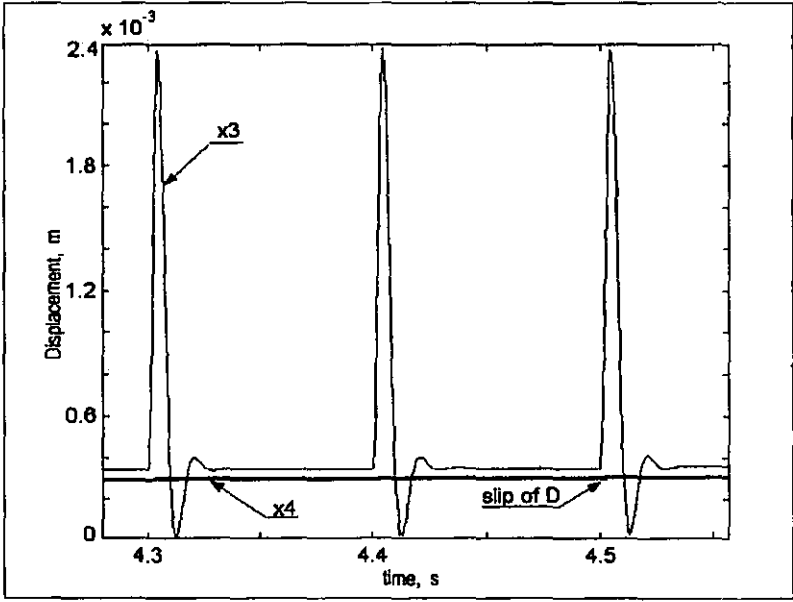


Figure 6.15: Response of the system with slip initiation of dry friction; $\zeta=0.5$

However, as the stiffness of the medium increases, the slip of the dry friction element begins. Figure 6.15 displays the initiation of the slip in the dry friction element for $k_3=0.01\text{MN/m}$ and the configuration is given in Table 6.2. Figure 6.16 illustrates the displacement (x_d) in very soft media. It is seen that impact loading is not effective in such a soft medium as there is no slippage of the dry friction element.

The amplitude of oscillation in Figure 6.14 is twice as much as the amplitude of vibration of the system in Figure 6.15, however no slippage of the dry friction element occurred. A large difference between amplitudes is observed when comparing the results in Figure 6.11 with those in Figure 6.15 where hardly any displacement is noticeable.

Table 6.3

<u>Parameter</u>	<u>Numerical values</u>
Impact frequency, Hz	10 to 40
Impact magnitude, kN	150; 300
Threshold force, kN	$D=150; 250$
Mass, kg	$m_1=250$
Stiffness, MN/m	$k_3=100$ to 500
<u>Damping ratio</u>	<u>$\zeta = 1.1$</u>

The results shown in Figure 6.17 for $D=150\text{kN}$, impact force of 150kN and those illustrated in Figure 6.18 for $D=250\text{kN}$ and impact force of 300kN show the relationship between the rate of penetration and rock stiffness k_3 . These results were obtained by running the simulation model in two loops for 20 to 40 times with the configuration of the system as specified in Table 6.3. For each run, one single point was collected for a given frequency and a particular value of stiffness k_3 . The same procedure was applied to acquire the data for the relationship illustrated in Figure 6.19. Observation of these pictures shows that the rate of penetration increases with the increase in stiffness. This means that the harder the medium, the easier it is demolished by impact.

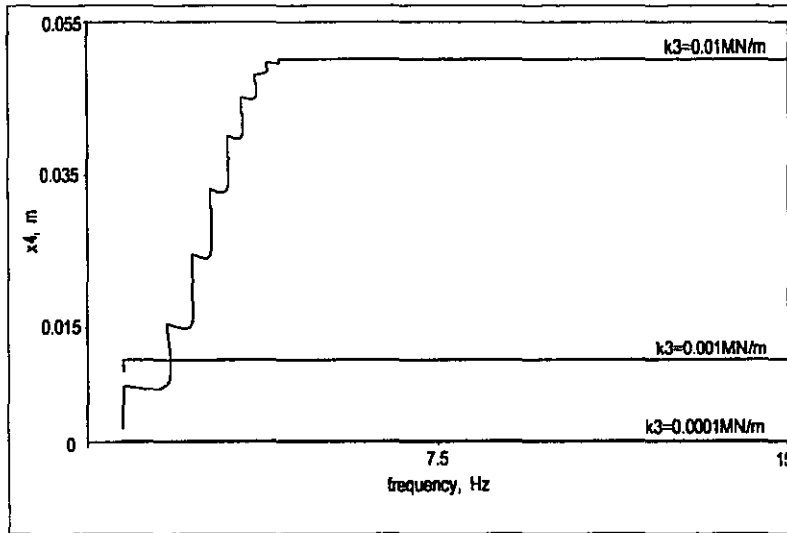


Figure 6.16: Displacement of dry friction element in very soft rocks

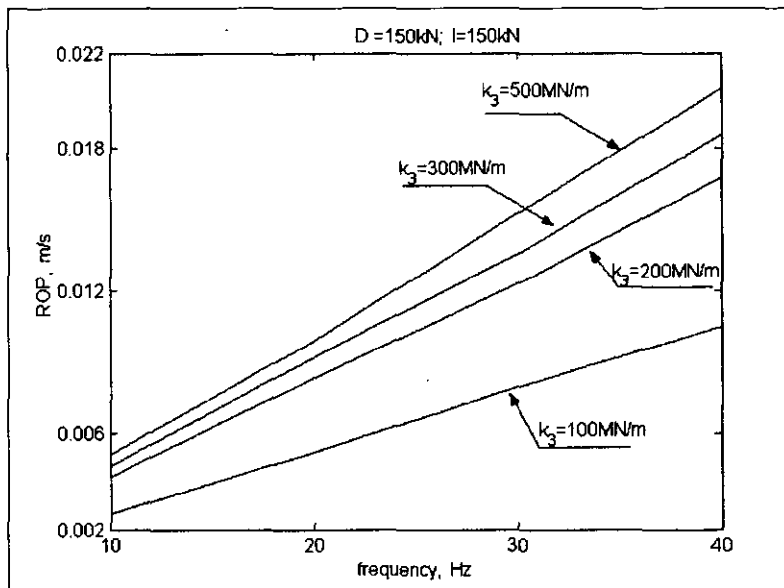


Figure 6.17: Speed of penetration for different values of stiffness k_3

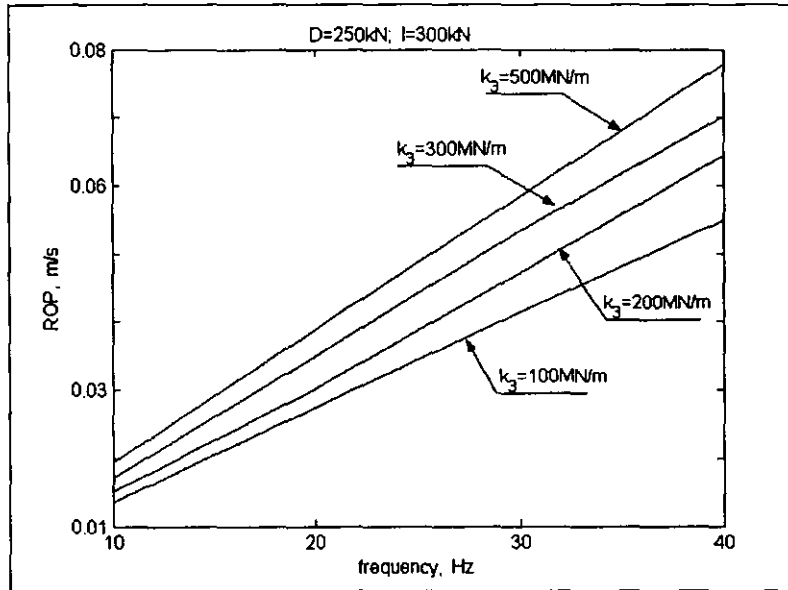


Figure 6.18: Speed of penetration for different values of stiffness k_3

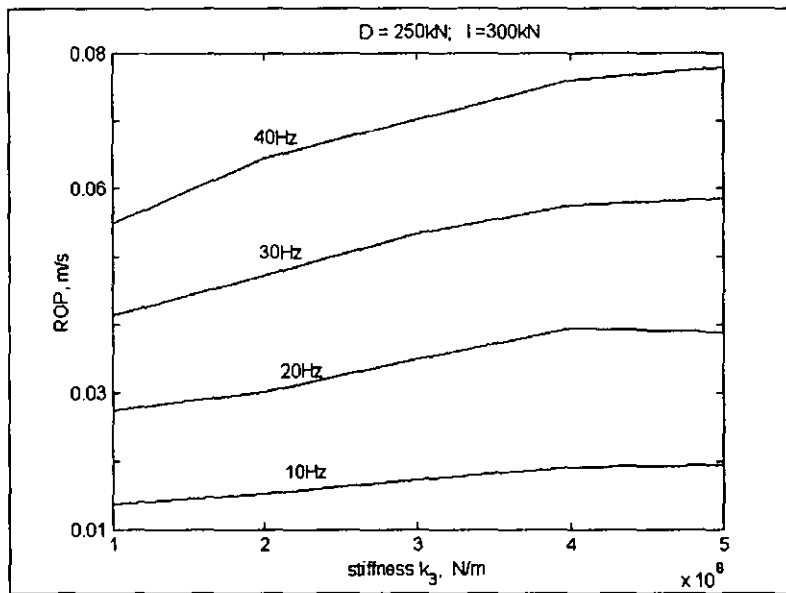


Figure 6.19: Penetration rate with increasing impact frequency

In Figure 6.19 where the rate of penetration is shown for various frequencies of impact, it is seen that though penetration increases with the increase in stiffness, in a very hard medium the slope of the penetration decreases. This shows that harder material offers more resistance to the demolishing process and it underlines the correctness of the model. However, during the simulation, a linear relationship between penetration and stiffness was observed in soft rocks (less than 50MN/m). The rate of penetration increases with the increase in impact force and frequency.

The efficiency of the system under impact load can be expressed as the relationship between the rate of penetration and the overall reduction of the thrust required. The rate of penetration is affected by the stiffness k_3 , the threshold force D , the magnitude of impact force and its frequency. Though penetration is a multivariable function, optimisation procedures cannot be applied in order to obtain a best performance of the system. This is because rocks are a natural product and bear unique physical and mechanical properties unknown beforehand. Consequently, simulation was carried out by varying two parameters at a time and keeping the others constant. This allowed a study of the response of the system for a given combination of the parameters and made it possible to observe the rate of penetration in a three-dimensional representation.

To summarise the effect of stiffness, Figure 6.20 shows two side-views of the rate of penetration as a function of rock stiffness k_3 and the relief of the drive P/D for impact force magnitude of 200kN and a threshold force $D=150\text{kN}$. It is seen in Figure 6.20a that for small values of the ratio P/D i.e. at low frequency, the rate of penetration increases linearly with an increase in stiffness. However, a view of the other side of the same 3-D plot (Figure 6.20b) shows a nonlinear relationship. With an increase in ratio P/D and in stiffness, nonlinearity becomes more accentuated. The illustrated surface shows that the penetration rate has a complex relationship with rock stiffness and the ratio P/D . More simulation results are given in appendix 6-1.

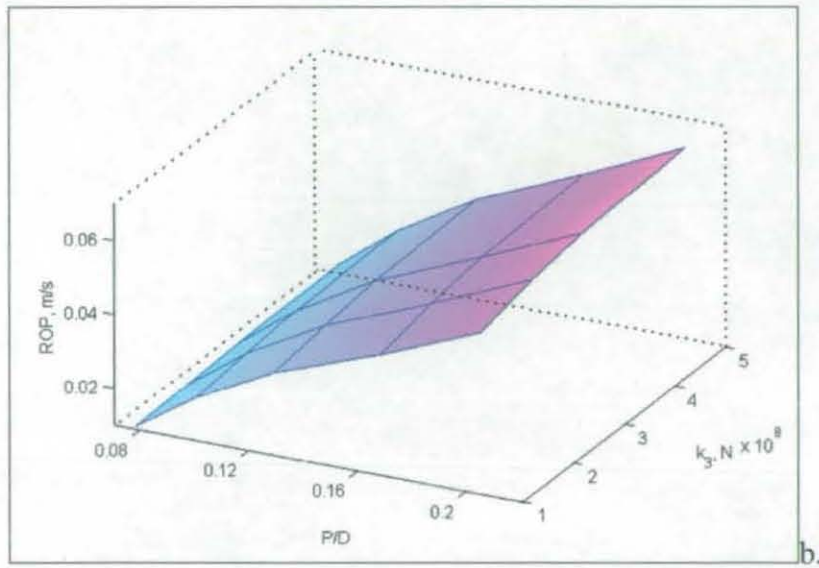
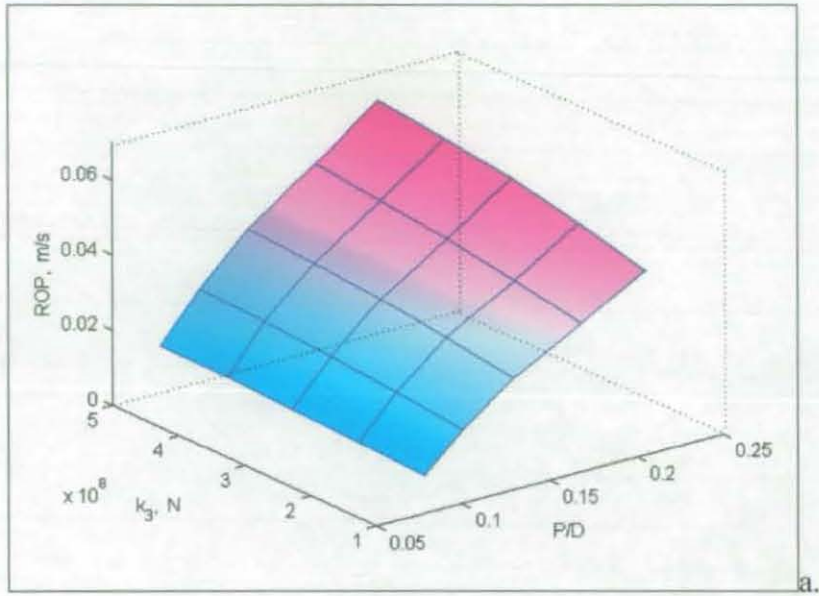


Figure 6.20: Penetration rate as a function of stiffness k_3 and the relief P/D

4.2.4 EFFECT OF IMPACT FREQUENCY ON THE PENETRATION RATE

The frequency of impact has a direct influence on the average force P and the penetration rate. For a given impact force magnitude, penetration increases with the increase in frequency. However, as it was shown with the sweep sine test, the impact frequency must not exceed the natural frequency of the subsystem bit-spring k_3 because beyond the resonant frequency, the displacement of the dry friction element does not occur. As the vibrational velocity α_3 is proportional to the frequency, the penetration is represented in this section as a function of the velocity α_3 and the relief of the drive P/D . It has been noticed that in a soft material, for different values of the vibration velocity α_3 , the rate of penetration increases linearly when a relatively small impact force is applied to the system.

Figure 6.21 shows a nonlinear relationship between the penetration rate and the ratio P/D . The magnitude of the impact force was 250kN and the stiffness k_3 was equal to 300MN/m. The penetration increases with the increase of the vibrational velocity α_3 because with any increase in frequency, the average force P increases and the dry friction element is frequently and largely displaced. It is seen from this graph that in vibro-impact regime, to initiate the displacement of the dry friction element, only 12 percent of the static load is required.

Figure 6.22 is a three-dimensional illustration of the rate of penetration with the vibrational velocity α_3 and relief of the drive P/D when an impact force of 300kN was applied to the system with stiffness k_3 equal to 500MN/m. It shows that given an amplitude of impact force, the penetration increments linearly with the increase of the velocity of vibration i.e. with the increase in frequency. Table 6.4 gives the parameters of system configuration.

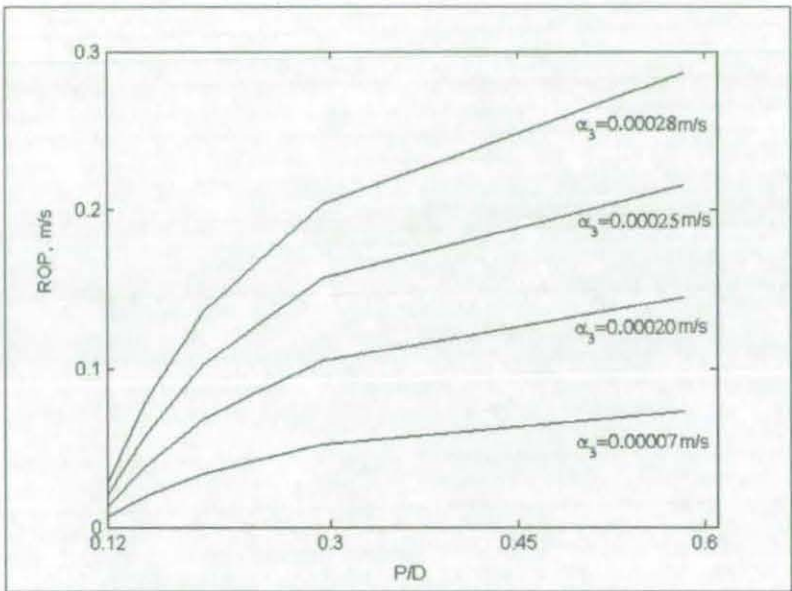


Figure 6.21: Penetration rate for different intensity of vibration

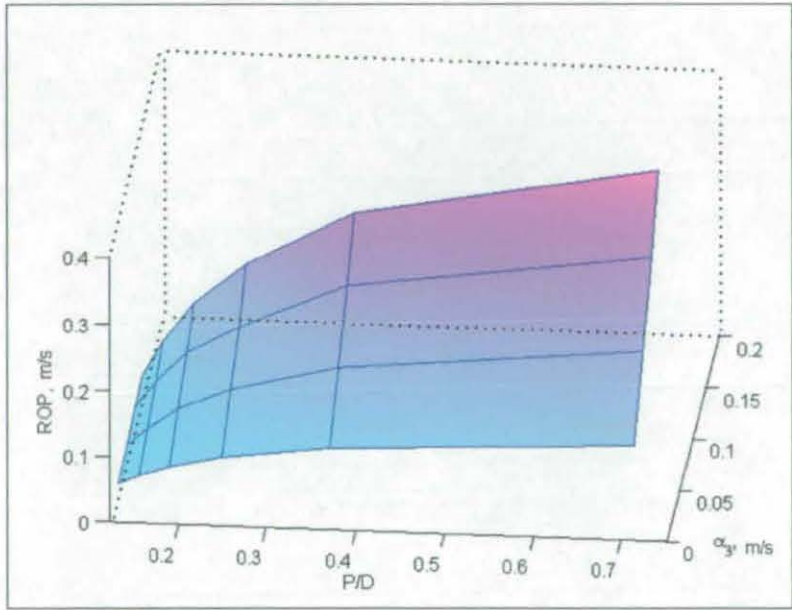


Figure 6.22: Penetration rate as a function of α_3 and the relief P/D

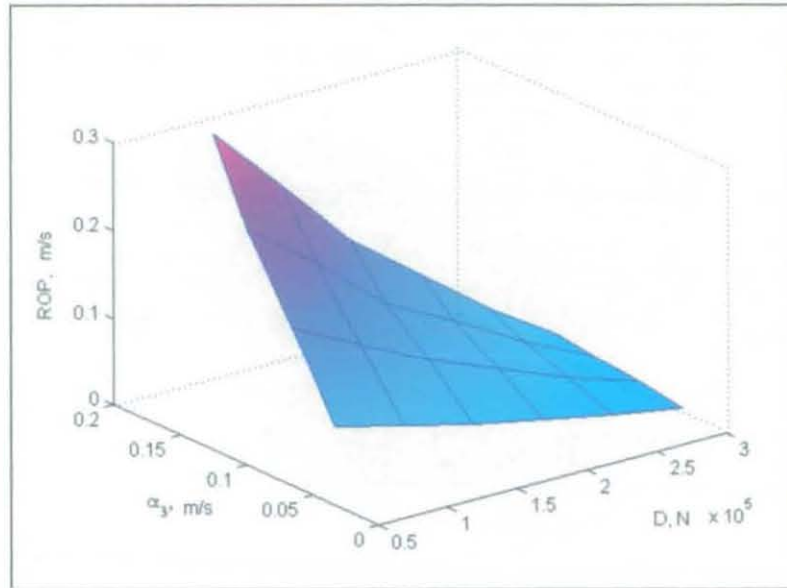


Figure 6.23: Penetration rate as a function of α_3 and the threshold force D

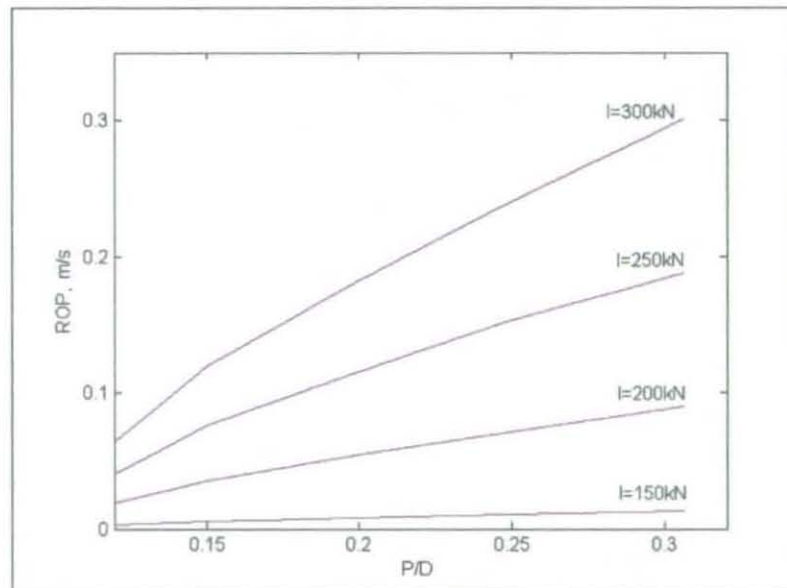


Figure 6.24: Penetration rate for different values of impact force

The graph in Figure 6.23 is a surface, which shows the relationship between the penetration, the vibrational velocity and the rock threshold resistance D . It is seen that the penetration rate decreases considerably with the increase of the force threshold force D . The configuration of the system is shown in Table 6.4.

Table 6.4

Parameter	Numerical values
Impact frequency, Hz	10 ~ 40
Impact force, kN	300
Threshold force, kN	$D = 50 \sim 250$
Mass, kg	$m_1 = 250$
Stiffness, MN/m	$k_3 = 500$
Damping ratio	$\zeta = 1.1$

4.2.5 INFLUENCE OF THE MAGNITUDE OF IMPACT FORCE ON PENETRATION

In percussive rock drilling, the magnitude of the instantaneously imparted impulse is the most important parameter for the initiation and propagation of cracks into the formation. It is obvious that for a given type of rock, the rate of penetration will increase with the increase of the magnitude of the impact force.

It was observed that the rate of penetration increases linearly when a relatively small impact force is applied to the system. However, as the impact force increases, the dependence of the rate of penetration on the ratio P/D is not linear. This is observed in Figure 6.24, which displays the efficiency of the vibro-impact process as a plot of the rate of penetration (ROP) versus the ratio P/D for various impact force magnitudes when the threshold force D was 150kN and the stiffness k_3 equal to 100MN/m. It is seen that for an impact force of 150kN, a straight line with a small slope describes the relationship. However, when the impact force is of 300kN, the relationship tends to curve.

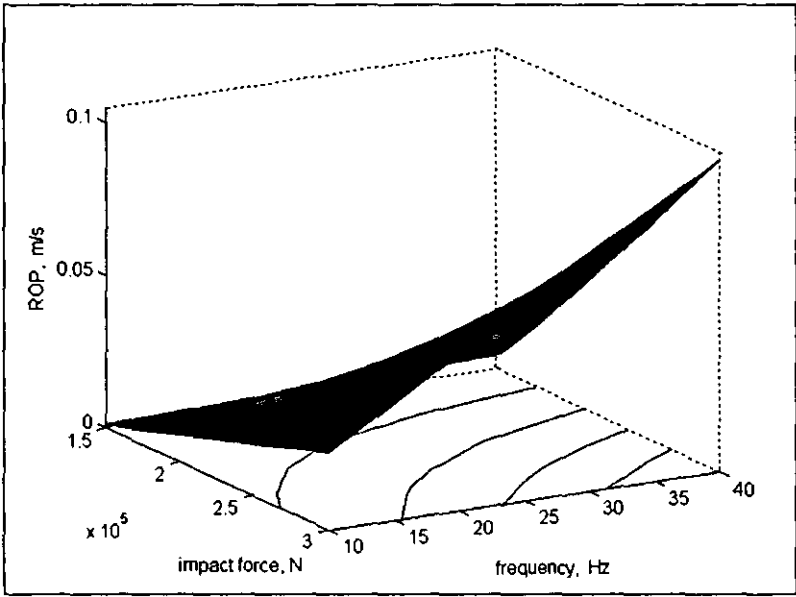


Figure 6.25: Penetration as a function of frequency and impact force

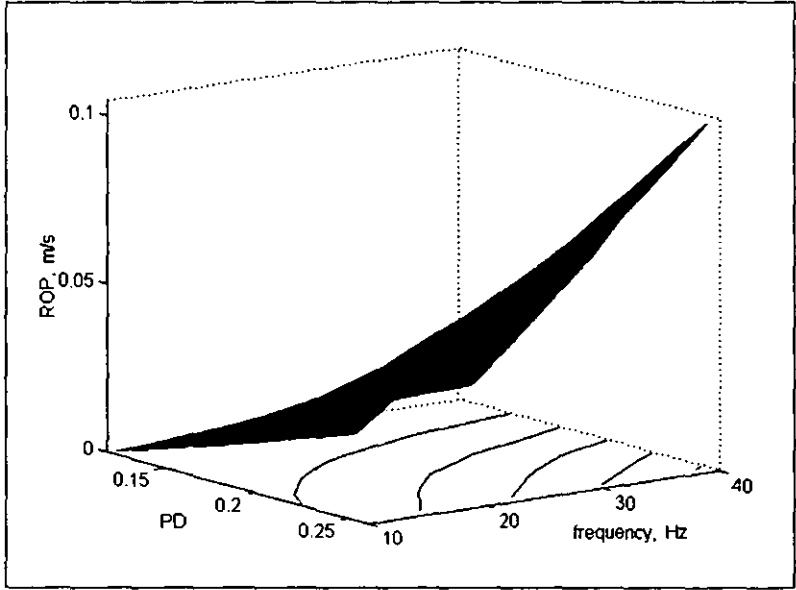


Figure 6.26: Penetration rate as a function of frequency and the relief P/D

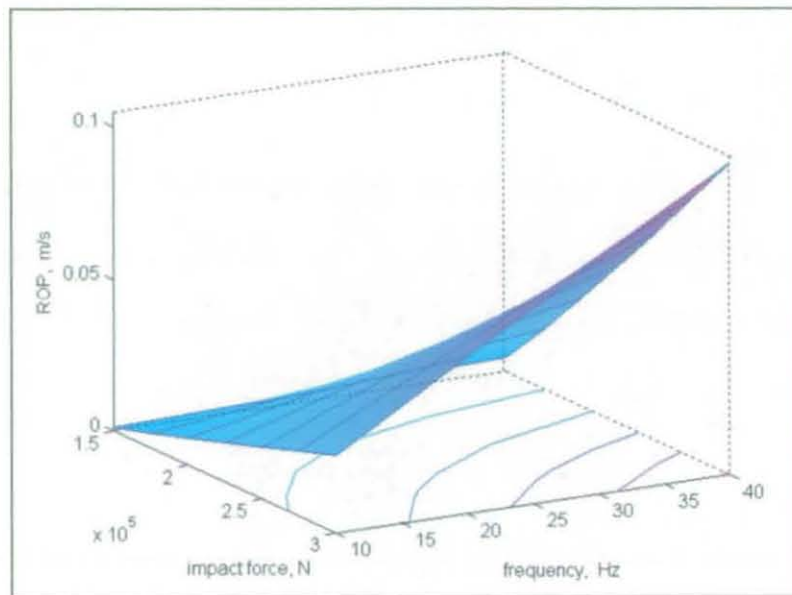


Figure 6.25: Penetration as a function of frequency and impact force

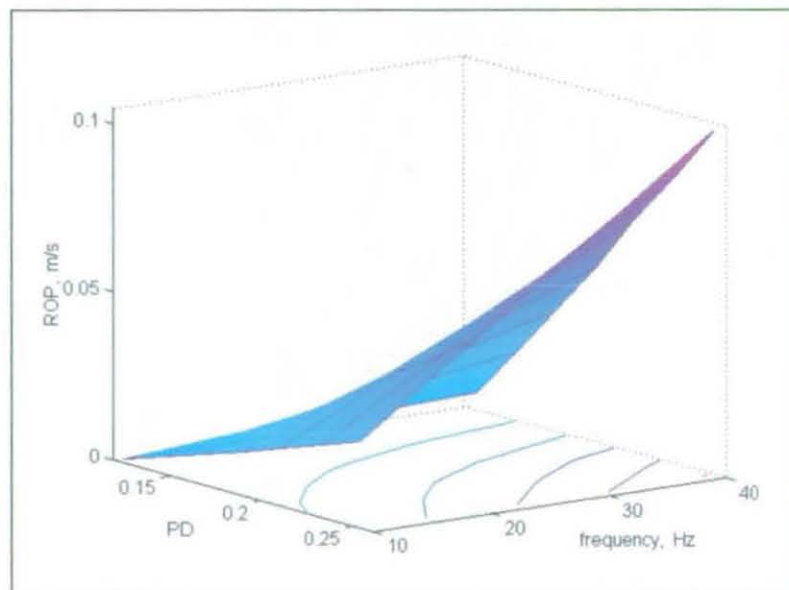


Figure 6.26: Penetration rate as a function of frequency and the relief P/D

Figure 6.25 shows the relationship between the rate of penetration (ROP), the Impact force and the frequency. A threshold force $D=150\text{kN}$ and a rock stiffness $k_3=500\text{MN/m}$ were used for this simulation, Table 6.5 giving the configuration of the system. The shape of the surface is shown as a projection on a horizontal plane.

Figure 6.26 illustrates the relationship between the rate of penetration, the frequency and the relief of the drive P/D for the same system parameters as shows in Table 6.5. It is seen that both surfaces are similar because the average force P is proportional to the impulse magnitude.

Both figures 6.25 and 6.26 show a nonlinear relationship between the force applied, the frequency of vibration and the resulting rate of penetration. The penetration increases with the increase of both the frequency and the amplitude of the impulse due to the impact.

Table 6.5

Parameter	Numerical values
Impact frequency, Hz	10 ~ 40
Impact force, kN	100 ~ 300
Threshold force, kN	$D = 150$
Mass, kg	$m_I = 250$
Stiffness, MN/m	$k_3 = 100; 500$
Damping ratio	$\zeta = 1.1$

5. DISCUSSION

The results obtained show that the penetration increases with the increase of the impact force and the frequency. However, with an increase in stiffness, a small reduction in the rate of the penetration is observed towards very high stiffnesses. Observation of the graphs indicates that the relationship between the rate of penetration and the relief of the drive P/D is logarithmic.

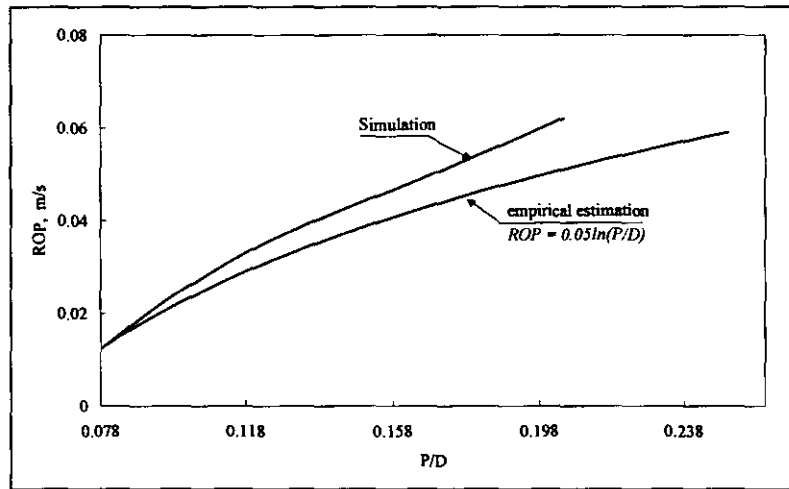


Figure 6.27: Empirical estimation of penetration rate
for impact force of 200kN and $k_3=50\text{MN/m}$

Analysis of the results revealed that the penetration rate could be related to the relief of the thrust by the following empirical expression.

$$ROP = C \ln(\eta) \quad (6.4)$$

Where $\eta = P/D$ and C is a parameter characterising the configuration of the system. The configuration parameter C depends on the rock stiffness k_3 and the magnitude of the impulse. C was found to vary from 0.046 to 0.189 for k_3 varying from 300 to 500MN/m and impact force of 200; 250 and 300kN. It was noticed that C is strongly affected by the impulse amplitude whereas stiffness has little effect on the value of C .

Figure 6.27 compares the penetration rate from simulation with the empirical estimation for $I=200\text{kN}$; $k_3=50\text{MN/m}$. From the graphs, it is seen that equation (6.4) underestimates the rate at high values of η . A thorough investigation of the coefficient C is needed in order to establish the relationship and the mutual effect of the involved parameters (k_3 and I). This will allow an exact determination of the value of C . However, it could be more practical to define the value of C when testing the prototype. This is a matter for further research.

6. RESPONSE OF THE SELF-OSCILLATORY SYSTEM

The final system makes use of the main model studied in chapter five as source of impact force, which is applied to the model in Figure 6.2c. The frequency of impact interaction is defined by the stiffness of the springs 3 and 6 (see Figure 5.11). In this section, a study of the entire system is undertaken with the system frequencies set at 6, 12 and 14Hz.

Figure 6.28 shows the Simulink model of the entire vibro-impact system. The penetration model is illustrated as an added subsystem in the section marked VII.

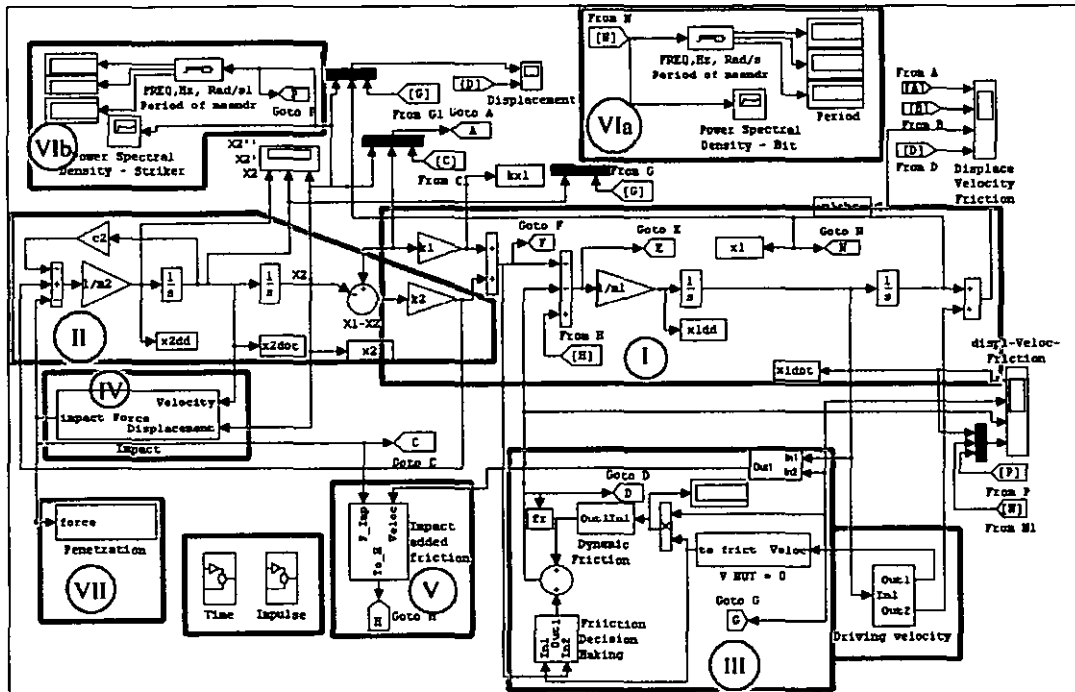


Figure 6.28: Simulink model of the entire system with penetration

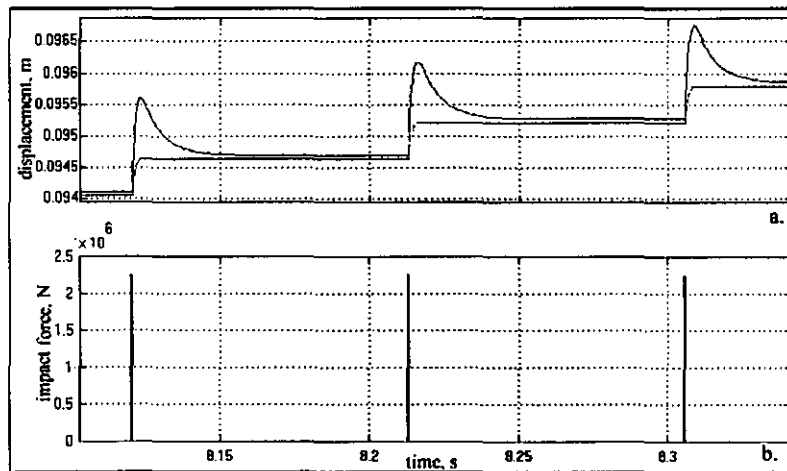


Figure 6.29: Screenshot of simulation process

Figure 6.29 is a screenshot of the simulation process of the entire system with a typical response. It displays the bit motion at the top and the motion of the dry friction element underneath, Figure 6.29a. The dry friction element exhibits a stepwise motion where slippage occurs only at the instant of impact. The dry friction element slips for the duration of the impact. Between the intervals of impacts it is motionless.

Figure 6.29b displays a typical impact force, the value of which depends on the contact stiffness and the gap between the striker and the bit. The impact force was calculated with the help of Equation 5.18, described in chapter five. For a given configuration of the system, the magnitude of the impact force increases with the increase of the gap between the striker and the bit. Figure 6.30 show the magnitude of the impact force for Δ between 0.010 and 0.020m.

Table 6.6

Parameter	Numerical values
System response frequency, Hz	5.8; 11.6; 13.9
Mass, kg	$m_I=250$ $m_I=100$
Stiffness, MN/m	$k_0= 20$ $k_3=100 \sim 500$
Stiffness, kN/m	$k_I=246,490$ $k_2=55.46$
Damping coefficient, N.s/m	$c_0= 10$ $c_2= 250$
threshold force, kN	$D= 50 \sim 300$
Damping ratio (bit-medium)	$\zeta = 1.5$

Table 6.6 gives the numerical values of the parameters used to configure the system during this simulation.

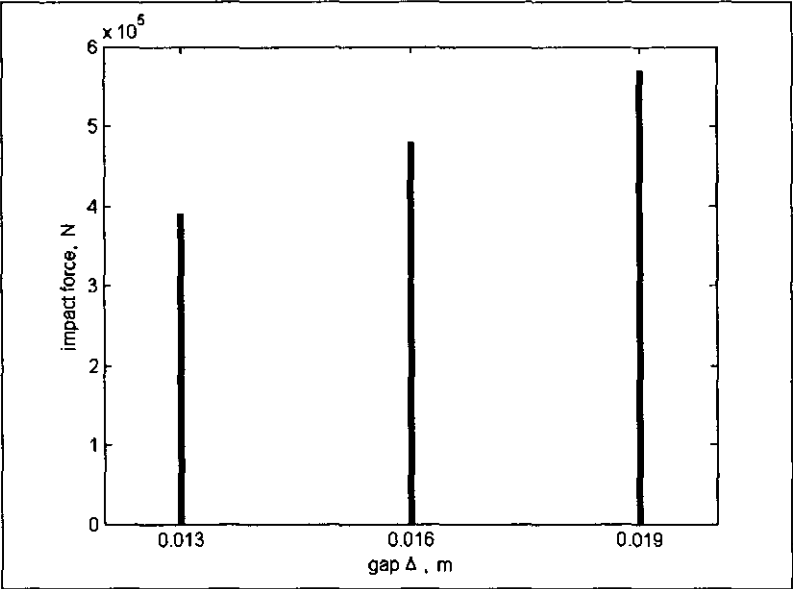


Figure 6.30: Impact force as a function of the gap Δ

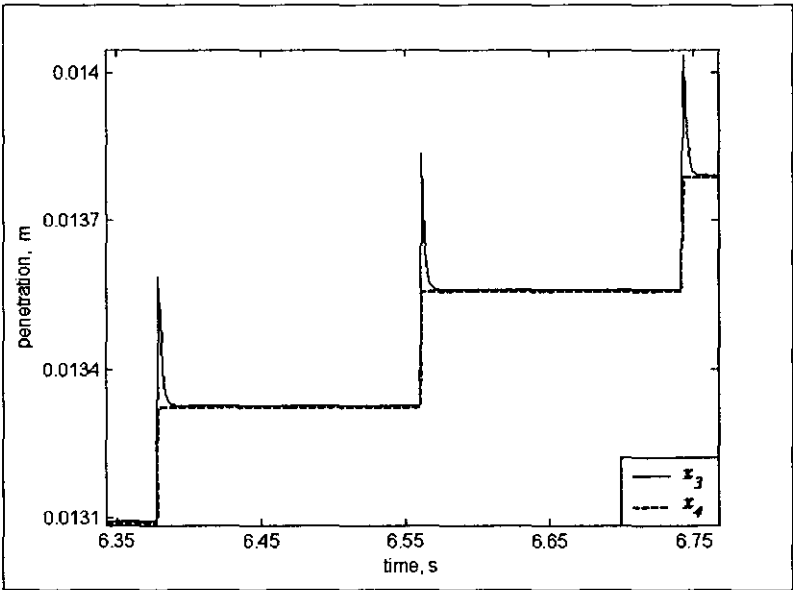


Figure 6.31: Displacement of bit-medium subsystem

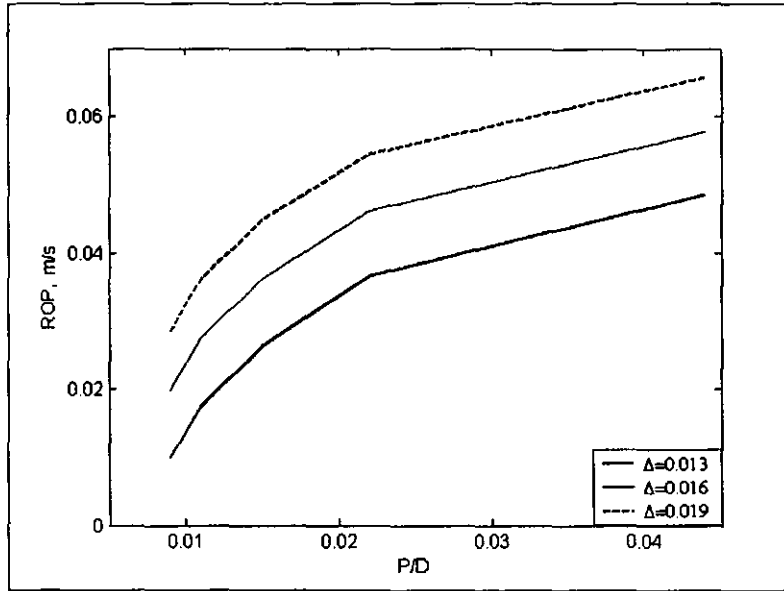


Figure 6.32: Rate of penetration for various values of Δ

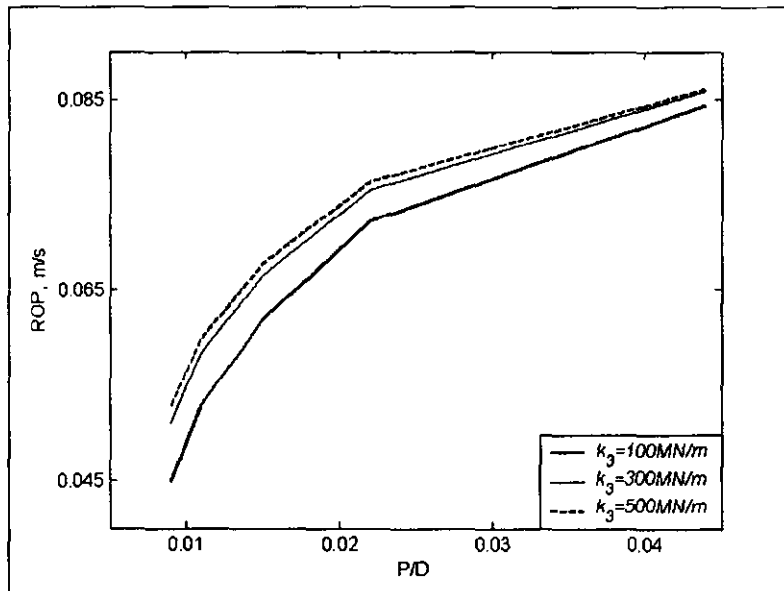


Figure 6.33: Rate of penetration for various values of k_3

Similar to previous results, Figure 6.31 shows the displacement of the bit (x_3) and the medium (x_4). It is seen that at impact, the medium undergoes a plastic deformation followed by a restitution phase due to elastic deformation.

Figure 6.32 shows the penetration rate for three settings of the clearance Δ between the striker and the bit, i.e. the penetration produced by the forces shown in Figure 6.30. It is observed that for a given medium ($k_3=300\text{MN/m}$ in this plot) the speed of penetration increases with the increase of the force of impact.

Figure 6.33 represents the relationship between the rate of penetration and the force ratio P/D for different stiffnesses of the medium. It shows that higher rates of penetration are produced in hard materials. This observation was made in previous results. For increasing stiffness of the medium, the energy of the impact is almost entirely converted into the work of penetration. In a hard material, a small deformation produces large force which exceeds the threshold force of the material. For a soft medium, part of the imparted energy is transformed into oscillation of the bit.

However, it is noticed from Figure 6.33 that only a small increment occurs between $k_3=300\text{MN/m}$ and $k_3=500\text{MN/m}$. This means that though the penetration increases with the stiffness, harder media offer considerable resistance to deformation and require a large magnitude of impact force. The effect of increased resistance with large values of stiffness k_3 is illustrated in Table 6.7, which shows the displacement of x_4 for an impact force of 470kN and $D=250\text{kN}$

Table 6.7

$k_3, \text{MN/m}$	x_4, mm	increment, mm
100	0.58	
300	0.73	0.15
500	0.77	0.04

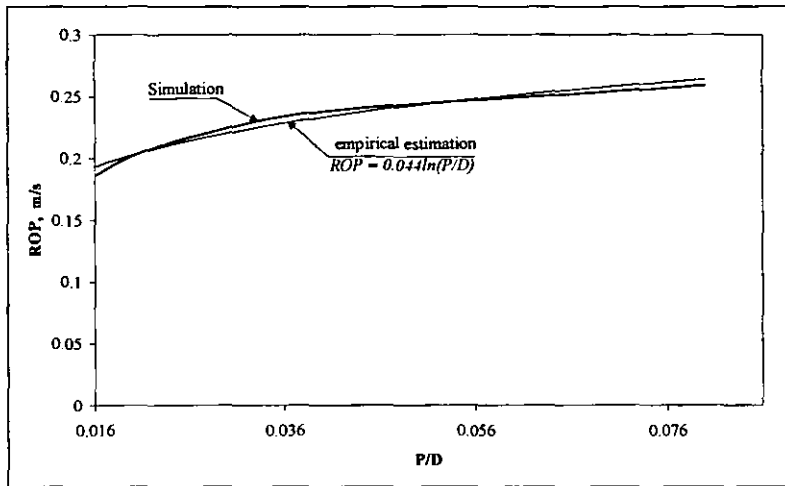


Figure 6.34: Estimation of penetration rate as a function of P/D

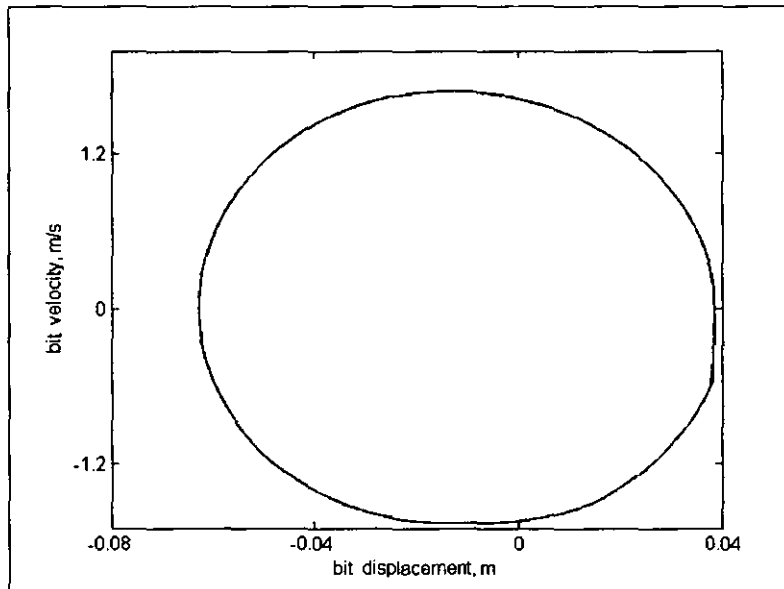


Figure 6.35: Phase portrait of bit motion

The trend of the penetration rate obtained with application of impulses was observed during the simulation of the entire system. Figure 6.34 compares the trend of the rate of penetration acquired from the simulation with the trend generated from the empirical equation (6.4) for $C=0.44$. There is a small discrepancy between both results. However, for estimation purposes, the empirical formula gives an accurate approximation of the penetration rate.

Phase portraits of the motion of the bit and the striker during the penetration process are illustrated in Figure 6.35 and Figure 6.36 respectively. These two plots show that the main structure studied in chapter five has kept its self-sustained periodic performance regardless of the process of penetration.

In the study of the main model in chapter five, it was assumed that the interaction with the medium does not influence the response of the system, i.e. the rotational motion of the bit is not affected by the superimposed impact. The results shown in Figure 6.35 and 6.36 are in agreement with the aforementioned assumption. The penetration process and the periodic impacts are to some extent perturbations introduced into the system. However, this does not affect the stability of the limit cycle. The motion of the bit is always positive and this means that the bit is kept constantly in contact with the medium and separation does not occur.

Figure 6.37 displays typical velocities and frequency spectra of the signal of both bit and striker after fast Fourier transformation. For an identical configuration of the system, no change was recorded in the frequency response when compared to the investigation in the previous chapter.

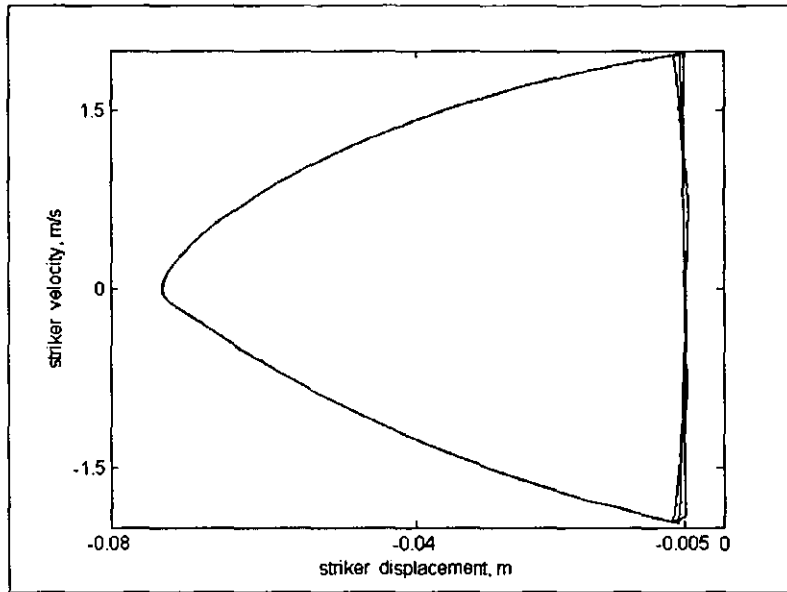


Figure 6.36: Phase portrait of striker motion

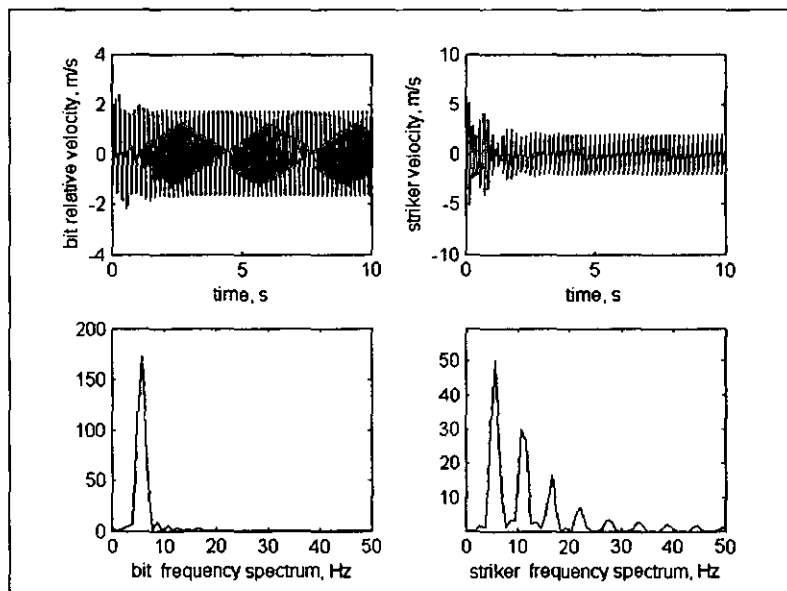


Figure 6.37: Bit and striker velocities and frequency spectra

7. DISCUSSION

It is assumed that impact loading does not affect the rotational motion of the bit. The entire structure is a self-excited system which comes to a stable and steady motion. The introduction of impact causing a braking effect on the bit rotational motion and the sudden downward dislocation of the equilibrium position are regarded as strong perturbations of system stability. However, the limit cycles of bit and striker motion show no change compared to the results in chapter five, thus revealing its robustness. This means that the system has kept its stability regardless of normal displacement. The results obtained show that the mechanism studied has a stable regime of operation for realistic parameters.

The results of this study show that it is possible to obtain considerable reduction in the thrust required. The relief of the thrust is expressed by the force ratio P/D . The smaller is this ratio, the higher is the effect of the superimposed vibro-impact process. The impact load produces not only fast penetration but it also weakens the upper layer of the medium straight underneath the tool due to propagation of cracks. The depth of the propagation of cracks depends on the magnitude of the impact force, the shape of the tool and the type of rock. Impact significantly eases the rotary ploughing process because cutting occurs in the pre-fractured layer of the medium.

It is observed that the added vibration greatly reduces the required thrust. An average force of about 10 percent of the threshold force is sufficient to dislocate the dry friction element. Knowing the average force of the vibro-impact process and the threshold force, the rate of penetration can be estimated by the empirical equation (6.4). This formula estimates the penetration due to superimposed vibration and does not take into account the penetration generated by rotary cutting. In general, the penetration caused by rotary action is slow compared to impact cutting. However, to account for rotary cutting, a constant could be added to equation (6.28) to reflect the penetration rate of rotary action.

Chapter 7
Conclusion

Conclusion

The system developed in this work effectively uses the existing friction arising from the drilling process. The novelty of the model studied is that the frictional energy, which stays redundant in most mechanical structures, is here converted into useful work. In drilling practice, every effort is made to minimise the persisting friction and avoid frictional vibration.

The coupling of two strongly nonlinear and non-smooth processes (friction and impact) into one single mechanism and the idea of using the system friction as a source of energy defines the originality of this investigation. To the knowledge of the author, structures with two-degrees-of-freedom incorporating simultaneously dry friction and impact (which is excited by frictional instability and its direct engineering application) have never been explored before.

The innovation introduced here into drilling engineering has a seminal feature, the system self-adjustment capability. This means that the mechanism, depending on the hardness of the rock, can regulate the impact action. The stiffness of spring 3 is set to match a given rock hardness. Consequently, in soft rocks, the cutting proceeds in conventional rotary drilling because the rock matter is not hard enough to cause considerable deformation of spring 3. However, whenever the target compressive strength is reached, the stick-slip process begins and the impact action is superimposed. This simple mechanical system has a great advantage over gauging and controlling stick-slip vibration, which requires complex and expensive techniques. These techniques, including telemetry, are often not reliable because of the harshness of the conditions in which the sensors and the transmitting units are submerged.

There may be two ways of achieving the excitation close to resonant frequency:

1. The self-excited mechanism studied in chapter 5 could be designed with its frequency response such that a given type of rock could excite the bit close to the desirable frequency. After geo-seismic exploration of the formation to be drilled, a set of springs (3 and 6) with different stiffnesses matching major rocks may be used to adjust the system response near to the resonant frequency of the hardest rock of the formation.
2. The system may be excited externally with the frequency of excitation adjusted manually to obtain a best performance. An autoresonant approach could also be used. However, in this case, the system must be fitted with an intelligent device able to estimate the stiffness and the response frequency of the rock being drilled. The method suggested by Babitsky *et al.*, (1998) for the identification of the mechanical properties of a body by a single impact is one possible way to develop such an intelligent device. Nevertheless, it is worth mentioning that this approach is adequate only for soft materials. With hard materials such as steel and hard rocks, care should be taken to avoid the “ringing” of the impacting body. However, because hard rocks are very stiff, the natural frequency of the bit over the rock formation may be too high for a mechanical device to respond to such a frequency. Consequently, an autoresonant approach may be applicable for relatively soft rock.

The results obtained show that the structure investigated in this work has a stable regime of operation over a range of realistic parameters. The mathematical tools developed allow optimal parameters of the system to be defined. It was shown that the desired performance of the system is obtained for $\gamma \in [0.7, 0.8]$ and $\beta \in [0.25, 0.4]$. In this range of frequency ratio and mass ratio, the system had a steady state synchronised motion with a single impact per cycle. This allows the design parameters of new vibro-impact drilling systems to be obtained. An empirical formula was derived to give an estimation for the response frequency of the system.

This mechanical device decouples the drill string from the bit, and thus effectively protects the drill string from vibration. A proper organisation of the decoupling mechanism would not transmit any axial oscillation to the string. The use of a single source of energy for driving and for excitation of the striker during the sticking of drill bit relieves the main drive from dynamic loading and permits effective application of vibration protection of the drill string.

The rate of penetration increased with the increasing frequency and magnitude of the impact force. It was shown that the vibro-impact process performs better in a very hard medium and this was supported by the experimental results when drilling in some samples of very hard limestone. The study of the vibro-impact penetration showed that considerable reduction of the required thrust can be obtained by superimposing the vibration onto rotary drilling. The results show that the applied load can be decreased to 10-20 percent of the conventionally required thrust. Such a relief of the thrust potentially extends the life of the drill string and the time between maintenance.

Drilling is a very costly process and the challenges of inaccessible sites are such that reduced drilling time is required to bring down the cost. The theoretical foundations developed here can supply design criteria for new vibro-impact drilling systems to accommodate the presented structure. A successful implementation of this mechanism will provide the drilling industry with an advanced technique which will protect the drill string from hazardous vibration, adjust itself to the drilling conditions, and increase the performance of drilling systems.

Chapter 8
RECOMMENDATION FOR FUTURE WORK

Recommendation for Future Work

In drilling, friction consumes the major part of the energy supplied to the system. Consequently, many aspects are still to be investigated for a specific understanding of the drilling process. The system introduced in this study ventures into an area known to engineering but not very well explored.

For further study of the system, the following plan of work is suggested.

1. Add a third degree-of-freedom to the system in order to confirm the assumptions admitted during the current study.
2. Undertake a full factorial (Taguchi methods) experiment with interaction of factors. This will allow the identification of the mutual effects of the parameters.
3. Experimental estimation of the configuration characteristics C in equation (6.4).
4. Investigate the effect of rock stiffness and impact magnitude on the characteristics C .
5. Explore the very high contact stiffness between the striker and the bit to maximise the magnitude of the impact force, and study the response of the system under such conditions.
6. A bifurcation analysis could contribute to the generic understanding of the behaviour of the system as a self-exciting mechanism.
7. Build a knowledge-based computational system able to provide engineers with a set of data on the desired design parameters because similar data are not yet available.
8. The prototype should be designed to respond at 3 to 10Hz to allow a detail study of the system behaviour.

REFERENCES

1. Astashev V, K, Babitsky, V, I, Kolovsky, M,Z, 2000, Dynamics and control of machines. Springer-Verlag, Berlin
2. ASTM Standard method of test for triaxial compressive strength of undrained rock core specimens without pore pressure measurements. ASTM Designation D-2664-67.
3. ASTM Standard method of test for unconfined compressive strength of rock core specimens. ASTM Designation D-2938-71a.
4. Azbel G, G; Savinov, O, A; Tseitlin, M, G, 1981, Vibratory machines for pile driving and geological drilling. Ed. Lavendel E, E, 325-335 (in Russian)
5. Babitsky V I, 1998, Theory of vibro-impact systems and applications. (Russian revised translation, Nauka, Moscow, 1978)
6. Babitsky, V, I; Vepruk, A, M, 1998, Universal bumpered vibration isolator for severe environment. Journal of Sound and Vibration, 218(2) 269-292.
7. Barkan, D, D, 1959, Vibro-method in civil engineering, Moscow, Gossizdat; (in Russian)
8. Batuev G S, Golubkov U V, Efremov A K, Fedosov A A, 1977, Engineering methods of studying impact processes. Moscow, Mashinostroenie, (in Russian)
9. Beccu R & Lundberg B, 1987, Transmission and Dissipation of stress Wave Energy at a Percussive Drill Rod Joint, Int. J. Impact Engineering Vol. 6, No. 3, 157-173, Great Britain.
10. Bell F,G. , 1992, Engineering Properties of Soils & Rocks, Butterworth-Heinemann Ltd, London.
11. Bepalova L, V, 1957, The theory of vibro-impact mechanisms. Izvestiya ANSSR,OTN, (in Russian)
12. Blekhman, I I,, 1954, Investigation of the process of vibratory driving of plies; in Engineering collection, vol. 19; (in Russian).

13. Blekhman, I, I, 1979, Vibration of nonlinear mechanical systems; Vibration in engineering, vol. 2 (in Russian).
14. Blekhman, I, I, 1994, Vibrational mechanics, VO Nauka; (in Russian); Translation from Russian, World Scientific, Singapore, 1999
15. Blok, R, 1940, Fundamental aspects of boundary friction. J. Society of Automotive Engineers, 46, 275
16. Bonnie S Heck, Aldo A Ferri, 1997, Analysis of stick-slip motion in Coulomb damped systems. Proc. Of American Control Conference, Albuquerque, New Mexico, June.
17. Borse G J 1997, Numerical methods with MatLab: a resource for scientists and engineers. PWS Publishing (ITP), London.
18. Braiman F, Family F, Hentschel H G E, 1997 Nonlinear friction in the periodic stick-slip motion of coupled oscillators. Physical Review B, vol. 55 No. 8, 5491-5497
19. Brett, G, F, 1992, The genesis of torsional drillstring vibration. Society of Petroleum Engineers Drilling Engineering, 7,168-174.
20. Brockley, C; Cameron, R and Potter, A, F, 1967, Friction-induced vibration. ASME, J. Lubrication Technology 89, 101-108
21. Brown E T, 1981, Rock Characterization Testing & Monitoring, ISRM Suggested Methods, Pergamon Press, Oxford.
22. Chilingarian G V, Vorabutr P, 1983, Drilling and drilling Fluids, Elsevier Science Publishers B V, New York.
23. Christoforou A P, Yigit A S, 1997, Dynamic modelling of rotating drillstrings with borehole interaction. Journal of Sound and Vibration, 206, 2, 234-260
24. Christoforou A P, Yigit A S, 1998, Coupled torsional and bending vibrations of drillstrings subject to impact with friction. Journal of Sound and Vibration, 215, 1, 167-181
25. Chugh C P , 1985, Manual of Drilling Technology, Blakema, Rotterdam.
26. Dabney J B Harman T L, 1998, Mastering Simulink, Prentice Hall Upper Saddle River, N.J.
27. Dareing, D, W; Livesay, B, 1968, Longitudinal and angular drillstring

- vibration with damping. ASME, Journal of Engineering for Industry, October 1-9.
28. Dawson, R, P; Lin, Y, Q; Spanos, P, D, 1987, Drill string stick-slip oscillations. Spring Conference of the society for Experimental Mechanics; Houston.
 29. Deliac E P & Fairhurst C, 1988, Theoretical and practical investigation of improved hard rock cutting systems, Proc. 29th US Symp. On Rock Mech. (Cundall P A, Sterling R L & Starfiel A M, editors), pp. 554-562
 30. Derjaguin, B, C; Push, V, E; Tolstoi, D. M, 1957, A theory of stick-slip of solids. Proc. Conference on lubrication and wear, London.
 31. Dudley, B, R; Swift, H, W, 1949, Frictional relaxation oscillations. The Philosophical Magazine, London, Series 7, 40, 849
 32. Dufeyte Henneuse, M, P, 1991, Detection and monitoring of the stick-slip motion: field experiment. SPE/IADC Drilling Conference. Amsterdam.
 33. Elsayed, M, A; Dareing, D, W; Vonderheide, M, A, 1997, Effect of torsion on stability, dynamic forces, and vibration characteristics in drillstrings. ASME, Journal of Energy Resources Technology, 119, 11-19.
 34. Fairhurst C, and Kim D, K, 1958, Energy transfer in percussive drilling. Proc. 8th Drilling and Blasting Symp. Univ. of Minnesota.
 35. Fairhurst, C, 1961, Wave mechanics of percussive drilling. Mine and Quarry Engineering, vol. 27.
 36. Finnie, I; Bailey, J, J, 1960, An experimental study of drillstring vibration. ASME, Journal of Engineering for Industry, May, 129-135.
 37. Fischer C, 1959, On longitudinal impact, I-III. Appl. Scient. Res., A8, 105-139, 277-308, A9, 9-42.
 38. Fischer H C , 1958, On Longitudinal Impact II. Elastic Impact of Bars with Cylindrical Sections of Different Diameters and of Bars with Rounded Ends, Appl. Sci. Res. Section A, Vol. 8, pp. 278-308
 39. Fish B, G, 1956, Percussive Rotary drilling. The Mining Magazine,

March, 133-142

40. Galvanetto U, Bishop S, R, Briseghella L, 1995, Mechanical stick-slip vibrations. *Int. J. of Bifurcation and Chaos*, vol. 5 No. 3 637-651
41. Göktan R M, 1990, Effect of cutter pick rake angle on the failure pattern of high-strength rocks, *Mining Science and Technology*, 11:281-285.
42. Hanselman D Littlefield B, 1998, *Mastering Matlab5*. A comprehensive tutorial
43. Harris C M, 1988, *Shock and Vibration Handbook*, McGraw-Hill, Inc, New York
44. Ibrahim R, A, 1994, Friction induced vibration, chatter, sequeal and chaos. Part II Dynamics and modelling. *Appl. Mech. Rev.* vol. 47, No.7 , 227-253
45. Ingraffea A R, Gunsallus K L, Beech J F & Nelson P, 1982, A fracture toughness testing system for prediction of tunnel boring machine performance, *Rock Mechanics. Proc. of the 23rd Symp.* 463-470, University of California
46. Inman D J, 1996, *Engineering Vibration*, Prentice Hall, Englewood Cliffs, New Jersey
47. International Society for Rock Mechanics. Committee on Laboratory Tests. Suggested methods for determining the uniaxial compressive strength and deformability of materials.
48. Jaeger C, 1979, *Rock mechanics and Engineering*, Cambridge University Press, Cambridge
49. Jansen J D, Van Dne Steen L, 1995, Active damping of self-excited Torsional vibrations in oil well drillstrings. *Journal of Sound and Vibration*, 179, 4, 647-668
50. Jansen, J, D, 1991, Non-linear rotor dynamics as applied to oil well drill string vibration. *Journal of Sound and Vibration*, 147, 115-135.
51. Jansen, J, D, 1992, Whirl and chaotic motion stabilized drill collars. *Society of Petroleum Engineers Drilling Engineering*, 7, 107-114.
52. Den Hartog, J, P, 1931, *Forced vibration with combined coulomb and*

viscous friction. ASME Transactions, Vol. 53, 9, 107-115

53. Kaidanovski, N, L; Khaikin S, E, 1933, J. Tech. Phys, 3, 1, USSR
54. Karlsson L G, Lundberg B, Sundin K G, 1989, Experimental Study of a Percussive Process for Rock Fragmentation, Int. J. Rock Mech. Min. Sci. & Geomech. Abstr. Vol. 26, No. 1, pp. 45-50
55. Kaski, J, 1993, On the generation of bending vibration in drilling rod. Proceedings of the 4th Biannual, ASME Design Technical conference on vibration and noise, Albuquerque, MN, DE-60, 355-362.
56. Kobrinski, A, E, 1969, Dynamics of mechanisms with elastic connections and impact systems. Ilif Books, London.
57. Koodinov, V, A, 1958, An investigation of the vibration of machine tools. Machgiz (State Mech. Eng. Press), 251, Moscow.
58. Kragel'skii I V, 1982, Friction and wear, Pergamon, Oxford
59. Kragel'skii I V, Mikhin N M, 1988, Handbook of friction Units of Machines. ASME Press, New York
60. Kragelsky I V, Dobychin N M, Kombalov V S, 1982, Friction and wear calculation methods.
61. Kumabe J, 1979, Vibrating Cutting, Mashinostroenie, Russian translation, Moscow, 1985
62. Gekker, F, P, 2001, Sliding friction of dry non-lubricated surfaces of rigid bodies- a vibro-impact process. XIII Russian symposium, "Dynamics of vibro-impact systems"; (in Russian).
63. Kyllingstad, Å; Halsey, G, W, 1988, A study of slip stick motion of the bit. Society of Petroleum Engineers Drilling Engineering, 3, 369-373.
64. Lacabanne W, D, and Pfeleider E, P, 1955, Rotary-Percussive blast hole machine may revolutionise drilling. Mining Engineering, vol. 7 No.9, 850-855
65. Leine L, L, Van Campen D H and De Kraker A, 1998, Stick-slip vibrations induced by alternate friction models. Nonlinear Dynamics, 16: 41-54.
66. Liang J W, Feeny B F, 1998, Identification of Coulomb and viscous friction from free-vibration decrements. Nonlinear Dynamics, 16, 337-

- 347.
67. Lukomskii S, I, 1959, Investigation into the operation modes of vibratory hammers. Transactions of VNII Stroidormasha, 24, 3-40, (in Russian)
 68. Lundberg B & Karlsson L G, 1986, Technical Note. Influence of Geometrical Design on the Efficiency of a Simple Down-the-hole Percussive Drill, Int. J. Rock Mech. Min. Sci. & Geomech. Abstr. Vol. 23, No. 3, pp. 281-287, Great Britain
 69. Lundberg B, 1985, Microcomputer Simulation of Percussive Drilling, Int. J. Rock Mech. Min. Sci. & Geomech. Abstr. Vol. 22, No. 4, 237-249.
 70. Lundberg, B, 1973, Energy transfer in percussive rock destruction. Parts I, II, III. Int J. of Rock Mechanics, vol. 10 No. 5 381-435
 71. Masri S F, 1972, Forced Vibration of a Class of Non-Linear Two-Degree-Of-Freedom Oscillators, Int. J. Non-Linear Mechanics. Vol. 7, 663-674
 72. Mcugh S; Gupta Y; Seaman L; 1981, Pipe Missile impact experiment on concrete models; SRI International, Menlo Park, CA (USA).
 73. Meirovitch L, 1997, Principles and Techniques of vibrations, Prentice Hall, Upper Saddle River, New Jersey
 74. Mitchell, R, F; Allen, M, B, 1985, The key to BHA failure analysis. World Oil, March, 101-104.
 75. Muro T, Takegaki Y, Yoshikawa K, 1997, Impact Cutting Property of Rock Material Using a Point Attack Bit, Journal of Terramechanics, Vol. 34, No. 2, pp. 83-108.
 76. Neilson R D, Rodger A A, Stevenson R G, 1995, Development of computer based model of vibro-impact driving. Machine Vibration, 3, 164-175, Springer-Verlag, London
 77. Neimark, Yu, I, 1953, Theory of vibration driving and vibro-penetration; in Engineering collection, vol. 16; (in Russian).
 78. Nougaro J, 1963, Le forage rotary; Institut Français du petrole et Societe des Editions Technip.
 79. Palmov, V, 2000, Vibration of elasto-plastic bodies, Berlin: Springer-

- Verlag. Translation from Russian, Nauka, Moscow 1976.
80. Panovko Ya G, 1977, Introduction to the theory of mechanical impact. Moscow, Nauka, (in Russian)
 81. Panovko Ya G, Gubanov I I, 1967, Stability and Vibrations of elastic systems. Moscow, Nauka, (in Russian)
 82. Paone J, and Madson D, 1966, Drillability studies – Impregnated diamond bits. Washington, US, Bureau of Mines, R.I. 6776
 83. Pasley, P, R; Bogy, D, B, 1963, Drill string vibration due to intermittent contact of bit teeth. ASME, Journal of Engineering for Industry, May, 187-194.
 84. Pavone, D, R, 1994, SPE 28324, Application of high sampling rate downhole measurements for analysis and cure of stick-slip.
 85. Protodyakonov M, M, 1963, Mechanical properties and drillability of rocks. 5th Symp. on Rock Mechanics, Univ. Minnesota, 103-118
 86. Rao S S, 1995, Mechanical vibrations, Addison-Wesley Publishing Company, New-York.
 87. Rappold, Keith, 1993, Drillstring vibration measurements detect bit stick-slip. Oil & Gas Journal, Mar, 1, 66-70
 89. Rebrik B, M, 1979, Drilling during engineering-geological exploration. Nedra, Moscow (in Russian)
 90. Robinowicz E, 1965, Friction and wear of materials, Wiley & Sons, New York
 91. Rodger, A, A, and Littlejohn, G, S, 1980, A study of vibratory driving in granular soils. Geotechnique, 30, No.3 269-293.
 92. Sakamoto T, 1985, Normal displacement and dynamic friction characteristics in a stick-slip friction process; Tribology International, 20, 1, 25-31
 93. Sakamoto T, 1985, Normal displacement of the sliding body in a stick-slip friction process; Proc. Of JSLE Intl. Trib. Conf. Tokyo, 141-146.
 94. Savinov, O, A, Luskin, A, Ya, 1960, Vibrational method of pile driving and its application in civil engineering, Moscow, Gossizdat; (in Russian).
 95. Schiehlen W, (ed.) 1990, Nonlinear dynamics in engineering systems.

IUTAM Symp., Stuttgart, Germany, August 21-25, 1989, Springer-Verlag.

96. Schmidt R, L, 1972, Drillability studies – percussive drilling in the field. Washington, US, Bureau of Mines, R.I. 7684
97. Shah S M A, 1992, The optimisation of PCD bit performance in coal measures rocks. PhD Thesis, Univ. Nottingham, UK.
98. Simon, R, 1956, The theory of rock drilling. 6th Annual Drilling Symp. Univ. Minnesota, 1-14.
99. Simon, R, 1964, Transfer of the stress wave energy in the drill steel of percussive drill to the rock. *Int. J. Rock. Mech. Min. Sci.*, 1, 397-411
100. Sinclair, D; Manville, N, J, 1955, Friction vibration. *ASME J. Appl. Mech.* 207-213
101. Singh D, P, 1969 Drillability and physical properties of rocks. *Proc. Rock Mechanics Symp.* Sidney, Inst. of Engrs. Australia.
102. Smith Tool, 1979, The technique, tools, and technology of drilling. Irvine, Calif., 92713:11
103. Soundranayagam, S, A, 2000, Investigation of nonlinear transformation of impulses in impact units for improvement of hammer drill performance. PhD Thesis, Loughborough University.
104. Spektor M, 1981, Motion of soil-working tool under impact loading. *J. of Terramechanics*, vol. 18, No.3, 133-156
105. Spektor M, 1981, Principle of soil-tool interaction. *J. of Terramechanics*, vol. 18, No.1, 51-65.
106. Spektor M, 1983, Working processes of cyclic-action machinery for soil deformation – Part I. *J. of Terramechanics*, vol. 20, No.1, 13-41
107. Spektor, M, 1980, Minimisation of energy consumption of soil deformation. *J. Terramechanics*, 17, No.2, 63-77
108. Stevenson R G, 1992, An investigation into the use of vibro-impact techniques in the design of a ground moling system. PhD Thesis, Univ. Aberdeen, UK
109. Stribeck R, 1902, Die wesentlichen Eigenschaften der Gleit- und Rollenlager- The key quantities of sliding and roller bearing, *Zeitschrift*

- desVereins deutscher Ingenieure, 46(38,39), 1342-48, 1432-37
110. Thill R, E, and Peng, S, S, 1974, Statistical comparison of the pulse and resonance methods of determining elastic moduli. Washington, US, Bureau of Mines, R.I. 7831
 111. Thomas, S, 1930, Vibrations damped by solid friction. The Philosophical Magazine, London, Series 7 vol. 9, 392
 112. Timoshenko S, 1955, Vibration Problems in Engineering
 113. Timoshenko, S, and Goodier, J,N, 1951, Theory of elasticity. 2nd edit., McGraw-Hill, New York.
 114. Tolstoi D M, 1967, Significance of the normal-degree-of-freedom and natural normal vibration in contact friction; Wear 10, 199-213.
 115. Tolstoi D M, Borisova G A, Grigorova S R, 1971, Role of intrinsic contact of oscillations in normal direction during friction; in Nature of the friction in solids; Nuyka I Teknica, Minsk.
 116. Tsaplin S, A, 1953, Vibro-impact mechanisms for road and bridge construction. Avtotransizdat, Moscow (in Russian), National Laboratory Translation No.1003
 117. Tseitlin, M, G, Verstov, V, V, and Azbel, G, G, 1987, Vibrational techniques and technology in pile driving and drilling; (in Russian).
 118. Van De Vrande B L, Van Campen D H and De Kraker A, 1999, An Approximate Analysis of Dry-Friction-Induced Stick-Slip Vibrations by a Smoothing Procedure, Nonlinear Dynamics Vol. 19, pp. 157-169, Netherlands.
 119. Veytukov M M, Dobroslavskii S V, Nagaev R F, 1990, Self-excited vibration in a system with dry friction, Characteristic of hereditary type. Izv. AN SSSR. Mekhanika Tverdogo Tela, vol. 25, No. 1 23-28.
 120. Vutukuri V S, Lama R D, Saluja S S, 1974, Handbook on Mechanical properties of Rocks, Volume 1.
 121. Wang Yu, Mason Matthew T, 1992, Two-Dimensional Rigid-Body Collisions With Friction, Journal of Applied Mechanics Vol. 59, pp. 635-642.
 122. Wells, J, H, 1929, Kinetic boundary friction. The Engineer, London,

- 147, 454.
123. Wootton D, 1974, Aspects of energy requirements for rock drilling. PhD Thesis, Univ. Leeds, UK
 124. Wu C M and Lundberg B, 1994, Efficiency of Percussive Drilling of Rock With a Bent Drill Rod, *Int. J. Impact Engng* Vol. 15, No. 6, pp. 735-747, Great Britain
 125. Yao-Qun Lin, Yu-Hwa Wang, 1991, Stick-slip vibration of drill string. *Transaction of ASME, J. of Engineering for Industry*, vol. 113, 38-43.

Appendices

Appendix 1: Published papers and views of experts

During the course of this investigation, two papers were published and a research proposal was developed and submitted to EPSRC for a grant to support further work toward the development of a prototype device. Bellow is the extract from the referees' comments on the project.

Published papers:

1. Batako A D; Babitsky V I; Halliwell N A, 2003, A self-excited system for percussive-rotary drilling; Journal of sound and vibration, 259(1), pp 97-118
2. Batako A D; Babitsky V I; Halliwell N A, Modelling of vibro-impact penetration of a self-excited drill bit; Journal of sound and vibration, *in press*

Proposal reference GR/R91335/01 - Views of EPSRC referees

Referee G7ZYHC:

Expertise area: Research in drilling technology and drilling measurement diagnostics in the oil and gas industry.

"...While both stick-slip bit vibration and percussive drilling are well known, the concept of using the stick-slip constructively to drive percussion is new. Indeed, I am not aware of other research on positively exploiting of the self-generated stick-slip oscillations"

Referee 41Z3X2,

Expertise area: Mechanical design,; Vibratory technology and vibration control.

" The proposed drilling technology is original, as far as the reviewer knows. It can definitely be a subject of a patent application. I believe that the proposed project may become an interesting application of vibro-impact systems for an important technological area."

Referee Q615E1,

Expertise area: Petroleum engineering for 27 years.

"...If the outcomes were positive it would add a very significant dimension not just in the understanding of drilling rocks but also in adding the potential of new technology and potential cost savings in what is a very significant cost element in oil and gas field exploration and development."

Appendix 2: Actual view of the drilling rig



DS – Drilling structure
FT – Fluid tank
LC – Loading conveyor
RS – Rock samples
PC – Data logging PC

MTM – Material testing machine
HCU – Hydraulic control unit
FG – Function generator
Sc – Two-channel oscilloscope
TC – Thyristor controller (motor speed)

Appendix 3: Sample programmes in MatLab code.

A3-1

```
%cyclic running of Rop_effectiv.mdl
% to estimate the relieve of the main drive.
% the amplitude of Impact and the frequency change for each simulation
% the Threshold force is fixed
clear all;

tt= cputime;
tic ;          %sim_start, start time
mu = 0.4;
g = 9.81;
Vcr = 3;
m1 = 250;
mas_rat =.4;
c2 = 250;
% changing variables, for getting different working regimes.
F1=250e3; % Treshold force, N
fre= 2; % frequecy in Hz
A=250e3; % impact force amplutide 2e6 by default;
K3=30e7 % rock stiffness;
% for a coef. of restitution R=0.1~0.3,
% the loss factor zeta= 0.5~0.91
C3=20e4;      % default rock damping
zeta= 0.9;
C3= zeta*2*sqrt(m1*K3);

slip=[];
PD=[];
Fav=[];
Rop=[];
Gama=[];
Neta=[];
Zeta=[];
a3=[];
A3=[]; %Full swing of X3

D=F1;          % F1= D, force required to overcome the threshold force D.
n=0; % counter
n=0;s=0; s1=0; % counter

temp_name='dat.t'; % Temporary file name where data are save and then copied
data_name ='data_out'; %Variable containing all data
fname='Ampl_freq_'; % file to be saved after running the simulation 20 times
Fre_stop=40;
```



```

for fre=10:10:Fre_stop
    sl=s1+1
    s=fre;
    omega=fre*2*pi;
    fout=strcat(fname,num2str(s), '.txt');

    for A=150e3:25e3:300e3    % impulse magnitude, N
        n=n+1;
        sim('Rop1_Effectiv');
        % locate the beginning of the slop
        for j = 45:1:110
            if ((x4(j+1)==x4(j))& (x4(j+2)>x4(j+1)))
                slop_start=x4(j+1);
                b=j+1; % X4 index where the slop of he slip starts.
                break
            end
        end
        % locate the end of the slop
        for k = b:1:b+15
            if ((x4(k+1)>x4(j))& (x4(k+2)==x4(k+1)))
                slop_end=x4(k+1);
                %bk=k+1    % debugging purpose only
                break
            end
        end
        slip0=slop_end-slop_start;
        periode=1/omega;
        x4_rate=slip0/periode;
        a3n= mean(amp_x3_x4(length(amp_x3_x4)-200:length(amp_x3_x4)));
        Ful_a3=a3n*2;    %full swing of X3
        a3(n)=a3n;
        A3(n)= Ful_a3;
        slip(n)=slip0;
        Fav(n)=mean(force(length(force)-200:length(force)));
        PD(n)=round((Fav(n)/D)*1000)/1000; %Fav(n)/D;
        Rop(n)=x4_rate;    % ROP= rate of penetration or speed of penetration.
        Neta(n)=slip(n)/a3n ;
    end
    if (s1<=1)
        Z_Rop=Rop;
        Z_PD=PD;
        Z_Fav=Fav;
        Z_Neta=Neta;
        Z_A3=A3;
        Z_slip=slip;
    else

```

```

Z_Rop=[Z_Rop; Rop];
Z_PD=[Z_PD; PD];
Z_Fav=[Z_Fav; Fav];
Z_Neta=[Z_Neta; Neta];
Z_A3 =[Z_A3; A3];
Z_slip=[Z_slip; slip];
end
% reset values to zero
if (fre< Fre_stop)
    slip=[];
    PD=[];
    Fav=[];
    Rop=[];
    Neta=[];
    a3=[];
    A3=[];
    n=0;
end
end
Fin='DONE'
toc ;
duration = (cputime-tt)/60    %computing time in minutes

```

```

%fft.m
%computes the FFT of the system response signal
%sampling time

p=9; L=2^p; %FFT buffer length
xd10=[];
lx= length(x1dot);
x1d0=x1dot(lx-512:lx); %number of FFT point
y=fft(x1d0,L);
yy=y.*conj(y)/L;
f=1000*(0:L/2-1)/L;

figure(1);

subplot(2,1,1); plot(t, x1dot, '-k');
xlabel ('time, s')
ylabel ('bit relative velocity, m/s')

subplot(2,1,2);
plot(f,yy(1:L/2), '-k');
%bar(f,yy(1:L/2));
xlabel ('frequency, Hz')
%set(gca,'XLim',[0 20],'YLim',[auto]);

figure(2)

lx1= length(x1);
plot(x1(lx1-1000:lx1), x1dot(lx1-1000:lx1), '-k');
xlabel ('bit displacement, m')
ylabel ('bit velocity, m/s')

figure(3)

plot(x1(lx1-2000:lx1), x1dotabs(lx1-2000:lx1), '-k');
xlabel ('bit displacement, m')
ylabel ('bit absolute velocity, m/s')

figure(4)

%plot3(t(lx1-4000:lx1), x1(lx1-4000:lx1), x1dotabs(lx1-4000:lx1), '-k');
plot3(t, x1, x1dotabs, '-k');
xlabel ('time, s')
ylabel ('bit displacement, m')
zlabel ('bit velocity, m/s')

```

```

% *****
% striker section
% *****

lx2= length(x2dot);
x2d0=[];
x2d0=x2dot(lx2-512:lx2);
y1=fft(x2d0,L);
yy1=y1.*conj(y1)/L;
f1=1000*(0:L/2-1)/L;

figure(5);

subplot(2,1,1); plot(t, x2dot, '-k');
xlabel ('time, s')
ylabel ('striker velocity, m/s')

subplot(2,1,2);
%bar(f,yy(1:L/2),0.05); % '-k');
plot(f,yy(1:L/2), '-k');
xlabel ('frequency, Hz')

figure(6)

lx3= length(x2);
plot(x2(lx3-500:lx3), x2dot(lx3-500:lx3), '-k');
xlabel ('striker displacement, m')
ylabel ('striker velocity, m/s')

figure(7)

subplot(2, 1 ,1)
plot(t, x1 , t, x2, '-k', 'LineWidth',1)
set(gca,'XLim',[8.11 8.91], 'YLim', [-0.15 0.06])
xlabel ('time, s')
ylabel ('displacement, m')
legend('bit', 'striker');

subplot(2, 1 ,2);
plot(t, x1dot, t, x2dot, '-k', 'LineWidth',1)
set(gca,'XLim',[8.11 8.91], 'YLim', [-3 3])
xlabel ('time, s')
ylabel ('velocity, m/s')

figure (8)

```

```

%===== 4 subplots in one frame
%bit
subplot(2,2,1); plot(t, x1dot, '-k');
xlabel ('time, s')
ylabel ('bit relative velocity, m/s')
%title ('v = 1 m/s')

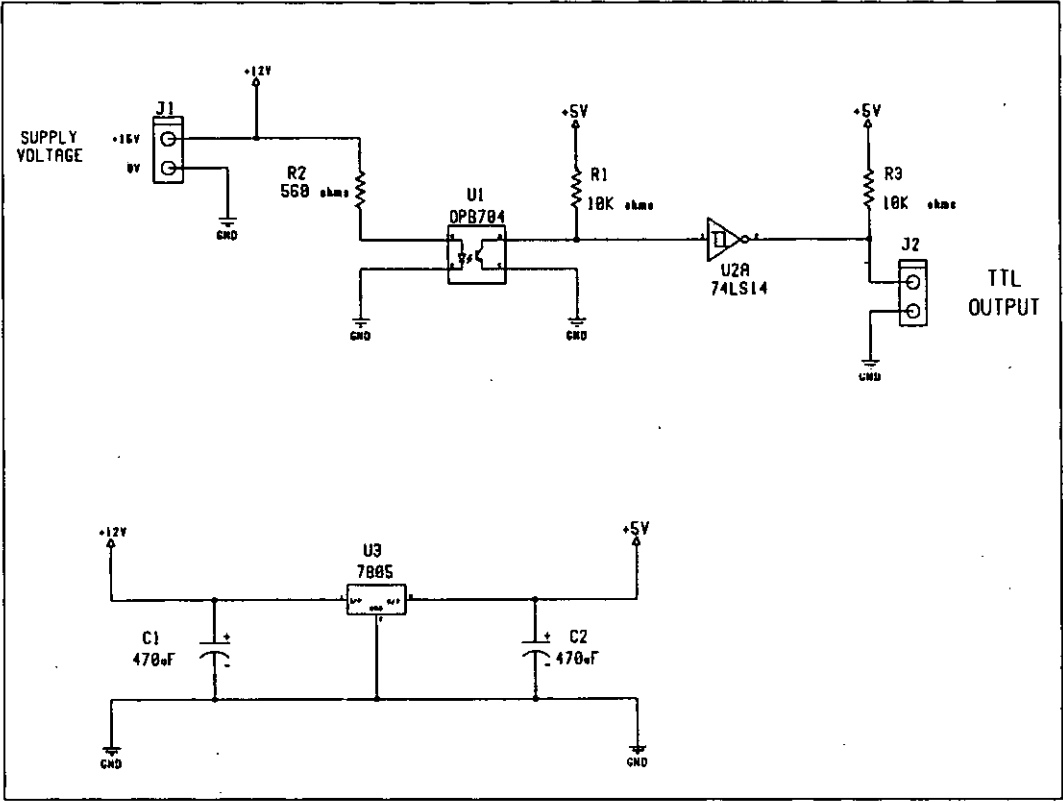
subplot(2,2,3);
plot(f,yy(1:L/2), '-k');
%bar(f,yy(1:L/2), 0.05);
xlabel ('bit frequency, Hz')
ylabel ('PSD');

%=====
%striker
subplot(2,2,2); plot(t, x2dot, '-k');
xlabel ('time, s')
ylabel ('striker velocity, m/s')

subplot(2,2,4);
%bar(f1, yy1(1:L/2),0.05)
plot(f1, yy1(1:L/2),'-k');
xlabel ('striker frequency, Hz')
ylabel ('PSD')
% set(gca,'XLim',[0 25],'YLim',[-0.02 0.02])

```

Appendix 4- 1: Electrical circuit of the opto-switch for monitoring the rotation speed



Opto-switch, electrical circuit

Appendix 4- 2: Results of rock samples test.

Department of Civil and Building Engineering
Loughborough University

Rock Sample Testing for Andre Batako

A core sample 54mm diameter was taken from each of the test blocks and prepared for Unconfined (uniaxial) Compressive Strength (UCS) testing. The density of each of the samples was also measured.

Sample Descriptions

Sandstone pale brown, medium grained, moderately cemented sandstone.
Limestone buff to pale brown, medium to coarse grained oolitic limestone.
Granite white and grey coarse grained granite.

Density

Sample	Density (Kg/m ³)
sandstone	2382
limestone	2480
granite	2687

UCS

These tests were carried out on a Denison Block Testing System and the machine print outs are enclosed. A loading rate of 0.17 KN/second was used.

Sample	Length (mm)	Diameter (mm)	Max load at failure (KN)	UCS (MPa)
sandstone	108	54	61.9	84.91
limestone	108	54	140.3	192.46
granite	108	54	204.5	280.52

The UCS values for the limestone and especially the granite seem rather high but your sample blocks are very good fresh dry rock samples. Several more tests on each rock type would be needed to confirm these values, but they are a guide.

Tests were carried out on 7th and 8th July 1999.

R.J.Elson
09/07/99

Appendix 4- 3: Uniaxial Unconfined Compressive Strength test; computer results.

DENISON
BLOCK TESTING SYSTEM

Wed, 07 Jul 1999, 16:39:46

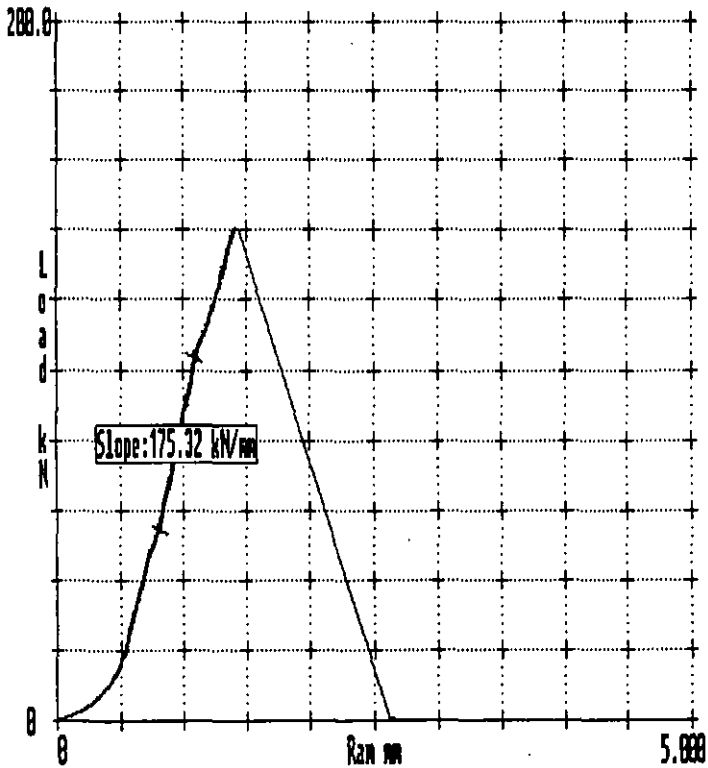
DENISON DATABASE RETRIEVAL SYSTEM

Page 1

Sample Ref	Batch Ref	Date	Graph	Sequence Id	# Functions
limestone		07/07/99	Yes	roger	1

1 Defined Function(s)			
1 :Slope	UNITS:Load/Ram	Slope :175.32	kN/mm

TEST COMMENT	TEST SEQUENCE DETAILS
Max Load 140.3 kN	roger
54mm dia / 100 long	civil lab 1



UCS test, Load-displacement plots; Limestone

DENISON
BLOCK TESTING SYSTEM
Wed, 07 Jul 1999, 16:13:07

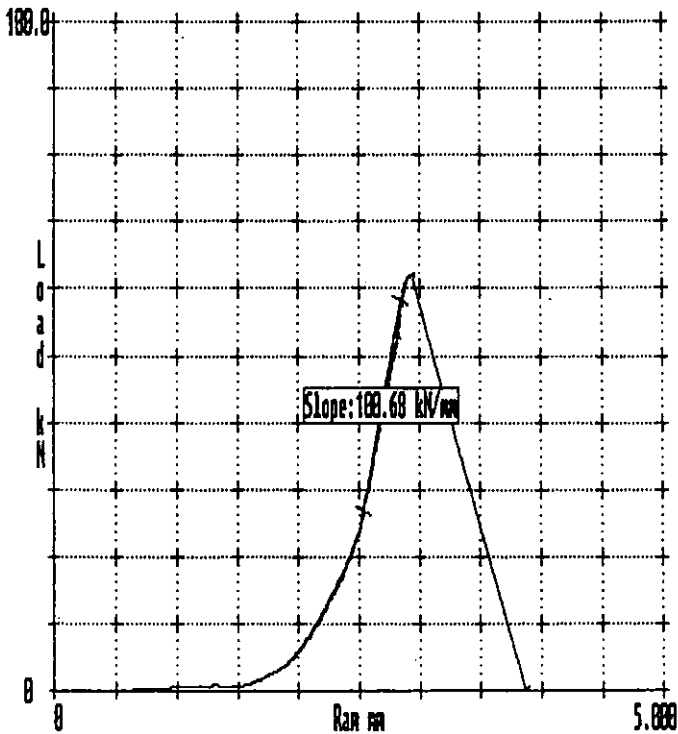
DENISON DATABASE RETRIEVAL SYSTEM

Page 1

Sample Ref	Batch Ref	Date	Graph	Sequence Id	# Functions
sandstone		07/07/99	Yes	roger	1

1 Defined Function(s)			
1 :Slope	UNITS:Load/Ram	Slope :100.68	kN/mm

TEST COMMENT	TEST SEQUENCE DETAILS
Max Load 61.9kN	roger
54mm dia / 108mm long.	civil lab 1



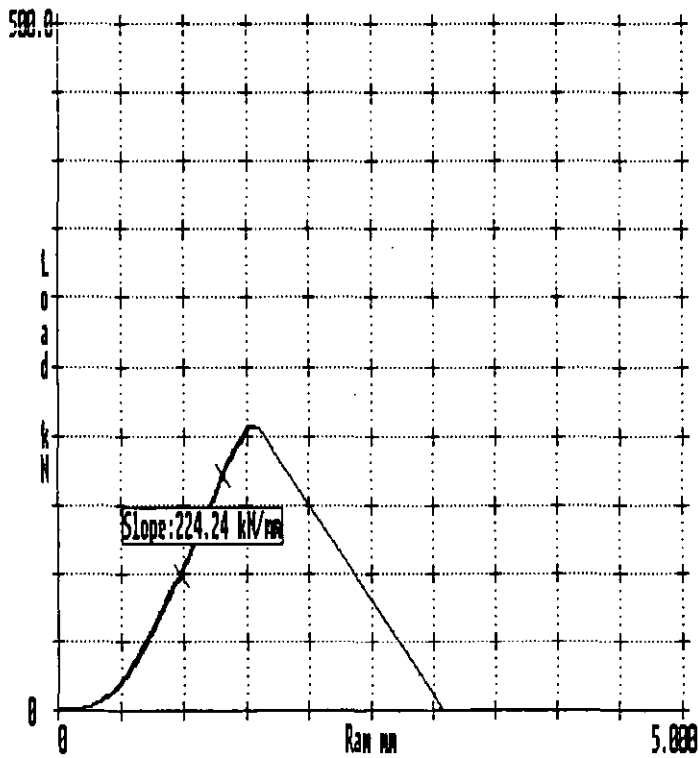
UCS test, Load-displacement plots; Sandstone

**DENISON
BLOCK TESTING SYSTEM**
Thu, 08 Jul 1999, 08:55:33

Sample Ref	Batch Ref	Date	Graph	Sequence Id	# Functions
granite		08/07/99	Yes	roger	1

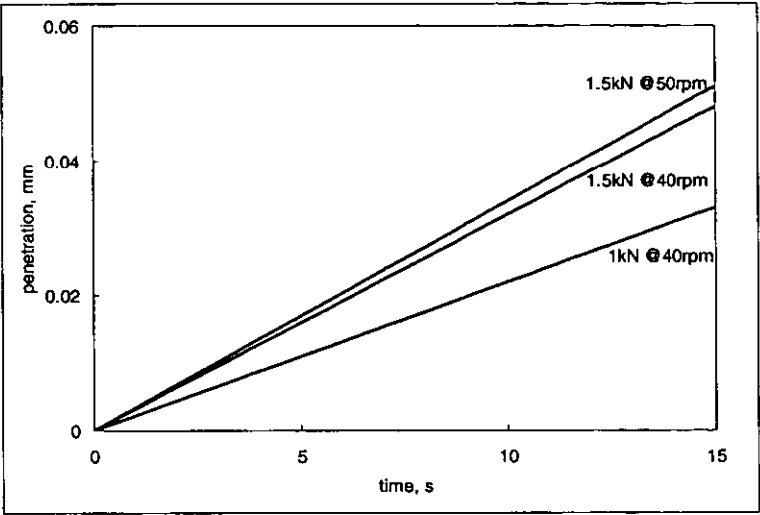
1 Defined Function(s)			
1 :Slope	UNITS:Load/Ram	Slope :224.24	kN/mm

TEST COMMENT	TEST SEQUENCE DETAILS
Max Load 204.5 kN	roger
54mm dia / 108mm long	civil lab 1

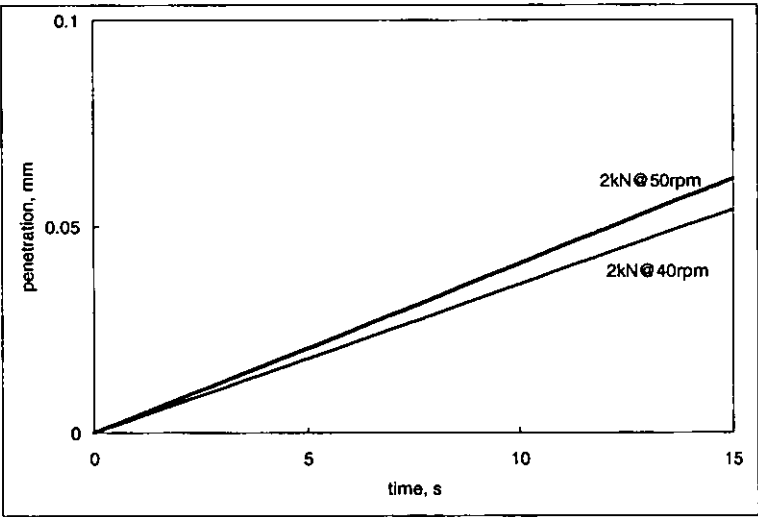


UCS test, Load-displacement plots; Granite

Appendix 4- 4: Rate of penetration with variable speed of rotation

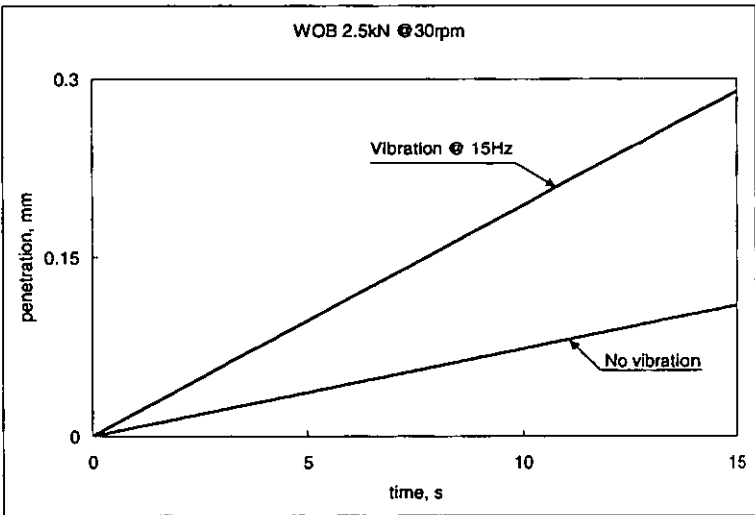
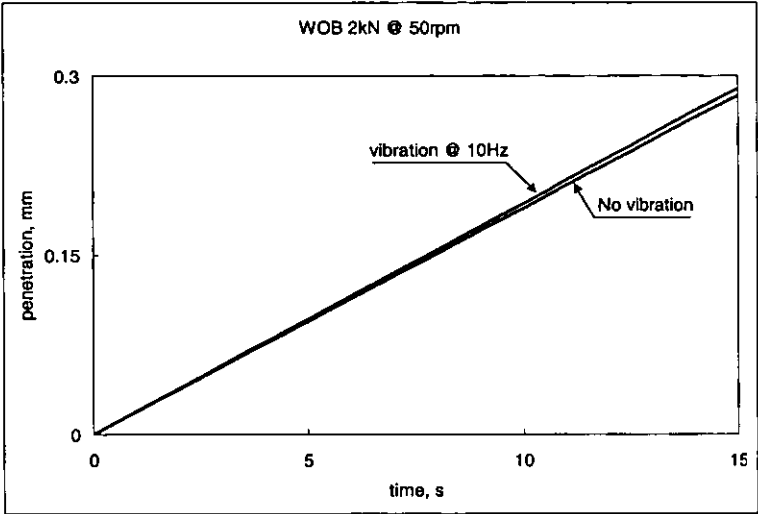


Penetration in limestone with WOB= 1kN, 1.5kN

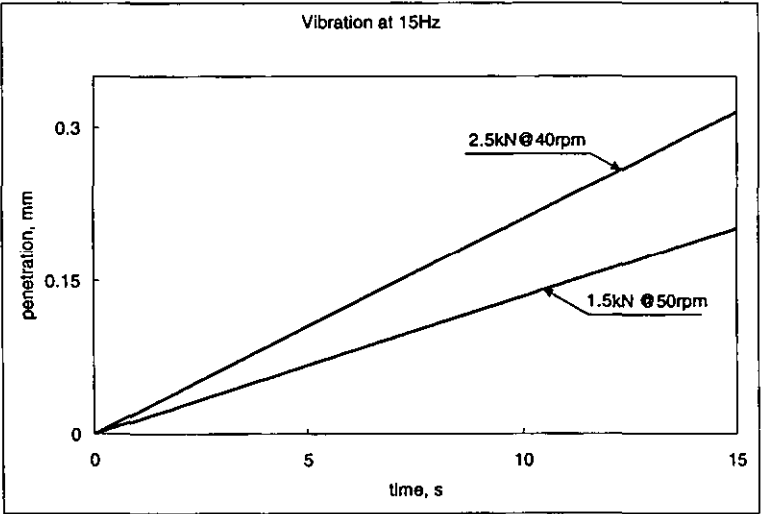


Penetration in limestone with WOB= 2kN

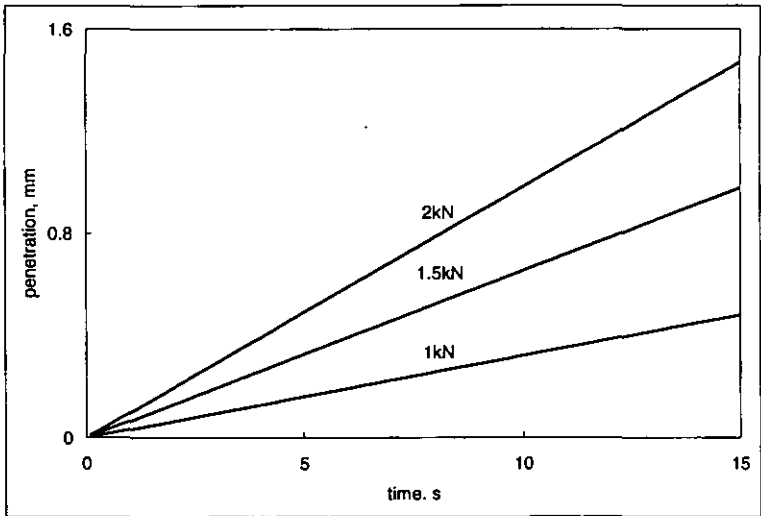
Appendix 4- 5 Rate of penetration in vibration drilling



Drilling in sandstone with vibration.

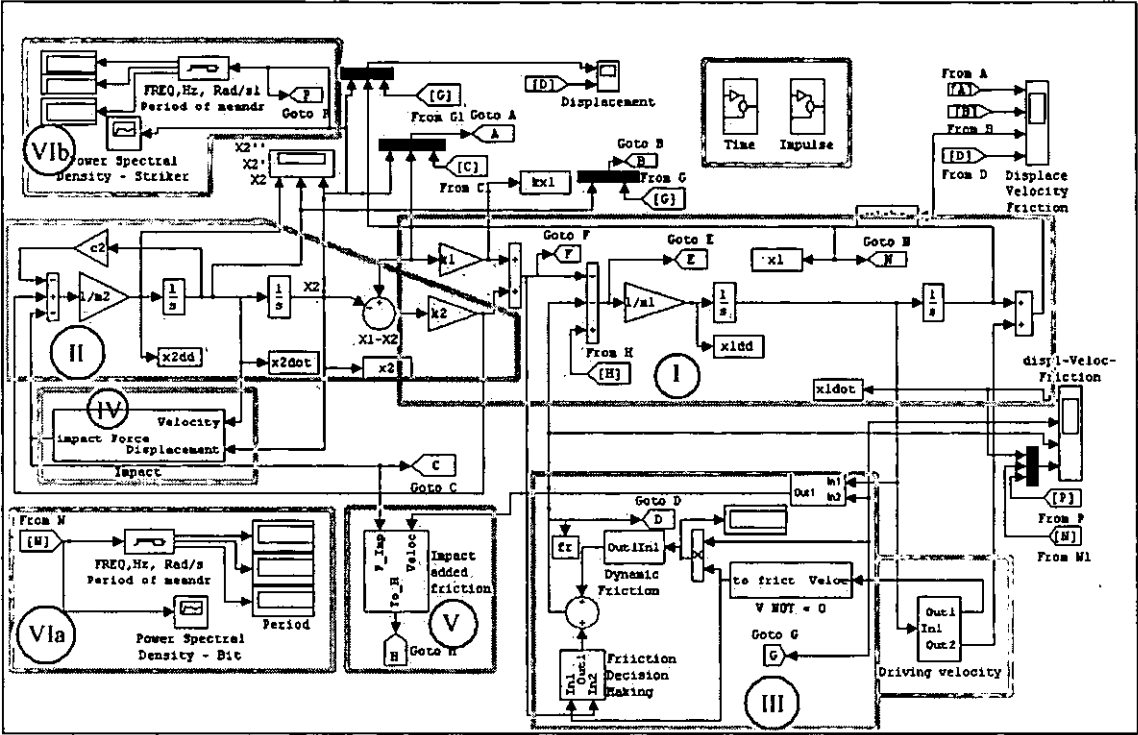


Drilling in sandstone with vibration at 15Hz.



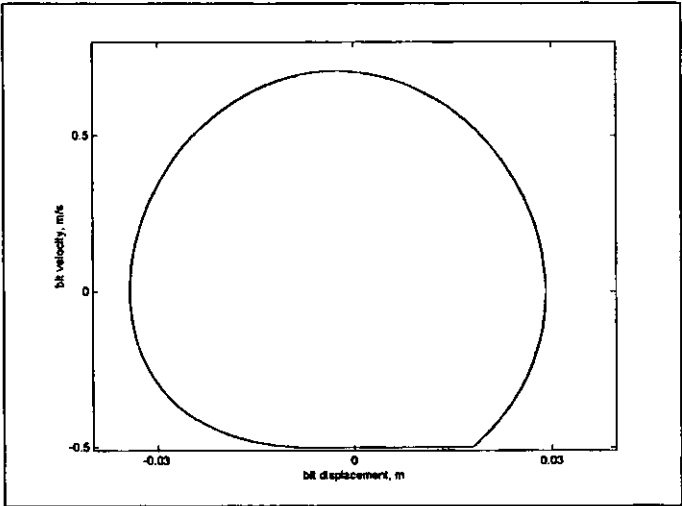
Drilling in limestone with vibration at 15Hz

Appendix 5- 1: Simulink model of the main system

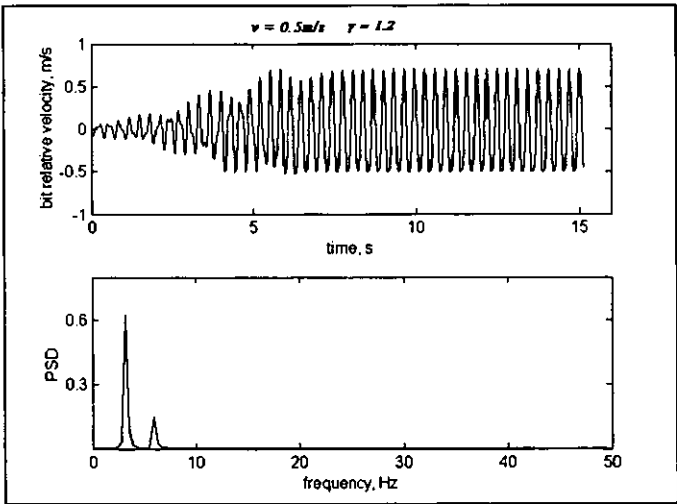


Appendix 5- 2: Results of further simulation for $\beta=0.3$; $\gamma \in [1.2 \ 12]$

$m_I=250\text{kg}$; $k_I=156250\text{N/m}$; $c_2= 75 \text{ N.s/m}$; $v=0.5\text{m/s}$;

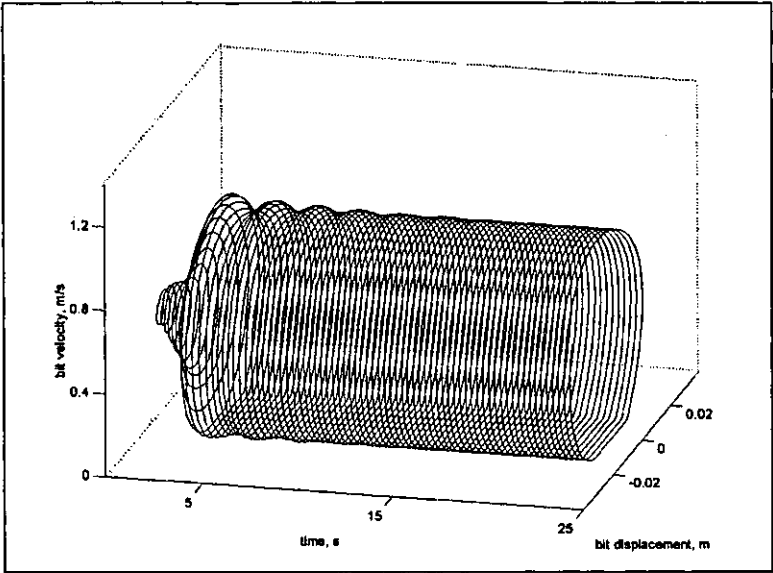


Phase portrait of bit motion for $\gamma=1.2$,

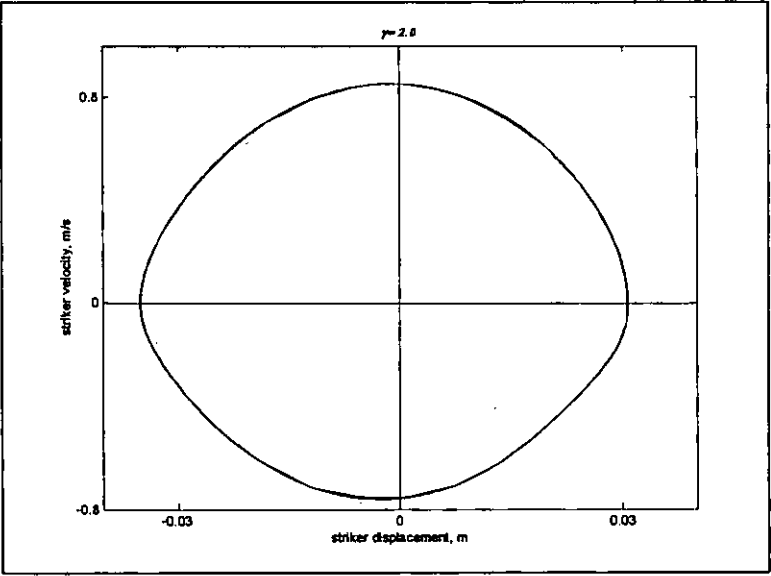


Time history of bit velocity showing the system response at 3.2HZ for $\beta=0.3$; $\gamma=1.2$; $v=0.5\text{m/s}$

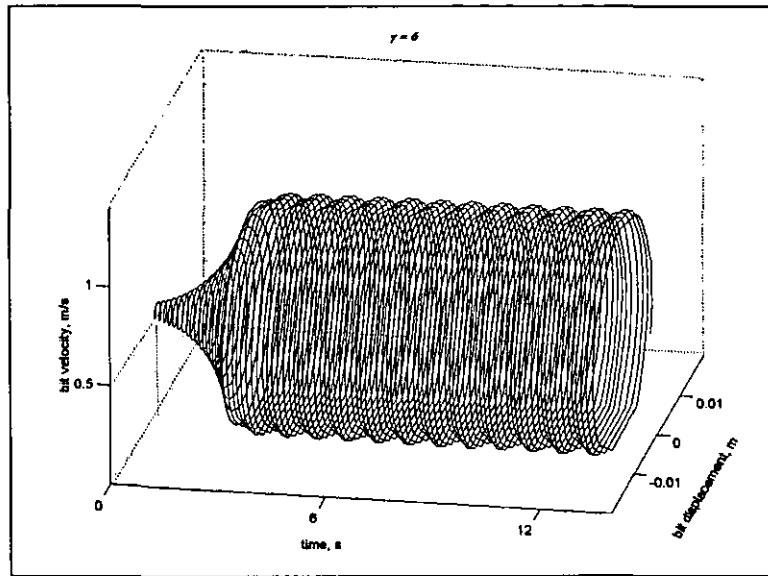
With the configuration of the system as given above, the normal frequencies calculated from equation 5.17 are $\omega_{h1}=5.93\text{Hz}$; $\omega_{h2}=3.2\text{Hz}$. It is seen that the system vibrates at its lower normal frequency.



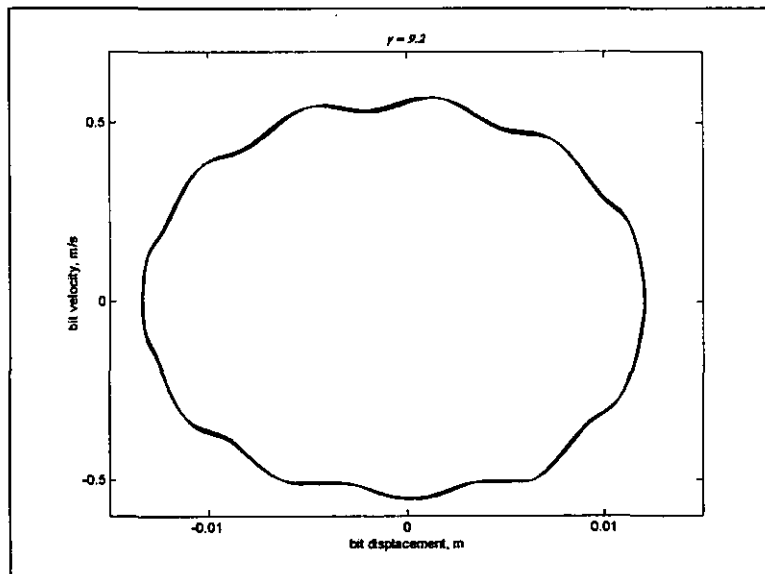
Time contained phase plot of bit motion for $\gamma=1.5$; $v=0.5\text{m/s}$



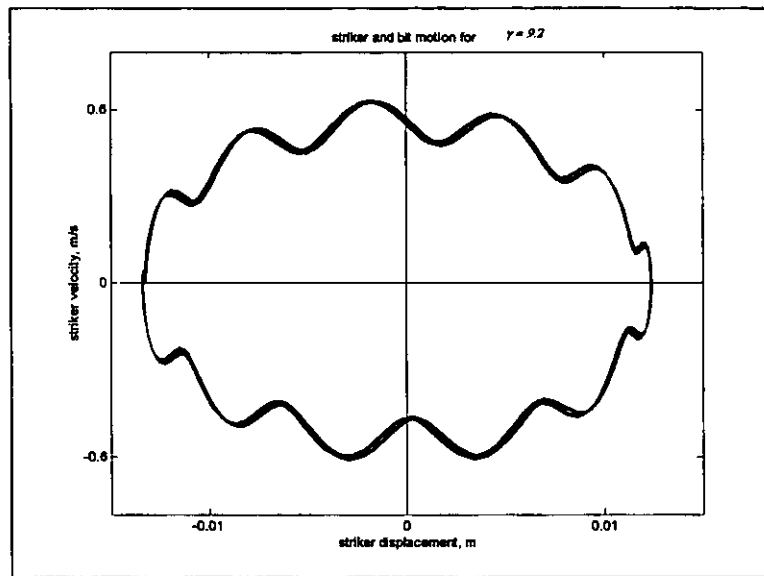
Phase portrait of striker motion for $\gamma=2$; $v=0.5\text{m/s}$



Time contained phase plot of bit motion for $\gamma=6$; $v=0.5\text{m/s}$



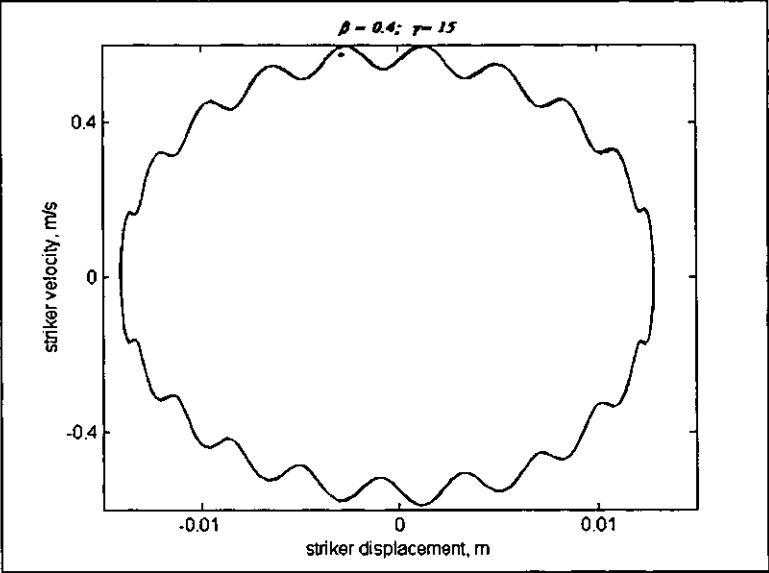
Phase portrait of bit motion for $\gamma=9.2$; $v=0.5\text{m/s}$



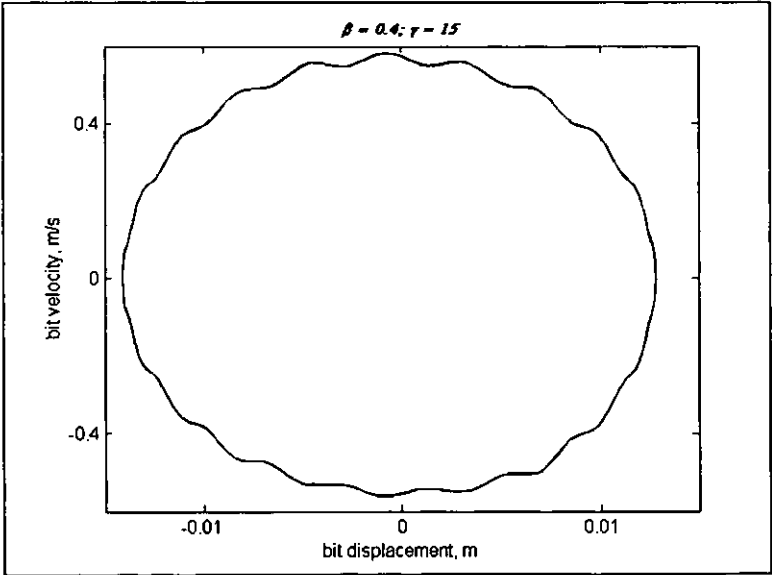
Phase portrait of striker motion for $\gamma=9.2$; $v=0.5\text{m/s}$

Appendix 5- 3: Results of further simulation for $\beta=0.4$; $\gamma \in [12 \ 15]$

$m_I=250\text{kg}$; $k_I=625000\text{N/m}$; $c_2=75\text{ N.s/m}$; $v=0.5\text{m/s}$;



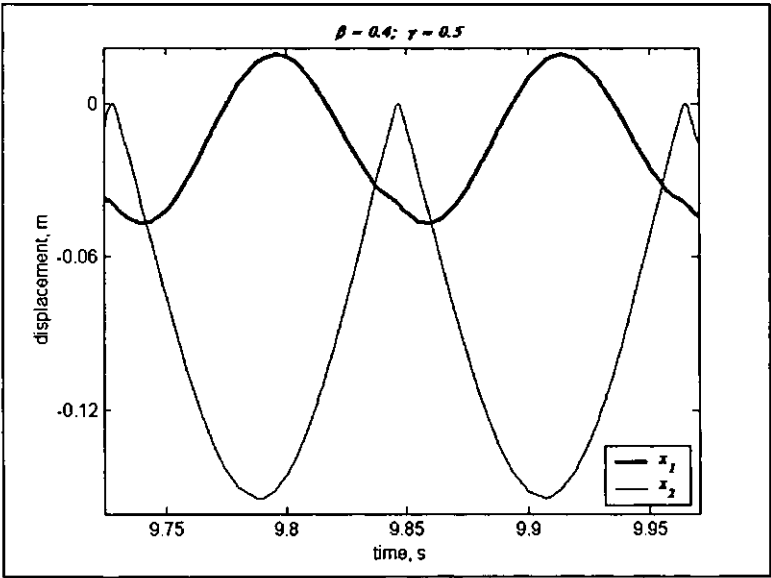
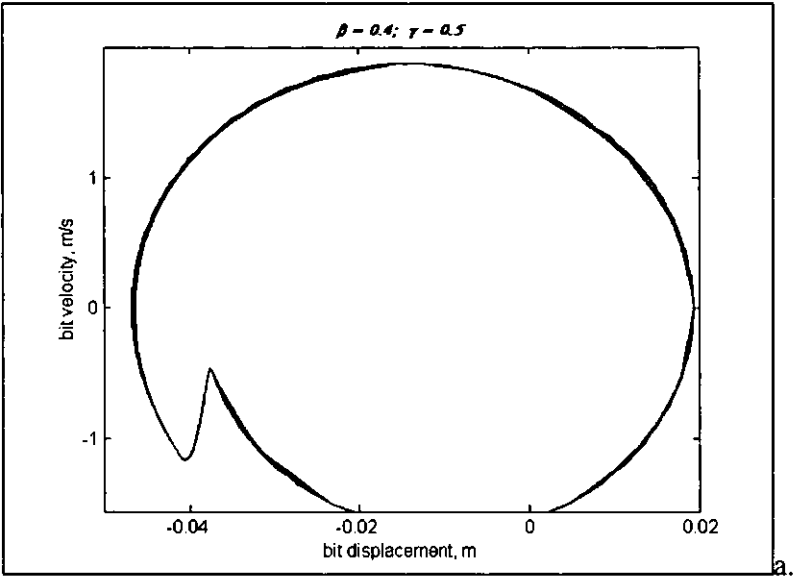
Phase portrait of striker motion for $\beta=0.4$; $\gamma=15$



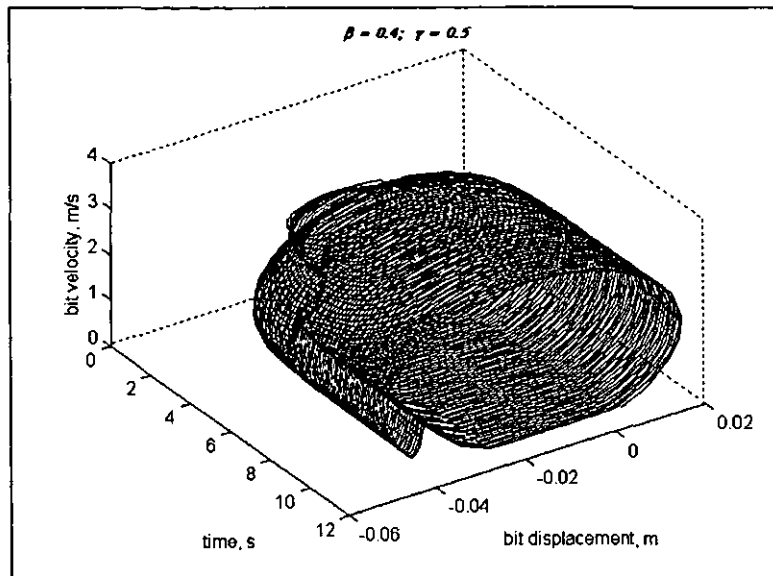
Phase portrait of bit motion for $\beta=0.4$; $\gamma=15$

Vibro-Impact Motion

Appendix 5- 4: System response for values of $\gamma < 0.6$

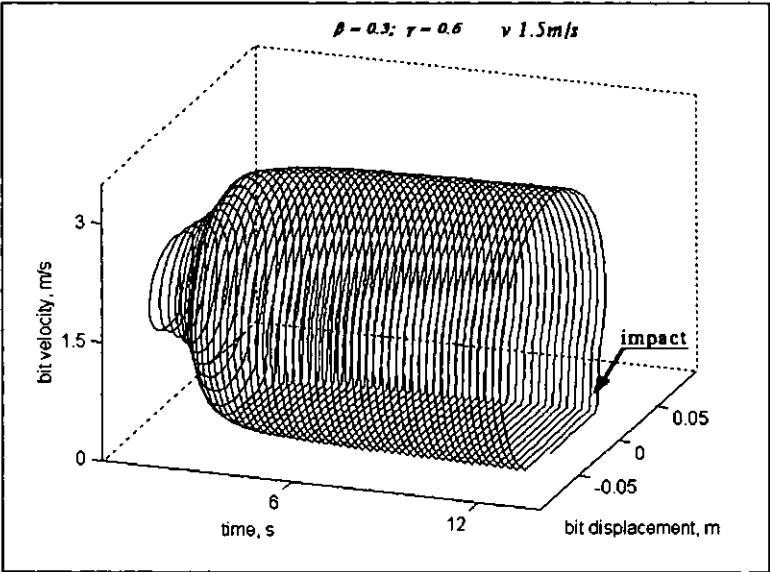


Striker and bit displacement $\beta=0.4; \gamma=0.5$

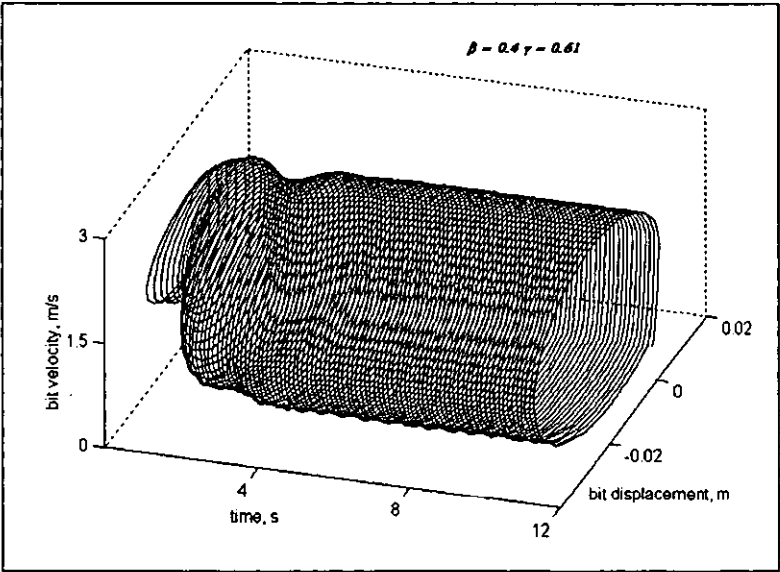


Time contained phase portrait of bit motion $\beta=0.4; \gamma=0.5$

Appendix 5- 5: System response for values of $0.6 \leq \gamma \leq 0.8$



Time contained phase plot of bit motion for $\beta=0.3$ and $\gamma=0.6$; $v=1.5 \text{ m/s}$

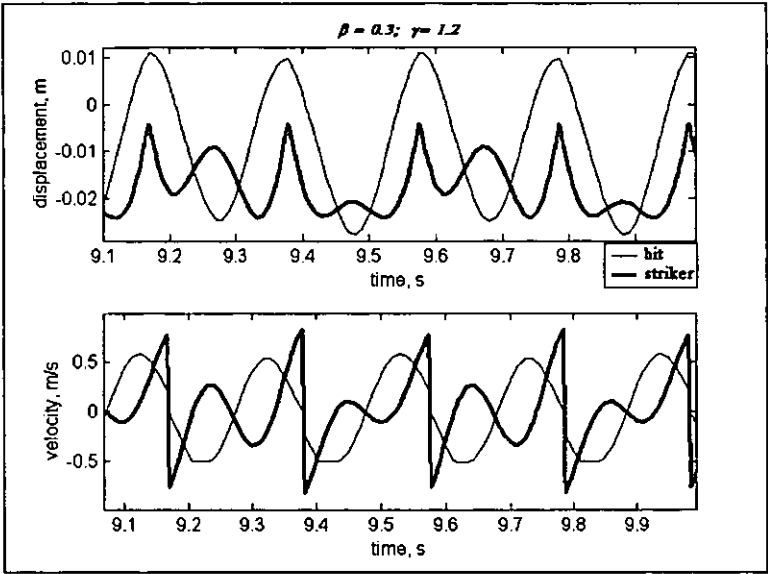


Time contained phase plane of the bit for $\beta=0.4$; $\gamma=0.61$

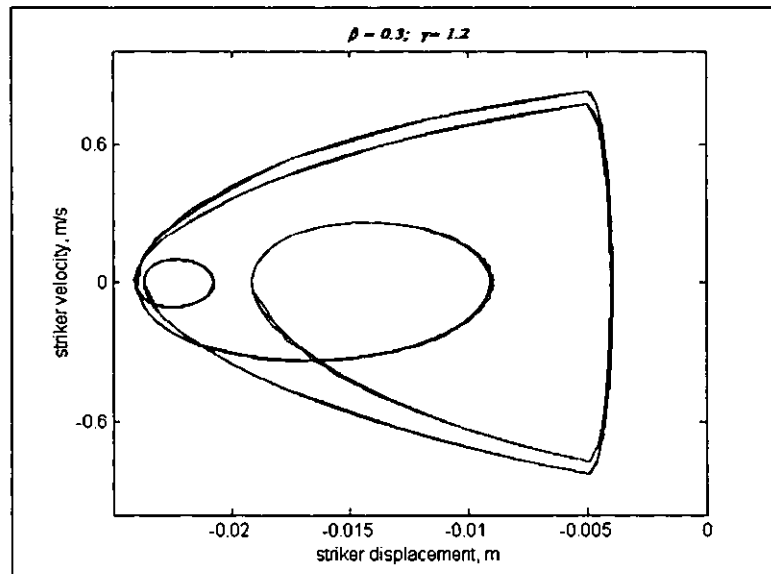
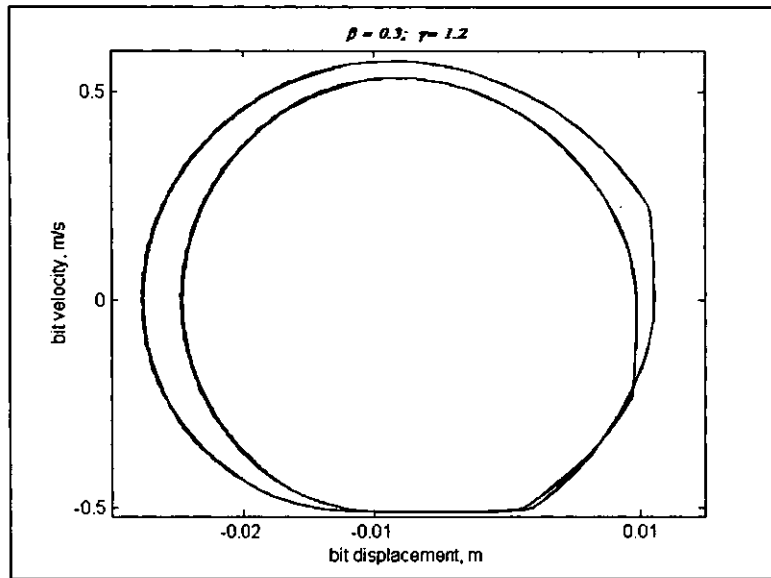
Appendix 5- 6: System response for values of $\gamma > 0.8$

Table A5. 1

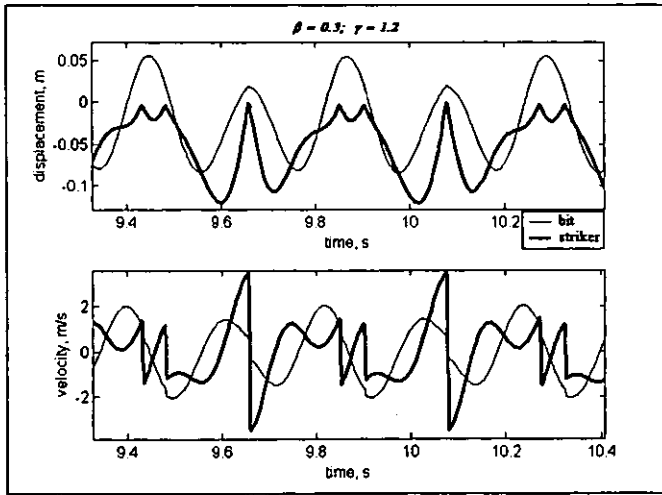
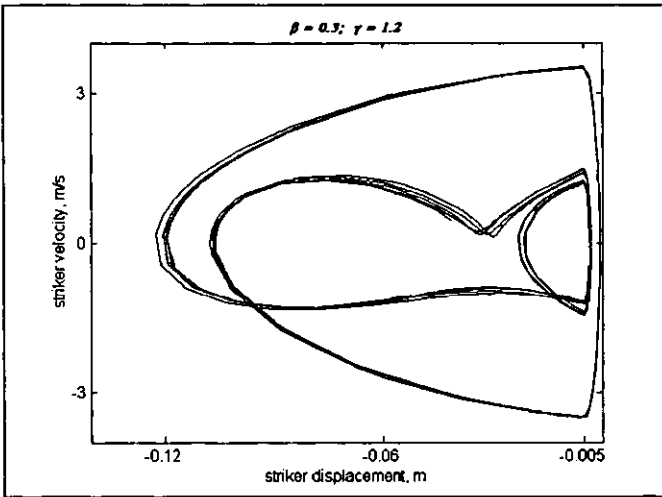
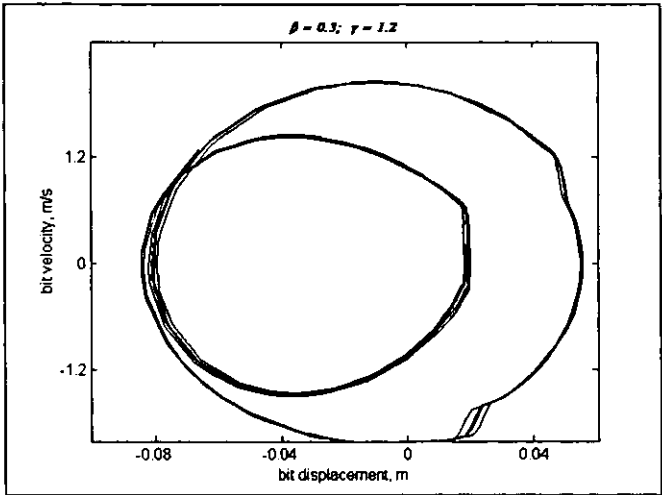
Parameter	Numerical values
Driving velocity, m/s	$v = 1.5$ (unless specified)
Mass, kg	$m_I = 250$;
Stiffness, N/m	$k_I = 156250$
Viscous damping, Ns/m	$c_I = 250$ (unless specified)
Ratio	$\beta = 0.3$; $\gamma = \text{variable}$



System response for $\beta=0.3$ and $\gamma=1.2$ with displacement and velocity profile



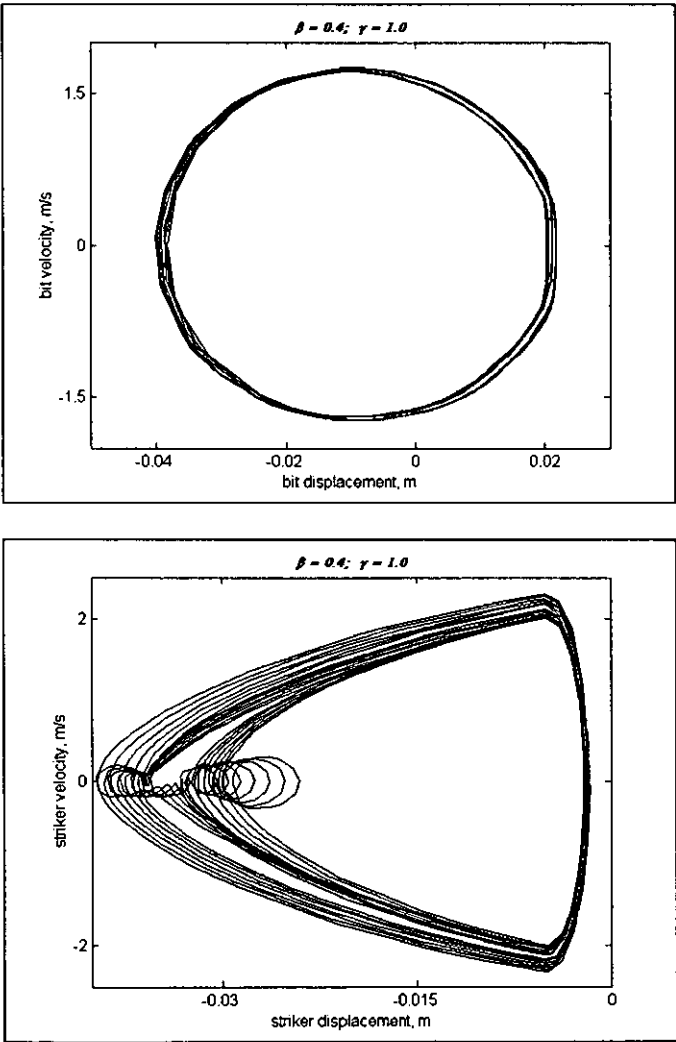
System response for $\beta=0.3$ and $\gamma=1.2$ Phase portraits



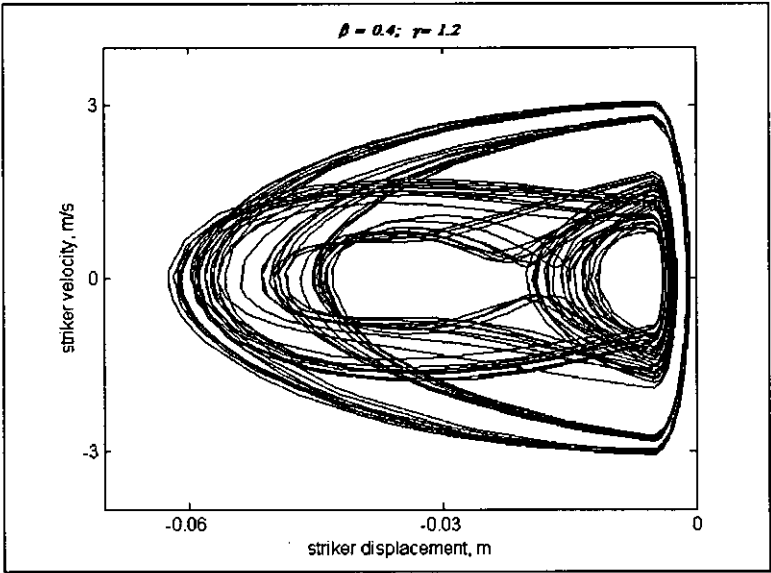
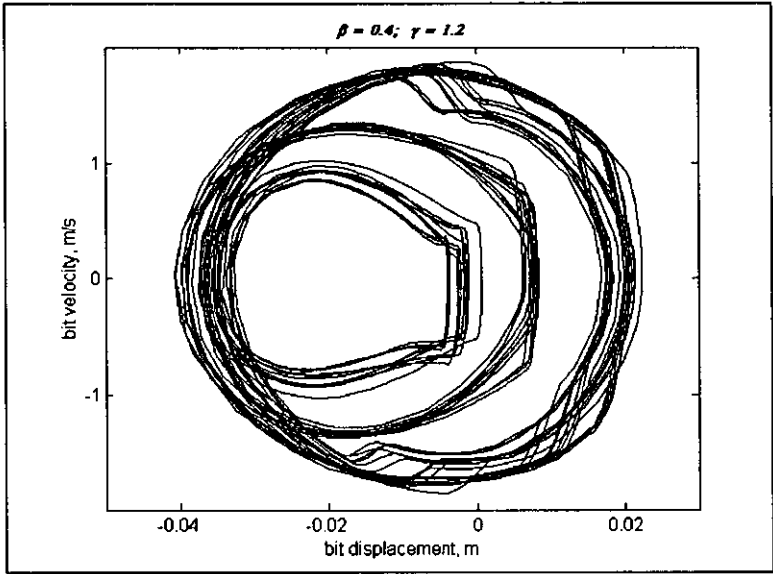
Same as previous, with 30% of the damping applied

Table A5. 2

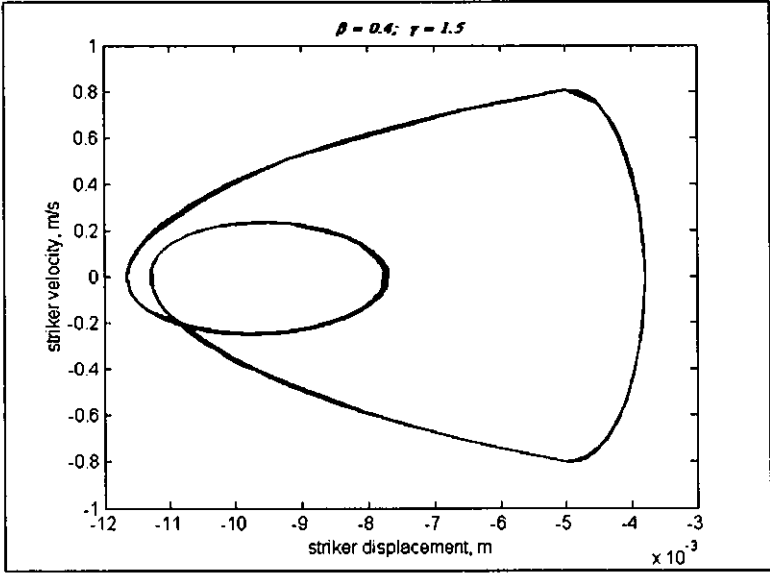
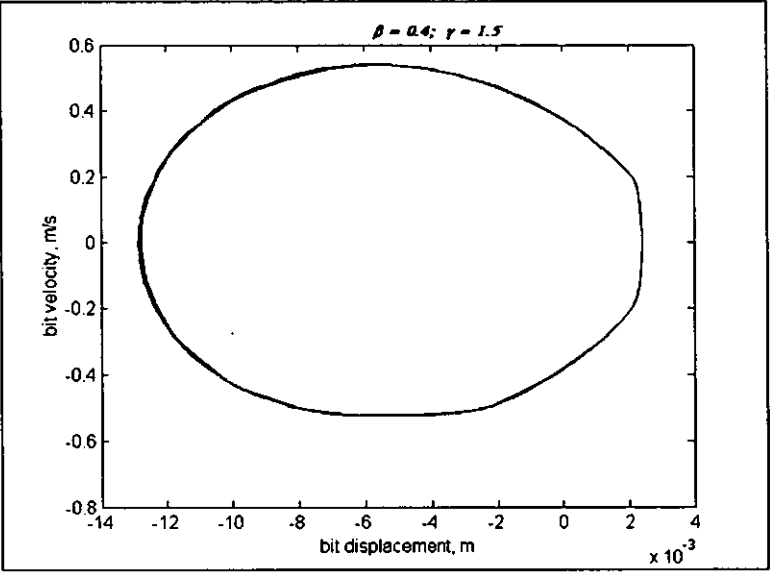
Parameter	Numerical values
Driving velocity, m/s	$v = 1.5$ (unless specified)
Mass, kg	$m_I = 250$;
Stiffness, N/m	$k_I = 625000$
Viscous damping, Ns/m	$c_I = 250$ (unless specified)
Ratio	$\beta = 0.4$; $\gamma = \text{variable}$



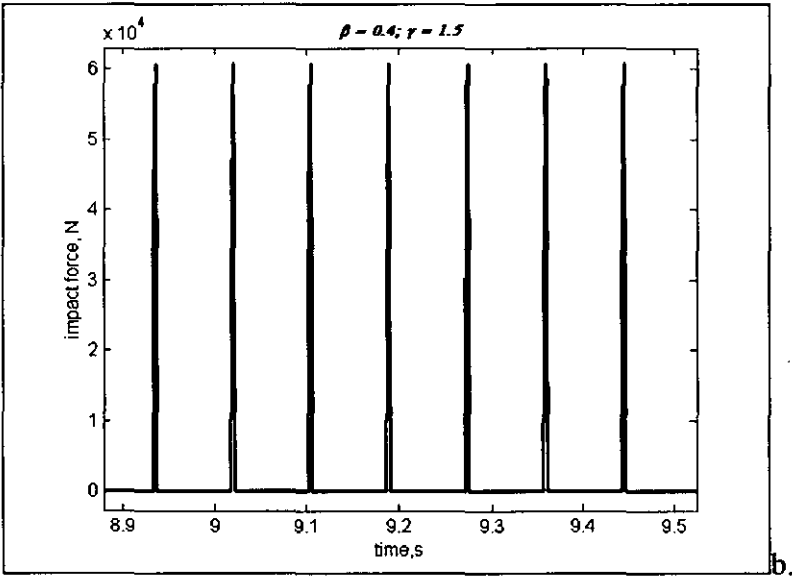
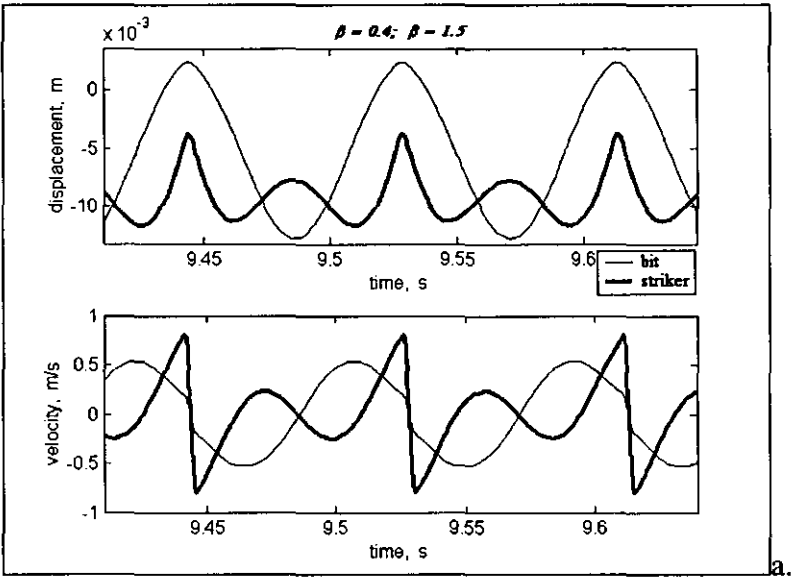
Motion of the system for $\beta=0.4$ and $\gamma=1.0$



Motion of the system for $\beta=0.4$ and $\gamma=1.2$



Motion of the system for $\beta=0.4$ and $\gamma=1.5$



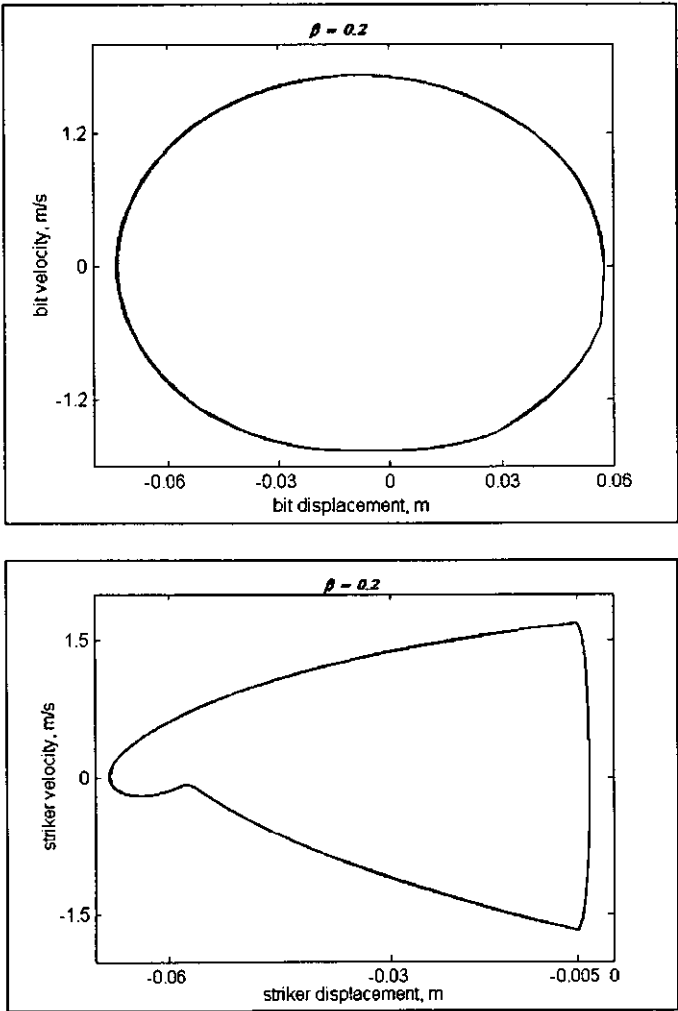
System displacement and velocity profile (a.) and developed impact force (b.)
for $\beta=0.4$ and $\gamma=1.5$

Appendix 5- 7: Effect of Mass ratio on system response.

$\beta \leq 0.25$

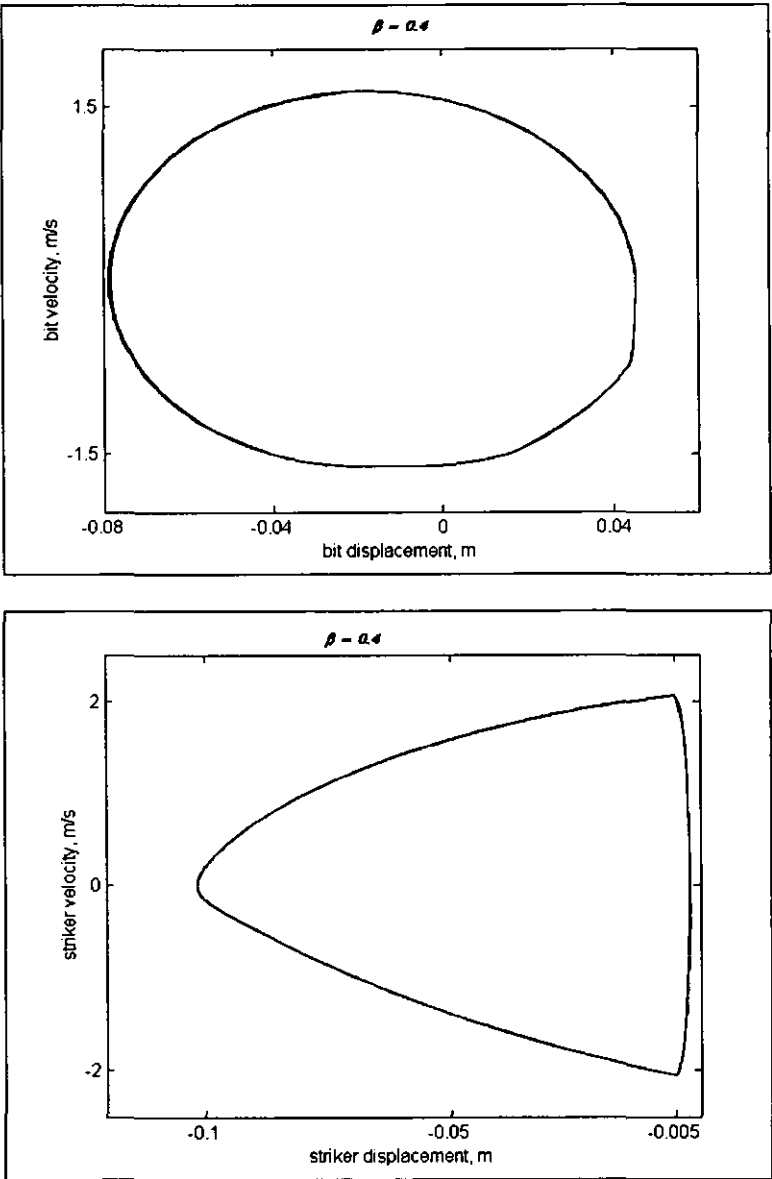
Table A5. 3

Parameter	Numerical values
Driving velocity, m/s	$v = 1.5$ (unless specified)
Mass, kg	$m_I = 250$;
Stiffness, N/m	$k_I = 156250$
Viscous damping, Ns/m	$c_I = 250$ (unless specified)
Ratio	$\gamma = 0.75$; $\beta = \text{variable}$



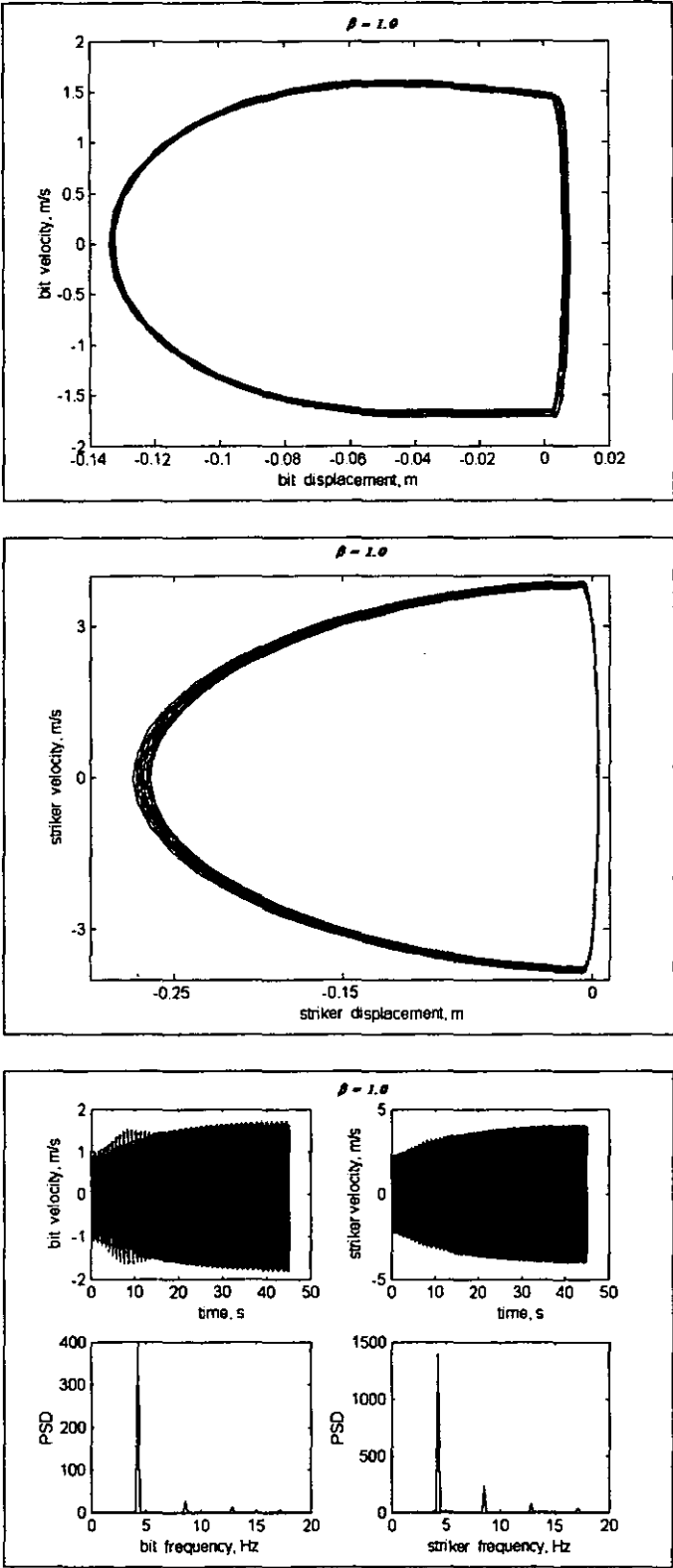
System response for $\beta=0.2$

$0.25 < \beta \leq 0.6$

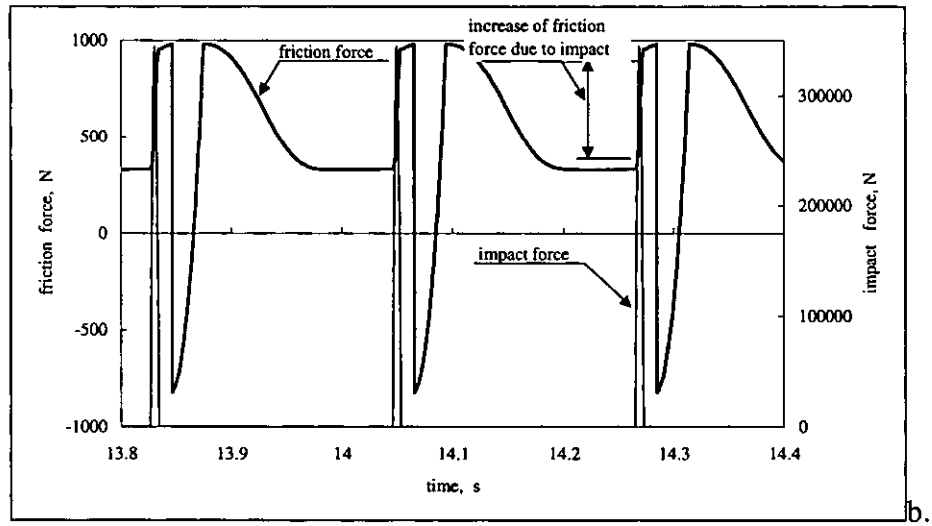
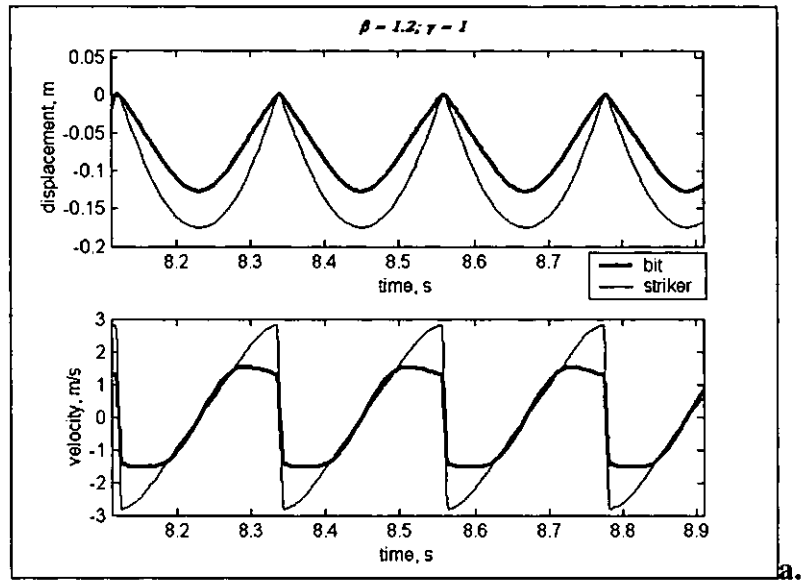


System response for $\beta=0.4$

$0.7 \leq \beta < 1.0$

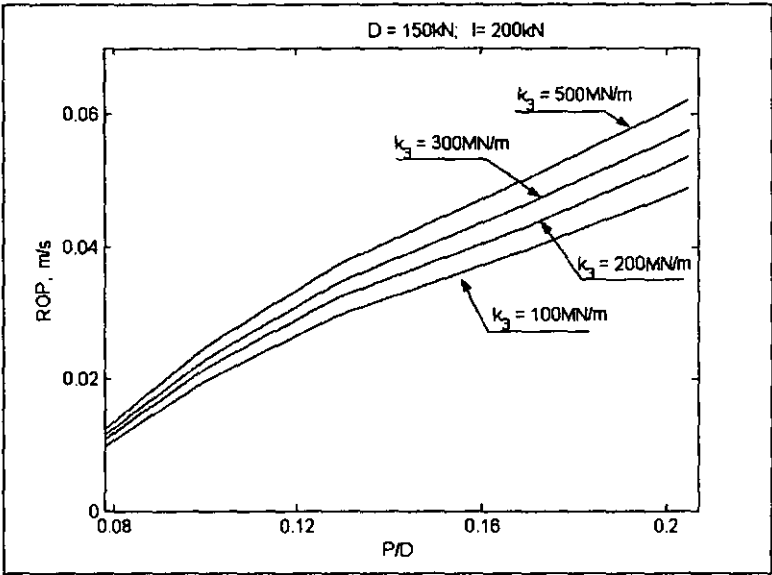


System response for $\beta=1.0$

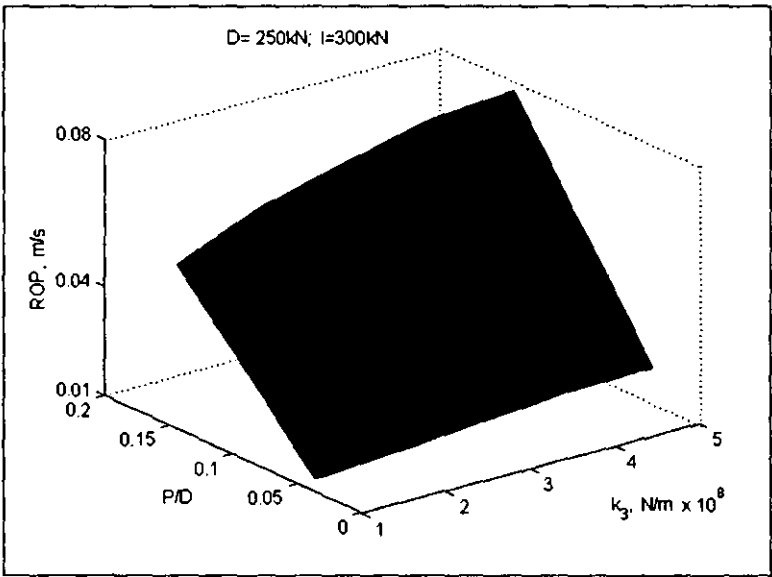


System response for $\beta=1.2$ and $\gamma=1.0$: a.- displacement and velocity profile;
b.- impact and friction force.

Appendix 6- 1: Effect of the stiffness of the medium on penetration rate

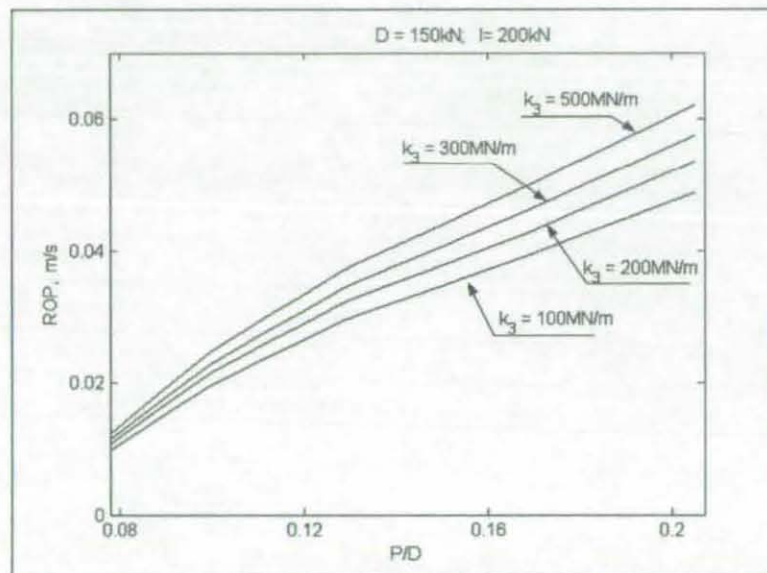


Rate of penetration for various values of the stiffness k_3

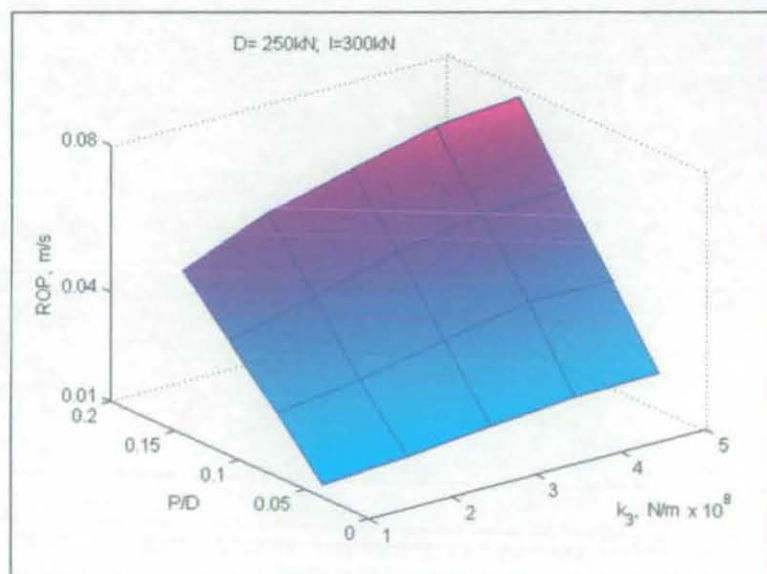


3-D plot of ROP as a function of stiffness k_3 and the relief of the thrust P/D

Appendix 6- 1: Effect of the stiffness of the medium on penetration rate

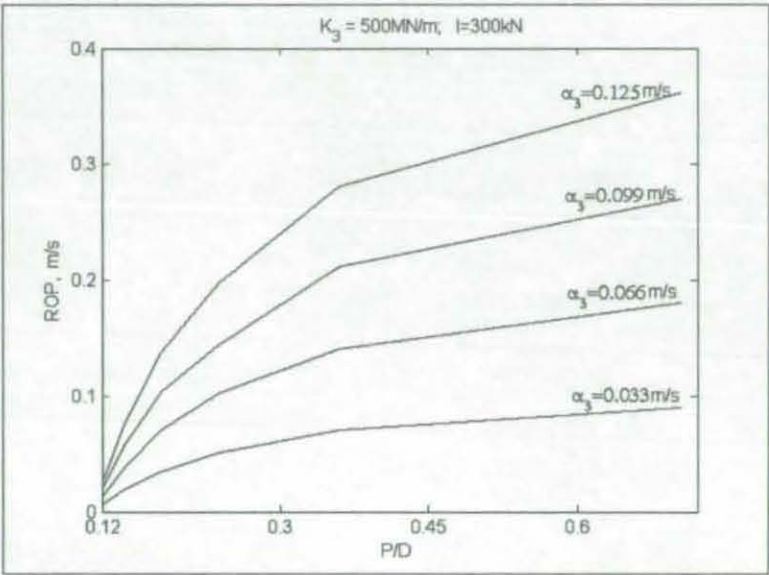


Rate of penetration for various values of the stiffness k_3

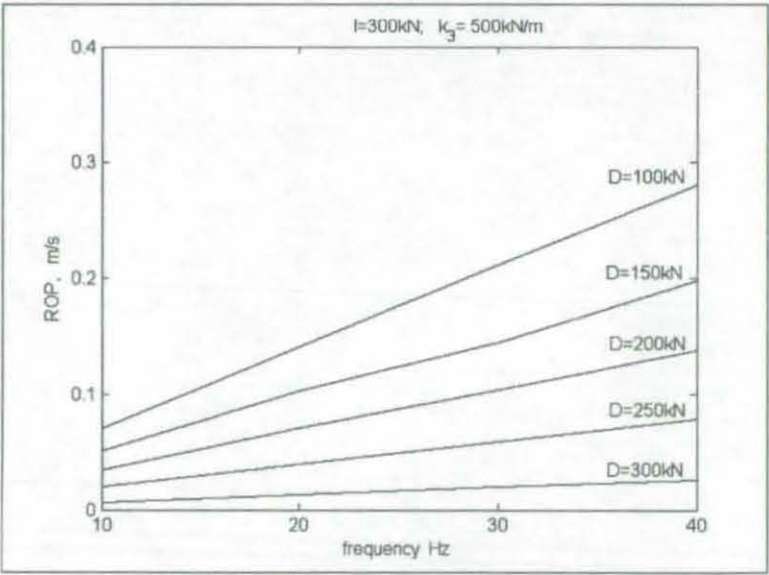


3-D plot of ROP as a function of stiffness k_3 and the relief of the thrust P/D

Appendix 6- 2: Influence of frequency of impact on penetration rate

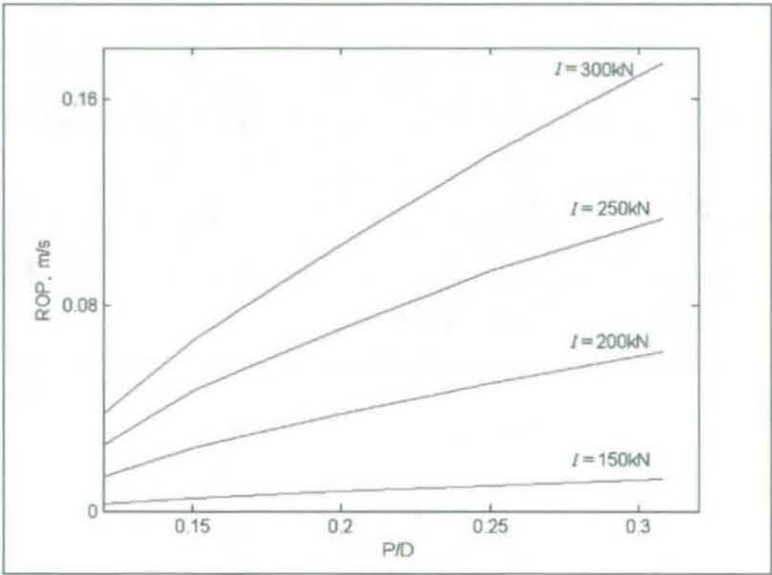


Rate of penetration for various values of vibration intensity α_3

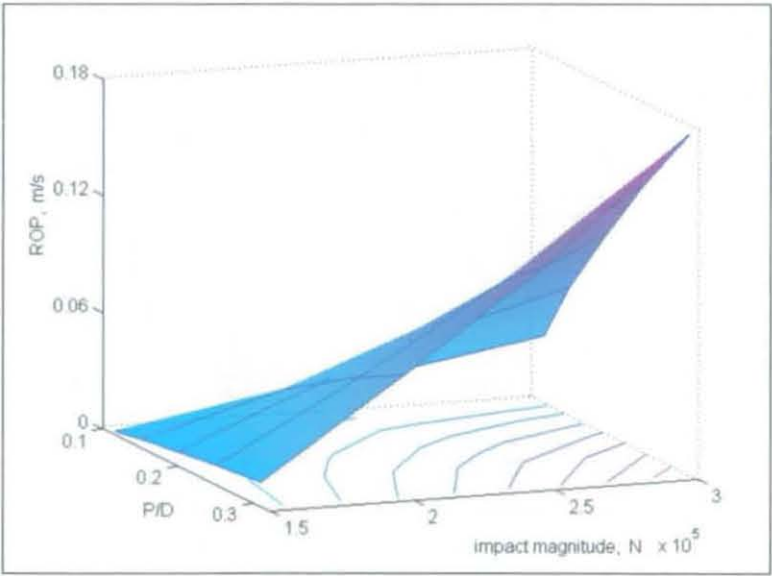


ROP for different threshold force D

Appendix 6-3: Effect of impulse magnitude on penetration rate



Rate of penetration for various magnitude of impact; $D=150$ and $k_3=50$



3-D plot of ROP as a function impact force magnitude and the relief of the thrust

